Nanoparticulate hydroxyapatite and calcium-based CO_2 sorbents

Matthew William Bilton

Submitted in accordance with the requirements for the degree of

Doctor of Philosophy

The University of Leeds
Institute for Materials Research
School of Process, Environmental and Materials Engineering
Leeds, LS2 9JT
United Kingdom

September 2012

The candidate confirms that the work submitted is his own, except where work which has formed part of jointly authored publications has been included. The contribution of the candidate and the other authors to this work has been explicitly indicated below. The candidate confirms that appropriate credit has been given within the thesis where reference has been made to the work of others.

List of Publications:

1. Bilton, M., A.P. Brown, and S.J. Milne, *Sol-gel synthesis and characterisation of nano-scale hydroxyapatite.* Journal of Physics: Conference Series, 2010. **241**(1).
2. Qaisar, S.A., M. Bilton, et al., *Sol-gel synthesis and TEM-EDX characterisation of hydroxyapatite nanoscale* powders modified by Mg, Sr or Ti. Journal of Physics Conference Series, 2010. **241** (1).
3. Bilton, M., A.P. Brown, and S.J. Milne, *Comparison of Hydrothermal and Sol-Gel Synthesis of Nano-Particulate Hydroxyapatite by Characterisation at the Bulk and Particle Level.* Open Journal of Inorganic Non-metallic Materials, 2012. **2**(1): p. 1-10.
4. Bilton, M., A.P. Brown, and S.J. Milne, *Investigating the optimum conditions for the formation of calcium oxide, used for CO_2 sequestration, by thermal decomposition of calcium acetate*. Journal of Physics: Conference Series, 2012. **371**(1).

All work contained within publications 1, 3 and 4 is directly attributable to M.W. Bilton, under the guidance of academic supervisors A.P. Brown and S.J. Milne. These publications directly relate to results presented and discussed in Chapters 4 and 5 of this thesis. Publication 2 is a co-authorship paper and M.W. Bilton is responsible for the data collection using TEM-EDX. Results of this publication are briefly discussed in the summary of Chapter 4 (Section 4.4) of this thesis.

Acknowledgements

I must firstly express my utmost gratitude to supervisors Dr Andrew Brown and Dr Steve Milne; without their continuous encouragement and unrivalled support, this project would not have been possible.

Secondly, I would like offer sincere thanks to all those who have provided me with experimental training and assistance throughout the course of this study, most notably Dr Mike Ward (Leeds Electron Microscopy and Spectroscopy Centre, LEMAS) for his assistance with TEM, and also Mr John Harrington and Dr Richard Walshaw (now of the School of Earth and Environment), for their assistance with SEM. I must kindly thank Dr Tim Comyn for his support with XRD, and also Dr Adrian Cunliffe, Miss Sara Dona (Energy Research Institute) and Mr Stuart Micklethwaite (now of LEMAS) for their assistance with TGA and FTIR spectroscopy. For data collection by LA-ICP-MS I would like to acknowledge Dr David Banks (School of Earth & Environment) and for XRF, Mr Nick Marsh (University of Leicester).

Further thanks must be expressed to Dr Lars Jeuken and undergraduate research students Gregory Dyson, Emma Horncastle and Jessica Jones of the Faculty of Biological Sciences, for their research on HA cytotoxicity.

Additionally, I would like to thank the numerous colleagues who have directly or indirectly provided me with support throughout this project, most notably Prof Rik Brydson, Dr Nicole Hondow, Dr Roger Molinder and soon-to-be Drs Rachel Wallace and Adam Qaisar, as well as the many past and present faces of room 1.19.

Finally, I would like to gratefully acknowledge the EPSRC for their sponsorship of this project.

Abstract

This thesis is focused on the development of synthesis and characterisation protocols for two different nanoparticulate materials; hydroxyapatite (HA), a biomaterial well recognised as chemically akin to human bone, and CaO, a material often used for the sequestration of CO_2 at elevated temperatures. For the analysis of these materials various bulk and particle level characterisation techniques have been employed, which are complemented by the versatile analytical methods available in the transmission electron microscope (TEM).

The first chapter of results reveal that a hydrothermal synthesis route achieved phase-pure nanoparticulate HA with Ca/P atomic ratios close to the stoichiometric target (1.67). Impure HA nanopowders were produced by a sol-gel synthesis route with analysis by X-ray diffraction (XRD) revealing secondary phases of calcium phosphates, $CaCO_3$ and CaO.

The Ca/P ratios of each powder were determined at the particle level using TEM with energy dispersive X-ray spectroscopy (TEM-EDX), having first established a threshold electron fluence below which significant electron-beam-induced alteration of the composition of HA does not occur. Results showed a greater variability of particle composition from the sol-gel preparation route compared to the hydrothermal route. This technique provides results in reasonable agreement to bulk Ca/P ratio analysis carried out by X-ray fluorescence (XRF) and laser ablation inductively coupled plasma mass spectrometry (LA-ICP-MS).

The second component of the thesis relates to the production of nanoparticulate CaO powder sorbents for the sequestration of CO_2 gas. The CaO nanopowders were produced by the thermal decomposition of calcium acetate

hydrate (CaAc); this process was analysed by thermogravimetric analysis (TGA) and by *in-situ* hot-stage XRD. The CO_2 uptake capability of the CaO powder sorbents was analysed by TGA following the reaction:

$$CaO + CO_2 \leftrightarrow CaCO_3 \quad (A.1)$$

Results showed a molar conversion ratio, χ (of CaO to $CaCO_3$) of 0.92, after 15 minutes of carbonation with structural analysis by SEM and TEM showing consistent growth and densification of rounded $CaCO_3$ crystals upon carbonation. Multiple cycles of carbonation and decarbonation were then carried out by TGA to investigate sorbent regenerability. A 0.32 decrease in χ was found after 9 cycles which is attributed to the sintering (reduction in surface area) of the sorbent with progressive decarbonations at 800 °C. Structural analysis of decarbonated samples extracted from the TGA, by XRD, SEM and TEM, highlighted the issue of sorbent hydration upon storage, sample preparation and analysis.

A TEM based technique has been developed for the structural analysis of multicycle CO_2 capture using an *ex-situ* environmental cell (E-cell). This technique allows for multicycle capture to be carried out and then analysed in the TEM with minimal exposure to the atmosphere, therefore providing a closer microstructural match to what occurs in the TGA. Results showed that slow, low-vacuum decarbonation (in the E-cell) creates a densified 'skeleton' of CaO, consistent with the drop in capture capacity observed by TGA.

Finally, modifications of CaO sorbents using spacer materials has been carried out with the aim of declining the decay in sorbent performance during multiple cycles of carbonation and decarbonation in the TGA. Promising results were found using CaO sorbents modified a commercial YSZ powder and also with $CaZrO_3/ZrO_2$.

Contents

List of figures

List of tables

List of abbreviations

Abbreviations

ACP	Amorphous calcium phosphate
BSE	Back-scattered electrons
CaAc	Calcium acetate hydrate
DCPA	Di-calcium phosphate anhydrate
DCPD	Di-calcium phosphate dihydrate
DLS	Dynamic light scattering
DMEM	Dulbecco's modified Eagle's medium
E-cell	Environmental heating cell
EDX	Energy dispersive X-ray analysis
FEG	Field emission gun
FTIR	Fourier transform infrared spectroscopy
FWHM	Full width at half maximum
HA	Hydroxyapatite
ICDD	International Centre for Diffraction Data
LA-ICP-MS	Laser ablation inductively coupled plasma mass spectrometry
SAED	Selected area electron diffraction
SE	Secondary electrons
SEM	Scanning electron microscope
STEM	Scanning transmission electron microscopy
TCP	Tri-calcium phosphate
TEM	Transmission electron microscope
TGA	Thermogravimetric analysis
XRD	X-ray diffraction
XRF	X-ray fluorescence
YSZ	Yttria stabilised zirconia

Chapter 1. Introduction

There is a significant push for the synthesis of nanoparticles with highly desirable properties that can be utilised in increasing applications, from biomedical materials through to industrial processes such as carbon capture and storage (CCS). In order to optimise the performance of nanoparticles it is important to develop commercially viable particle synthesis routes for producing a range of pure or chemically modified nanoscale materials. It is also therefore essential to develop careful characterisation protocols with which the chemical and physical properties of nanomaterials can be fully understood, both at the bulk and particle levels.

1.1. Aims

The overall aim of this project is to explore methods of nanoparticle characterisation. The first part of this project investigates two techniques for the synthesis of nanoparticulate hydroxyapatite (HA); hydrothermal and sol-gel synthesis. The aim of this study is to develop a protocol for the careful characterisation of the HA nanoparticles both in bulk and at the individual nanoparticle level. The latter achieved by developing a novel low-fluence analytical technique in the TEM that allows for the critical determination of particle composition (Ca/P ratio) without damaging the material by electron irradiation. Two phase pure and near-stoichiometric composition HA samples (Ca/P ratio = 1.67), prepared by the hydrothermal synthesis route, were subsequently exposed to in-vitro cell lines to measure their impact on cell viability (for potential biomedical applications).

The second part of this project is focussed on the development of CaO based nanoparticulate sorbents for the capture of CO_2 gas. The principle aim of this part of the study is to utilise various bulk and particle level analytical techniques to fully understand the thermal decomposition of calcium acetate hydrate, and also the carbonation and decarbonation processes of the resulting CaO. Firstly, the thermal decomposition of calcium acetate hydrate for the preparation of nanoparticulate CaO sorbents is assessed and understood. The multicycle carbonation-decarbonation performance of the decomposed CaAc was then measured and the products analysed. Finally the use of secondary particulate spacer-materials was utilised to modify the CaO powder sorbents with the aim of improving sorbent regenerability, by reducing sorbent sintering, upon multiple cycles of carbonation and decarbonation. For nanoscale analysis, a TEM technique will be developed utilising a self contained *ex-situ* environmental cell ('E-cell') that allows for multicycle CO_2 capture to be analysed on the same particle areas.

1.2. Objectives

- To prepare hydroxyapatite powders following hydrothermal and sol-gel synthesis routes.
- To characterise the HA powders prepared in-house using bulk and particle level techniques, and compare to a commercially available HA powder.
- To develop a new low fluence EDX technique for the representative compositional analysis of HA in the TEM.
- To examine HA powders prepared by the hydrothermal method for potential cytotoxicity to in-vitro cell lines.

- To analyse the thermal decomposition of calcium acetate for the production of nanoparticulate calcium oxide.
- To analyse the CO_2 capture capacity of nanoparticulate calcium oxide powder sorbents produced by the thermal decomposition of calcium acetate, using TGA.
- To examine the performance of nanoparticulate calcium oxide powder sorbents for CO_2 capture using a multicycle carbonation/decarbonation method by TGA.
- To develop an *ex-situ* TEM based technique (using an environmental cell) for the direct observation of the structural changes of a nanoparticulate calcium oxide powder sorbent during multicycle carbonation and decarbonation.
- To improve sorbent regenerability during the multicycle CO_2 capture process by modifying nanoparticulate calcium oxide powder sorbents with second phase, particle spacer, materials.

1.3. Chapter overview

This thesis presents a total of six Chapters. Chapter 1 provides an introduction to the work, with a subsequent outline of the project objectives. Chapter 2 presents a detailed review of previous work reporting the properties, synthesis techniques, characterisation and toxicity of nanoparticulate hydroxyapatite. This is followed by an overview of carbon capture and storage, and a review of the production and performance of current nanoparticulate CaO sorbents. The synthesis methods of both nanoparticulate hydroxyapatite and CaO sorbents are explained in Chapter 3,

along with the background science of the key characterisation techniques to be employed. Chapter 4 presents and discusses the results of the synthesis and characterisation of the hydroxyapatite powders produced in-house, and compares these to a commercial hydroxyapatite powder. The appendix of Chapter 4 presents and discusses results of nanotoxicity analysis performed on two hydrothermally synthesised hydroxyapatite powders exposed to in-vitro cell lines. The assays we undertaken by an undergraduate research group in the Faculty of Biological Sciences here at Leeds. Chapter 5 presents and discusses results of the production of nanoparticulate CaO powder sorbents used for the capture of CO_2. The recyclability of CaO powder sorbents during multicycle CO_2 capture is the discussed and sorbent-modifications are carried out with the aim of improving overall CO_2 capture performance. Additional research into the effects of hydration of nanoparticulate CaO is also discussed. Final conclusions and potential future work for this research are presented in Chapter 6.

2. Chapter 2. Literature review

2.1. Hydroxyapatite

2.1.1. Properties of hydroxyapatite

Hydroxyapatite (HA), $Ca_{10}(PO_4)_6(OH)_2$, is a form of calcium phosphate which most commonly exists, in a chemically modified form, as the main mineral found within bone and tooth enamel. Bone is typically composed of a combination of various apatitic materials, of which HA constitutes to about 70% in weight [1]. Additional components of bone include ions of carbonate (CO_3^{2-}), hydrogenophosphate (HPO_4^{2-}), sodium (Na^+), potassium (K^+), magnesium fluoride (MgF_2) and chloride (Cl^-) [1, 2].

Stoichiometric HA has a composition of 39.68 wt% Ca, 18.45 wt% P with a Ca/P weight ratio of 2.15 and Ca/P atomic ratio of 1.67, and within a pH range of 4.2 - 12.0 it exhibits a greater stability in aqueous media and at ambient temperatures compared to other calcium phosphate ceramics [3, 4]. Table 2.1 displays Ca/P ratios for alternative calcium phosphates compounds [4, 5]. Amorphous calcium phosphate (ACP, $Ca_x(PO_4)_y\ nH_2O$) is missing from the table as it is regarded as a microcrystalline mixture of other calcium phosphate compounds, and it has been suggested to be the initial phase formed in the early stages of HA mineralisation [2]. Amorphous calcium phosphate can most commonly exist in the form $Ca_9(PO_4)_6$ where the Ca/P ratio is 1.50 [6], however varying Ca/P ratios for ACP have been reported in the range 1.20 - 2.20 [4, 5].

Table 2.1: Ca/P ratios for various calcium phosphate compounds

Compound name	Molecular formula	Ca/P ratio
Monohydrate calcium phosphate (MCPH)	$Ca(H_2PO_4)_2 \cdot H_2O$	0.50
Monocalcium phosphate (MCP)	$Ca(H_2PO_4)_2$	0.50
Dicalcium phosphate dihydrate (DCPD)	$Ca(HPO_4) \cdot 2H_2O$	1.00
Dicalcium phosphate anhydrate (DCPA)	$Ca(HPO_4)$	1.00
Octacalcium phosphate (OCP)	$Ca_8H_2(PO_4)_6 \cdot 5H_2O$	1.33
Tricalcium phosphate (TCP)	α- and β- $Ca_3(PO_4)_2$ *	1.50
Hydroxyapatite (HA)	$Ca_{10}(PO_4)_6(OH)_2$	1.67

**α-TCP = monoclinic form, β-TCP = rhombohedral form*

The compositional similarities with bone provide HA with excellent biocompatibility properties and therefore it is utilised in many biomedical applications related to bone substitution and repair, however the mechanical properties of sintered HA, as displayed in Table 2.2, render the material unsuitable for load bearing applications: the fracture toughness (K_{Ic}) of HA does not exceed of 1.0 MPa $m^{½}$, whereas human bone = 2 – 12 MPa $m^{½}$. Additionally, the Weibull modulus (n) is low in wet environments (n = 5 – 12) which indicates a low reliability of HA implants [3]. A low Weibull modulus indicates a greater variability in the strength across seemingly identically produced samples mechanically tested under fixed conditions (i.e. there is increased likelihood of flaws and defects within the material) [7]. Therefore, HA is primarily utilised in non-load bearing applications, such as bioactive coatings or as materials for the development of scaffolds for bone tissue engineering [3, 8, 9].

Table 2.2: Mechanical properties of hydroxyapatite [3, 5, 10].

Property	**Typical Values**
Density (g cm^{-3})	3.15
Young's modulus (GPa)	85-90
Knoop Hardness (MPa)	3450
Tensile Strength (MPa m^{-2})	120
Poisson Coefficient	0.3
Thermal Expansion	11
Melting Point (°C)	1660
Specific Heat (cal g^{-1} K^{-1})	0.15
Thermal Conductivity (W cm^{-1} K^{-1})	0.01
Fracture Toughness (MPa $m^{½}$)	< 1.0
Weibull Modulus	5.0 - 12.0

The interest in the use of HA as a material for bone implantation increased in the 1980's and 1990's, leading HA to be utilised in various areas including spinal fusion, craniomaxillofacial reconstruction, treatment of bone defects, fracture treatment, total joint replacement (bone augmentation) and revision surgery [11-16]. More recent applications of HA include tissue scaffolds [17-19], tubule infiltration in dentine [20, 21], enamel and dentine remineralisation [22], dental and orthopaedic implants and coatings [3, 23] and as matrices for controlled drug release [24, 25]. Hydroxyapatite is also utilised in many non-biomedical applications such as packing media for column chromatography, gas sensors, catalysis and as host materials for lasers [26, 27].

Many applications of synthetic HA require careful control of the particle size, shape and phase. The use of nano-scale HA allows for better tissue integration and heightened biocompatibility with bone which itself contains nano-scale HA crystals ordered within a collagen fibre matrix [28].

Global interest in HA synthesis and it's applications, most notably with regards to biomedical uses, has significantly increased in recent years as shown from the rising numbers of HA-based papers currently being published per year (Figure 2.1); since 2008 over 4,000 papers have been published per year, in comparison to < 2,000 papers per year from 2000 to 2008, and < 1000 papers per year prior.

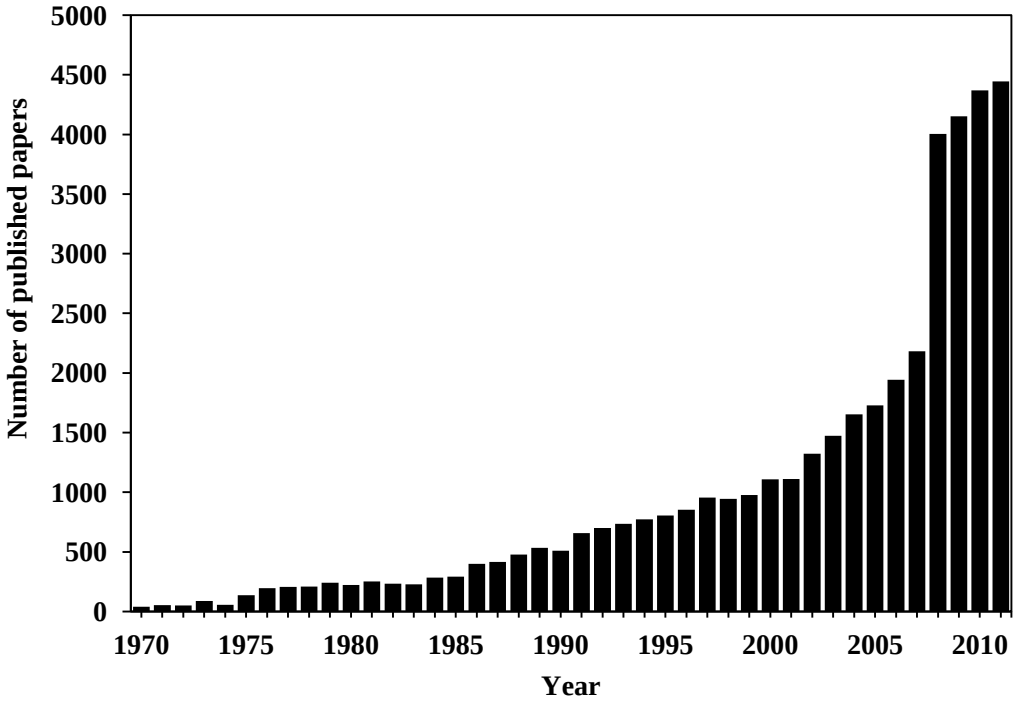

Figure 2.1: Approximate number of papers published per year on hydroxyapatite from 1970 to 2011. Data collected from Thomson Reuters Web of Knowledge, keyword: "hydroxyapatite".

2.1.2. The structure of hydroxyapatite

In 1926, de Jong was the first to report the similarities between the X-ray diffraction patterns of bone mineral and the calcium phosphate compound, hydroxyapatite [29].

The crystallographic structure of HA was first identified in the 1930's, with the structure shown to comprise of units of Ca^{2+}, $(PO_4)^{3-}$ and OH^- [30-32]. Further refinement of the HA structure was carried out in the 1950's and 1960's where it was found that the presence of carbonate in bone and tooth mineral and HA can be observed directly using infrared spectroscopy and indirectly using X-ray diffraction [11, 33-36]. Figure 2.2 displays the powder X-ray diffraction reference (ICDD) file for hydroxyapatite as reported by Sudarsanan and Young in 1969 [37].

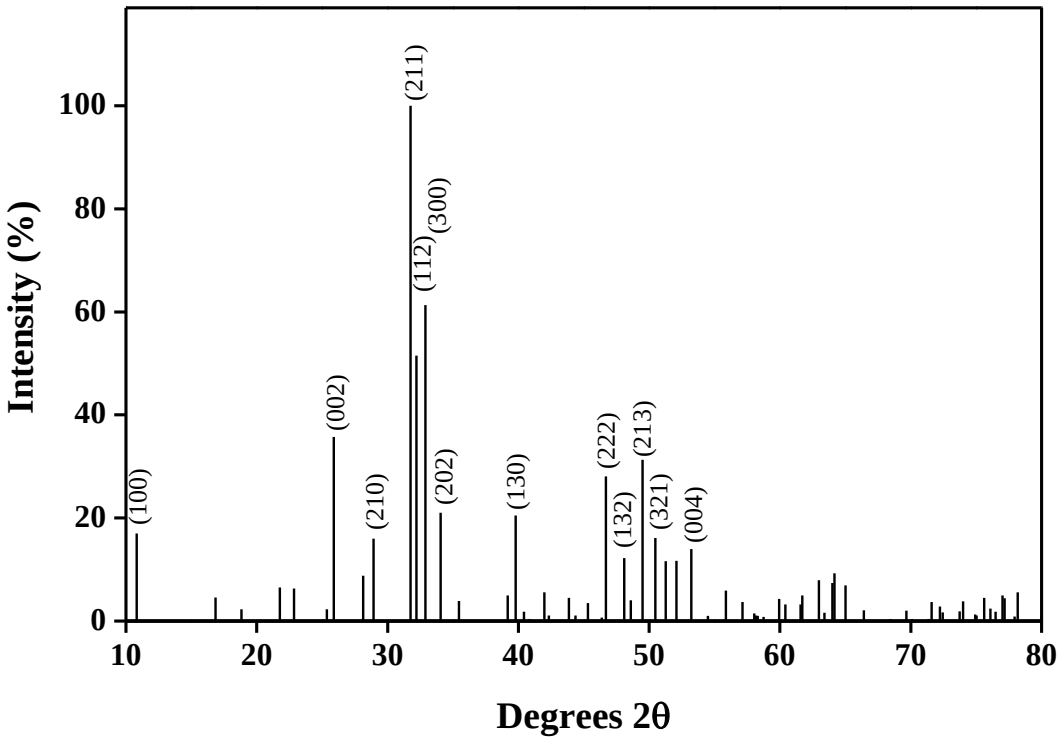

Figure 2.2: XRD peak data for hydroxyapatite from ICDD ref: 01-074-0566 [37].

Hydroxyapatite exhibits a hexagonal space group $P6_3/m$ where $a = b \neq c$ (a = 0.943 nm and c = 0.688 nm), $\alpha = \beta = 90°$ and $\gamma = 120°$ [34, 36]. Figure 2.3 displays the hexagonal nature of hydroxyapatite as produced using the CrystalMaker software [36, 38]. One distinctive feature of the HA structure are columns of OH, which occur parallel to the c axis at the edges of the unit cell [36]. These columns pass through the centres of alternating Ca atoms with 3-fold trigonal planar coordination, at z = ¼ and ¾, and successive rotations of 60° observed about the c axis, see Figure 2.3b. The repetition of this pattern leads an OH-channel where the building unit is formed by two monopyramidal polyhedra; each with a triangular base (labelled *i* and *ii* in Figure 2.3b) and occupied by three Ca atoms and one OH [38]. These equivalent Ca atoms are termed Ca(I) in Figure 2.3, with 6 Ca(I) atoms found per unit cell [27, 38].

Additional Ca atoms (termed Ca(II)) are equivalent at z = 0 an ½. These Ca(II) atoms form columns which pass through the centre of alternating triangles of O atoms (termed O(I) and O(II) atoms), see Figure 2.3c. In total, crystalline HA has 10 cation (Ca^{2+}) sites arranged in two non-equivalent positions within the unit cell, six Ca(I) atoms and four Ca(II) atoms [38]. The Ca(II) and OH columns within the hexagonal symmetry subsequently give rise to a honeycomb structure centred around the OH-columns as visible in Figure 2.3a [38].

Another notable feature of the HA structure is the tetrahedral form of phosphate (PO_4^{3-}), see Figure 2.3a. These tetrahedra form basic structural units that do not corner share oxygen atoms, they are held together, instead, by the bridging Ca(II) atoms [34, 39, 40]. The HA unit cell comprises of six PO_4 tetrahedrons, with the central P atoms found at z = ¼ and ¾, see Figure 2.3a [27, 38].

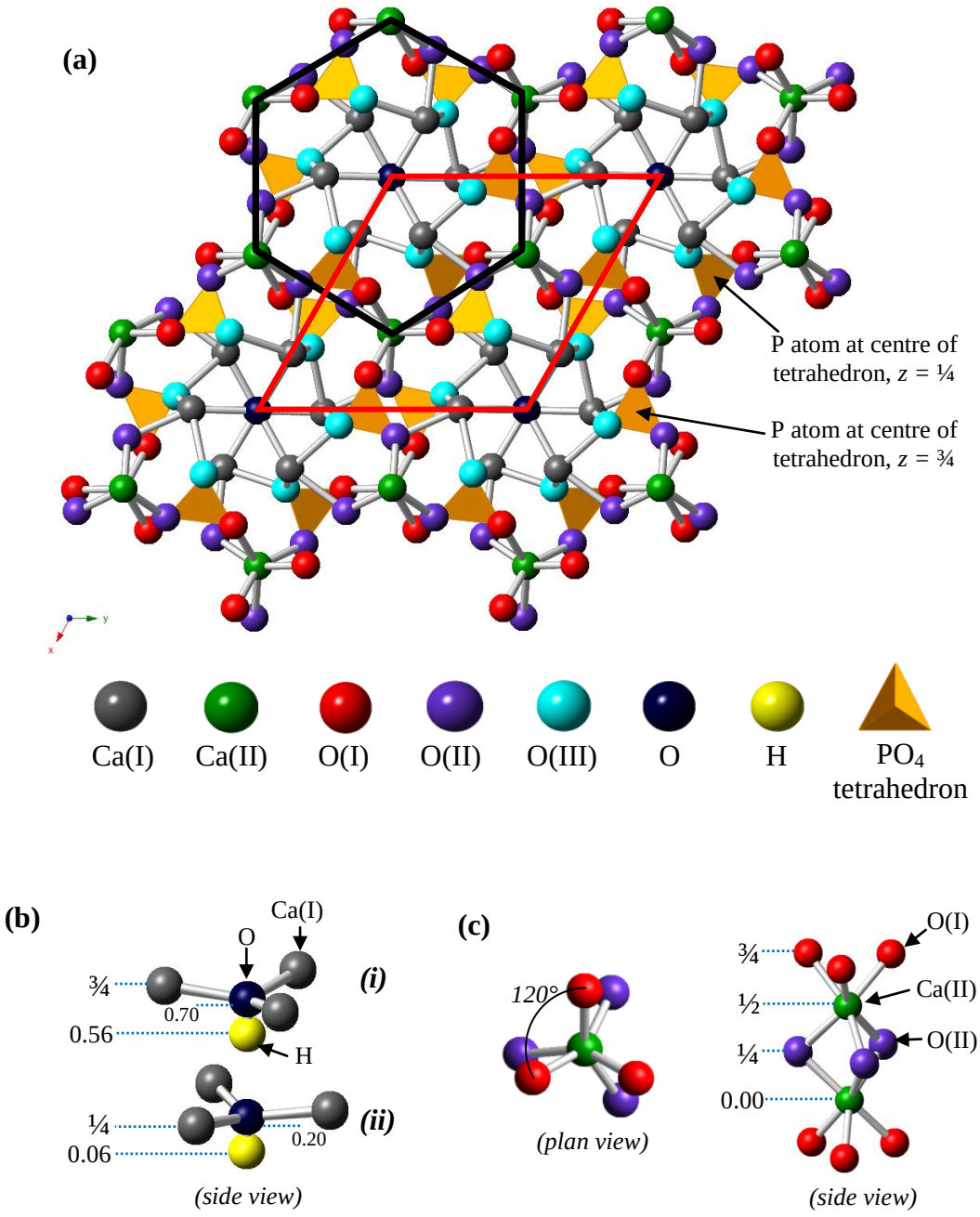

Figure 2.3: Pure HA structural model: (a) plan view with unit cell highlighted by red line, (b) amplified side view of adjacent (*i* and *ii*) Ca(I)- hydroxyl monopyramidal polyhedra with fractional heights of atoms labelled, and (c) amplified plan and side view of Ca(II) column, with fractional heights of atoms labelled. Data modified using CrystalMaker® from [36, 38].

One of the main structural characteristics of HA is its ability to allow a large amount of isomorphic substitutions whilst always maintaining its hexagonal space group [41]. The Ca^{2+}, OH^- and $(PO_4)^{3-}$ ions within the HA structure can be substituted for divalent cations including Zn^{2+}, Fe^{2+}, Cu^{2+}, Mg^{2+}, Ni^{2+}, Cr^{2+}, Mn^{2+}, Co^{2+}, Sr^{2+}, Pb^{2+} and Cd^{2+}, and anions including F^-, Cl^-, CO_3^{2-} and VO_4^{3-} [38]. Such substitutions modify the thermal stability, the solubility, textural properties and the surface reactivity of HA [38]. Table 2.3 highlights some other possible substitutions, with respect to the following general formula:

$$Me_{10}(XO_4)_6(Y)_2 \qquad (2.1)$$

Imbalances in charge of the substituting ion can generate disorder within the HA and require a change in total anionic charge to maintain charge balance [11, 42].

Table 2.3: Some examples of substitutional ions in the HA structure [11, 38, 42, 43]

Me			**XO_4**			**Y**		
REE^{3+}	Ca^{2+}	Na^+	SiO_4^{4-}	PO_4^{3-}	SO_4^{2-}	CO_3^{2-}	OH^-	O_2^-
	Sr^{2+}	K^+		AsO_4^{3-}	HPO_4^{2-}	S_2^{2-}	F^-	H_2O
	Pb^{2+}			CO_3F^{3-}	CO_3^{2-}	O^{2-}	Cl^-	N_2
	Mg^{2+}			VO_4^{3-}			I^-	
	Ba^{2+}						Br^-	
	Mn^{2+}							
	Zn^{2+}							
	Fe^{2+}							
	Cu^{2+}							
	Ni^{2+}							
	Cr^{2+}							
	Co^{2+}							
	Pb^{2+}							
	Cd^{2+}							

2.2. Hydroxyapatite synthesis

There are two principal methods for the synthesis of hydroxyapatite: solid-state synthesis and wet chemical methods. Well crystallised powders are often produced via solid-state [44, 45] reactions however these require high temperatures (typically 1000 °C or higher) and long heat treatment times (> 24 hours). Wet-chemical methods offer lower temperature synthesis reactions from component oxides/carbonates, these include: precipitation [46-48], hydrothermal synthesis [49-58] and solution-gelation (sol-gel) [1, 26, 59-73]. Hydrothermal and sol-gel techniques will be discussed further in Sections 2.2.1 and 2.2.2 respectively.

Low temperature precipitation techniques (typically < 100 °C) can provide nanoparticulate HA of various morphology (blade, rods, needles or equiaxed shaped particles) however the Ca/P ratio and crystallinity of these powders is highly dependent on the preparation conditions, with most cases reporting Ca/P ratio's lower than the stoichiometric target (1.67) [3, 46-48].

Alternate preparation techniques include electro-crystallisation, spray-pyrolysis, freeze-drying [74], microwave irradiation [75, 76], mechano-chemical methods and emulsion processing [3].

2.2.1. Hydrothermal synthesis

Hydrothermal synthesis describes a nano-particle preparation route which utilises heat and pressure to instigate a reaction between reagents dissolved in water, or solvent (solvothermal), often carried out within a sealed hydrothermal pressure vessel [52, 53]. These conditions open up reaction chemistry not accessible under ambient conditions, and crystalline HA can be produced without the requirement for

post reaction calcination. The technique is beneficial due to its low running cost and simple operation, and is attractive for HA synthesis as it produces regular nanosized particles with minimal or no agglomeration [49].

Hydrothermal pressure vessels are typically thick-walled steel cylinders designed to operate at mild reaction temperatures and high pressure, and are Teflon lined to work inertly with respect to water and solvents. A typical general purpose Parr produced hydrothermal reactor has a maximum working temperature of 350 °C, and maximum working pressure of 200 bar [77].

A high degree of crystallinity and stoichiometry in HA can be obtained through hydrothermal methods [3]. Needle or blade shaped HA particles are often reported ranging from the nano to the micrometer scale in size [3, 49-58]. Particle size is controlled by the low temperature (often < 100 °C) hydrolysis of the phosphate precursor during preparation and it is often found that stoichiometry is inconsistent after hydrolysis, with Ca/P ratios ranging from 1.50 to 1.71 [3]. Increasing the pH of the starting suspensions has demonstrated more controlled growth of smaller crystalline HA particles, with improved stoichiometry [56, 57]. Particle morphology is considered more controllable by the hydrothermal route in comparison to alternate methods, such as solid-state and wet-chemical processes, with greater particle homogeneity often achieved [52].

Typical hydrothermal routes for HA synthesis utilise preparation temperatures between 100 and 200 °C and pressures between 1 and 2 MPa; these conditions produce HA with rod, needle or whisker morphologies ranging in lengths from < 100 nm to > 1 μm [49-58]. The technique offers high particle crystallinity and a Ca/P ratio close to the stoichiometric target (1.67) [49, 78].

2.2.2. Solution-gelation synthesis

Solution-gelation (sol-gel) chemistry describes the process of metal alkoxides converted to amorphous gels of metal oxides via hydrolysis and condensation reactions [79]. The sol-gel process was first identified by Ebelman in 1846 [80] and has since been utilised for the production of ceramic powders, coatings and also bulk materials such as glasses [81].

Hydroxyapatite can be typically produced via a widely used sol-gel method whereby chemical reactions take place between calcium and phosphorus ions under a controlled pH and solution temperature [26]. Many calcium and phosphorus precursors have been used for HA synthesis all of which vary in chemical activity (hydrolysis, polycondensation etc); most commonly these include calcium diethoxide, calcium acetate and calcium nitrate, and triethyl phosphate, triethyl phosphite and ammonium dihydrogen phosphate [26, 60-62]. It is recognised that the temperature required to develop the apatitic structure is dependent on the chemical activity of the precursors used in the sol, with reports of a typical gel calcination temperature range of 300 - 1100 °C to produce a crystalline stoichiometric (Ca/P = 1.67) apatitic structure, depending on the precursors used [1, 26, 60-66, 68-71].

Deviations from stoichiometry in the final product can often occur through fast titration of the phosphate solution, and Ca-deficient HA can often form in low pH (< 9) solutions [26]. However, this can prove advantageous as Ca-deficient materials, such as TCP (Ca/P = 1.50), are more resorbable by bone than HA and have displayed beneficial properties with regards to the promotion of bone regrowth [67].

Phosphorous alkoxides are popular precursors for sol-gel HA preparations, with triethyl phosphite ($C_6H_{15}PO_3$) [26, 65-69] and triethyl phosphate ($C_6H_{15}PO_4$) [1, 60] most commonly utilised. Triethyl phosphite is often preferred over triethyl phosphate due to its higher hydrolysis activity and a shorter time period needed to develop the HA phase [26]. Development of the HA phase during sol-gel synthesis methods is promoted by solution aging, for example phosphorus-31 nuclear magnetic resonance (31P NMR) spectroscopy has shown a valence transition from P (III) to P (V) upon aging a solution of triethyl phosphite and calcium diethoxide, at the formation of HA after 24 hours [68]. This suggests a nucleophilic addition of negatively charged OH^- groups to the positively charged metal P that subsequently leads to an increased coordination number of the phosphorus atom, and is indicative of a polymerisation reaction [26, 68].

Sol-gel synthesis can involve either an ethanol-based or aqueous-based preparation route. Ethanol based synthesis has been shown to provide a thermally stable HA phase, whereas aqueous-based preparation can result in a calcium-deficient material [26]. A typical aqueous-based synthesis route is described in [69]. Triethyl phosphite is firstly diluted in a fixed amount of water and stirred vigorously until completion of hydrolysis. A stoichiometric amount of calcium nitrate is diluted in 25 ml of water and subsequently added drop-wise into the phosphite sol with continuous stirring for a further 4 min and then statically aged at 50 °C for 125 minutes. Further treatment at ~85 °C results in a dry white gel which can be ground with a pestle and mortar and subsequently calcined in a furnace at desired temperatures. Similarly, HA has also been prepared using triethyl phosphate and calcium acetate precursors [79].

Sol-gel synthesis offers a greater flexibility over solid state reaction, hydrothermal and wet precipitation techniques with respect to molecular level

mixing of the calcium and phosphorus precursors, which allows for improved homogeneity of the resulting HA to a significant extent [26]. Sol-gel methods are often preferred for the production of HA used for prosthesis coatings as the technique allows for the production of crystalline and phase pure coatings with good adhesive properties and which are thin enough (typically < 1 μm) to avoid complications such as cracking and delamination [68, 81]. Furthermore, sol-gel offers a lower temperature preparation route (typically < 800 °C) for HA coatings than alternative methods such as thermal spraying (typically > 1000 °C) [81-83], avoiding complications with structural instability which HA experiences at higher temperatures [68].

The thermal spraying method for preparing HA coatings utilises a plasma or ionised gas (typically argon) to partially melt and carry hydroxyapatite particulates in a high-temperature plasma-gas stream. This gas-stream is then accelerated towards the substrate; creating a coating which typically contains a mixture of crystalline HA, amorphous HA and tricalcium phosphate phases to a thickness of between 50 and 200 μm [81, 84, 85]. Several disadvantages of the technique include poor adhesion, non-uniform thickness, poor crystallinity, poor integrity, uneven resorption, mechanical failure and increased prosthesis wear [5].

2.3. Hydroxyapatite characterisation

Various bulk and particle level analysis techniques have been utilised for HA characterisation; bulk compositional characterisation methods include X-ray diffraction (XRD), X-ray fluorescence (XRF), Fourier transform infrared spectroscopy (FTIR) and laser ablation inductively coupled plasma mass spectrometry (LA-ICP-MS). X-ray diffraction provides details of the crystal phases present in a sample (phase purity) and also the materials crystallinity [86]. Fourier

transform infrared spectroscopy typically identifies functional groups present within a sample, and it is often used for the identification of carbonate within apatitic materials [87, 88]. X-ray fluorescence and ICP-MS are typically employed in HA characterisation for the determination of the bulk Ca/P ratio [89, 90].

At a particle level, scanning electron microscopy (SEM) and transmission electron microscopy (TEM) techniques are employed for direct nanoparticle imaging, providing details of particle size, shape and atomic configuration (in the TEM) [91, 92]. Spectroscopic techniques such as energy dispersive X-ray analysis (EDX) in the SEM and TEM can provide estimates of a samples elemental composition. Electron diffraction in the TEM provides a useful tool for the confirmation of a materials structure and crystallinity [93]. Analysis by TEM offers a greater resolution (~0.1 nm) than in the SEM (~10 nm) and, with a smaller interaction volume of the electron beam with the sample, TEM-EDX can allow for the analysis of individual nanoparticles, enabling structural and compositional variability that may not be detected by SEM or the bulk characterisation techniques such as XRD, XRF, FTIR and LA-ICP-MS, to be identified.

The principles of these characterisation methods are discussed in more detail in Chapter 3.

2.3.1. Electron fluence

Electron fluence can be defined as the number of electrons per unit area (electrons nm^{-2}) which, in a TEM, can be controlled using a condenser aperture, spot size and exposure time. With respect to many materials, including HA, exposure using a high energy (typically > 5 keV) electron beam can induce damage in terms of changes in structure (e.g. atomic displacement) and composition [93-95]. Work

by Eddisford *et al* (2008) investigated the effects of electron fluence on the Ca/P atomic ratio in HA, and showed that a fluence above 100 x 10^6 electrons nm^{-2} at 200 keV induces a radiolytic damage process involving phosphorus and oxygen loss, amorphisation and eventual re-crystallisation to calcium oxide (CaO) [94]. The damage is the result of ions in the HA structure, excited by electrons, not returning to their original electronic state upon de-excitation i.e. crystallinity is lost beyond a recoverable limit due to the extensive movement of the atoms once chemical bonds have been broken by the excitation. The bond breaking subsequently results in mass loss, particularly amongst lighter atoms such as hydrogen, oxygen, and even phosphorus [95].

Results collected by Eddisford are shown in Figure 2.4 and display the Ca/P ratio of HA as a function of cumulative fluence for current densities varying between 0.2 A/cm^2 and 24 A/cm^2, measured on a high density field emission gun (FEG-) TEM (FEI CM200). The change in Ca/P ratio is observed as relatively constant up to a electron fluence of 100 x 10^6 electrons nm^{-2}, beyond this 'threshold' the Ca/P ratio can be seen to rapidly increase from the expected stoichiometric HA baseline (~1.67) as radiolytic damage accelerates [94].

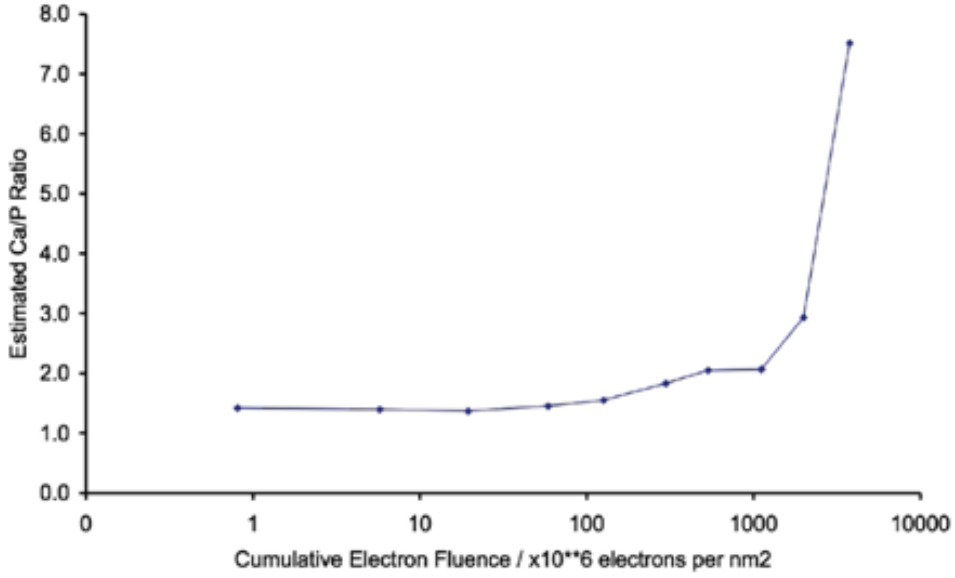

Figure 2.4: EDX Ca/P ratio in HA plotted as a function of cumulative electron fluence [47].

2.4. Nanoparticle toxicity

There have always been nanoparticles in the environment that provide risk to human health, these include airborne salts, sands, soils and also pollens, and it has long been recognised that exposure to dusts can lead to ill health and lung disease, most notably for those involved in mining [96]. Growing scientific interest is now leading to the increasing production of a broad range of 'engineered nanoparticles', examples include carbon based nanoparticles (e.g. carbon black, graphite, graphene, carbon nanotubes and buckyballs), metals (e.g. Al, Fe, Co, and Ag), metal oxides (e.g. TiO_2, ZnO, SiO, Fe_2O_3, and Al_2O_3), clays (e.g. $Mg_3Al_2(SiO_4)_3$) and quantum dots (e.g. Au and Si), and it is well recognised that exposure to these can lead to detrimental effects to human health, however these are currently being examined on a case-by-case basis [97-100].

The production of nanoparticles is projected to rise from an estimated 2,300 tonnes in 2008 to 58,000 tonnes in 2020 [101], and with ever increasing biomedical applications there is an essential need to understand the nature of nanoparticle toxicology on a cellular level [102, 103]. It is recognised that nanoparticles can display toxicity despite the material in bulk being considered more inert; this effect is likely to be caused by a higher surface area to volume ratio of particles as a greater proportion of 'surface' atoms change the surface chemistry of the material, tending to make it more chemically reactive [96, 102-104]. In the chemical industry this principle provides the basis for the production of heterogeneous nano-catalysts (e.g. platinum catalysts) [96]. An example of particle size dependent toxicity has been demonstrated by Donaldson *et al* (1999) where 14 nm sized carbon black particles were approximately 3 times more toxic than 50 nm sized carbon black

particles and 10 times more toxic than 250 nm sized carbon black particles [96, 105].

Nanoparticles can enter the human body by various means: inhalation (respiratory tract), ingestion (gastrointestinal tract), injection (blood circulation) and dermally (skin), which can cause problems including adverse respiratory effects (e.g. pulmonary inflammation), fibrosis and oxidative stress [102, 104].

Nano- (and micro-) particles of HA are known proinflammatory's in a number of pathological conditions such as vascular calcification and HA deposition disease; and these particles can typically enter the body as wear debris from coated implants [103]. Research by Motskin *et al* (2009) suggests that toxicity of HA nanoparticles varies with method of synthesis, with HA prepared by a gel method showing the greatest toxic effects at concentrations between 31 - 500 μg ml^{-1}, with a co-precipitated HA showing toxic effects only at high doses > 250 μg ml^{-1} [103]. The amount of particle uptake was shown to correlate directly with cytotoxicity, however no individual particle characteristic was shown to control the degree of uptake [103]. Cell viability (MTT) assays carried out using hydroxyapatite (prepared by a hydrothermal method) particle doses in the range 10 - 100 μg ml^{-1} have shown no adverse affect on the viability of a gastric cancer cell line; effects of higher doses were unreported [106]. A study by Shi *et al* (2009) showed that cytotoxicity of nanoparticulate HA is dependent on particle size, with larger particles (> 200 nm length) producing a higher percentage of apoptosis (death of cells) of MG-63 (human osteoblast) cells [107]. Hydroxyapatite particles ~20 nm in size were observed to pass through the cell membrane, inhibiting apoptosis and also promoting cell growth [107].

2.5. Carbon capture and storage (CCS) using calcium based particulates

2.5.1. Preface

As of 2010, fossil fuels account for 86% of the worlds energy supply [108] and the increasing use of fossil fuels to satisfy the worlds growing energy needs has led to higher emissions of CO_2 and other pollutants (e.g. NO_x and SO_x) [109]. Carbon dioxide is considered the most important of these anthropogenic gases, accounting for up to 64% of an enhanced greenhouse effect [108]. Current energy solutions involve coupling current fossil-fuel energy systems with economical capture, transport and safe storage schemes of CO_2 gas emissions with longer term strategies for low or zero carbon-emission technologies including nuclear power, hydrogen generation and renewable sources (e.g. solar, hydro, wind, biomass and geothermal) [108]. Carbon capture and storage (CCS) technologies have gained significant interest due to the recognised effects of global warming caused by emissions of CO_2 and other greenhouse gases; such effects have led to the 1997 Kyoto Protocol which set a target for 37 industrialised countries, and the European community, to reduce greenhouse gas emissions by an average of 5% (against 1990 levels) over the five-year period 2008 - 2012 [110]. The concentration of CO_2 in the atmosphere has risen from about 280 ppm before the industrial revolution, to 355 ppm in 1990, and 380 ppm in 2010 [108, 109, 111]. At the current carbon emission growth rate, the concentration of CO_2 in the atmosphere is predicted to reach 580 ppm within 50 years [108] and consequently the G8 nations have set a minimum worldwide target of a 50% reduction in CO_2 emissions (against 1990 levels) by the year 2050 for which CCS will play a pivotal role in helping to achieve this [112, 113].

The concept of CCS is not new [114] but there is a recent acceptance to drive towards cost-reductions and provide more energy efficient improvements in CCS systems [115, 116]. Strategies include capturing CO_2 from flue gases as well as developing renewable energy sources, of which hydrogen is regarded as a promising environmentally friendly energy carrier [117]. A proposed technique for H_2 production is steam gasification of methane or biomass; feedstock undergoes a reforming and catalysed water-gas-shift reaction at elevated temperatures, giving H_2 and CO_2 as products. The ability to remove CO_2 using a powder sorbent shifts the reaction to more favourable thermodynamics, thereby increasing the efficiency of hydrogen production [117, 118].

The technique currently considered the most commercially viable for CO_2 capture is amine scrubbing; which was first developed in 1930 and was successfully trialled on gas and coal power stations on a small scale in the early 1980's [119]. This technique utilises an aqueous solution of amine that can absorb CO_2 gas at near ambient temperatures. The amine is then regenerated by steam at ~100 °C to 120 °C and then condensed to leave pure CO_2 which can be compressed and geologically stored [108, 119]. However, due to various operational (e.g. corrosion) and environmental disadvantages, there is a drive to develop greener and more cost-effective methods [120]. Alternate technologies include absorption with soluble carbonate, adsorption with activated carbon and capture using an ionic liquid [121, 122], but these are not easily applied at temperatures above 500 °C, which would be necessary for incorporation into coal power plants where temperature conditions for coal combustion (and therefore CO_2 emission) are typically in the range 550 – 750 °C [108, 122-124].

2.5.2. Calcium oxide & CO_2 sequestration

Metal-oxide based sorbents (particularly calcium oxide, CaO) are well recognised materials for effective high-capacity capture and storage of CO_2 at a higher temperature range (550 – 950 °C) [125-130]. The concept of using lime based slurries for CO_2 capture was first applied into two British power plants in 1936; however the poor performance, reliability and high capital cost of lime-based CO_2 capture rendered the technology as less beneficial than amine scrubbing [119]. The study of limestone for CO_2 capture has continued to gain interest, with small scale applications trialled in US power plants in the 1980's, however these failed to gain government support and consequently work on CaO and other metal oxide sorbents for CO_2 capture has predominantly been pursued in research, with amine scrubbing expected to be the dominant technology pursued in industry until at least 2030 [119, 131].

Calcium oxide is a material known to be unstable at ambient and high temperature conditions due to its tendency to react with atmospheric moisture and CO_2 to form more stable compounds, calcium hydroxide ($Ca(OH)_2$) or calcium carbonate ($CaCO_3$) [132]. This high surface activity of CaO makes it suitable for a range of applications including as a catalyst for the production of biodiesels, and as a key component in cement manufacture [132]. Further owing to its high reactivity, calcium oxide can be utilised for the sequestration (capture and storage) of CO_2. Calcium oxide based precursors (e.g. limestone, $CaCO_3$) can be found naturally and in great quantity, and when decomposed to CaO they are considered ideal candidates as sorbent materials for CO_2 capture due to a high CO_2 sorption capacity [133].

Calcium oxide is known to absorb CO_2 in a flue gas to produce calcium carbonate, $CaCO_3$ (carbonation); a process which is reversible. Once the metal oxide

has reached its ultimate conversion, thermal regeneration can be utilised whereby $CaCO_3$ is heated beyond its calcination temperature (~750 °C) to reform CaO and CO_2 gas [109, 134-136].

$$CaO\ (s) + CO_2\ (g) \leftrightarrow CaCO_3\ (s) \qquad (2.2)$$

$\Delta H^{\circ}_{1023\ K} = -168.5\ kJ\ mol^{-1}$

The gas-solid reaction, between CO_2 and CaO, is most commonly carried out at temperatures between ~550 - 700 °C, with a temperature of 650 °C considered as the most effective for the highest carbonation conversion of a CaO sorbent produced by the thermal decomposition of precipitated calcium carbonate (PCC) [108, 109]. The kinetics of carbonation are well recognised to occur firstly by a rapid, linear reaction at the particle surface [136-139]. This progresses to slower diffusion-controlled phase as a product layer of $CaCO_3$ develops on the outer region of the CaO particle; subsequent carbonation then occurs by the diffusion of the reacting species (CO_2) through the $CaCO_3$ product layer, gradually slowing down the overall reaction rate due to limitations in solid-state diffusivity [140]. This leads to an incomplete conversion of CaO, with reported figures suggesting an ultimate conversion of up to 90% [109]. Regeneration of CaO from $CaCO_3$ typically occurs at temperatures > 800 °C.

A study by Lu *et al* (2006) compared the CO_2 uptake of four CaO sorbents formed by the decomposition calcium acetate monohydrate, CaAc ($Ca(CH_3COO)_2{\cdot}H_2O$), calcium carbonate ($CaCO_3$) calcium hydroxide ($Ca(OH_2)$) and calcium nitrate tetrahydrate ($Ca(NO_3)_2{\cdot}4H_2O$). Each CaO sorbent was subject to carbonation at 600 °C in CO_2 (20 ml min^{-1}) and it was found that the CaO formed from calcium acetate decomposition exhibited a carbonation conversion rate of 97% from CaO to $CaCO_3$. This result was attributed to a high surface area and large pore

volume of the CaO sorbent. The CaO produced from the decomposition of calcium nitrate exhibited only a 2.5% conversion and those from calcium hydroxide and calcium carbonate displaying 63% and 66% conversion respectively [128].

The low CO_2 uptake of CaO formed by the decomposition of calcium nitrate is reported to be caused by melting since calcium nitrate melts at just 45°C. This melting causes the formation of a solid solution during calcination, instead of a powder, a process which prevents the formation of pores upon the decomposition to CaO [128]. This in turn creates a very small surface area of the particles in comparison to the other sorbents, making subsequent CO_2 uptake difficult [128]. The decomposition of each calcium precursor was carried out in a helium atmosphere so as to prevent a reaction with airborne CO_2, which would likely form an intermediate phase of $CaCO_3$ [128]. The study by Lu *et al* (2006) concluded that superior CO_2 capture performance was obtained using a CaO sorbent produced by the decomposition of calcium acetate [128]. Therefore, in this study, calcium acetate will be sourced commercially (Acros Organics, 99%, extra pure) and will be utilised here for the production of CaO powder sorbents. Calcium acetate hydrate is synthesised by the reaction of calcium carbonate and acetic acid, however complete details of the reaction procedure are not disclosed by the supplier*. The following reaction is proposed for the production of calcium acetate monohydrate:

$$CaCO_3 + 2(CH_3COOH) \rightarrow Ca(CH_3COO)_2 \cdot H_2O + CO_2 \qquad (2.3)$$

It should be emphasised here that this research will focus on exploring the CO_2 uptake capabilities of nanoparticulate CaO sorbents, rather than proposing a specific route for their preparation.

---

* From discussion with Kate Jackman, Thermo Fisher Scientific (parent company for Acros Organics).

Using thermogravimetric analysis (TGA), Niu *et al* (2010) investigated the decomposition of CaAc in air and found that a temperature of ~750 °C is required to decompose this phase to complete CaO. Figure 2.5 shows the TGA and DTG (differential thermogravimetry) results of this study [141].

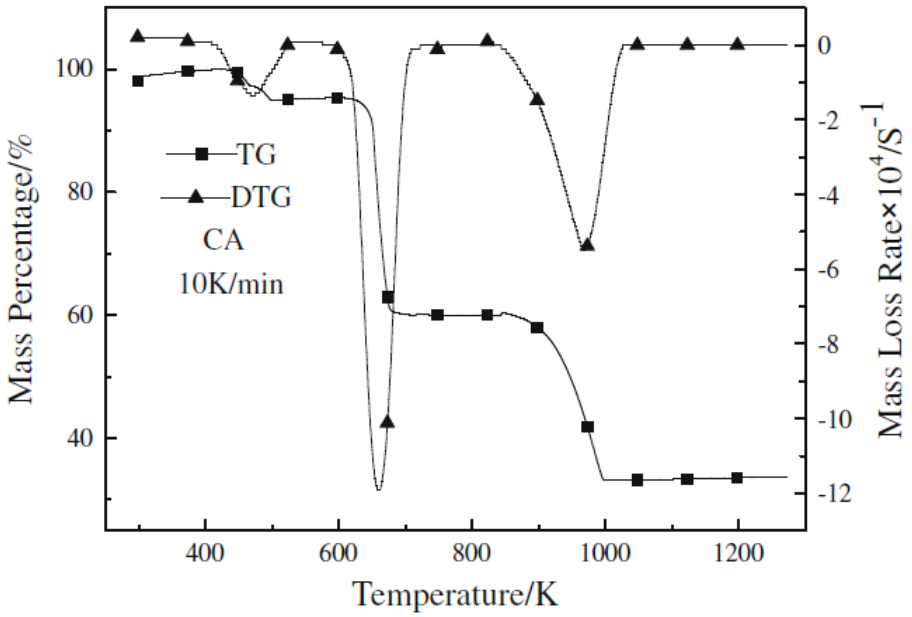

Figure 2.5: TGA and DTG (differential thermogravimetry) curves for the three step thermal decomposition of calcium acetate [141].

The thermal decomposition of CaAc occurs in three stages:

1) at 500 K – dehydration;
2) at 650 K – $CaCO_3$ formation;
3) at 1000 K – CaO formation.

2.5.2.1. Multicycle operations

For industrial carbon capture operations, it is required that CaO sorbents be used repeatedly in a continuous looping system of carbonation and decarbonation cycles; this allows for the regeneration of CaO by thermal decomposition of $CaCO_3$ and could offer significant cost reductions in CO_2 capture applications [109, 136, 142-144]. It is however widely accepted that perfect reversibility, with regards to recarbonation, is not possible due to structural property changes created during the cycling process [125, 136, 142, 145-150]. Figure 2.6 highlights the typical decay in overall CO_2 capture capability of a typical CaO sorbent precursor (produced by the thermal decomposition of $CaCO_3$) with multiple carbonation and decarbonation cycles, with the largest decrease in the carbonation of CaO, observed after the initial reaction [151].

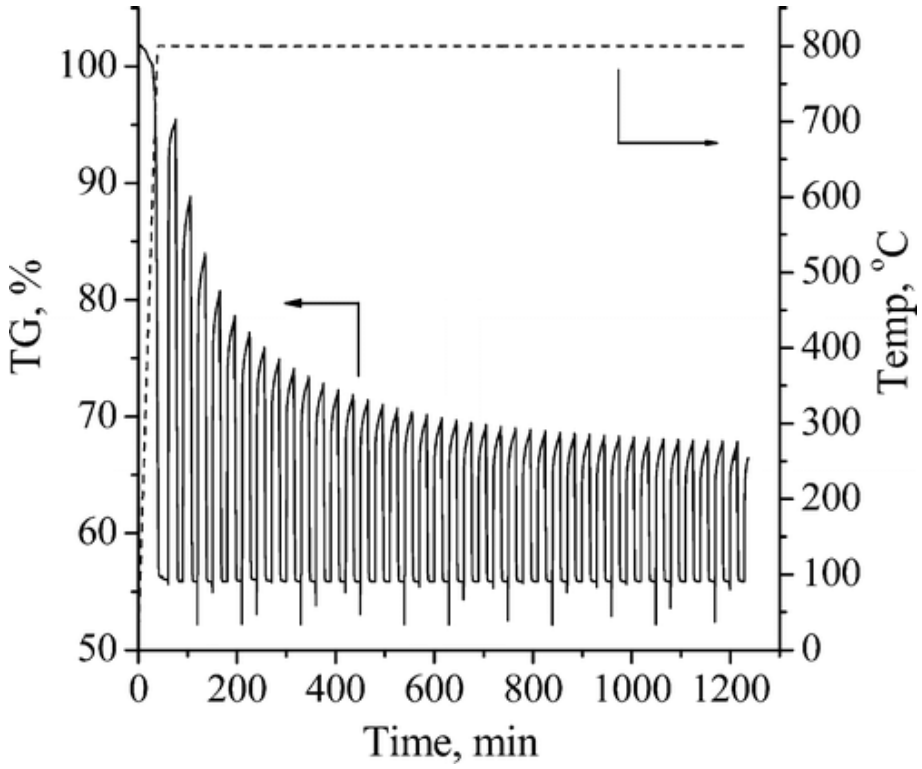

Figure 2.6: Temperature program and weight change in a typical TGA CO_2 multicycle process [151].

Maximum conversion (CO_2 diffusivity) of the CaO sorbent decreases per cycle due to densification of the material upon decarbonation and therefore a decrease in particle surface area available for the subsequent carbonation reaction [136]. It is acknowledged that the maximum carbonation capacity is strictly a function of the number of calcination/carbonation cycles [147]. This trend is typically replicated by various experiments on cyclic CO_2 capture using different CaO and natural limestones as sorbents [126, 138, 147, 152, 153]. A simple schematic that highlights the behaviour of a limestone-based sorbent during the multicycle process has been presented by Lysikov *et al* [151], and is shown here in Figure 2.7. This diagram shows that upon the first decomposition a highly porous and dispersed CaO sorbent is produced. Upon the first recarbonation, conversion is observed to be incomplete, which is likely due to blocking of pores, and potentially small amounts of sintering [151, 154]. Progressive recarbonations show an overall decline in CaO conversion, and this has been attributed to some of these pores occluding and not re-opening upon decarbonation. Coupled with progressive sintering, the sorbent surface area continually decreases with progressive cycles until an eventual interconnected 'skeleton' of CaO has formed [151, 154].

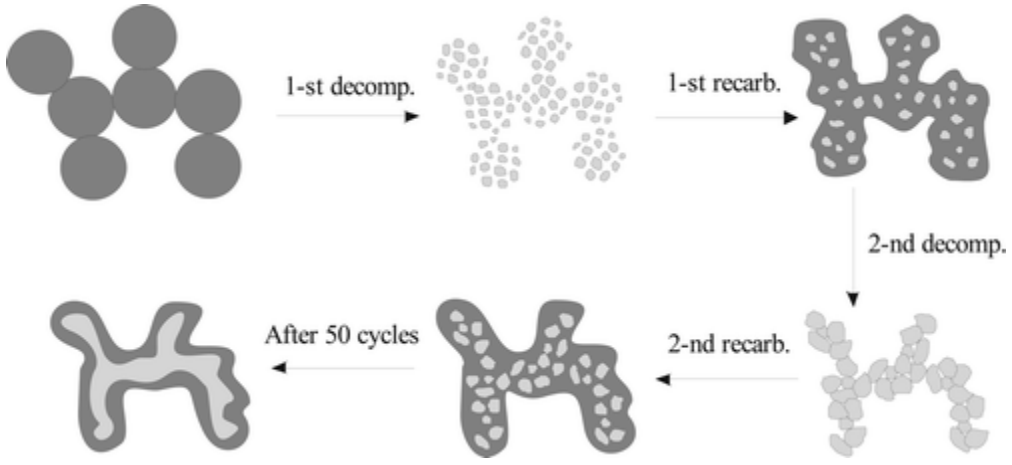

Figure 2.7: The multicycle CO_2 capture process on the textural transformation of the CaO sorbent. The $CaCO_3$ phase is shown by dark grey, and CaO is shown by light grey [151, 154].

2.5.3. Particle Spacers

There have been numerous attempts to improve the overall CO_2 capture capacity over multiple cycles by sorbent modification, with promising results currently being shown by regenerating the sorbent by hydration to $Ca(OH)_2$ with each cycle, before decarbonation back to CaO; this is reported to improve sorbent porosity and limit progressive sintering [149, 155-157].

Alternative approaches utilise inert particle spacer materials that are intimately mixed with the CaO sorbent. These include MgO, Al_2O_3, ZrO_2, $MgAl_2O_3$ and $Ca_{12}Al_{14}O_{33}$ (mayenite) [130, 158-160]. Particle spacers aim to reduce CaO densification by separating the $CaO/CaCO_3$ particles. The volume fraction of the inert spacer powder is likely to scale with improved durability of the CaO sorbent; however this will be a compromise with the initial uptake capacity of CO_2.

2.5.3.1. Yttria stabilised zirconia (YSZ)

Zirconia (ZrO_2) is a material notable for its ability to change its solid crystal phase at given temperatures, a phenomenon which is commonly employed to arrest the propagation of cracks (transformation toughening) in many ceramic materials [161]. Zirconia exhibits a high melting temperature of ~2700 °C, and upon cooling it will undergo a series of phase transitions, from an initial cubic phase to a tetragonal phase (at 2400 °C) and then to a monoclinic phase (at 1050 °C) [162]. When stabilised with yttria (Y_2O_3), the ability for the retention of the metastable tetragonal phase is possible at ambient conditions, rather than the stable monoclinic phase as displayed in the ZrO_2-$YO_{1.5}$ phase diagram in Figure 2.8 [162, 163]. For transformation toughening, this phase transformation can be triggered by the onset of a crack. The phase change creates a volume increase and internal compressive

stresses then generate around the crack subsequently restricting its propagation [164]. Inducing such local stresses in a CaO-YSZ skeleton similar to that in Figure 2.7 could produce microcracks that open up the structure of the skeleton and actually improve its subsequent CO_2 sorption capacity.

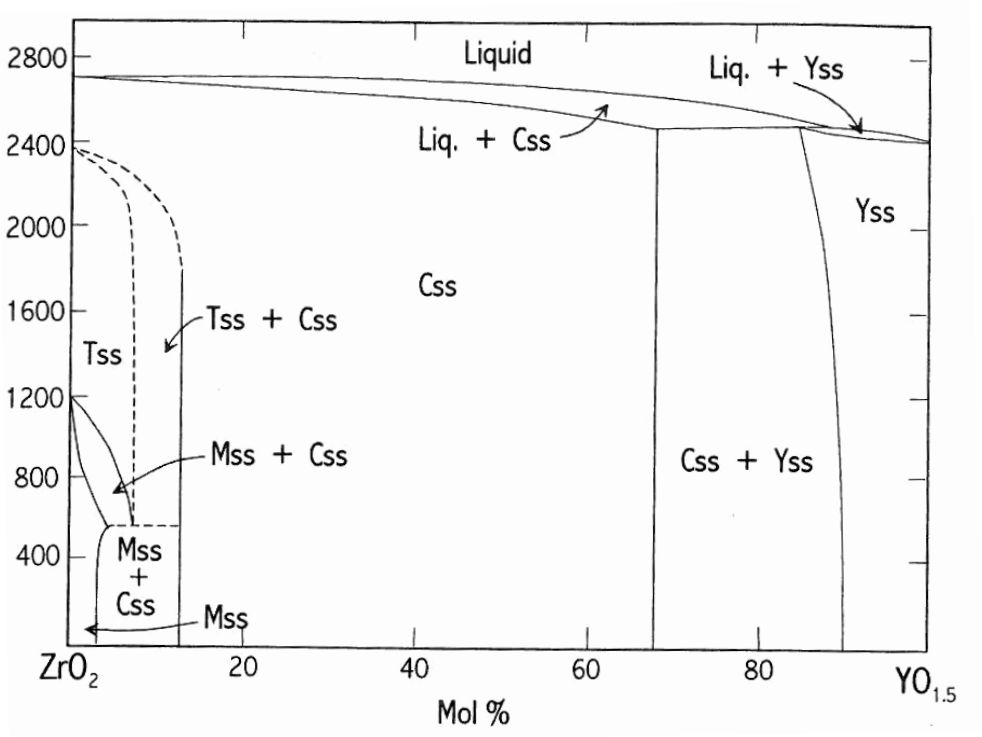

Figure 2.8: Phase diagram for the ZrO_2-Y_2O_3 system. C, M and T refer to the cubic, monoclinic and tetragonal polymorphs of zirconia, and their solid solutions, ss. Y = yttria, Y_2O_3 [162].

Various methods for the synthesis of ZrO_2 and YSZ have been reported, including hydrothermal [165-172], sol-gel [173, 174], spray pyrolysis [175] and microwave-based preparation [176, 177], with many reporting particle sizes < 10 nm. Such nanoparticulate materials with a tetragonal-monoclinic phase transition between CaO carbonation and decarbonation temperature could be used to provide an active spacer for CaO sorbent powders.

Chapter 3. Experimental methods

3.1. Hydroxyapatite

3.2. Hydrothermal HA synthesis

For the hydrothermal method [49, 58], 1.00 M stock solutions of calcium nitrate tetrahydrate ($Ca(NO_3)_2{\cdot}4H_2O$; Fisher Scientific, reagent grade; 11.807 g) and di-ammonium hydrogen phosphate ($(NH_4)_2HPO_4$, Fisher Scientific, analytical reagent grade; 6.603 g) were prepared using distilled water (50 ml), and subsequently diluted further to create 0.10 M solutions. A precipitate was formed by the drop-wise addition of the di-ammonium hydrogen phosphate solution (30 ml) to the calcium nitrate tetrahydrate solution (50 ml), with continuous stirring, until a nominal Ca/P ratio of 1.67 is reacted in the mixed solution. The pH of the resulting suspension was ~5.1, however the drop-wise addition of ammonium hydroxide (NH_4OH; Sigma-Aldrich, ACS reagent grade) during the mixing phase, allowed the pH to be raised to pH = 11.0 (monitored using a Hanna pH Checker). The addition of ammonium hydroxide to the synthesis solution allows for the control of pH, but also has an added benefit of preventing the formation of carbonate during synthesis [178, 179]. An increase of OH^- ions in the solution is also known to speed up the transformation rate from amorphous calcium phosphate (ACP) to hydroxyapatite, via a secondary octacalcium phosphate (OCP) phase [180-182].

Vigorous stirring of the resulting solution was carried out for a further 10 minutes. The solution was then transferred into a 125 ml Teflon-lined hydrothermal reactor (Model 4748, Parr Instruments) which was heated at 200 °C for 24 hours,

generating a pressure of between 1 and 2 MPa. Once air-cooled to room temperature, the particulate product was collected by centrifugation and washed to remove unwanted co-products by re-suspending the powder in distilled water, using ultrasonic agitation, for 5 min and then sedimenting the particles by means of centrifugation at 6000 rpm for 5 min. This process was repeated at least 6 times, until the pH of the solution has neutralised to ~7, which suggests the complete removal of ammonia. A final wash was carried out using methanol so as to limit particle agglomeration in the final dried powder. Drying was carried out in an oven at ~50 °C for ~4 hours [49].

3.3. Solution gelation (sol-gel) HA synthesis

Sol-gel synthesis of HA [26, 69], involved the hydrolysis of triethyl phosphite $(C_2H_5O)_3P$; Aldrich 98%; 10 ml) in distilled water (60 ml). The mixture is sealed immediately with parafilm in a glass beaker and stirred vigorously. After a few minutes, the cloudy solution turns clear to signal the completion of hydrolysis. A stoichiometric amount (Ca/P ratio = 1.67) of calcium nitrate tetrahydrate (Fisher Scientific, reagent grade; 19.683 g) was dissolved in 50 ml anhydrous ethanol, and subsequently added drop-wise into the hydrolyzed phosphite solution, followed by 10 minutes of more vigorous stirring. The resulting solution was clear and subsequently aged at room temperature for 16-24 hours before drying. The ageing process is crucial in that it allows for the solution system to stabilise such that a monophasic HA can be produced; the formation time can vary depending on the chemical nature of the precursors used [26]. Insufficient ageing can result in weight loss during pyrolysis, due to loss of unreacted phosphite, and the potential for undesired phases, such as CaO, to be observed [26, 81].

The aged sol was dried using a hot plate: the solvents were driven off at ~60 °C until a viscous liquid formed, which was further dried in an oven at 100 °C for 12 hours. The resulting white gel was ground into a powder with a pestle and mortar. Two samples were prepared by calcining the gel at 500 and 700 °C respectively, for 2 hours [26].

3.3.1. Thermogravimetric analysis (TGA) of sol-gel precursors

Thermogravimetric analysis (TGA) is a testing procedure which measures the change in mass of a sample as a function of temperature and time, under controllable atmospheric conditions [183]. It is utilised to monitor processes such as decomposition, evaporation, dehydration and gas adsorption [184]. The technique provides quantitative information resulting from any processes that may instigate detectable changes in mass at controlled temperature; this allows the stoichiometry and kinetics of any heat-induced reactions to be followed directly [185].

TGA analysis has been carried out to measure the decomposition of both triethyl phosphite $(C_2H_5O)_3P$, Aldrich, 98%) and triethyl phosphate ($(C_2H_5O)_3PO$, Aldrich, 99%) using a Stanton and Redcroft TGH-1000 thermo-balance. Samples (18.85 ml of triethyl phosphite and 17.16 ml of triethyl phosphate), were placed into a platinum crucible and heated, in air, at a rate of 15 °C per minute up to a maximum temperature of 900 °C. The percentage weight loss is recorded and plotted as a function of time (in seconds) and temperature (°C).

3.3.2. Stability of triethyl phosphite

The atmospheric stability of triethyl phosphite was compared to that of triethyl phosphate ($(C_2H_5O)_3PO$, Aldrich, 99%). An experiment was conducted measuring the relative mass change of both chemicals exposed in air at ambient temperature. Samples of triethyl phosphate (9.45 ml) and triethyl phosphite (8.95 ml) were placed in an evaporating dish on a balance for 15 minutes; mass measurements were recorded every 30 seconds.

3.4. Hydroxyapatite toxicology

Cytotoxicity (the degree to which a material is toxic to living cells) assays have been carried on two HA samples hydrothermally prepared at pH 9 and pH 11 (following the method outlined in Section 3.2). Bulk compositional analysis was performed by XRD (described in Section 3.12.1), and particle level analysis carried out using the TEM-EDX method, which is described in Section 3.13.4.

Cell viability was measured using the MTT assay [186] and has been carried out courtesy of Dr Lars Jeuken by undergraduate students Gregory Dyson, Emma Horncastle and Jessica Jones in the Faculty of Biological Sciences, University of Leeds.

Toxicity of hydrothermal HA samples prepared at pH 9 and pH 11 was investigated using three human (in-vitro) cell lines: Caco-2 (intestine) and A549 (lungs), and SH-SY5Y (brain). Testing against the Caco-2 and A549 cell lines might proxy effects of HA nanoparticles that are ingested or inhaled. Should HA nanoparticles pass into the blood-stream, neurological effects may be observed and thus effects on the SH-SY5Y cell line have been examined.

Media for cell culture was prepared by the addition of 50 ml foetal bovine serum (FBS) and 1 ml penicillin-streptomycin antibiotics into 500 ml of Dulbecco's Modified Eagle's Medium (DMEM). A 10 ml solution of the media was incubated (at 37 °C, 5% CO_2) and then seeded into 96 well plates at a density of 10,000 cells per 100 μL of medium. This was further left to incubate.

Dispersions of HA (0.1 wt%) were prepared using distilled water and further diluted in DMEM at various concentrations between 0 – 500 μg ml^{-1}. These suspensions were added to the cultured cells and tested for viability, after 24 and 48 hours, using the yellow MTT (3-(4,5-Dimethylthiazol-2-yl)-2,5-diphenyl tetrazolium bromide) colorimetric assay. The MTT solution reduces from a yellow tetrazole to purple formazan in the mitochondria of living cells (where reductase enzymes are active) and so cell viability is measured by the percentage of light absorbance at a certain wavelength (typically between 500 and 600 nm) using a spectrometer. Results are calibrated against untreated control wells (without HA particles), thus determining the effectiveness of the particles in causing cell death [187, 188].

3.5. Calcium oxide & CO_2 sequestration

3.6. Thermal decomposition of calcium acetate by thermogravimetric analysis (TGA) and evolved-gas analysis by Fourier transform infrared spectroscopy (FTIR)

The thermal decomposition of commercial calcium acetate hydrate, CaAc ($Ca(CH_3COO)_2 \cdot xH_2O$, Acros Organics, 99%, extra pure, value of x unreported by supplier) was firstly analysed using thermogravimetric analysis (TGA). Samples for TGA analysis are loaded into a 6 mm diameter x 2.5 mm alumina cell crucible which is placed onto a high precision balance and lowered into a sealed oven chamber. The thermal decomposition and evolved-gas analysis of the as received CaAc has been analysed by a Stanton Redcroft TGH-1000 TGA instrument connected to a Thermo Scientific Nicolet iS10 FTIR spectrometer running OMNIC processing software and fitted with an attenuated total reflection (ATR) accessory.

A sample of CaAc was heated from ambient temperature to 800 °C at a rate of 20 °C min^{-1}, in N_2, using the Stanton Redcroft TGH-1000 TGA thermo-balance (changes in mass and temperature are recorded every 1 second; accuracy = 0.001 mg). Results of thermal decomposition of CaAc by TGA are shown in Section 5.3, Figure 5.6, with results of evolved gas analysis by FTIR shown in Figures 5.7 and 5.8.

Detailed analysis of the CaO product, formed upon TGA decomposition of CaAc, has been carried out by XRD and TEM (Figure 5.10 and Figure 5.12). To observe the intermediate phase during decomposition, an additional sample has also been prepared by the TGA decomposition of CaAc at 500 °C (following the

previously outlined TGA conditions), and analysed by XRD and TEM (Figure 5.9 and Figure 5.11).

3.7. Thermal decomposition of calcium acetate by *in-situ* hot-stage XRD

The development of crystallographic phases during thermal decomposition of CaAc was carried out using XRD, with an *in-situ*, water-cooled heating stage. A CaAc sample was analysed with a temperature controlled heating stage (up to 800 °C) using a Philips PanAnalytical X'pert Diffractometer with Cu Kα radiation source. Each measurement temperature was reached at a rate of 20 °C min^{-1}, and then held for 1 hour to allow for X-ray diffraction analysis.

Samples for TEM were prepared by a slow decomposition of CaAc, in a furnace, from ambient temperature to 200, 500 or 800 °C (at 20 °C min^{-1}); each held at the respective temperatures for 1 hour. Samples were then removed from the furnace, and cooled in air.

3.8. CO_2 sequestration

Carbon dioxide capture was performed by thermogravimetric analysis (TGA) using a Shimadzu TGA-50 thermo-balance. A schematic showing the key components of the Shimadzu TGA-50 thermo-balance is shown in Figure 3.1.

Decomposition was performed at 800 °C under a N_2 atmosphere, with a CO_2 supply pressure of 2 bar controlled by a rotameter to a flow rate of 50 ml min^{-1}. For carbonation, the chamber temperature was then dropped to 650 °C and the gas stream supply switched to CO_2, at a 50 ml min^{-1} flow-rate. Gases are interchangeable

at a preset time or temperature limit, allowing for automatic valve control. The atmosphere within the chamber is purged with desired gases, prior to sample loading.

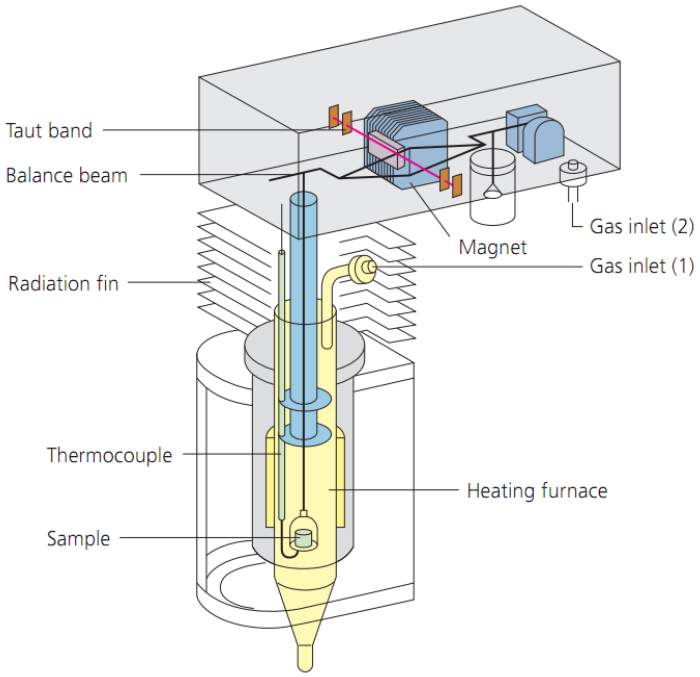

Figure 3.1: Schematic of the Shimadzu TGA-50 thermo-balance [189].

3.8.1. CO_2 uptake of CaAc-CaO

The CO_2 uptake of calcium acetate hydrate decomposed to calcium oxide after a fast and slow decomposition rate, were measured by TGA. Samples of CaAc were decomposed from room temperature to 800 °C (in N_2) at a rate of 20 °C min^{-1}. To mimic fast and slow decomposition, two samples were prepared; the first was decomposed to 800 °C followed by immediate chamber cooling to 650 °C for subsequent carbonation, the second was decomposed to 800 °C and held at that temperature for 1 hour before the chamber was cooled to 650 °C for carbonation. Carbonation conditions were held at 650 °C for 15 minutes. Upon completion, the gas stream was switched to N_2 and the chamber was cooled to room temperature. Results are shown in Figures 5.15 and 5.16.

3.8.1.1. CO_2 cycles

Repeat cycles of carbonation and decarbonation were performed by TGA, with a looping program prepared using the TA60 acquisition software. A sample of CaAc was firstly fully decomposed (in N_2, 50 ml min^{-1}) from room temperature to 800 °C, at a rate of 20 °C min^{-1}. Chamber temperature was immediately decreased to 650 °C upon which the gas stream was switched to CO_2 (50 ml min^{-1}). These carbonation conditions were held for 5 minutes. After this time the gas stream is switched back to N_2 and decarbonation takes place from 650 °C to 800 °C. This loop is repeated 10 times.

To analyse carbonated and decarbonated samples at given intervals during the cycle process, the looping experiment was repeated several times but terminated after specific periods of either carbonation or decarbonation. Samples collected have been labelled A-H, where:

A = Initial decomposition of CaAc to 800 °C;

B = after 1st carbonation cycle at 650 °C;

C = after 2nd decarbonation at 800 °C;

D = after 2nd carbonation cycle at 650 °C;

E = after 3rd decarbonation at 800 °C;

F = after 3rd carbonation cycle at 650 °C;

G = after 9th decarbonation at 800 °C;

H = after 10th carbonation cycle at 650 °C

Samples were cooled under N_2 conditions to room temperature upon conclusion of each experiment. Each sample was then analysed by XRD (Figure 5.25) and SEM and TEM (Figures 5.27 - 5.29).

3.8.1.2. Using TEM for the analysis of CO_2 cycles

Analysing the CaO sorbent at various stages during the looping process proved to be problematic due to the reactive nature of CaO in air at ambient conditions, forming $Ca(OH)_2$ and $CaCO_3$. Exposure to air during standard XRD, TEM and SEM sample preparation is unavoidable. Therefore, to examine the microstructural changes of the CaO sorbent during the looping process, without risk of hydration, novel TEM based techniques have been explored.

Firstly, a water cooled Gatan Single Tilt Heating Holder with SmartSet Hotstage Controller has been utilised with a Philips CM200 FEGTEM with Gatan Imaging Filter (GIF 200). The first carbonated sample (Sample B) has been prepared following the TGA cycle method and then decomposed, *in-situ* in the TEM, at 10 °C intervals (at ~20 °C min^{-1}) and held to allow for imaging. Images at selected temperatures taken by hot-stage TEM analysis are shown in Figure 5.30.

An additional novel technique has been employed that utilises an *ex-situ* bench mounted Gatan Environmental cell (E-cell) heating holder with a FEI Tecnai TF20 field emission gun (FEG-) TEM. The E-cell is a sealed unit that allows for a TEM sample to be loaded into a gas or vacuum environment, with controllable temperature, before being transferred into the TEM without exposure to air, thus eliminating potential hydration of, in this case, the nanoparticulate CaO. The technique allows for the carbonation and decarbonation of a single sample to be carried out, with the ability to analyse the effects of the process on a single area of particles by TEM.

A CaO sorbent has been prepared by decomposition of CaAc at 500 °C in a furnace, to produce calcium carbonate ($CaCO_3$). This was ultrasonically dispersed in methanol and drop cast onto an electron transparent silicon nitride membrane (Agar

Scientific). The grid was then secured on the detachable TEM sample holder of the E-cell. Decomposition of the sample to CaO was carried out within the E-cell by directly heating, at ~20 °C min^{-1}, from room temperature to 800 °C, followed by immediate cooling back to room temperature, all under continuous rotary vacuum, using an Edwards RV8 vacuum pump (lowest achievable vacuum pressure = ~10^{-3} Pa). The sample was then vacuum sealed within the detachable TEM sample holder and transferred to the TEM for analysis.

For carbonation, the E-cell chamber temperature was firstly raised to 650 °C under vacuum, with CO_2 then applied to fill the furnace chamber (controlled by a manual valve); carbonation of the sorbent then took place at 650 °C for 5 minutes before the gas supply was closed off and the vacuum pump reapplied during cooling to room temperature. Replicating the carbonation conditions from TGA (CO_2 pressure of 2 bar with rotameter controlled flow rate of 50 ml min^{-1}) was unachievable here as the pressure could not be supported by the holding seal of the chamber, and therefore the chamber was filled to a lower, 0.5 bar pressure of CO_2 during carbonation. Figure 3.2 displays a schematic of the decarbonation and carbonation process as carried out using the E-cell, where Figure 3.2a displays the sample (*2*) being loaded into the furnace chamber (*3*) which, along with the guide tube (*5*) and vacuum chamber (*7*), is kept under continuous vacuum by the pump connected at *1*. Sample release and decarbonation conditions are shown in Figure 3.2b where the sample is released by the retractable specimen holder (*8*) and then contained in the furnace chamber and heated under vacuum from room temperature to 800 °C prior to cooling. The connection tap for the interchangeable vacuum pump and CO_2 input supply is shown at *1*. Temperature is controlled by an external heater and thermocouple connected to the furnace chamber, and chamber cooling is

maintained by a continuous water flow which is connected from a cold-tap to pipes shown at *4*.

Sample carbonation is shown by Figure 3.2c where the sealed furnace chamber is firstly heated (under vacuum) to 650 °C and then filled with CO_2 (0.5 bar pressure); these conditions are maintained for 5 minutes prior to removal of the CO_2 supply, and the furnace chamber is then re-pumped to vacuum. Collection of the sample by the retractable specimen holder is shown by Figure 3.2d. The removal of the sample from the furnace chamber is shown by Figure 3.2e, where the sample is firstly withdrawn into the vacuum chamber (*7*) and sealed using the cell valve (*6*); the guide tube and vacuum chamber can then be detached from the furnace chamber, and can then be attached directly to the TEM goniometer, and the sample passed into the microscope whilst under rotary vacuum (at worst).

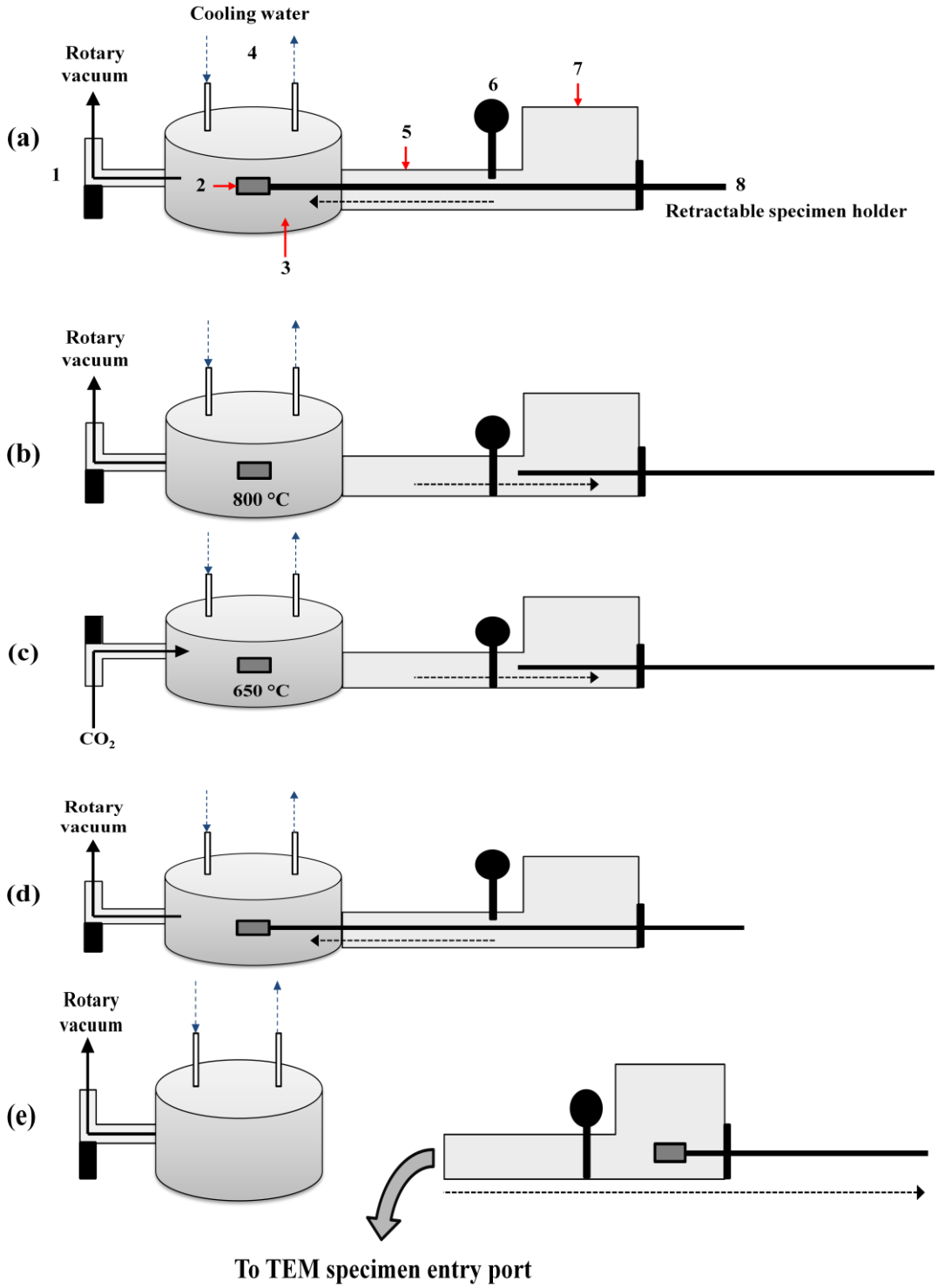

1 = Tap for connection of vacuum pump & CO_2 supply. 2 = Sample. 3 = Furnace chamber. 4 = Cooling water. 5 = Guide tube. 6 = Cell valve. 7 = Vacuum chamber. 8 = retractable specimen holder.

Figure 3.2: Schematic of the E-cell operation. Where (a) displays sample loading, (b) sample release for decarbonation and (c) carbonation, (d) sample collection and (e) sample removal and sealing prior to transfer to TEM.

3.9. Particle spacers

3.9.1. Yttria stabilised zirconia

Commercial zirconia, stabilised with 5.4 wt% yttria (YSZ), was purchased from Goodfellow, Cambridge. The phase content of the commercial YSZ was analysed by XRD, with particle morphology and size analysis by SEM and TEM.

3.9.2. CaO-YSZ preparation

A large sample (~20 g) of commercial 5.4%-YSZ powder (Goodfellow) was firstly vibro-milled, for 30 min in isopropyl alcohol using a McCrone Micronising Mill, to reduce agglomeration.

A small amount of the vibro-milled YSZ was then mixed with CaAc allowing for 70/30 wt% of CaO:YSZ in the final product when decomposed at 800 °C. Mixing was carried out using a small amount of ethanol, with the mixture ground with a pestle and mortar for 30 min. The powder (> 1 g) was then oven dried for 1 hour at 50 °C. A sample of the CaAc-YSZ blend was subjected to furnace decomposition at 800 °C for 10 minutes and analysed by XRD.

3.9.3. CaO-Zirconia preparation

Two samples of Zr-doped CaO (70/30 wt%), were prepared by solution precipitation of CaAc with zirconyl (IV) nitrate ($Zr(NO_3)_2$, 99.5% Fisher Scientific), and also calcium hydroxide ($Ca(OH)_2$, Alfa Aesar, ACS 95%) with $Zr(NO_3)_2$:

- For the CaAc/($Zr(NO_3)_2$ solution; CaAc (4.95 g) was firstly dissolved in 100 ml of ethanol. A stock ammonium hydroxide (NH_4OH; Sigma-Aldrich, ACS reagent grade) solution was prepared (pH 10) in distilled water, and 100 ml was added to the CaAc solution drop wise via a burette, under continuous stirring.

A second solution was prepared by dissolving $Zr(NO_3)_2$ (2.64 g) in 100 ml ethanol, with 100 ml of pH 10 ammonium hydroxide solution subsequently added drop wise via a burette with continuous stirring.

Finally, 50 ml of the $Zr(NO_3)_2$/ NH_4OH sol was added drop wise into 100 ml of the CaAc/NH_4OH sol, producing a cloudy solution with final pH = 6.9. Stirring continued for 1 hour after titration before a small amount of solution was placed into an evaporating dish and dried overnight in an 80 °C oven. A fine white powder was then collected and ground.

- The $Ca(OH)_2$/($Zr(NO_3)_2$ solution was prepared under the same conditions as the CaAc/($Zr(NO_3)_2$ powder; using $Ca(OH)_2$ (2.31 g) diluted in 100 ml ethanol with further drop wise addition of 100 ml of pH 10 ammonium hydroxide. Drop wise addition of 50 ml of the $Zr(NO_3)_2$/NH_4OH produced a milky solution with final pH = 11.9. A sample was collected and dried overnight at 80 °C, forming a fine white powder.

Samples of each powder were decomposed at 800 °C for 10 minutes and analysed for phase content by XRD.

3.9.4. Hydrothermal synthesis of YSZ with zirconia (IV) nitrate hydrate and yttrium (III) nitrate hexahydrate

Yttria-stabilised zirconia (YSZ) has been synthesised according to the route outlined by Guiot *et al* [169]†. Zirconia (IV) nitrate hydrate ($ZrO(NO_3)_2 \cdot xH_2O$, 99.5% Acros organics) and yttrium (III) nitrate hexahydrate ($Y(NO_3)_3 \cdot 6H_2O$, 99.9% Acros organics) is dissolved in 50ml of distilled water with the concentrations: $[Zr^{(IV)}]$ = 0.1 M and $[Y^{3+}]$ = 0.05 M. Acetylacetone, Acac (Aldrich, 99%+) is added with the molar ratio Zr:Acac = 1:1. Guiot's original study suggests a solution pH of 7 proved optimal for a stable solution and prevents the rapid precipitation of the solid and so, in this preparation, ammonium hydroxide (Sigma-Aldrich, ACS reagent grade) was added drop wise to achieve this from an initially acidic solution. The solution was magnetically stirred for a further 5 minutes and then transferred to a 125 lm Teflon liner and hydrothermal reactor (model 4748, Parr Instruments) where it was heated to 160 °C for 72 hours. Figure 3.3 displays a basic schematic of the process [169].

† Guiot explains that the hydrothermal conditions allow for the formation of YSZ nanoparticles within a gel, which contracts upon expulsion from the liquid in a process known as syneresis. Cooling to room temperature creates a cylindrical macroscopic aggregate of YSZ within a clear supernatant.

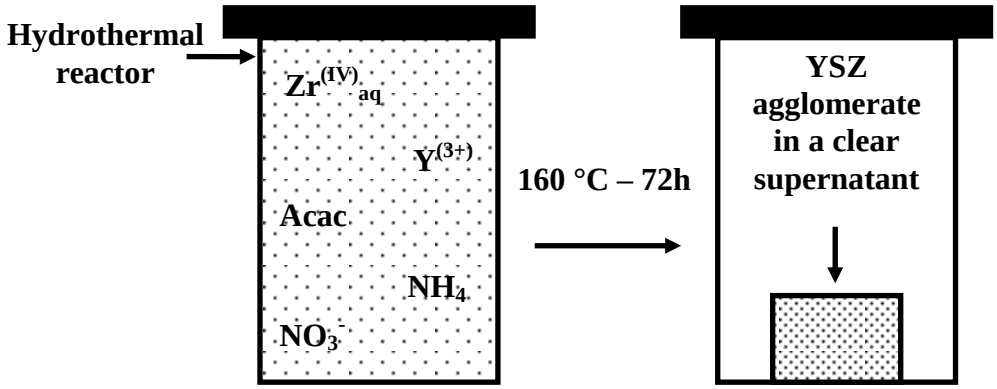

Figure 3.3: Guiot *et al's* hydrothermal synthesis of YSZ [169].

The powder-aggregate was collected and washed by re-suspension in distilled water, under ultrasonic agitation, for 5 min and then the particles were sedimented by means of centrifugation at 6000 rpm for 5 min. This process was repeated 6 times with a final wash carried out using methanol so as to limit agglomeration in the final dried powder. The solution was then dried in an oven at ~50 °C and the resultant white cake ground to a powder using a pestle and mortar. This synthesis method produces 9 mol% Y_2O_3-ZrO_2 powder, equivalent to 15.6 wt% yttria in zirconia [169]. Guiot reports the formation of cubic YSZ following this synthesis route [169]. Analysis of the hydrothermal (h-) YSZ powder was carried out by XRD and TEM.

A sample of CaAc containing hydrothermally synthesized YSZ (hYSZ) was prepared by dry mixing in ethanol using a pestle and mortar, allowing for 70/30 wt% of CaO:hYSZ in the final product when decomposed at 800 °C. Phase analysis of the CaO:hYSZ was carried out by XRD.

3.9.5. CaO-Mayenite preparation

A 75:25 wt% blend of CaO:$Ca_{12}Al_{14}O_{33}$ has been provided courtesy of postgraduate student Dr Roger Molinder of the Energy Research Institute, University of Leeds. Synthesis closely follows a sol-gel route outlined in [190]. Preparation involves the dilution of 26.2 g CaO and 28.4 g $Al(NO_3)_3$ into 760 ml of pre-heated distilled water (75 °C) and 130 ml of 2-propanol. The resulting solution is kept at 75 °C and stirred for 1 hour, before being placed into a 120 °C oven overnight to evaporate water from the sol. The resulting cake is ground into a powder with a pestle and mortar before being placed into a furnace. The powder is heated from ambient temperature to 500 °C (at 20 °C min^{-1}) and held for 3 hours. The sample is again ground, and subject to further heat treatment from ambient temperature to 120 °C for 2 hours. A final cycle involves grinding followed by heat treatment in a pre-heated furnace at 900 °C, for 1.5 hours. Upon cooling, the sample is collected and parafilm sealed in a glass container [190]. Phase analysis of the as received CaO:Mayenite powder blend has been carried out by XRD.

3.10. CO_2 sequestration of particle spacer materials

It is well recognised that CaO experiences a loss of CO_2 capture capacity within increasing cycles in the carbonation-decarbonation looping system [126, 147, 191]. This is attributed to particle densification and sintering producing smaller CaO particle surface area for pickup [136].

The CaO-zirconia materials synthesised in-house have been tested under the carbonation-decarbonation cycle conditions outlined in Section 3.8.1.1, using TGA. The following were tested:

- CaO-YSZ (from CaAc precursor and Goodfellow 5.4%YSZ)

- CaO-$CaZrO_3$ (from CaAc precursor)
- CaO-$CaZrO_3$ (from $Ca(OH)_2$ precursor)
- CaO-hYSZ (from CaAc precursor and hydrothermal YSZ)
- CaO-Mayenite (75/25 wt%)

Each mixture was synthesised to allow for 70/30 wt% CaO/spacer in the final decomposed product, unless otherwise stated. Results of the multicycle capture by TGA, with molar conversion data for each sample, are shown in Figure 5.43 and Table 5.8.

The CaO:YSZ powder blend was subsequently selected for analysis using the E-cell TEM technique previously described in Section 3.8.1.2. This blend was selected as results from multicycle capture (Figure 5.43) show the most promising effects with regards to reducing the decay in sorbent CO_2 capture. Results of this E-cell experiment are shown in Figures 5.44 - 5.46.

3.11. Material characterisation techniques

Bulk compositional and phase analysis has been performed by: (a) powder X-ray diffraction (XRD), (b) X-ray fluorescence (XRF), (c) Fourier-transform infrared (FTIR) spectroscopy and (d) laser ablation inductively coupled plasma mass spectrometry (LA-ICP-MS).

Scanning electron microscopy (SEM) has been used for the observation of larger particle agglomerates and aggregates. Individual particle size distribution and compositional analysis was carried out by transmission electron microscopy with energy-dispersive X-ray spectroscopy (TEM-EDX).

The size distribution profile, for HA samples dispersed in *Dulbecco's Modified Eagle Medium* (DMEM) and analysed for cytotoxicity, has been carried out by dynamic light scattering (DLS).

3.12. Bulk analysis techniques

3.12.1. X-ray diffraction

X-ray diffraction (XRD) is an effective, non-destructive tool that allows for the determination of atomic arrangement within a material, giving the crystalline phases from the atomic spacing's and symmetry. Developed on the basis of Bragg's law, the presence of lattice planes in a crystalline material are sought by the diffraction of X-rays, of a known wavelength e.g. Cu-Kα (wavelength. λ = 1.5416 Å), at specific angles between the X-ray source and detector, Figure 3.4. Each lattice plane of atoms in a material will cause constructive interference of diffracted X-rays at a certain angle of incidence, θ, known as the Bragg angle. The lattice spacing, d, can be identified by rearrangement of Bragg's Law:

$$n\lambda = 2d\ sin\,\theta \tag{3.1}$$

Where n denotes an integer.

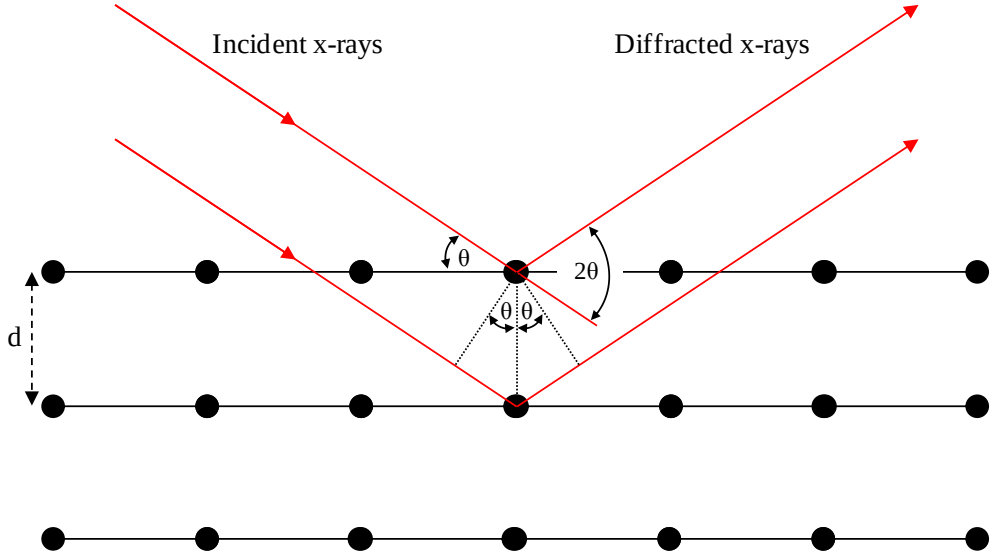

Figure 3.4: Schematic of X-ray diffraction from a set of crystal planes [86].

The determination of a material's crystal structure using XRD is accomplished using the scattering angles, and relative intensities of the diffracted X-rays. The measured scattering angles are used to obtain the crystal system of the material (i.e. size and shape of the unit cell) and the relative intensities of the diffracted beams are then used to determine the atomic positions within the unit cell [86, 192].

For powder XRD, identification of phases present, in the XRD pattern, is carried out by comparison to known reference patterns using powder diffraction files (PDF), held by the International Centre for Diffraction Data (ICDD), formerly JCPDS (Joint Committee for Powder Diffraction Standards). With PDF's, peak positions (2θ) and intensities can be comprehensively matched to identify single or multiple phases; and with careful (calibrated) measurement the precise *d*-spacing's of lattice planes (*hkl*) and unit cell parameters (abc) can be obtained. For a sample that contains sub-micrometer crystalline particles, the mean crystallite size, τ (of a specific crystal plane, *hkl*), can be obtained from the broadening of the diffraction peaks using the Scherrer equation:

$$\tau = \frac{K\lambda}{\beta \cos\theta} \quad (3.2)$$

Where *K* represents the shape factor (this is dimensionless and has a typical value of 0.9 or 1 for equiaxed crystals, but varies with crystallite shape), λ is the X-ray wavelength, β denotes the full width of the diffraction peak at half the maximum intensity (FWHM) in radians, and θ is the Bragg angle for the reflection [86, 193].

Characterisation by XRD has been carried out here using a Philips/PANalytical X'pert Diffractometer with Cu Kα radiation (λ = 1.5418 Å). Phase identification and crystallographic information were obtained using the PANalytical HighScore software. Sample analysis was carried out across the 2θ range of 10 – 80° for most samples; a starting angle of 5° 2θ was utilised for the analysis of calcium acetate hydrate where there are several high intensity peaks at low angles. High resolution scans were obtained using a step size of 0.017°, and scan speed of 0.018° s^{-1}, providing a total acquisition time of ~1 hour.

3.12.2. X-ray fluorescence

X-ray fluorescence (XRF) is a bulk elemental analysis technique first demonstrated by Glocker and Schreiber in 1928 [194]. Elemental composition is determined by the fluorescent emission of X-rays from the sample caused by the stimulation with an incident primary X-ray beam. When a primary X-ray is emitted from a tube or radioactive source and strikes a sample it can either be absorbed by the atoms in the material or scattered through. The 'photoelectric effect' describes the process whereby an X-ray is fully absorbed by a material and its energy is transferred entirely to an inner-shell electron. The energy of the incident X-ray instigates the ejection of the electron from the inner shell, generating a vacancy, in turn creating instability within the atom, see Figure 3.5. The atom regains stability as

electrons from the outer-shells transfer to lower energy states to fill the vacancies. With each transferring electron, X-rays of energies, *E*, characteristic of individual elements are emitted and can be detected so as to provide compositional data of the material [192, 195].

X-ray fluorescence analysis here has been carried out by a commercial laboratory at the University of Leicester, using a PANalytical Axios-Advanced XRF spectrometer with a 4kW Rhodium (Rh) anode end window, super sharp ceramic technology X-ray tube. Sample preparation involves dissolving the powder in a lithium tetraborate flux at high temperatures (> 1000 °C) which is cast then in a platinum/gold crucible to form a 32 mm homogenous fused bead. Fusion at this temperature causes the HA samples to breakdown and dissolve into the flux with the elements present in the sample subsequently becoming captured‡. Beads are loaded from a 96 position sample changer. Quantitative elemental analysis was carried out using PANalytical SuperQ system with IQ+, WROXI and ProTrace extensions. Calibrations are obtained by using values published on the GeoREM database which utilises the Philips based Fundamental parameters correction technique. This approach has replaced calibration using 70-75 International standard reference materials measured under the same experimental conditions and regressing the measured count ratios against recommended concentrations [196-199].

‡ From discussion with XRF specialist Mr Steve Davies of PANalytical Ltd.

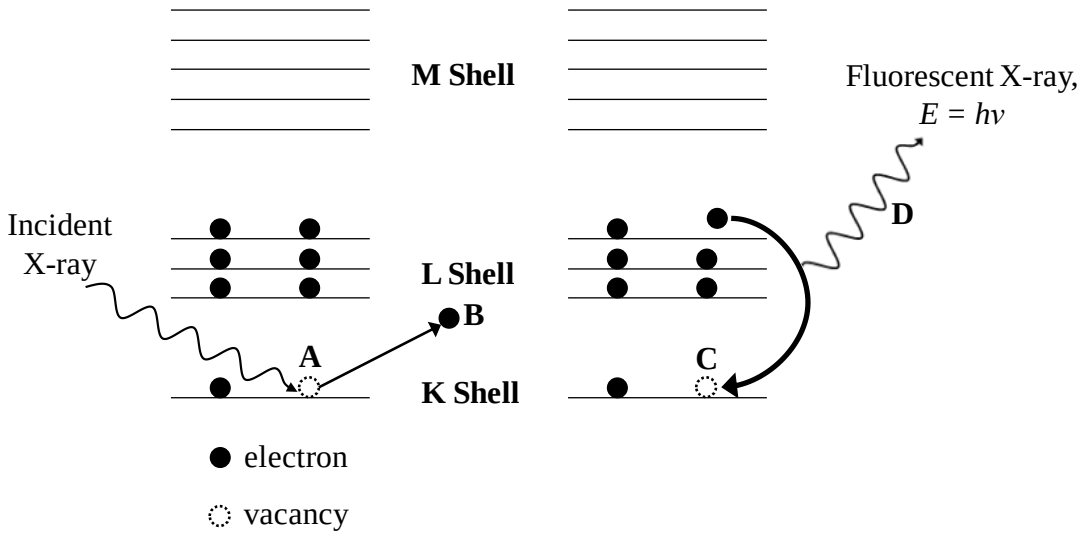

Figure 3.5: Schematic of the XRF process. Incident X-ray knocks out an inner shell electron from A to B. This vacancy is then filled by a higher shell electron, C, which releases excess energy, E, in the form of an X-ray photon, D. The energy of the emitted X-ray is characteristic of the host element. Modified from [200].

3.12.3. Fourier transform infrared spectroscopy

Fourier transform infrared spectroscopy (FTIR) is a chemical analysis technique utilised for the identification of chemical compounds and substituent groups through the absorption of infrared light [201]. As a sample is exposed to different wavelengths of infrared light, transitions between vibrational energy levels (modes) of different chemical bonds are detected, allowing for the functional groups within molecules in the sample to be identified (e.g. carbonates, C-O).

For FTIR, infrared wavelength, λ, is commonly presented as wavenumber, $\bar{\nu}$; this is expressed as the inverse of wavelength, in cm^{-1}.

$$\bar{\nu} = \frac{1}{\lambda} \tag{3.3}$$

The mid IR wavenumber range (most commonly utilised in standard FTIR analysis) is 4000 - 400 cm^{-1}, where an increase in wavenumber is related to a greater energy, *E*:

$$E = hc\bar{v} \tag{3.4}$$

Where *h* = Planck's constant (6.6 x 10^{-34} J s^{-1}), and *c* = the speed of light (3 x 10^{10} cm s^{-1}.

Fourier transform infrared spectroscopy has been carried out using a Thermo Scientific Nicolet iS10 FTIR spectrometer running OMNIC processing software and fitted with an attenuated total reflection (ATR) accessory. The ATR accessory utilises a diamond crystal to internally reflect the IR beam, allowing for transmission up to typically 0.5 - 5 μm into the sample. Energy is absorbed by the sample, attenuating the IR beam which then passes to a detector, generating an IR spectrum. Samples do not require pre-preparation; solid powders are placed in direct contact with the diamond crystal. A weight is placed over the sample, applying a pressure that encourages maximum contact with the crystal surface.

Characterisation of spectra is carried out by correlation against previous recorded reference data (using digital spectra databases or against reputable research), with peaks assigned to the vibration of specific functional groups.

3.12.4. Laser ablation inductively coupled plasma mass spectrometry

Laser ablation inductively coupled plasma mass spectrometry (LA-ICP-MS) has become an important analytical technique, most commonly applied for trace elemental analysis in geological samples [202]. The technique works by

decomposing (ionising) the sample into neutral elements using a high temperature argon plasma, these are then analysed, according to their mass to charge ratio using mass spectrometry [203].

Samples are firstly converted to aerosols by way of laser ablation. The aerosol is then passed into a torch body and mixed with heated argon gas (typical temperature = 10,000 °C), producing an argon plasma flame. This causes atomisation and ionisation of the sample. Ions are transferred into a pumped vacuum system through a quadrapole mass filter and to a mass spectrometer, with a typical detection limit of 0.1 μg^{-1}. A quadrapole mass filter uses variable voltages over four metal rods to allow for only specific ions (with specific mass/charge ratio) to pass through to the detector.

Laser ablation inductively coupled plasma mass spectrometry (LA-ICP-MS) has been carried out at the School of Earth and Environment, University of Leeds. Samples were prepared as 10 mm pressed pellets and were analysed using a Geolas Q Plus laser ablation system, with a 193 nm excimer laser, coupled to an Agilent 7500c ICP-MS.

3.13. Particle analysis techniques

Analysis of powder samples at the nanoscale level has been carried out using both Scanning and Transmission electron microscopy techniques, SEM and TEM. Hydroxyapatite nanoparticles for toxicology assays have also been analysed for their size distribution in solution using dynamic light scattering (DLS).

3.13.1. Scanning electron microscopy

Scanning electron microscopy (SEM) utilises the scanning of the surface of a sample by a focussed electron beam (typical energy = 3 - 30 kV), providing detailed morphological and micro-structural information via secondary (SE) and back-scattered electrons (BSE) at a resolution down to ~10 nm. Secondary electrons are low energy (< 50 eV) electrons that are ejected from inner shell orbital's of the atoms within the sample, and because they are readily reabsorbed they are utilised to provide topographical and micro-structural information of the sample surface. A basic schematic showing the key components of an SEM is shown in Figure 3.6.

Back-scattered electrons are high energy electrons that originate from the incident beam and are reflected from the sample through elastic scattering. The degree of electron backscatter is probabilistic in nature and is related to the composition and topography of the specimen. Atoms of a higher atomic number typically provide a larger degree of electron backscatter than lighter elements, and so the contrast in backscattered electron images, particularly for flat polished specimens can give an indication of the relative composition of a material.

To enable imaging, the sample surface must be of sufficient size and of a conductive nature to avoid accumulation of surface charge. Sample preparation here involves small amounts of powder dropped onto an aluminium support stub with an adhesive carbon leit-tab (Agar Scientific Ltd) fixed on top. Excess powder is removed with an air-jet and the sample is subsequently coated using an Agar High Resolution Pt/Pd Sputter Coater (thickness = 5 nm) to provide a conductive surface. Sample imaging was carried out, in high vacuum, using a LEO 1530 Gemini FEGSEM operated at 5 kV, at a 5 mm working distance and using an in-lens

detector. Sample analysis and image acquisition was performed using Zeiss SmartSEM™ software.

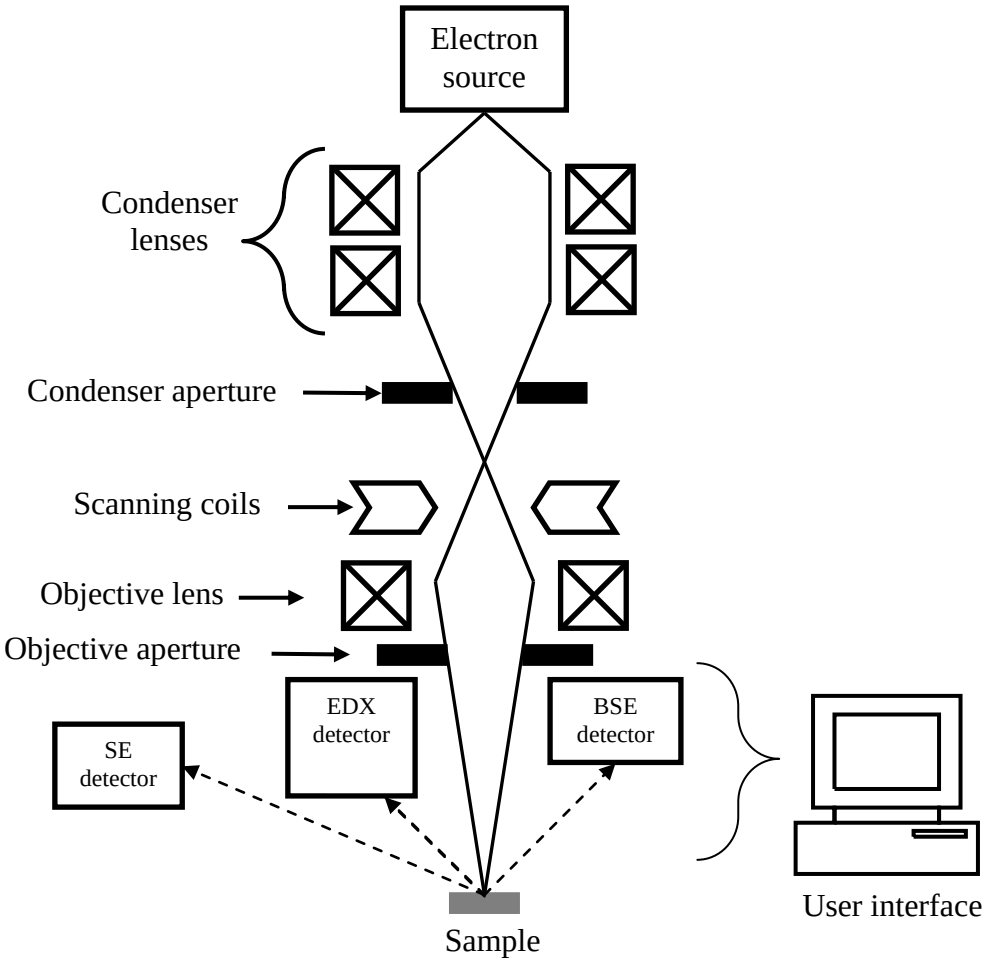

Figure 3.6: Schematic of typical SEM. Modified from [204].

3.13.2. Transmission electron microscopy

Transmission electron microscopy (TEM) analysis can provide information on powder morphology and internal microstructure utilising a variety of imaging and spectroscopic methods. High-resolution (HR) imaging, selected area electron diffraction (SAED) and spectroscopic techniques (e.g. energy dispersive X-ray (EDX) analysis) allow for a comprehensive analysis of a sample at the nanoparticle level.

A standard TEM instrument produces an electron beam using a tungsten filament (electron gun), which is typically accelerated at 50 - 200 kV. The wavelength of the electrons, λ is related to the accelerating voltage, V by

$$\lambda = h(2meV)^{-1/2} \quad (3.5)$$

Where *m* and *e* represent the mass and charge of an electron, and *h* is Planck's constant [162].

The generated electron beam passes through a series of electromagnetic lenses, with firstly condenser lenses which focus a parallel beam onto the specimen. Objective and projector lenses subsequently produce a magnified image of the specimen onto a fluorescent viewing screen. TEMs can offer a resolution down to ~0.1 nm. Figure 3.7 displays a schematic of the key components of a TEM [93, 205].

Sample preparation for TEM requires the specimen to be thin enough to transmit a high energy electron beam (ideally < 100 nm thick), to provide imaging through mass thickness contrast, diffraction contrast (if crystalline) or phase contrast at high-resolution, providing the sample is thin enough. The sample preparation for nano-powders involves ultrasonically dispersing the powder in a suitable dispersant

(e.g. methanol) and drop casting onto a holey carbon support film (Agar Scientific Ltd).

Powder sample imaging was acquired using; (a) a FEI Tecnai TF20 field emission gun (FEG-) TEM operated at 200 kV and fitted with a Gatan Orius SC600A CCD camera and fitted with an Oxford Instruments ultra thin window EDX spectrometer running INCA processing software, and (b) a Philips CM200 FEGTEM operated at 197 kV and fitted with a Gatan Imaging Filter (GIF 200) and an Oxford Instruments ultra thin window EDX spectrometer running ISIS processing software. Particle sizes, of 50 particles per sample, were measured using Gatan's Digital Micrograph software.

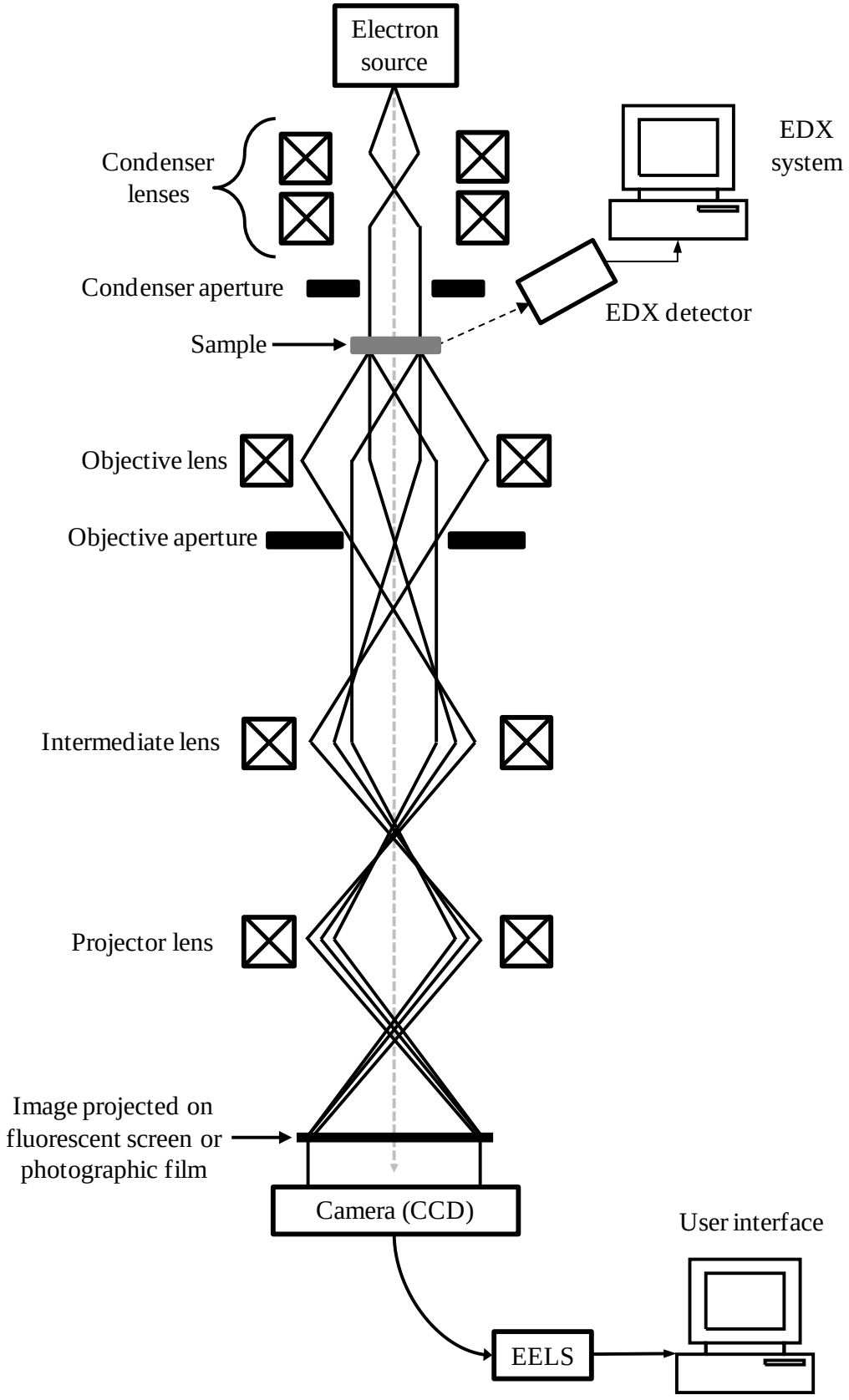

Figure 3.7: Schematic of typical TEM. Modified from [205].

3.13.3. Energy dispersive X-ray spectroscopy

Energy dispersive X-ray (EDX) spectroscopy is a method first developed in the 1960's, initially for nuclear applications [206]. The first EDX detectors were successfully applied to SEM's in about 1970, and were commonly adapted for both SEM and TEM by 1980 [206]. The technique utilises electrons focussed on a sample to trigger the release of X-ray photons (similarly to XRF, Section 3.12.2) that have energies characteristic of the elements of the specimen; allowing for the quantitative analysis of composition of the material to be obtained [93, 207].

The technique can also be utilised to track changes in composition of a material during exposure to a focussed high energy electron beam. Williams and Carter [93] discuss the EDX system as three key components:

- **The detector** receives the X-ray photon signal and generates a charge pulse proportional to the energy of the X-ray;
- **Processing electronics** convert the charge pulse into a voltage, which is isolated from other pulses, amplified and recorded as a digital signal specific to an X-ray of specific energy;
- **The computer** stores the signals assigned to that energy, presenting it in an element-compositional spectrum of energy (eV) against intensity (%) using analysis software. The computer ultimately controls the detector, processing electronics and the display [93].

Figure 3.8 displays a basic schematic of this process.

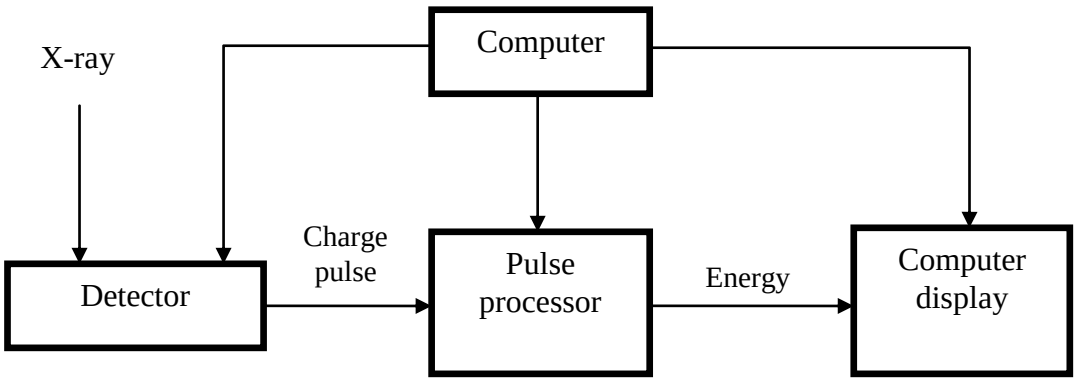

Figure 3.8: Schematic of the principles of EDX [93].

Due to detector materials absorbing low energy X-rays, most EDX systems have limited detectability of elements with a low atomic number (Z) [93, 208]. Typical EDX systems utilises a Si(Li) crystal detector or, more recently, silicon drift detectors (SDD), which offer greater energy resolution particularly at lower X-ray energies (typically 140 eV). Detectors can be capped with either a beryllium window, an ultra-thin window (UTW) or be left windowless. Beryllium windows are generally not preferred as they absorb low energy Kα X-rays, preventing detection of elements where Z < 11 [93]. Ultra-thin windows are more commonplace and provide low-energy X-ray absorption, with some UTW's allowing for the analysis of Be Kα X-rays [93]. They can comprise of < 100 nm polymer films, diamond, boron nitride or silicon nitride. Windowless detectors are more common in ultra-high vacuum (UHV) instruments and can routinely detect Be Kα X-rays [93].

For the TEM-EDX analysis here, samples were examined using a Philips CM200 FEGTEM operating at 197 kV and fitted with an Oxford Instruments ultra thin window ISIS energy dispersive X-ray (EDX) spectrometer. The Ca and P content of HA samples was measured in the TEM by quantification of a stationary

focused probe, (typically 500 nm diameter); the Ca/P ratio, as determined from the Oxford ISIS processing software using virtual standards for the Ca and P Kα X-ray peaks, was monitored, at a take-off angle of 20° and a specimen tilt angle of 15°.

3.13.4. Electron fluence analysis

Previous experiments demonstrating the beam sensitivity of hydroxyapatite have been carried out by Eddisford *et al* [94] and were based on the assumption that electron beam damage of inorganic materials is a function of cumulative fluence (total number of electrons per unit area) and fluence rate (number of electrons per unit area per second) at a given beam energy [95]. This information, regarding the effects of electron beam energy, has been identified by tracking the changes in the Ca/P ratio over time by exposing single particles to a fine focussed electron beam and measuring the Ca/P ratio with EDX [94].

Following these TEM conditions, the beam current at a fixed illumination (spot size 8 and largest, 200 μm, condenser aperture) was estimated by using an FEI calibration curve based on the measured brightness (i.e. exposure time) on the (large) fluorescent viewing screen of the TEM: current (in nA) = 4.875/(Exposure time for an emulsion setting of 2.0). Beam currents were then converted to electron fluence rates and fluence by measuring the area of illumination and the total exposure time respectively.

The TEM-EDX method allows compositional analysis to be carried out on small clusters of particles, providing valuable information on fine-scale compositional homogeneity within a sample. However it is important to ensure that the sample is not subjected to an electron beam so intense that damage occurs and erroneous levels of Ca and P are detected. Therefore, a series of prior experiments were undertaken to establish the optimal electron fluence for obtaining reliable data.

The electron fluence can be controlled in the microscope using a condenser aperture, spot size and exposure time. These experiments will be described in Section 4.3.4 of the Chapter 4.

3.13.5. Dynamic light scattering

For the measurement of nanoparticle size and size distribution within an aqueous environment, dynamic light scattering (DLS) can be utilised [209]. This technique provides a quantitative assessment of particle size distribution and can complement the primary particle size measurements from TEM; however it is limited by the inability to differentiate between particle shape and is reliant on a high quality dispersion of particles. This quality is also dependent upon the polydispersity, which is the relative number of primary (single) particles in comparison to agglomerates (bound clusters of particles held together by weak inter-particle forces) or aggregates (chemically bound clusters of particles) [210]. Accuracy of particle size measurement is also reliant on knowing the refractive index of the nanoparticles as well as the refractive index and viscosity of the suspending solution [209, 211, 212]. The refractive index for HA is reported in the range $\eta = 1.63 – 1.64$ [213], and for DMEM $\eta = 1.33$ (water = 1.33).

Dynamic light scattering uses a coherent light source (typically a red laser) focused through a particle suspension where particles scatter light in all directions as they undergo Brownian motion (random movement of particles within a suspension). Scattering causes light intensity fluctuations which is collected by a detector positioned at a specific angle to the incident ray (typically 90 °). These signals are converted into electrical pulses and correlated to particle diameter by monitoring the time-dependent variation in the scattering intensity. A schematic of the process is shown in Figure 3.9 [214].

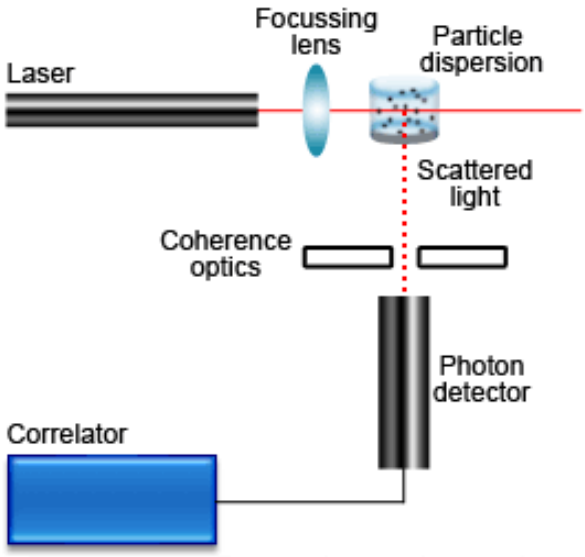

Figure 3.9: Schematic of the DLS process [214].

To replicate the conditions utilised in the toxicity assays, stock suspensions of 0.1% w/v pH 9 and pH 11 hydrothermal HA were prepared in distilled water. These were further prepared as 10 and 50% v/v suspensions in Dulbecco's modified Eagle's medium (DMEM) and measured using a Malvern Zetasizer Nano DLS instrument, operating with red laser light source (wavelength = ~633 nm). Data manipulation was carried out using Zetasizer software (version 5.02). Sample measurements were repeated 5 times, with the overall average mean size distribution and ‘z-average diameter’ (cumulant average particle diameter) results presented.

Chapter 4. Results & discussion - Hydroxyapatite

Preface

Hydroxyapatite is a material commonly used in various biomedical applications due to its excellent properties such as biocompatibility, bioactivity and osteoconductivity, closely matching that of natural bone. The specific application of HA, at the nanoscale, is strongly dependent on the properties of the nanoparticles such as crystallinity, morphology and stoichiometry, all of which are controlled by the method of synthesis [90, 215].

Work in this Chapter aims to firstly prepare nanoparticulate hydroxyapatite powders following two established methods of synthesis, hydrothermal and sol-gel. The nanoparticle morphology and chemical composition of these powders will be carefully analysed using a variety of bulk (FTIR, LA-ICP-MS, XRD and XRF) and particle level (SEM and TEM) characterisation techniques, and compared to a commercially available HA powder purchased from Sigma-Aldrich. A novel, low-fluence analytical technique will be developed in the TEM that allows for the safe characterisation of the chemical composition of HA nanoparticles without risk of irradiation damage by electron beam.

Two phase-pure and near stoichiometric composition (Ca/P = 1.67) HA powders are to be subsequently prepared by the hydrothermal method, and analysed for nano-cytotoxicity.

4.1. Preliminary analysis of phosphorus-based precursors for sol-gel HA synthesis

Preliminary experiments have been carried out to examine the stability of triethyl phosphite on exposure to air, in comparison to the more stable triethyl phosphate. Figure 4.1 displays the chemical formulae and molecular structures of (a) triethyl phosphite and (b) triethyl phosphate:

Triethyl phosphite: $C_6H_{15}PO_3$

Boiling temperature = 156 °C

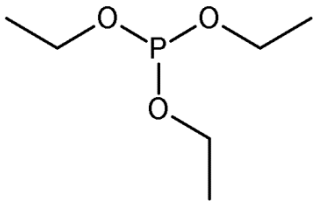

Triethyl phosphate: $C_6H_{15}PO_4$

Boiling temperaturre = 215 °C

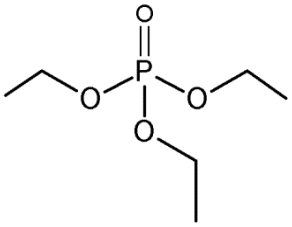

Figure 4.1: Chemical formula and molecular structure for (a) triethyl phosphite and (b) triethyl phosphate.

It is reported that triethyl phosphate has a relatively low reactivity for hydrolysis towards the formation of HA, and so long aging times and high solution temperatures are required; therefore, due to a higher reactivity for hydrolysis, and despite its less stable nature, triethyl phosphite is often preferred as a precursor for HA synthesis [26, 62, 216]. Figure 4.2 displays the change of mass of triethyl phosphite and triethyl phosphate with increasing temperature by decomposition in air, using a TGA (temperature gradient = 20 °C min^{-1}). It is observed that the triethyl phosphite has fully evaporated by ~125 °C, and the triethyl phosphate by ~170 °C.

Most notably, the onset of mass loss of triethyl phosphite is seen to begin almost immediately, suggesting instability at ambient conditions. However, the onset of evaporation of the triethyl phosphate does not occur until ~50 °C. The mass loss of these two precursors, at ambient conditions, is further analysed in Figure 4.3. Figure 4.3 displays the relative change of mass of triethyl phosphate and triethyl phosphite when placed into an evaportating dish, on a balance, and exposed to ambient room conditions (~20 °C) for 15 minutes. The volatile nature of triethyl phosphite is clearly apparent with an observed mass loss rate of ~0.2 wt% min^{-1}. The triethyl phosphate remains relatively stable, but is observed to gradually gain mass at a rate of ~0.03 wt% min^{-1}. This mass gain may be attributable to hydrolysis with air. To observe whether potential drifting of the balance has an effect here, an empty control dish was analysed under the same conditions and it's mass is seen, in Figure 4.3, to remain near- constant for the 15 minute period, with a standard deviation of ± 0.003%. This discards any significant effect on the results by drifting of the balance.

The mass loss of triethyl phosphite, observed here, can be attributed to its readiness to evaporate when exposed to air at atmospheric pressure [217]. Conversely, triethyl phosphate does not readily undergo similar evaporation [218]. As a vapour, triethyl phosphite will subsequently oxidise, in air, producing the more stable vapour of triethyl phosphate [219, 220].

For sol-gel HA synthesis here, triethyl phosphite was utilised due to its superior reactivity for hydrolysis, however these preliminary experiments highlight the significant instability of the precursor when exposed to ambient conditions. To prevent loss of precursor by evaporation during HA synthesis, certain measures to minimise exposure to air must be employed and therefore prompt parafilm sealing of all glassware has been utilised during all sol-gel HA preparations.

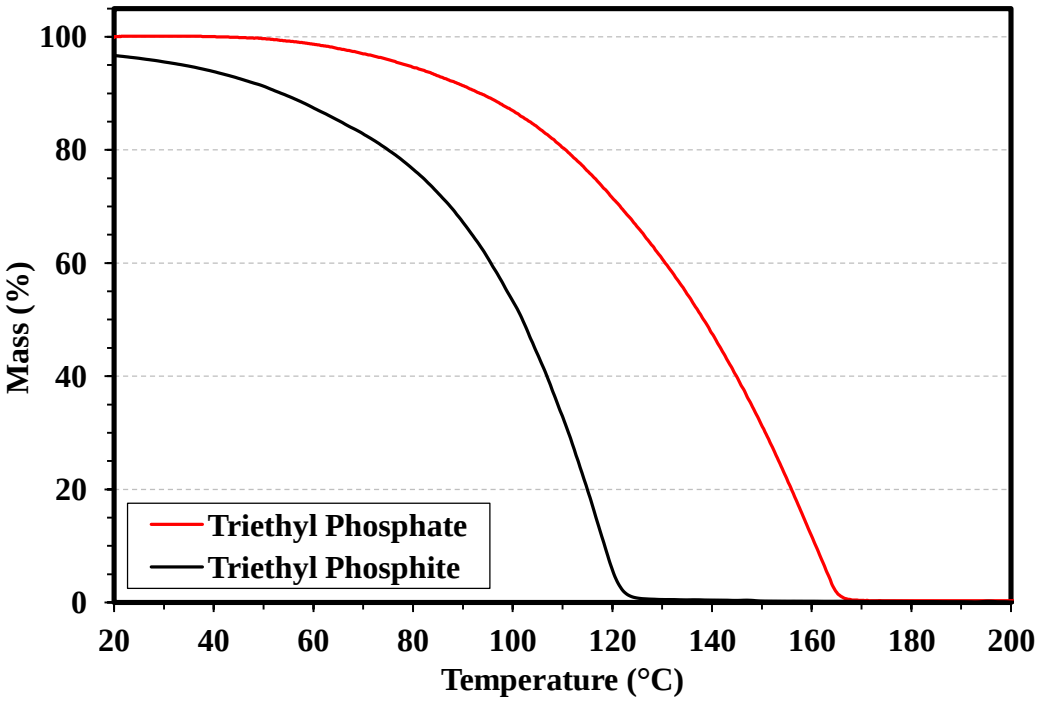

Figure 4.2: Decomposition of triethyl phosphate and triethyl phosphate by heating by TGA. Heating rate = 20 °C min^{-1}. Starting volume = 17.16 ml of triethyl phosphate and 18.85 ml of triethyl phosphite.

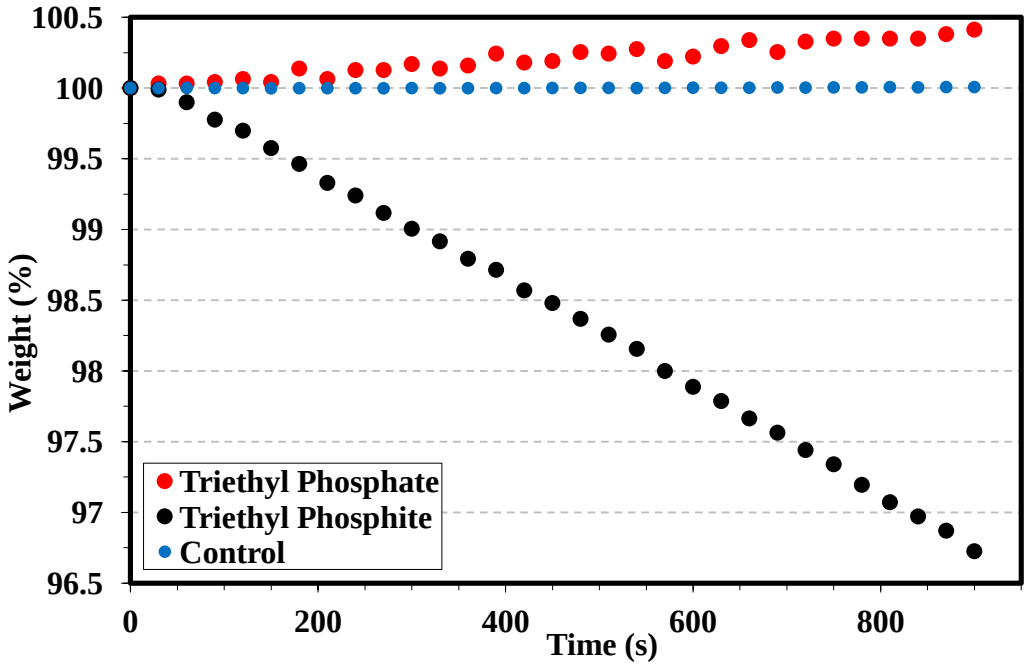

Figure 4.3: Percentage mass change of triethyl phosphate (9.45 ml) and triethyl phosphite (8.95 ml) when exposed to air. Measurements were taken every 30 seconds for 15 minutes using a balance. An empty control dish was also measured to observe potential drifting of balance (blue data points).

4.2. Hydroxyapatite characterisation

Hydroxyapatite ($Ca_{10}(PO_4)_6(OH)_2$) powders have been produced by sol-gel and hydrothermal methods. Elemental and compositional characterisation of these powders has been carried out at the bulk and particle level utilising a variety of analytical techniques with results compared to a commercial HA powder purchased from Sigma-Aldrich.

Two further HA samples, prepared via hydrothermal method, have also been examined for cytotoxicity by an undergraduate research group led by Dr Lars Jeuken at the Leeds Faculty of Biological Sciences.

Table 4.1 summarises all the synthesis conditions of the six HA samples that are to be analysed in this Chapter.

Table 4.1: Summary of all HA samples to be characterised.

Sample Number	Hydroxyapatite sample	Preparation conditions
1	Sigma-Aldrich HA	Synthesis method unreported by supplier despite request
2	Hydrothermal HA	Produced with starting suspension pH 11
3	Sol-gel HA	Calcined at 500 °C
4	Sol-gel HA	Calcined at 700 °C
5	*Hydrothermal HA*	*Produced with starting suspension pH 9*[§]
6	*Hydrothermal HA*	*Produced with starting suspension pH 11*[§]

[§] Synthesised for cytotoxicity analysis.

4.2.1. Bulk analysis

4.2.2.1. X-ray diffraction (XRD)

X-ray powder diffraction patterns for samples 1-4 are shown in Figures 4.4 - 4.7 with corresponding peak list data shown in the appendix, Tables A2 - A5. The Sigma-Aldrich powder (Figure 4.4) and the pH 11 hydrothermal powder (Figure 4.5) showed only diffraction peaks due to hydroxyapatite (ICDD ref: 01-074-0566 [37]); peaks were sharper for the hydrothermal powder which is consistent with a larger particle size and good degree of crystallinity as noted by TEM imaging and by selected area electron diffraction (SAED) in TEM (Figures 4.20 - 4.23).

The sol-gel derived HA, calcined at 500 °C (Figure 4.6), showed HA reflections plus a faint extra peak at $2\theta = 29.4°$, indicating a minor amount of second-phase calcium carbonate ($CaCO_3$, 'calcite', ICDD ref: 00-005-0586 [221]). The presence of carbonate in the 500 °C sol-gel HA could be attributed to evaporative losses of the phosphite precursor reagent during synthesis, or alternatively could be the result of CO_2 pickup from the air during handling [222].

Increasing the calcination temperature to 700 °C resulted in significant levels of other secondary phases (Figure 4.7); β-tricalcium phosphate, β-TCP ($Ca_3(PO_4)_2$, ICDD ref: 04-008-8714 [223, 224]), along with small amounts of dicalcium phosphate anhydrate, DCPA ($CaHPO_4$, ICDD ref: 01-070-0360 [225]) and calcium oxide (CaO, ICDD ref: 04-003-7161 [226]).

Whilst evaporation of un-reacted triethyl phosphite from the sol or gel could contribute to a net excess of Ca, leading to $CaCO_3$ formation in the 500 °C sample for example, the other secondary phases observed after heating a gel to 700 °C may be a result of thermal decomposition of HA. Previous studies suggest HA may decompose above temperatures as low as 600 °C [227]. Increasing the calcination

temperature to 700 °C and above, causes the decomposition of HA into β-TCP and CaO, following the proposed reaction [227, 228]:

$$Ca_{10}(PO_4)_6(OH)_2 \rightarrow 3Ca_3(PO_4)_2 + CaO + H_2O \quad (4.1)$$

To confirm this, the Sigma-Aldrich powder was subject to calcination for 1 hour at both 700 °C and 800 °C. X-ray powder diffraction patterns for these samples are shown in Figure 4.8, and it is noted that the onset of decomposition, of HA to β-TCP, began at 700 °C, with a greater amount of β-TCP formed at 800 °C.

The decomposition temperature of HA may be strongly dependent on the particle characteristics and synthesis route for the HA powder [228, 229].

In the present work, the calcium carbonate phase observed in the 500 °C sol-gel sample, which could be due to evaporative losses of the phosphite precursor reagent (see Figure 4.3), would be expected to decompose to calcium oxide at 700 °C. However carbonated apatite has been shown to decompose at temperatures as low as 400 °C [230]. This could explain the absence of $CaCO_3$, and presence of CaO, in the 700 °C sol-gel powder [231].

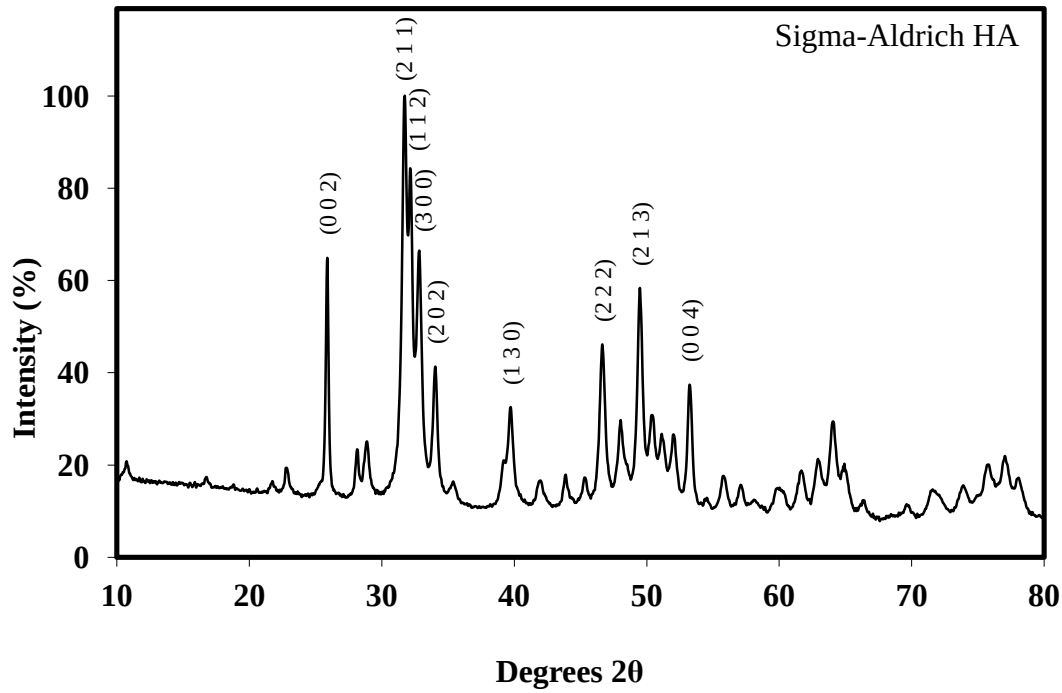

Figure 4.4: XRD pattern for Sigma-Aldrich HA. All peaks correspond to a pure HA phase. Major peaks are indexed to ICDD ref: 01-074-0566 [37]. Full peak data in the appendix, Table A2. Mean crystallite size, τ = 62.68 nm (using Scherrer equation).

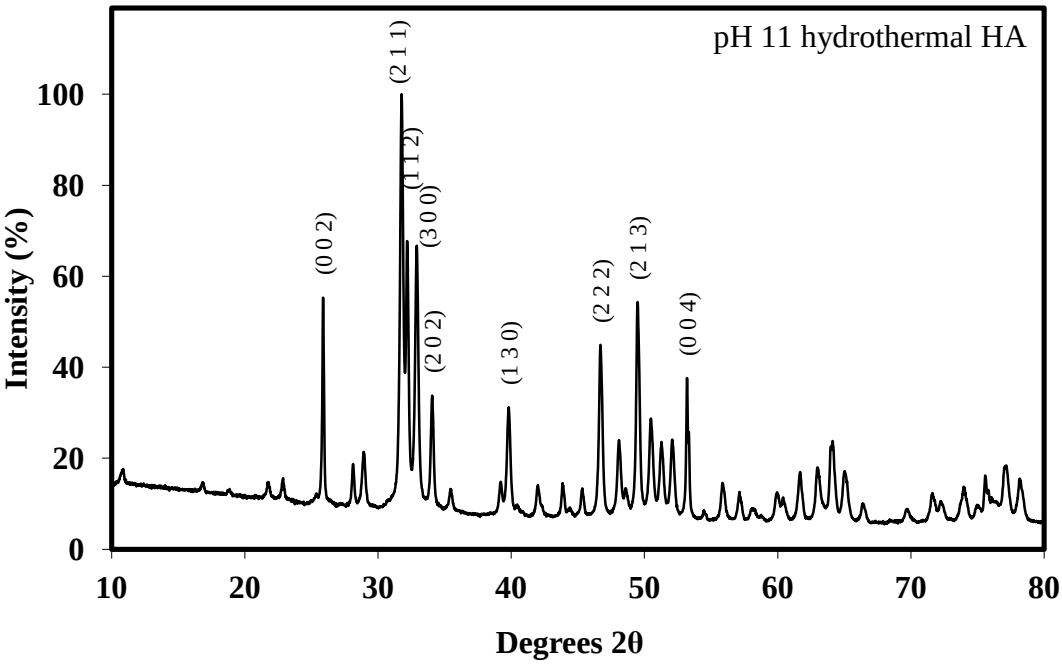

Figure 4.5: XRD pattern for pH 11 hydrothermal HA. All peaks correspond to a pure HA phase. Major peaks are indexed to ICDD ref: 01-074-0566 [37]. Full peak data in the appendix, Table A3. Mean crystallite size, τ = 106.51 nm (using Scherrer equation).

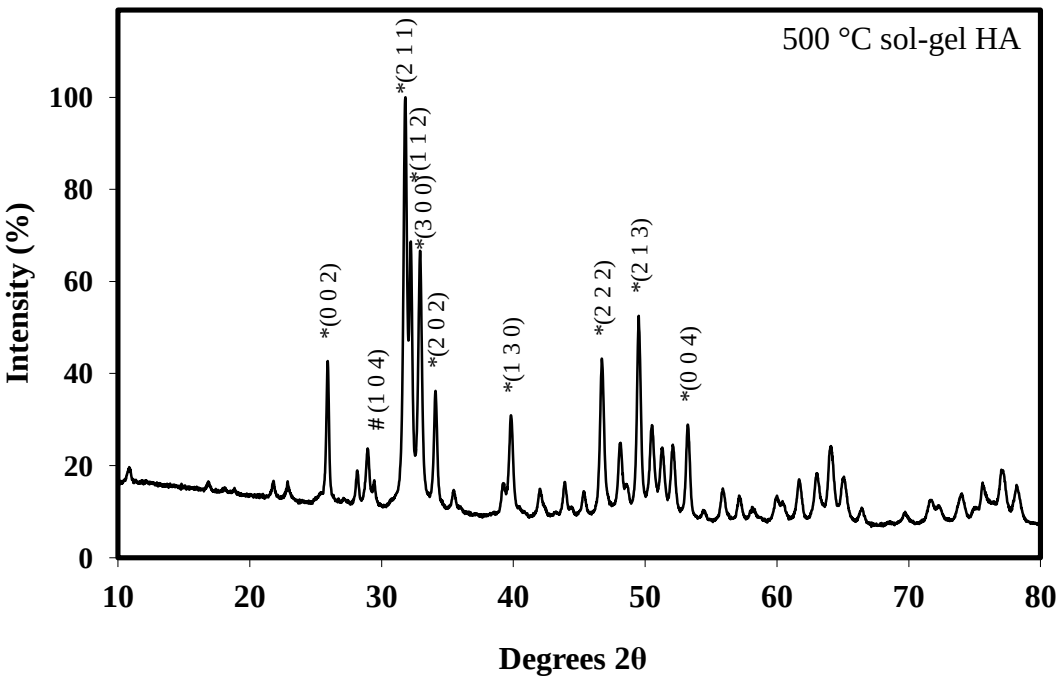

Figure 4.6: XRD pattern data for 500 °C sol-gel HA. Indexed peaks labelled '*' and unlabelled peaks correspond to HA, ICDD ref: 01-074-0566 [37]. '#' denotes the most intense peak of calcium carbonate, $CaCO_3$, indexed to ICDD ref: 00-005-0586 [221]. Full peak data in the appendix, Table A4. Mean crystallite size (of HA), τ = 73.74 nm (using Scherrer equation).

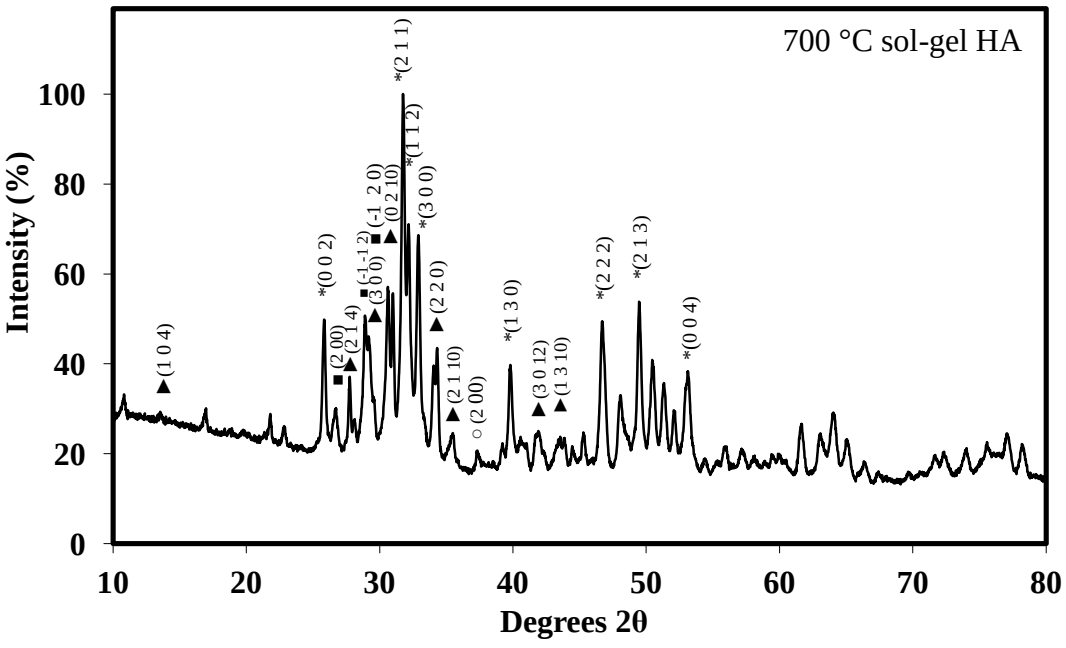

Figure 4.7: XRD pattern for 700 °C sol-gel HA. Indexed peaks labelled '*' and unlabelled peaks correspond to a HA phase ICDD ref: 01-074-0566 [37]. '▲' denotes indexed peaks of β-tricalcium phosphate, β-TCP ($Ca_3(PO_4)_2$) ICDD ref: 04-008-8714 [232], '■' denotes indexed peaks of dicalcium phosphate anhydrate, DCPA ($CaHPO_4$) ICDD ref: 01-070-0360 [225], '○' denotes indexed peak of calcium oxide (CaO) ICDD ref: 04-003-7161 [226]. Full peak data in the appendix, Table A5. Mean crystallite size (of HA), τ = 68.47 nm (using Scherrer equation).

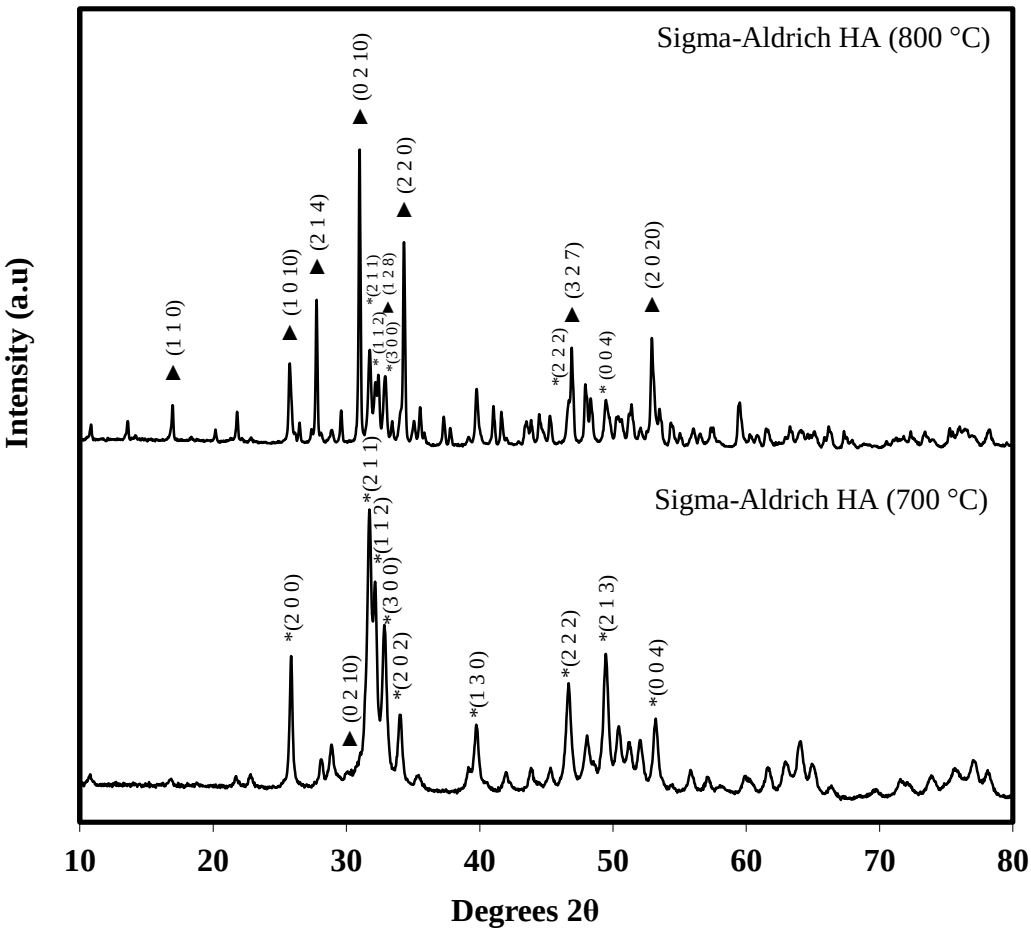

Figure 4.8: Powder XRD patterns for Sigma-Aldrich HA decomposed for 1 hour at 700 and 800 °C. Indexed peaks '*' and unlabelled peaks at 700 °C correspond to a HA phase, ICDD ref: 01-074-0566 [37] with '▲' denoting single most intense peak of β-TCP ($Ca_3(PO_4)_2$) indexed to ICDD ref: 04-008-8714 [232]. Indexed peaks labelled '▲' and unlabelled peaks at 800 °C correspond to β-TCP ($Ca_3(PO_4)_2$) ICDD ref: 04-008-8714 [232]. Peaks labelled '*' at 800 °C are indexed to HA, ICDD ref: 01-074-0566 [37]. At 800 °C most of the HA has decomposed to β-TCP. Full peak list data in the appendix Tables A6 and A7.

4.2.2.1.1. HA samples prepared for cytotoxicity analysis

Two hydrothermal HA samples prepared at pH 9 and 11 (samples 5 and 6 in Table 4.1) for cytotoxicity assays reported in the appendix, have also been analysed by XRD, with patterns displayed in Figures 4.9 and 4.10 respectively. Peak lists are shown in the appendix, Tables A8 and A9. Both samples showed only reflections due to hydroxyapatite (ICDD ref: 01-074-0566 [37]), with sharp peaks indicating a large particle size and good crystallinity confirmed by TEM and corresponding selected area electron diffraction (SAED) pattern (Figure 4.25a-d).

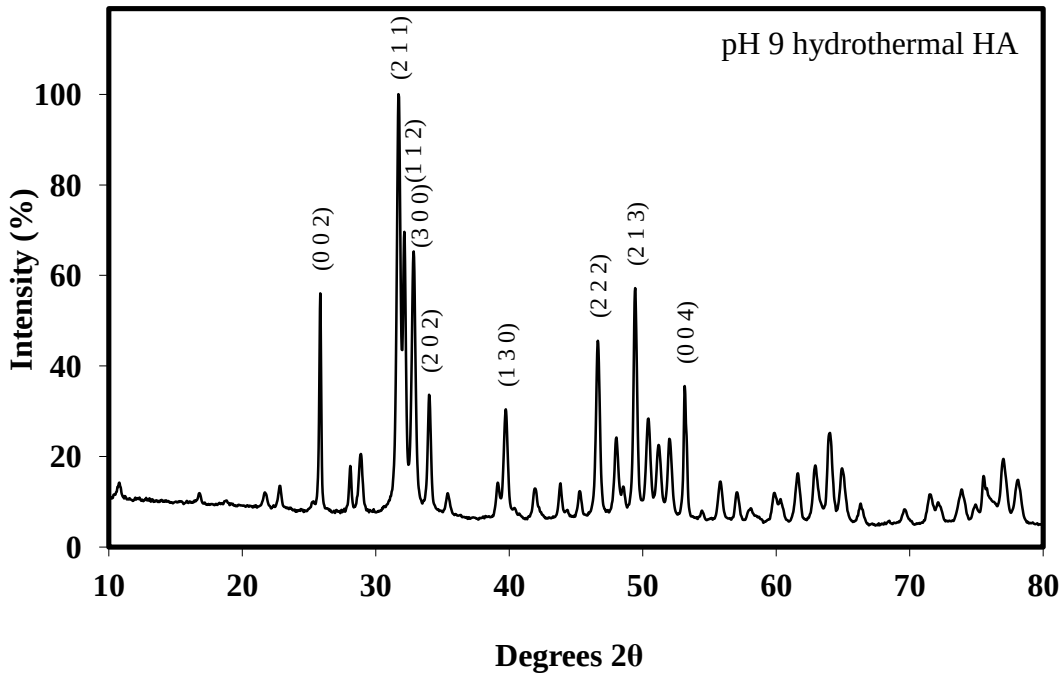

Figure 4.9: XRD pattern for pH 9 hydrothermal HA for prepared cytotoxicity analysis. All peaks correspond to a pure HA phase. Major peaks are indexed to ICDD ref: 01-074-0566 [37]. Full peak list data in the appendix, Table A8. Mean crystallite size, τ = 108.85 nm (using Scherrer equation).

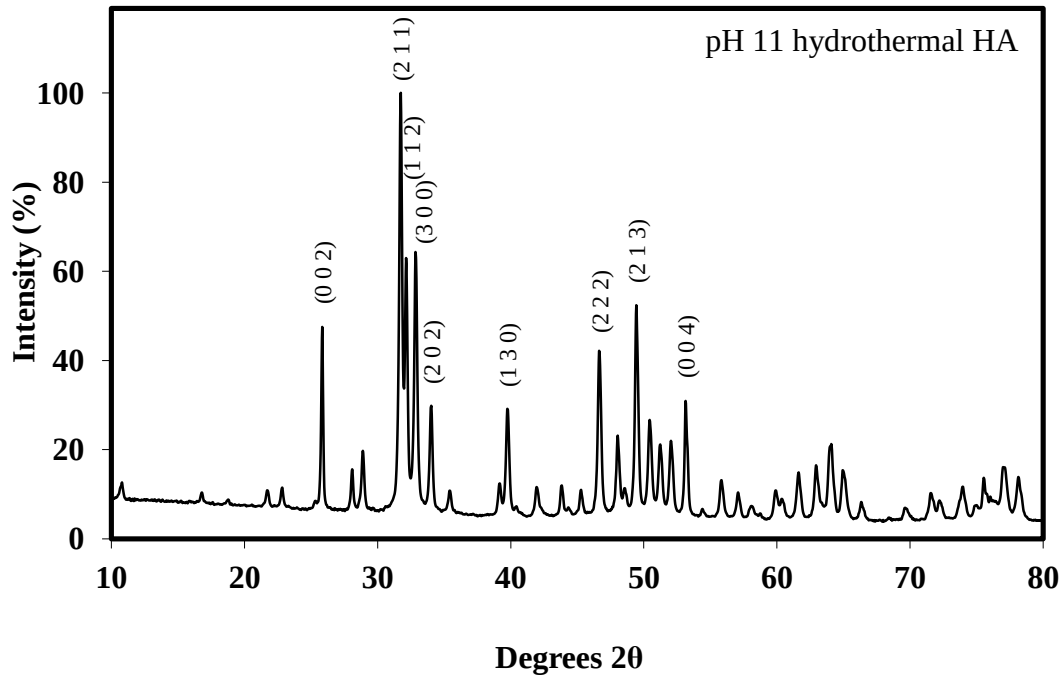

Figure 4.10: XRD pattern for pH 11 hydrothermal HA prepared for cytotoxicity analysis. All peaks correspond to a pure HA phase. Major peaks are indexed to ICDD ref: 01-074-0566 [37]. Full peak list data in the appendix, Table A9**.** Mean crystallite size, τ = 81.48 nm (using Scherrer equation).

4.2.2.2. Fourier transform infrared spectroscopy (FTIR)

The presence of carbonate or hydrated secondary phases, in HA samples 1-4, was investigated using FTIR [233, 234], Figure 4.11. All four HA samples exhibited absorption bands due to OH^- groups, (stretching vibration at ~3570 cm^{-1} and libration mode at 630 cm^{-1}); these were most intense in the pH 11 hydrothermal powder and weakest in the Sigma-Aldrich powder. Additional strong absorption bands at low wavenumber (< 1200 cm^{-1}), are also common across all four HA samples; bands observed in the region ~950 - 1100 cm^{-1} can be assigned to P-O stretching modes [45, 87, 235, 236].

It is observed that some of the absorption bands are visible only as shoulders to neighbouring peaks; this is most notable in the 700 °C sol-gel HA with the OH^- band at 630 cm^{-1}. This is indicative of poorer crystallinity in comparison to the Sigma-Aldrich, 500 °C sol-gel and pH 11 hydrothermal HA samples where this peak becomes increasingly sharper [235]. Additional shoulders in the sol-gel HA calcined at 700 °C are also observed at 945 and 970 cm^{-1} and may indicate the presence of α- and/or β-TCP [4, 237].

The 500 °C sol-gel sample showed medium absorption bands at 875 and 1420-1456 cm^{-1}, which can be attributed to carbonate (CO_3^{2-}) stretching vibrations [235, 236, 238-240]. The band at 875 cm^{-1} has also been assigned to hydrogen phosphate ion (HPO_4^{2-}) in calcium-deficient HA [235, 241]. Very faint bands in these regions were also detected in the 700 °C sol-gel and pH 11 hydrothermal powders. A band at ~875 cm^{-1} is noted in all four samples; and this has been previously linked with the presence of HPO_4^{2-} and $Ca(OH)_2$ [40, 235, 241]. Whilst it is difficult to assign individual bands unambiguously in this low frequency region, the stronger intensity

of the ~875 cm^{-1} band in the 500 °C sol-gel sample, coupled with bands at 1420 and 1456 cm^{-1}, may signify the presence of structural carbonate [235]. It is reported that HA can host carbonate ions at two different sites: site-A, where they substitute for OH^- ions, and site-B, where they substitute for PO_4^{3-} ions ; absorptions bands at 875 and 1420-1456 cm^{-1} are characteristic of carbonate ion occupation of site-B [238, 240].

As already suggested, evaporation of unreacted triethyl phosphite from the sol or gel could contribute to the presence of carbonate in the 500 °C sol-gel powder, however carbonate could also form in a partially decomposed sol-gel system due to interaction between the inorganic product (HA) and the organic decomposition vapours (CO_2-rich). In addition, the formation of an interfacial $CaCO_3$ phase could occur as a result of interaction of the nano-HA with atmospheric CO_2 during storage in air, and this might explain the low levels detected in the 700 °C sol-gel and pH 11 hydrothermal powders [222].

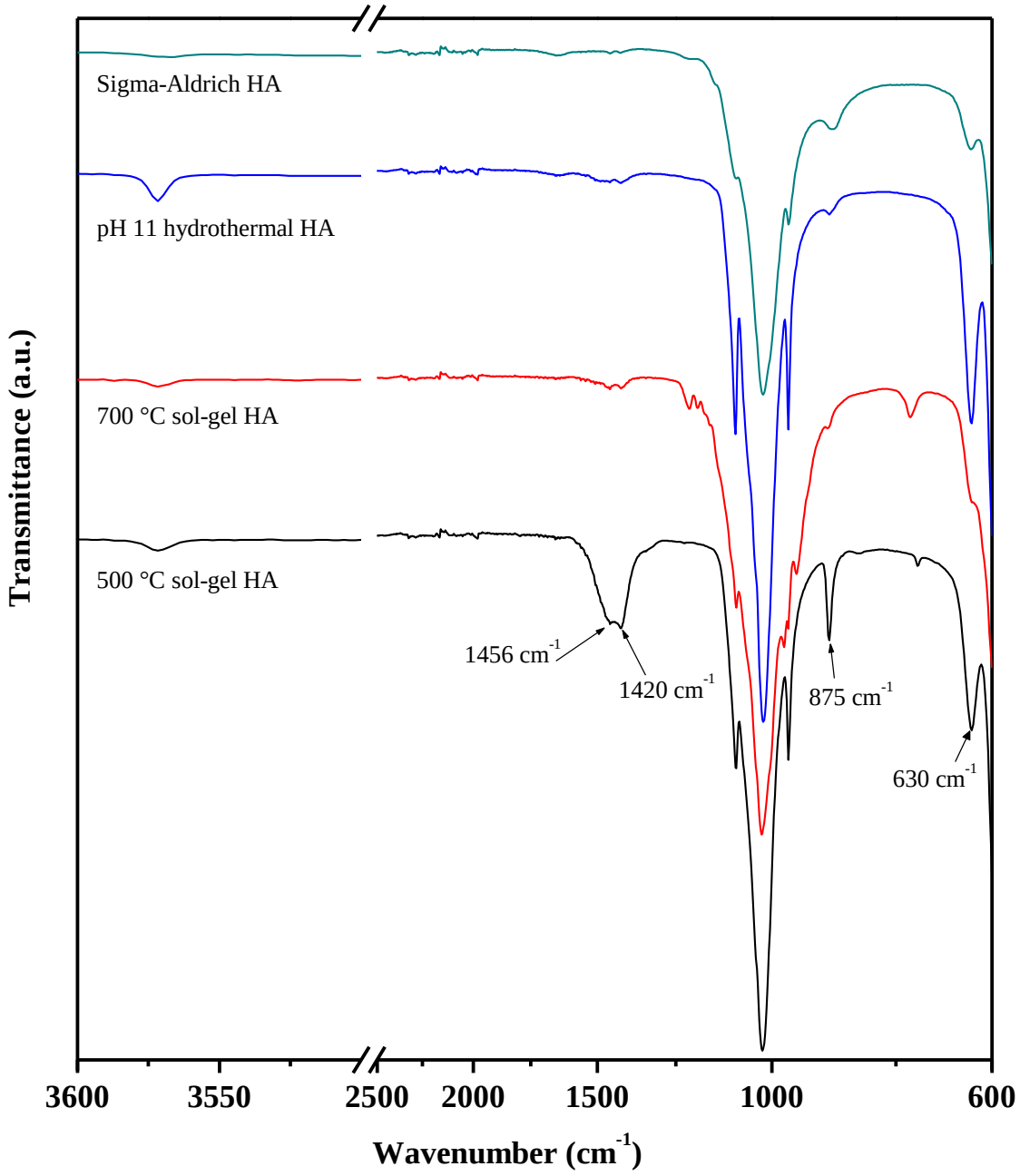

Figure 4.11: FTIR spectra of Sigma-Aldrich HA, pH 11 hydrothermal HA, 700 °C sol-gel HA and 500 °C sol-gel HA. The main lattice vibrations of HA are at < 1200 cm^{-1} along with OH stretches at 3570 cm^{-1}. Likely second phase carbonate stretches, as discussed in the text, are clearly visible in the 500 °C sol-gel powder (at 1456, 1420 and 875 cm^{-1}).

4.2.2.3. X-ray fluorescence (XRF) and laser ablation inductively coupled plasma mass spectrometry (LA-ICP-MS)

The Ca/P ratios of all HA powder samples have been measured in bulk using XRF, by a commercial laboratory (University of Leicester), and also by LA-ICP-MS with the Ca/P ratio data shown in Table 4.2. These are compared to the particle Ca/P ratios measured by TEM-EDX, also shown in Table 4.2 but described in further detail in Section 4.3.4.

The expected Ca/P ratio for stoichiometric hydroxyapatite is 1.67, and both XRF and TEM-EDX data suggest low Ca/P ratios for the Sigma Aldrich powder of 1.50 and 1.45 respectively; the TEM-EDX value is in agreement with previous reports [94].

The XRF average values of bulk Ca/P ratio for the 'in-house' powders (1.68 for the pH 11 hydrothermal HA, 1.83 for the 500 °C sol-gel HA and 1.47 for the 700 °C sol-gel HA) were in broad agreement with the Ca/P values collected by particle TEM-EDX (1.61 for the pH 11 hydrothermal HA. 1.72 for the 500 °C sol-gel HA and 1.65 for the 700 °C sol-gel HA), as the XRF values were each within the range of the standard deviation of the average TEM-EDX value (standard deviations for the XRF powders were not reported by the commercial XRF facility despite repeated requests).

Data collected using LA-ICP-MS showed a higher Ca/P ratio for the Sigma-Aldrich powder of 1.64. This is close to the stoichiometric target, 1.67, however it is not consistent with XRF (1.50) or TEM-EDX (1.45 ± 0.16) data, or previously reported values for this material [94]. The pH 11 hydrothermal HA, shows a near stoichiometric Ca/P ratio of 1.65, a value which is in good agreement with both XRF

(1.68) and TEM-EDX (1.61 ± 0.17) data. The 500 °C sol-gel HA displays a higher than stoichiometric Ca/P ratio of 1.84, which is in agreement with the XRF data (1.83) and within the standard deviation range of the TEM-EDX data (1.72 ± 0.38). The 700 °C sol-gel HA shows a near stoichiometric Ca/P ratio by LA-ICP-MS, 1.66, which closely corresponds to TEM-EDX data (1.65 ± 0.35), but is inconsistent with the much lower value from XRF, 1.47.

Overall the Ca/P ratio values measured in bulk by XRF and LA-ICP-MS and at the particle level by TEM-EDX, for the Sigma-Aldrich and 'in-house' prepared samples show inconsistency across the three techniques. The pH 11 hydrothermal HA and 500 °C sol-gel HA show the most agreeable Ca/P ratios as measured by all three methods (both < 5% difference). Greater variance is observed in the Sigma-Aldrich and the 700 °C sol-gel HA (both ~ < 10% difference). The aforementioned evaporation of phosphorous during sol-gel HA synthesis causing the presence of β-TCP, DCPA and CaO in the 700 °C sol-gel HA, as measured by XRD (Figure 4.7), may be a reason for this observation.

For comparison, a bone-meal standard reference material (NIST 1486, preparation method unreported) with a previously determined Ca/P ratio of 1.67 (as measured by using XRF by W.F. Koch *et al* of the NIST Inorganic Analytical Research Division [242]) was also analysed by the LA-ICP-MS facility and displayed a high Ca/P ratio, 1.86[**]. This may be explained by the well recognised inconsistencies with phosphorus detection using an argon-plasma [243-245]. It is reported that phosphorus detection is restricted due to its relatively high first ionisation potential (~10.5 eV) and interference may occur with ions of C, O, N and H [243-245]. Additionally, it is reported that phosphorus loss can occur due to

[**] full LA-ICP-MS compositional data for all powders in appendix, Table A11.

condensation on cool container walls of the instrument, an issue shown to be overcome by injection of hydrogen and hydrogen chloride into the argon plasma [243].

The full analytical procedure carried out by the LA-ICP-MS facility remains unreported, despite repeated request for the details. Although unconfirmed, phosphorus detection problems discussed above may be a potential cause of the phosphorus deficient Ca/P values observed by LA-ICP-MS for the Sigma-Aldrich HA and the bonemeal standard.

Table 4.2: Ca/P ratios for respective HA powders from bulk XRF and LA-ICP-MS analysis. Full data displayed in the appendix, Tables A10 (XRF) and A11 (LA-ICP-MS).

Sample	Sigma-Aldrich HA	pH 11 hydrothermal HA	500 °C sol-gel HA	700 °C sol-gel HA
Bulk Ca/P ratio (XRF)	1.50	1.68	1.83	1.47
Bulk Ca/P ratio (LA-ICP-MS)	1.64 ± 0.03	1.65 ± 0.02	1.84 ± 0.09	1.66 ± 0.02
Average particle Ca/P ratio (TEM-EDX)	1.45 ± 0.16	1.61 ± 0.17	1.72 ± 0.38	1.65 0.35

4.3. Particle analysis

Particle morphology for the samples 1-4 are shown by SEM and TEM images, Figures 4.12 - 4.21. Particle size information was obtained by manually measuring, from TEM images, the dimensions of 50 particles per sample using Gatan Digital Micrograph software, Figure 4.24.

Analysis by SEM shows that the as received Sigma-Aldrich HA consists of large (> 10 μm) spheroidal aggregates of fine particles (Figure 4.12). By TEM analysis, the Sigma-Aldrich HA consists of elongated primary particles ≤ 200 nm in length (Figure 4.20), with the greatest proportion in the 50-75 nm range; aspect ratios varied from 1.0 to 13.9, with an average of 3.6 (Figure 4.24a). Selected area electron diffraction (SAED) confirms crystalline, single phase HA (Figure 4.20c), consistent with XRD (Figure 4.4).

Analysis of the pH 11 hydrothermal HA by SEM shows well-defined rod-like particle morphologies with a relatively short length and a low amount of particle agglomeration in comparison to the other HA samples (Figures 4.14 and 4.15). From TEM analysis (Figure 4.21a and b) particles show lengths ≤ 300 nm and aspect ratios range from 1.8 to 7.8, with an average of 4.0 (Figure 4.24b). Selected area electron diffraction confirms crystalline, single phase HA (Figure 4.21c) as previously shown by XRD (Figure 4.5). Furthermore, the SAED pattern shown in Figure 4.21d, taken of a single pH 11 hydrothermal HA particle, suggests that HA particles here exist as single crystals.

HA powders prepared via the sol-gel method, at 500 °C (Figures 4.16, 4.17 and 4.22) and 700 °C (Figures 4.18, 4.19 and 4.23), possessed a more equiaxed morphology than the other powders (average aspects ratios < 2); particle lengths were mostly 25-100 nm with a maximum of ~250 nm.

By SEM (Figures 4.16 and 4.17), the sol-gel HA calcined at 500 °C shows large agglomeration of particles typically < 200 nm in length (average = 70 nm). Selected area electron diffraction in TEM (Figure 4.22c) is in agreement with previous XRD data (Figure 4.6c), confirming the presence of HA phase with an additional diffraction ring assigned to $CaCO_3$. Particle length measurements the 500 °C sol-gel HA by TEM show an average particle length of 70 nm, and the highest proportion of sub 50 nm particles of any powder (Figure 4.24c).

The sol-gel HA prepared at 700 °C shows large agglomeration by SEM (Figures 4.18 and 4.19). Analysis by TEM (Figure 4.23a and b) shows rounded particles, with selected area electron diffraction (Figure 4.23c) confirming the presence of multiple phases, HA, β-TCP, DCPA and CaO as previously observed by XRD (Figure 4.7). Increasing the calcination temperature from 500 °C to 700 °C shifted the size distribution to higher values; an average particle length of 108 nm was observed, with some particles reaching lengths of 225-250 nm (Figure 4.24d).

4.3.1. Scanning electron microscopy (SEM)

Sigma-Aldrich HA

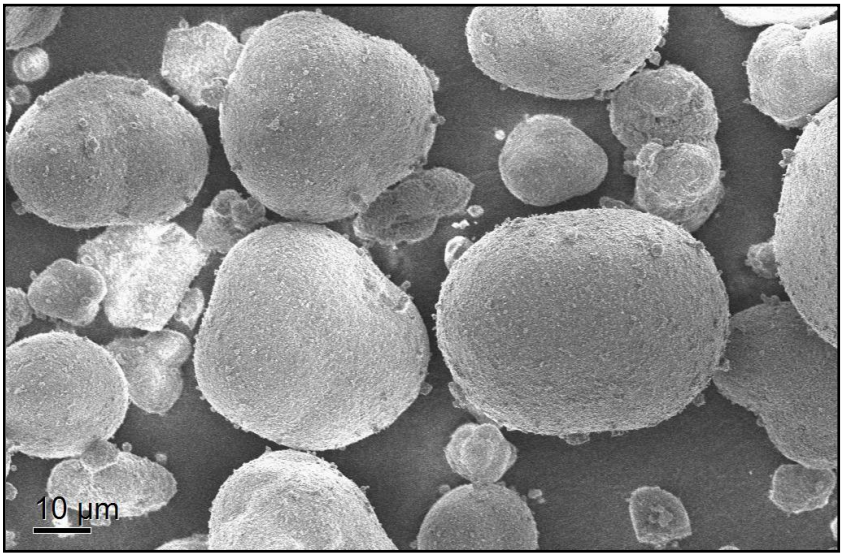

Figure 4.12: Low magnification SEM image showing spheroidal aggregates of the as received Sigma-Aldrich HA.

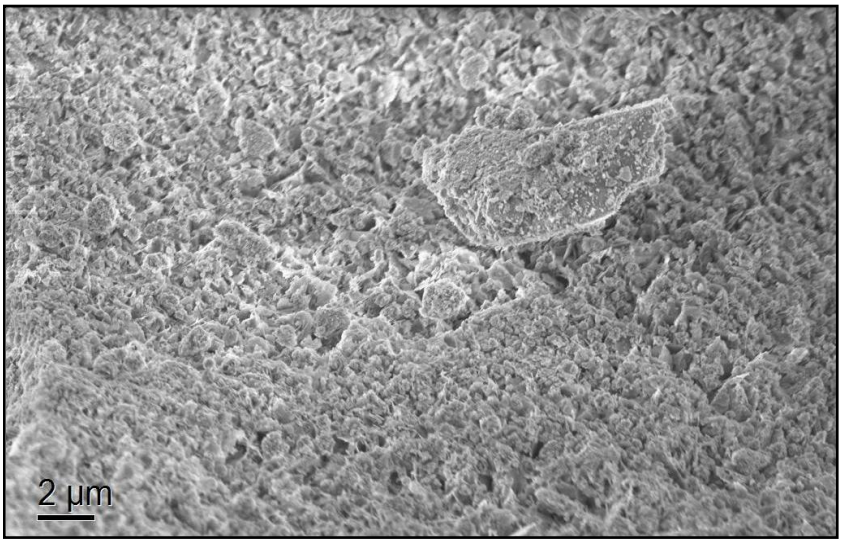

Figure 4.13: High magnification SEM image of the as received Sigma-Aldrich HA revealing a sub-micron primary particle size. Primary particle size range = 25 – 175 nm.

pH 11 hydrothermal HA

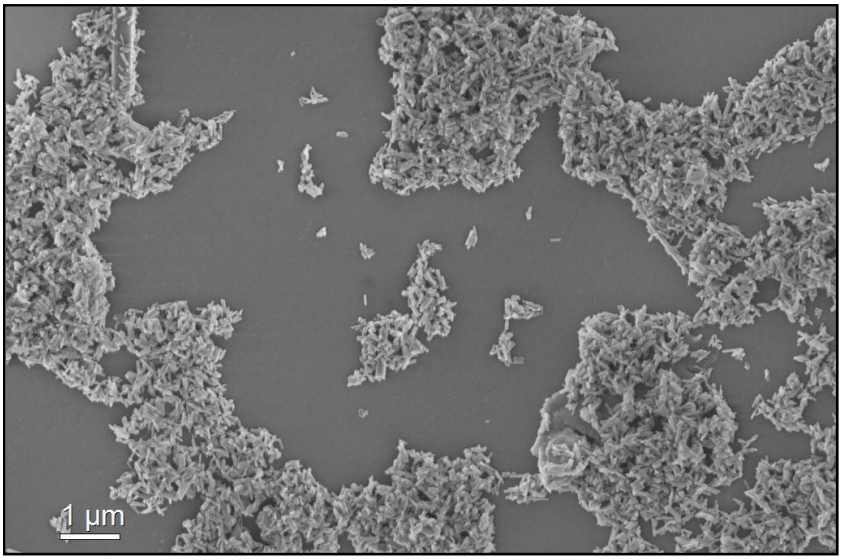

Figure 4.14: Low magnification SEM image of hydrothermal HA prepared at pH 11.

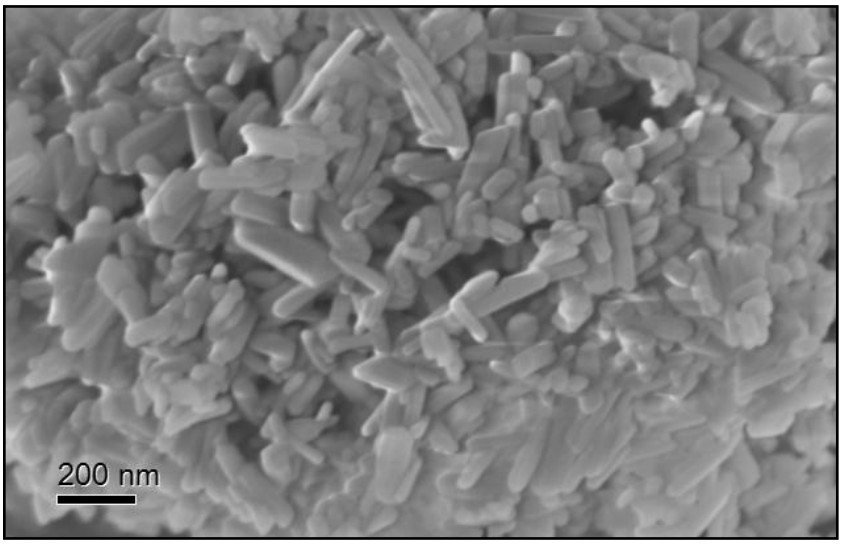

Figure 4.15: High magnification SEM image of hydrothermal HA prepared at pH 11. Primary particle size range = 25 – 300 nm.

Sol-gel synthesised HA

500 °C sol-gel HA

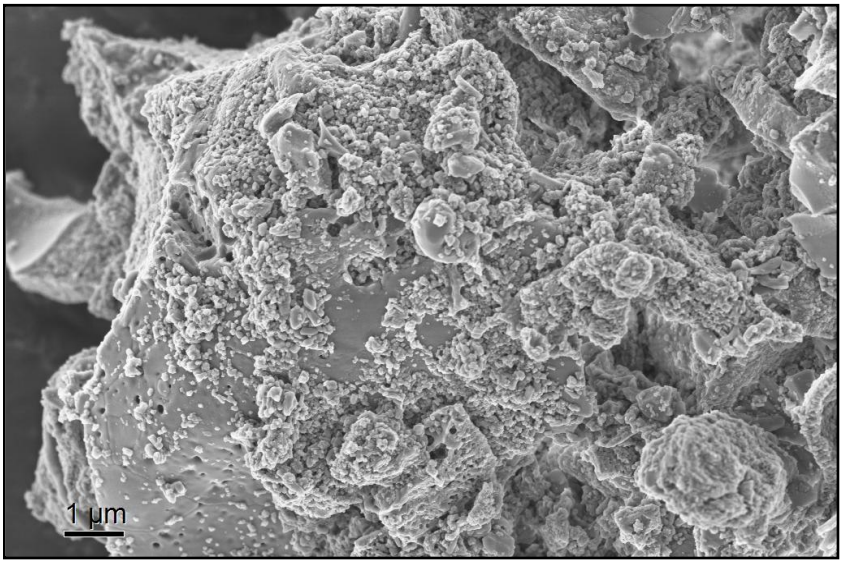

Figure 4.16: Low magnification SEM image of sol-gel HA calcined at 500 °C.

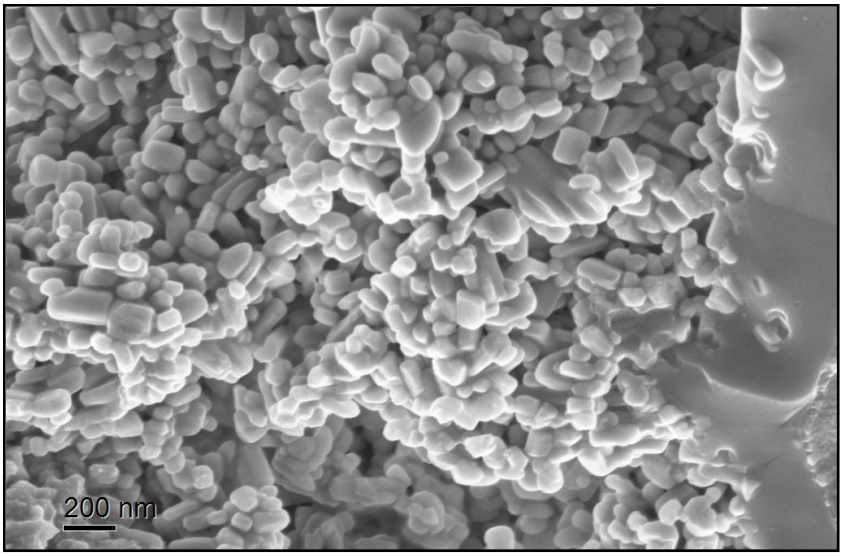

Figure 4.17: High magnification SEM image of sol-gel HA calcined at 500 °C. Primary particle size range = ~25 - 225 nm.

700 °C sol-gel HA

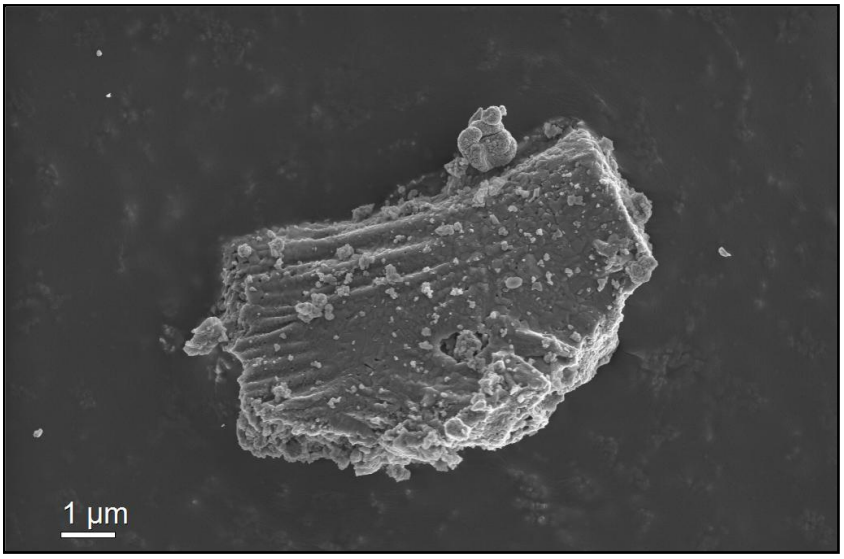

Figure 4.18: Low magnification SEM image of sol-gel HA calcined at 700 °C.

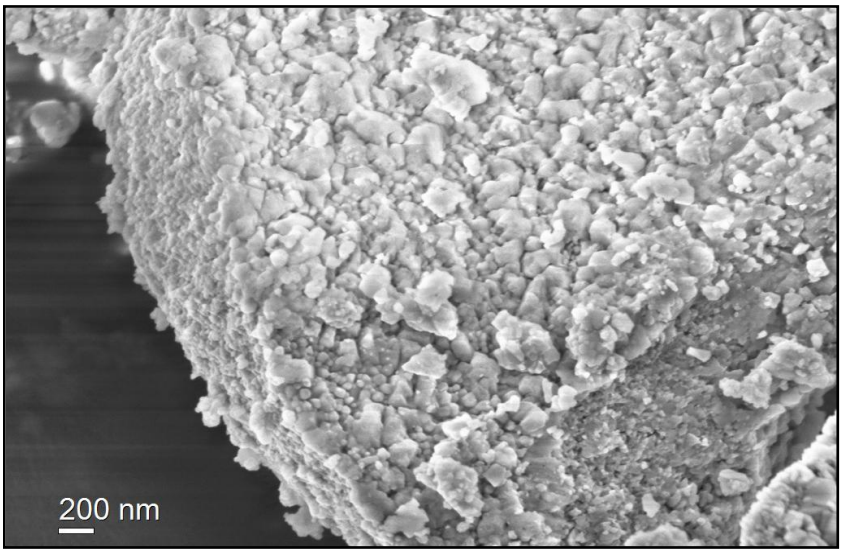

Figure 4.19: High magnification SEM image of sol-gel HA calcined at 700 °C. Primary particle size range = 25 – 250 nm.

4.3.2. Transmission electron microscopy (TEM)

Sigma-Aldrich HA

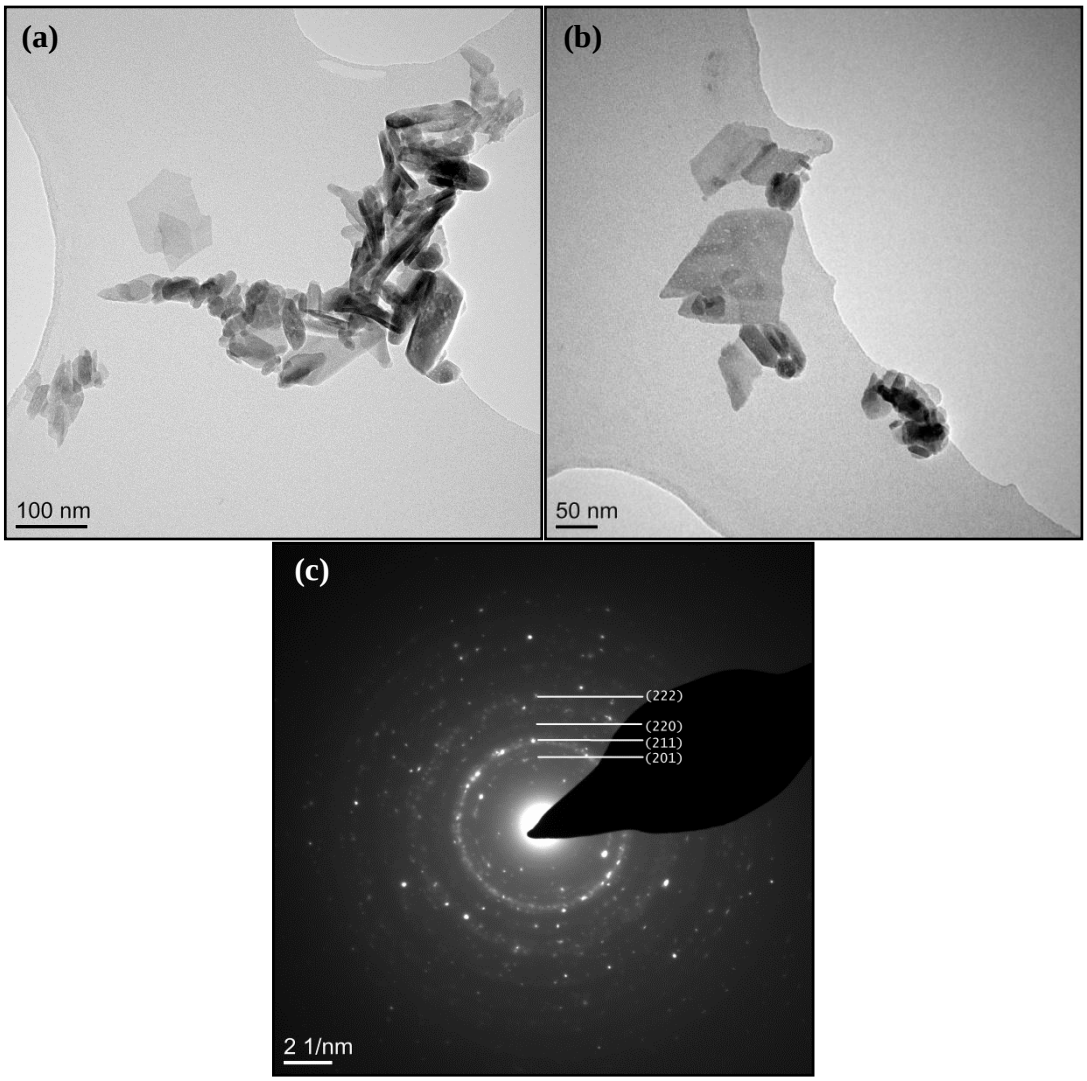

Figure 4.20: Bright field TEM images (a & b) of the Sigma-Aldrich HA, with (c) a selected area electron diffraction pattern from image (a), all rings correspond to a HA phase, ICDD ref: 01-074-0566 [37].

pH 11 hydrothermal HA

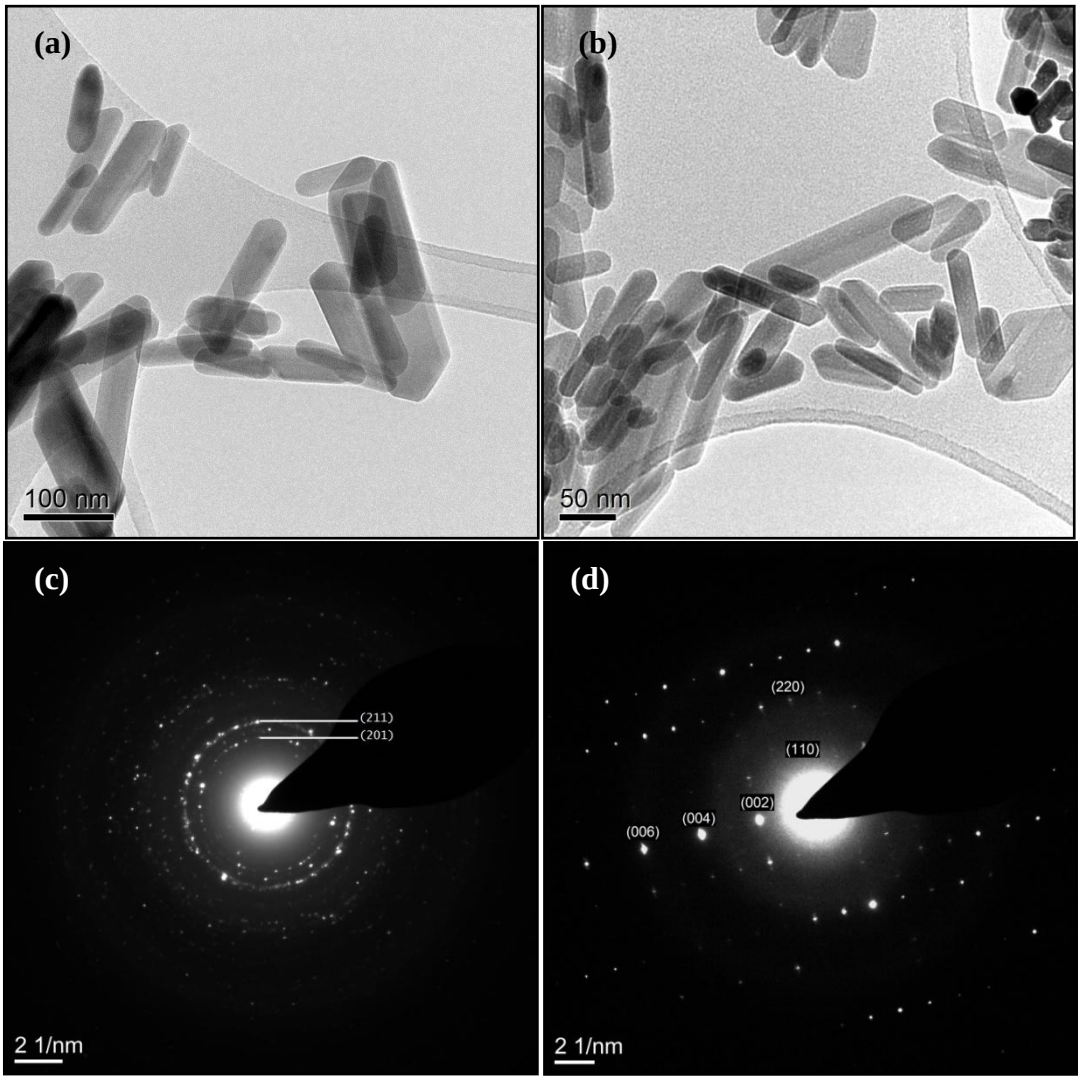

Figure 4.21: TEM images (a & b) of hydrothermal HA prepared at pH 11, with (c) a selected area electron diffraction pattern for (a) showing a dominant (211) ring, and (d) SAED pattern of single crystal HA particle. All rings and spots correspond to a HA phase ICDD ref: 01-074-0566 [37].

Sol-gel synthesised HA

500 °C sol-gel HA

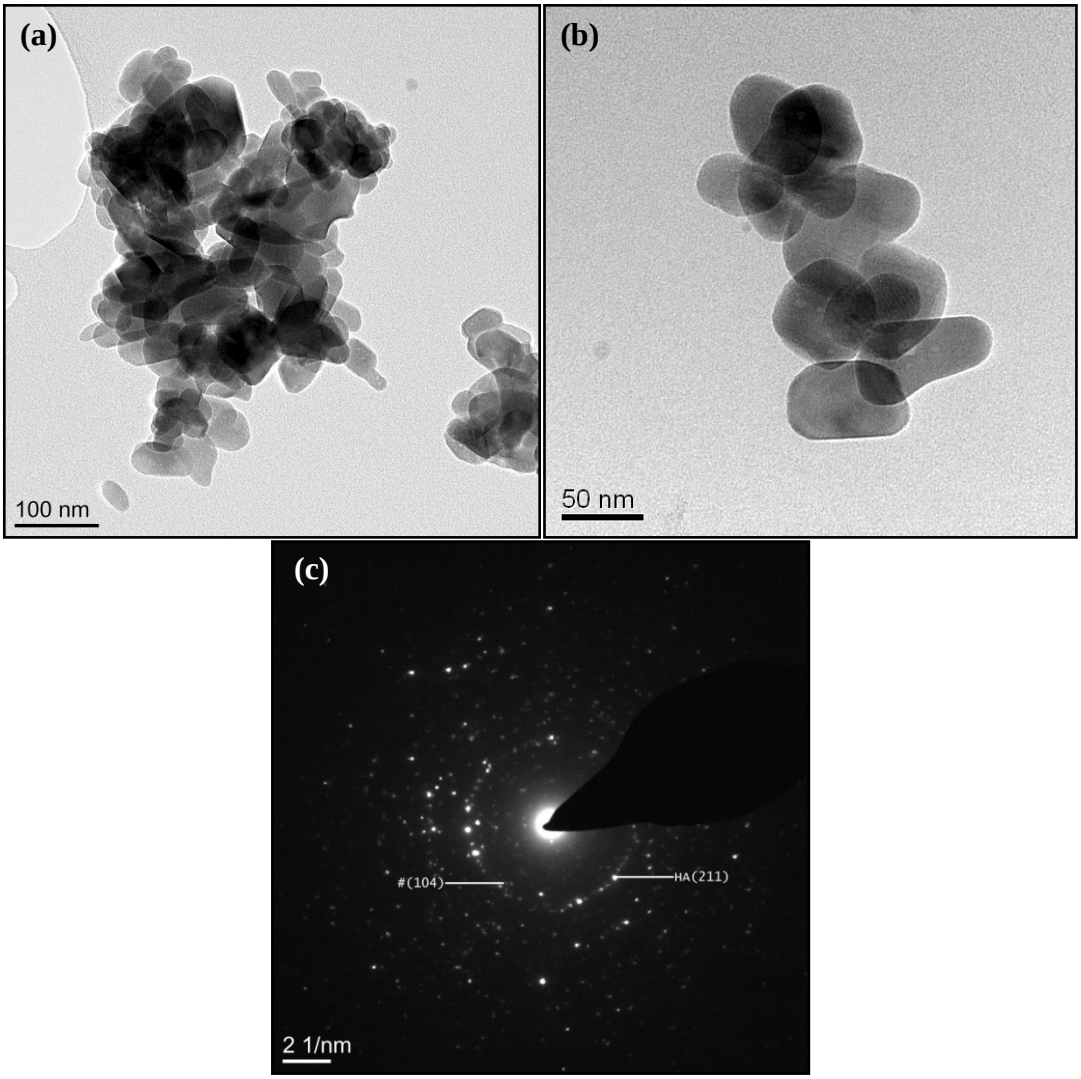

Figure 4.22: TEM images (a & b) of sol-gel HA calcined at 500 °C, with (c) a selected area electron diffraction pattern for area (a) showing faint ring (labelled '#') corresponding to $CaCO_3$, hkl = (104), ICDD ref: 00-005-0586 [221], other rings denote HA phase ICDD ref: 01-074-0566 [37] with ring labelled 'HA' indexed to hkl = (211).

700 °C sol-gel HA

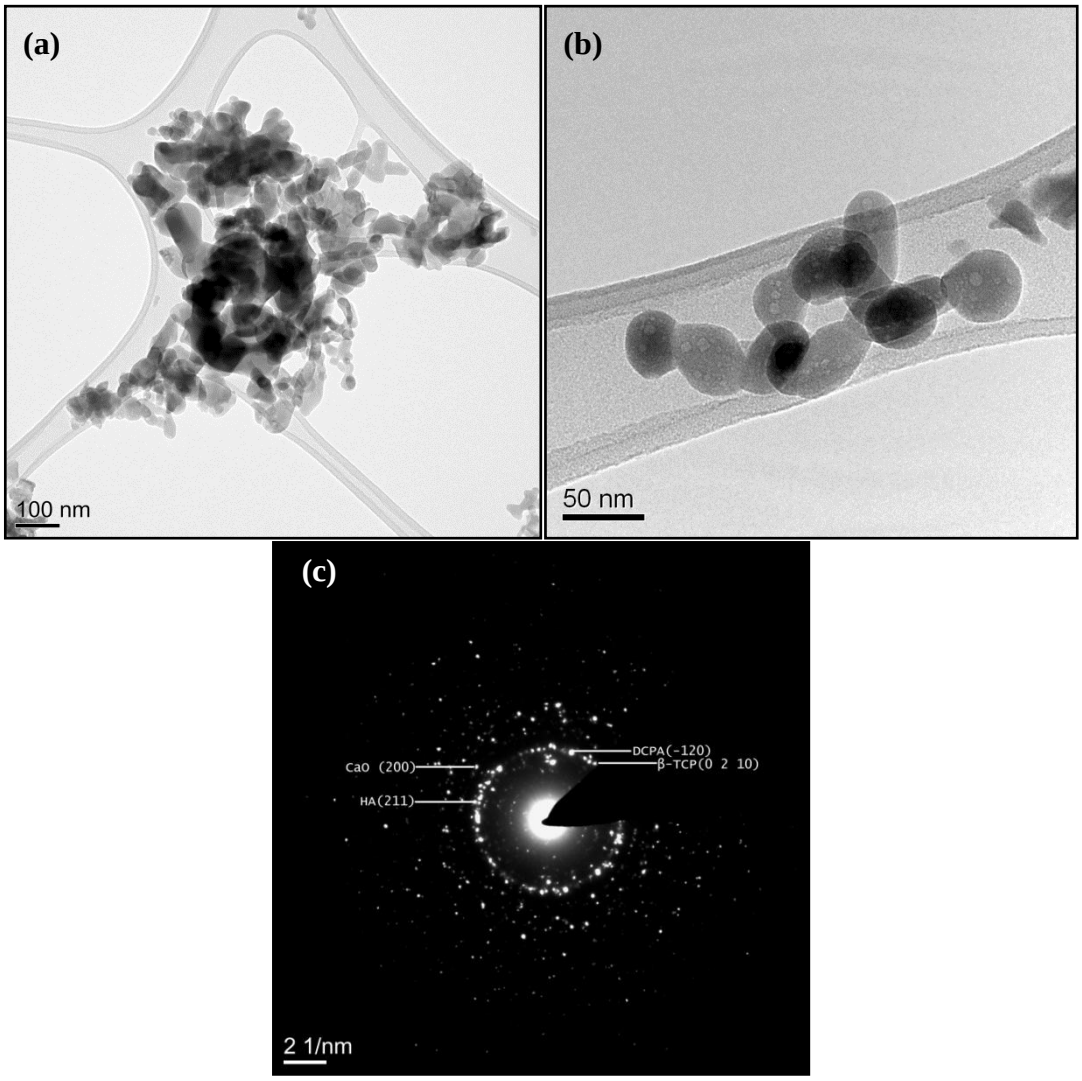

Figure 4.23: TEM images (a & b) of sol-gel HA calcined at 700 °C, with (c) multiphase selected area electron diffraction pattern for (a), with key HA (ICDD ref: 01-074-0566 [37]), β-TCP (ICDD ref: 04-008-8714 [232]), DCPA (ICDD ref: 01-070-0360 [225]) and CaO phases labelled (ICDD ref: 04-003-7161 [226]).

4.3.3. Particle length distributions from TEM

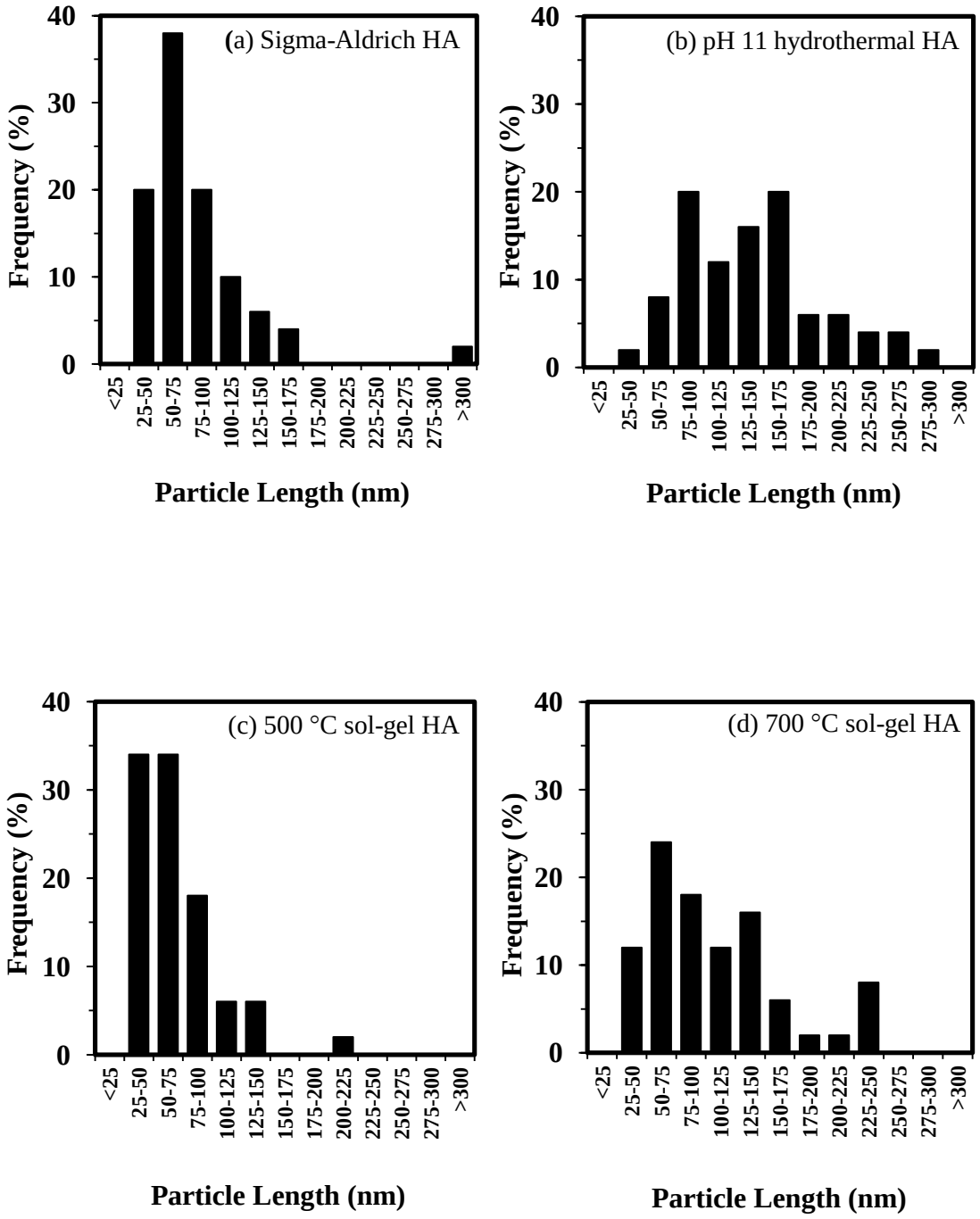

Figure 4.24: Distribution of particle lengths (50 particles per sample) measured from TEM images of (a) Sigma-Aldrich HA, (b) pH 11 hydrothermal HA, (c) 500 °C sol-gel HA and (d) 700 °C sol-gel HA.

4.3.3.1. HA samples prepared for cytotoxicity analysis

The two HA samples that have been prepared hydrothermally at pH 9 and pH 11 for cytotoxicity analysis (Section 4.5.1), have been analysed by TEM, with images and selected area diffraction patterns shown in Figure 4.25a-d. Particle size distribution plots for 50 particles of each sample are displayed in Figure 4.26a-b. TEM images of both the pH 9 and pH 11 hydrothermal HA's (Figure 4.25a and c) show that both samples displayed well-defined, short (< 300 nm) rod-shaped particles, with a single-phase, crystalline HA confirmed for both samples by SAED (Figure 4.25b and d).

The HA prepared at pH 9 shows average particle lengths ~200 nm (Figure 4.26a) with the greatest proportion in the 175 – 200 nm range; aspect ratios range from 1.1 to 12.4. A small proportion of particles show lengths > 300 nm. The HA prepared at pH 11 shows average particle lengths ~130 nm (Figure 4.26b) with the greatest proportion in the 75 – 100 nm range; aspect ratios range from 1.6 to 12.0. No particles show lengths > 300 nm.

Particle size data here conforms to the work by Meyer and Nancollas [182], whereby an increase in basicity contributes to a shorter particle length. Previous studies have suggested that a high pH reduces particle growth due to the increased number of OH^- ions in the solution creating surface defects, and lowering surface energy in the preferred plane of growth [181, 246]. An increase in pH also has the benefit of preventing the formation of unwanted calcium phosphate phases, such as dicalcium phosphate anhydrate, DCPA ($CaHPO_4$) and dicalcium phosphate dihydrate, DCPD ($CaHPO_4 \cdot (H_2O)_2$); these are known to be unstable at pH values greater than 6 - 7 and subsequently convert to the more stable HA phase [247].

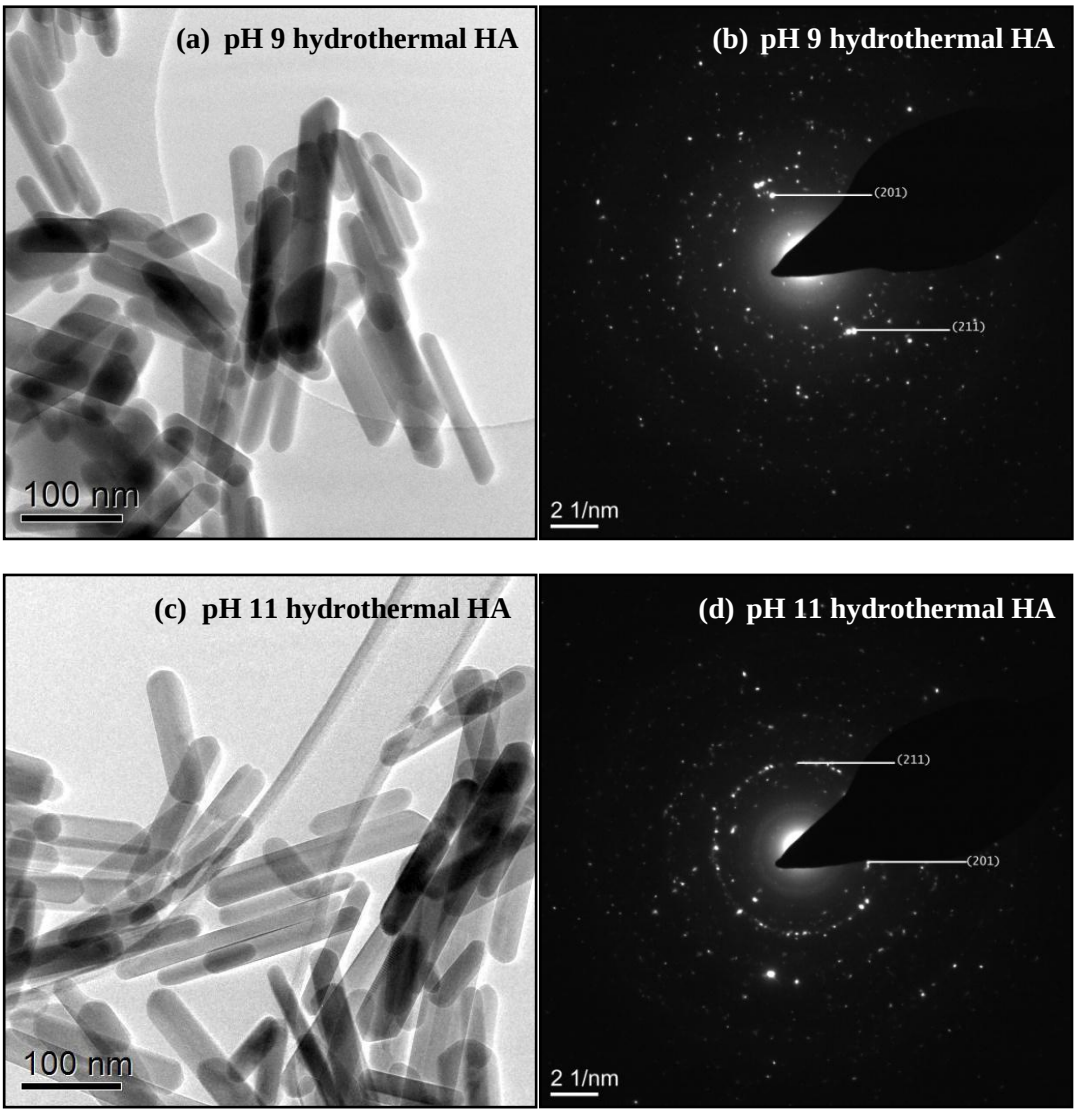

Figure 4.25: TEM images and corresponding selected area electron diffraction pattern for hydrothermal HA prepared at pH 9 (a & b) and pH 11 (c & d) for cytotoxicity analysis.

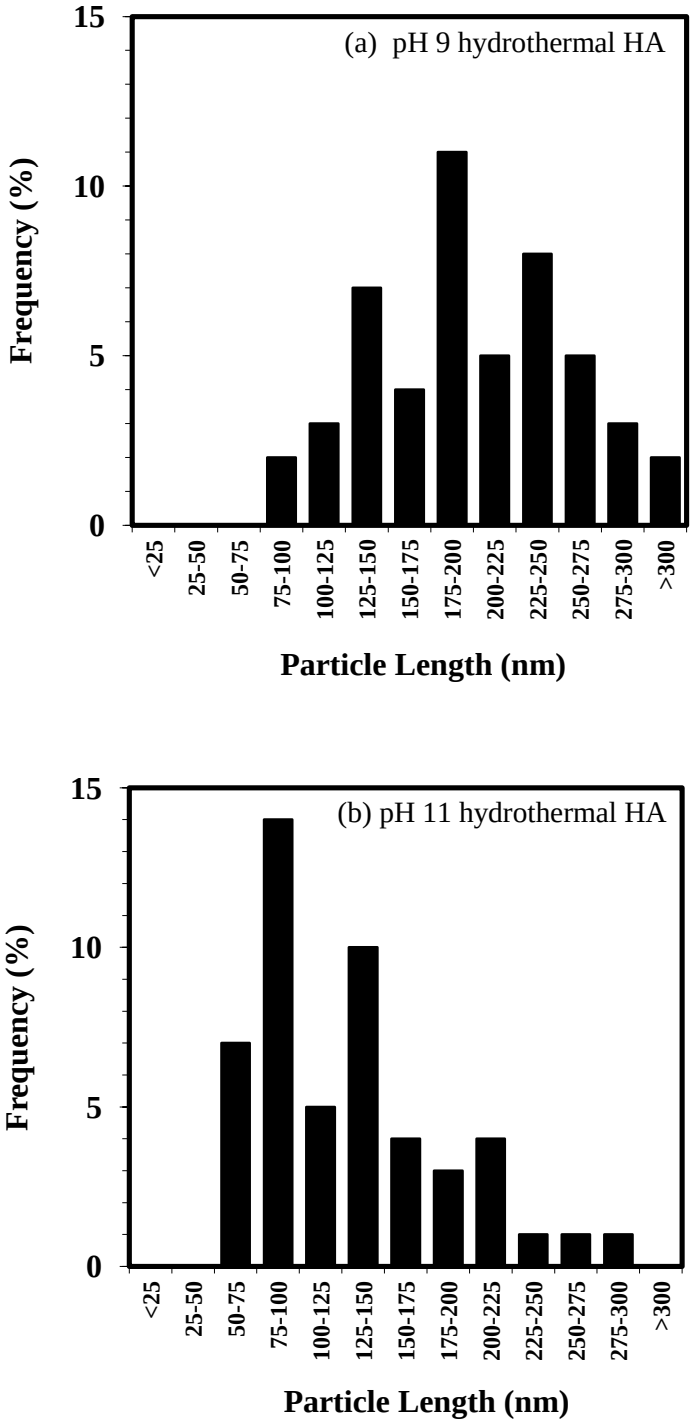

Figure 4.26: Distribution of particle lengths (50 particles) measured from TEM images of hydrothermal HA prepared at pH 9 (a) and pH 11 (b) for cytotoxicity analysis.

4.3.4. Energy dispersive X-ray spectroscopy (TEM-EDX)

4.3.4.1. Determination of critical electron fluence threshold

To determine a threshold-fluence, whereby accurate and representative compositional data can be obtained by EDX without significant damage to the samples, two experiments were carried out using the Sigma-Aldrich HA powder, expanding on the method in [94]. First, a series of spot EDX measurements of different, small, particle clusters were made across the fluence range ~10^5-10^9 e nm^{-2} (by changing fluence and fluence rate) and the spectra quantified, using ISIS processing software, to obtain Ca/P ratios (Figure 4.27*a* and [27]). Secondly, spot EDX measurements were taken across a single cluster of particles, at a fixed irradiation area, to really isolate the effects of increasing fluence at a fixed fluence rate (10^6 e nm^{-2}) on the Ca/P ratio (Figure 4.27b). Figure 4.27a shows that the Ca/P ratio remains stable up to ~10^7 e nm^{-2}; beyond this point the Ca/P ratio rises and specimen alteration was observed. Prolonged irradiation of a single area of particles (Figure 4.27b) demonstrates a progressive rise in the Ca/P ratio (1.45 to 1.65) up to a final, cumulative fluence of 10^8 e nm^{-2}.

Supplementary TEM images (with Ca/P ratios measured by EDX) that highlight the physical effect of rising electron fluence on a small particle cluster area of the Sigma-Aldrich HA are shown in Figure 4.28a-c††. These images show that the HA particles undergo no physical change with fluence levels at ~10^5 and ~10^7 e nm^{-2} (Figure 4.28a and b respectively), with the average Ca/P ratio (from EDX) rising by 0.03 from 1.46 to 1.49. However at a fluence level of ~10^9 e nm^{-2} (Figure 4.28c) significant radiolytic particle damage was observed, which is most notable at the

†† Note: these images were acquired as a separate experiment due to the changes in magnification and beam brightness required to allow for imaging. This subsequently alters the fluence rate and therefore values are given as rough estimates. The TEM-EDX data here was measured according to the previously outlined conditions, and was acquired prior to each image being taken.

particle edges. Large amounts of porosity were visible and the average Ca/P ratio shows a large increase to 2.81.

These results demonstrate the need for controlled fluence particle characterisation of hydroxyapatite in the TEM. Subsequent TEM-EDX analysis of the Sigma-Aldrich HA and all ‘in-house’ prepared HA’s uses a maximum threshold fluence of 10^7 e nm^{-2} to gather reliable Ca/P ratios for 100 small particle clusters of each HA powder.

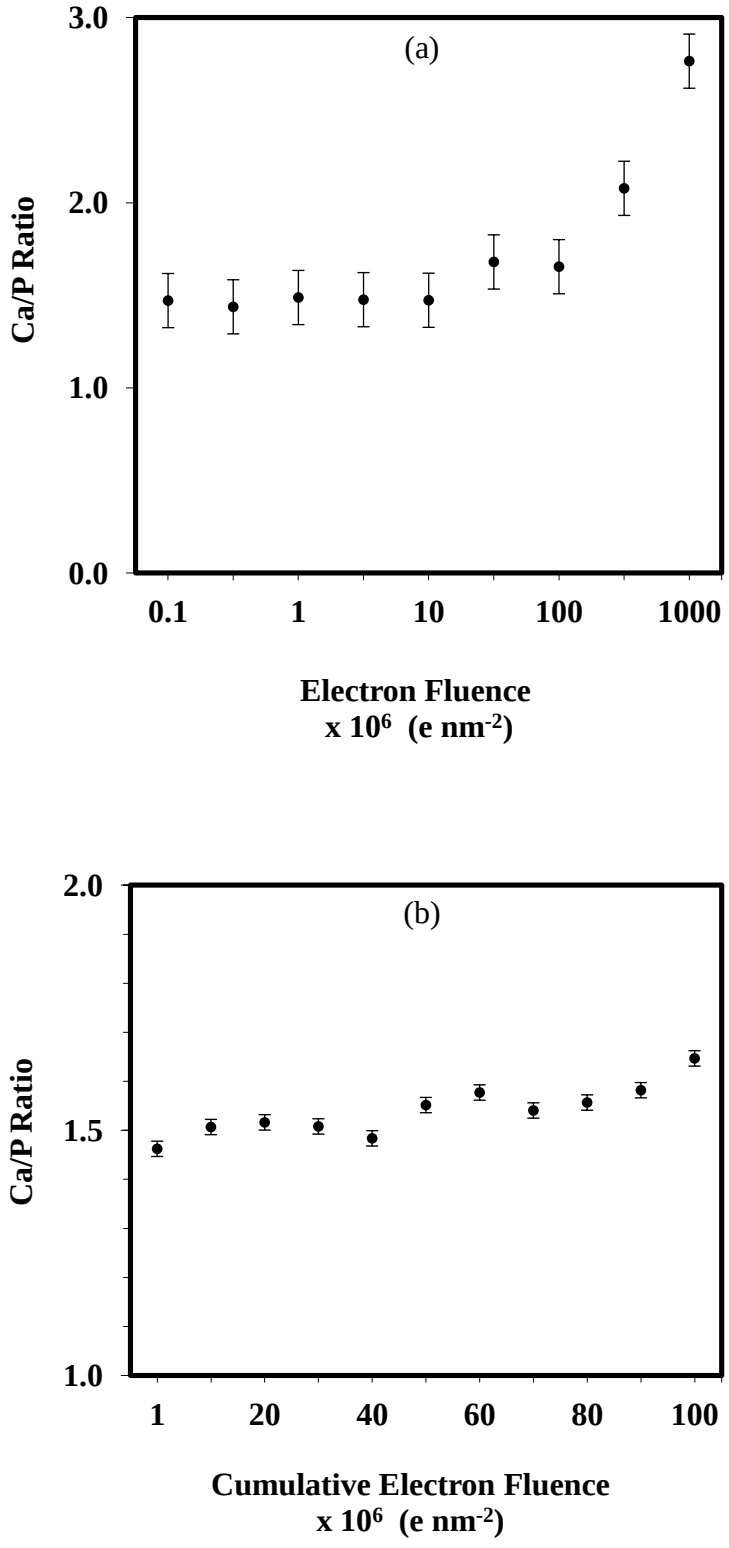

Figure 4.27: (a) TEM-EDX Ca/P ratio of the Sigma-Aldrich HA as a function of electron fluence obtained by varying fluence at fluence rate (b) TEM-EDX Ca/P ratio data, over a fixed particle area of the Sigma-Aldrich HA, as a function of cumulative fluence obtained at a fixed fluence rate.

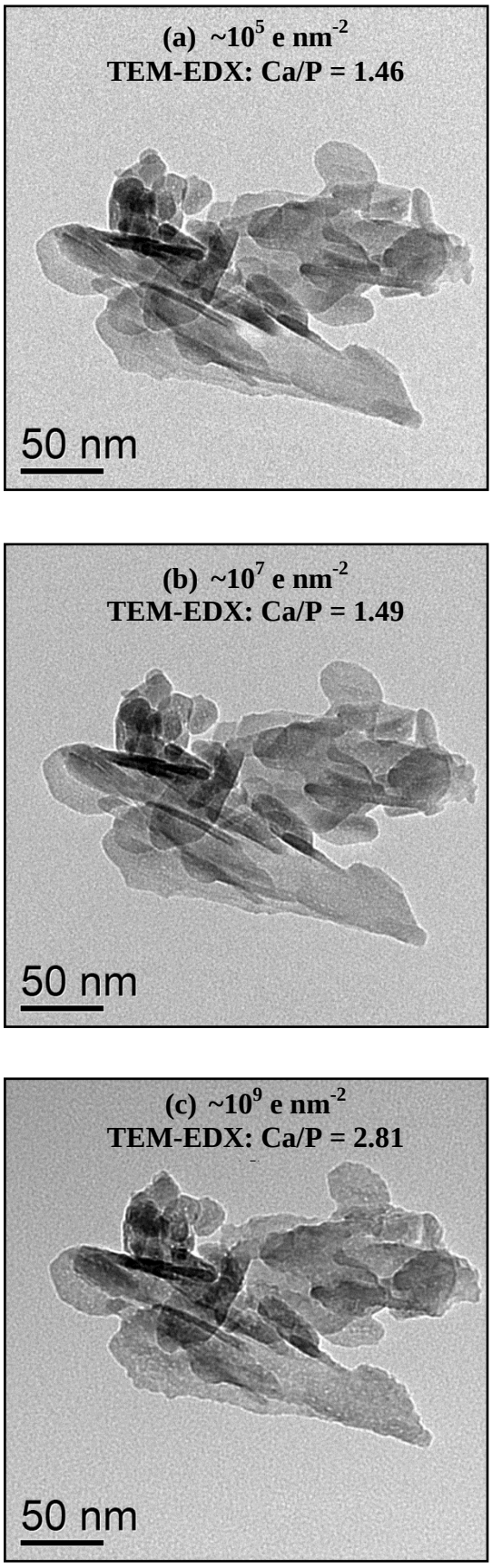

Figure 4.28: TEM images displaying the effect of rising electron fluence on the Sigma-Aldrich hydroxyapatite at approximate fluence levels of (a) ~10^5 e nm^{-2}, (b) ~10^7 e nm^{-2} and (c) ~10^9 e nm^{-2}.

4.3.4.2. Particle TEM-EDX analysis of HA samples

The Ca/P ratios calculated from EDX peak ratios for 100 small particle clusters of samples 1-4, have been acquired by working below the threshold fluence for irradiation damage (10^7 e nm^{-2}), with results shown in Figure 4.29a-d and Table 4.2. These values have previously been compared to bulk Ca/P ratio data collected by XRF and LA-ICP-MS in Section 4.2.4.

The Sigma Aldrich powder displayed the least variability in particle Ca/P ratio (Figure 4.29a), but the average Ca/P ratio was only 1.45 (standard deviation, S.D. = 0.16), significantly below the stoichiometric target of 1.67, however this is in agreement with previous reports [94].

The pH 11 hydrothermal powder (Figure 4.29b) showed similar consistency in inter-particle Ca/P ratios to the Sigma-Aldrich powder, but the average Ca/P ratio, 1.61 (S.D. = 0.17), was in closer agreement with the stoichiometric target.

The sol-gel powders calcined at 500 and 700 °C displayed a greater variability between particle Ca/P ratios (Figure 4.29c and d), with average values of 1.72 for the 500 °C HA and 1.65 for 700 °C HA, with larger standard deviations of 0.38 and 0.35 respectively. This was mainly due to a few particles with extreme Ca/P ratios, 2.50-4.50 (Figure 4.29c and d); which may arise due to an overlap of more calcium rich phases; $CaCO_3$ in the 500 °C sample and CaO in the 700 °C sample. As previously discussed from FTIR data (Figure 4.11), carbonate ions may substitute for PO_4^{3-} ions (site-B) in the HA structure [238, 240]. This may also explain the higher average Ca/P ratio's observed here as both sol-gel powders showed peaks due to carbonate absorption in FTIR; these peaks were significantly more intense in the 500 °C sol-gel HA, which corresponds with a higher Ca/P ratio obtained by TEM-EDX.

This high level of variability within a small fraction of particles in the sol-gel samples contrasts to the hydrothermal powder, as none of the 100 particle clusters in the pH 11 hydrothermal sample had a Ca/P ratio > 2.10.

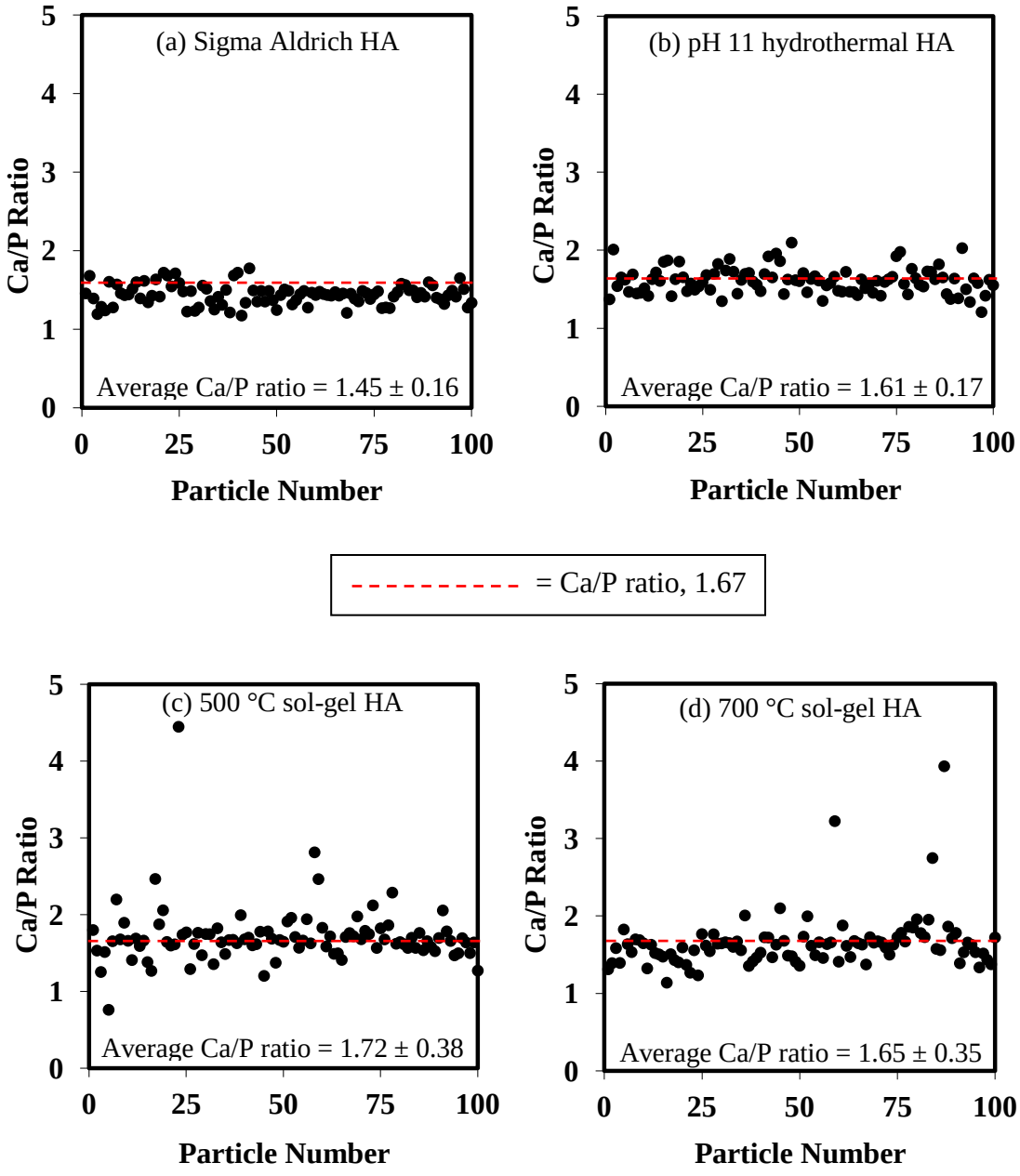

Figure 4.29: TEM-EDX of 100 small particle clusters (with noted average Ca/P ratios) each taken at the threshold fluence of 10^7 nm^{-2} for (a) Sigma-Aldrich HA, (b) hydrothermal HA prepared at pH 11, (c) sol-gel HA calcined at 500 °C, (d) sol-gel HA calcined at 700 °C. The stoichiometric target of Ca/P of 1.67 is marked (red dotted line) in each figure.

4.3.4.3. Particle EDX of HA samples for prepared cytotoxicity analysis

TEM-EDX data showing the distribution of Ca/P ratios for 100 small particle clusters of the hydrothermal HA samples prepared for cytotoxicity analysis at pH 9 and pH 11, is shown in Figure 4.30a-b. Data here displays good inter-particle consistency for both samples; consistent with the previous hydrothermal preparation (Figure 4.29b) the average Ca/P ratio values were slightly lower than the stoichiometric target of 1.67. The hydrothermal HA prepared at pH 9 had an average Ca/P ratio of 1.55 (S.D = 0.11) with no particle clusters displaying a Ca/P ratio > 2. The average Ca/P value for the hydrothermal HA prepared at pH 11 was 1.60 (S.D = 0.11), and in good agreement with the previously prepared hydrothermal HA sample at pH 11, 1.61 (S.D = 0.17; Figure 4.29b), only two particle clusters in this sample displayed a Ca/P ratio > 2.

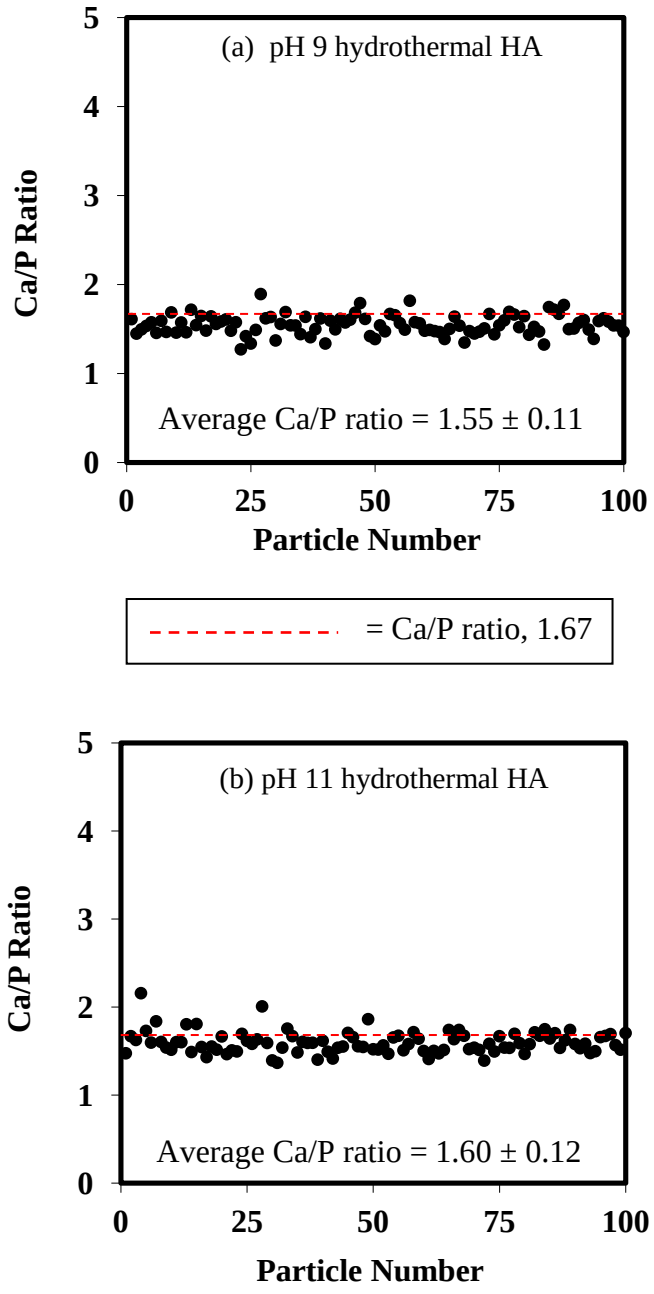

Figure 4.30: EDX Ca/P ratios for of 100 small particle clusters from hydrothermal HA samples prepared at (a) pH 9 and (b) pH 11 hydrothermal HA, with noted average Ca/P ratio, taken at the threshold fluence 10^7 nm^{-2}. The stoichiometric target of Ca/P of 1.67 is marked (red dotted line) in each figure.

Overall, the results show that elemental analysis at the particle level is a valuable tool in assessing hydroxyapatite nanopowders. The TEM-EDX technique of measuring the Ca/P ratio of individual particles at or below a threshold electron fluence confirms that the hydrothermal synthesis technique produces a consistent, single phase powder with an average Ca/P ratio in close agreement with the value for stoichiometric hydroxyapatite, 1.67. By contrast, the sol-gel synthesis route produced powders with greater variability in Ca/P ratio, each batch containing a small percentage of Ca-rich particles. This may be linked to volatility of the phosphite precursor reagent during processing (Section 4.1). A Ca-deficient composition was identified in the Sigma-Aldrich powder, with Ca/P = ~1.50, which is in agreement with previously reported data [94].

This work demonstrates the need for careful consideration of the electron fluence in TEM-EDX analysis of HA. Levels of compositional variability revealed by particle to particle quantification of the Ca/P ratio, at controlled electron fluence ($\leq 10^7$ e nm^{-2}), are essential to collect reliable analytical data and avoiding radiolytic damage. This measurement is a valuable addition to the more typical characterisation methods employed for HA analysis. This method of analysis will be particularly useful for assessing the homogeneity of synthetic HAs that have been chemically modified to more closely match the composition of natural HA to gain further improvements in biocompatibility and osteointergration.

4.3.5. Dynamic light scattering (DLS) analysis of hydrothermal HA samples prepared for cytotoxicity analysis

Particle size distribution curves, as measured by dynamic light scattering (DLS), of agglomerates of the hydrothermal HA samples prepared at pH 9 and pH 11, to be used for cytotoxicity analysis, are shown in Figure 4.31. Z-average data (cumulant average particle diameter) for both samples is shown in Table 4.3. Two concentrations of each powder were prepared, firstly as 0.1% w/v of HA in distilled water and then this was mixed further as 10 and 50% v/v dispersions in cell culture medium (Dulbecco's modified Eagle's medium, DMEM).

The DLS data here shows a wide size distribution of particle agglomerates across both samples. At 10% v/v concentration of HA in DMEM, the pH 11 hydrothermal HA exhibits the lowest particle agglomeration range ~100 – 500 nm (z-average = 500 nm). At a 50% v/v concentration of HA in DMEM, this range greatly increases to ~400 – 4000 nm (z-average = 2746 nm), providing the greatest agglomeration of all samples.

At 10% v/v concentration of HA in DMEM, the pH 9 hydrothermal HA exhibits agglomerates in the size range ~300 – 1100 nm (z-average = 893 nm). At a 50% v/v concentration of HA in DMEM, this size range increases to ~700 – 2000 nm (z-average = 1191 nm).

The hydrothermal HA prepared at pH 9 shows a larger z-average value (893 nm) than the HA prepared at pH 11 (500 nm) at 10% v/v concentration of HA in DMEM. Larger agglomerates would be expected due to the larger overall crystallite size of the pH 9 HA (see TEM Figure 4.26) which would provide a greater surface area for charge build up.

At 50% v/v concentration of HA in DMEM, the hydrothermal HA prepared at pH 11 shows a much larger z-average (2746 nm) in comparison to the hydrothermal HA prepared at pH 9 at the same concentration (1191 nm): the hydrothermal HA prepared at pH 11 (at 50% v/v concentration of HA in DMEM) displays both a standalone single scattering peak and also a very broad two-peaked curve, which is indicative of significant variability in agglomeration and overall a poor dispersion in solution [248]. In the case where there are multiple scattering peaks for a sample, it is considered more representative to report the position of the peak maxima, rather than the z-average [211, 249], which for the hydrothermal HA prepared at pH 11 (at 50% v/v concentration of HA in DMEM) this is observed at 1718 nm. In comparison, the hydrothermal HA prepared at pH 9 at this concentration shows only a single scattering peak curve (maxima at 1106 nm), which suggests the sample is more evenly agglomerated, however broadness here does indicate the presence of some fragments [248].

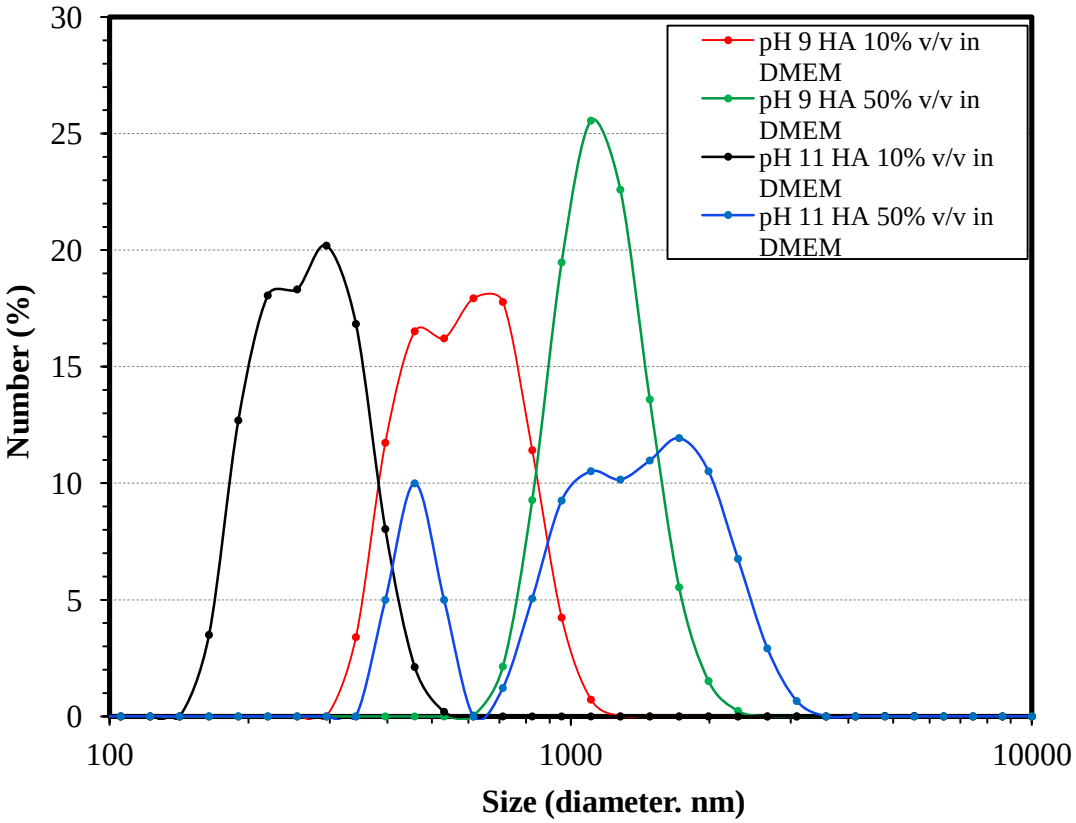

Figure 4.31: Size distribution (by number) of 10 and 50% v/v dispersions of pH 9 and pH 11 hydrothermal HA in Dulbecco's modified Eagle's medium (DMEM). Significant agglomeration of the 200 nm primary particles is noted.

Table 4.3: Z-average (particle diameter cumulant average) as measured by DLS for 10 and 50% v/v dispersions of pH 9 and pH 11 hydrothermal HA in Dulbecco's modified Eagle's medium (DMEM)

Sample	z-average (d.nm)
pH 9 HA 10% v/v in DMEM	893
pH 9 HA 50% v/v in DMEM	1191
pH 11 HA 10% v/v in DMEM	500
pH 11 HA 50% v/v in DMEM	2746

4.4. Summary

This work has presented two solution-based techniques for the preparation of nano-particulate HA: hydrothermal and sol-gel synthesis routes. The physical and chemical properties of the powders have been compared to a commercial HA powder (Sigma-Aldrich) using a range of bulk (XRD, XRF, FTIR and LA-ICP-MS) and particle (SEM and TEM-EDX) level analysis techniques [250, 251].

Hydrothermal synthesis produced single phase HA of rod-like nano-particles, the growth and morphological variation of which is restricted with rising basicity, by the increased addition of ammonium hydroxide (Figures 4.14, 4.15, 4.21, 4.25, 4.26 and 4.31). The sol-gel synthesis method produced non phase-pure samples of HA nano-particles, which were a mixture of equiaxed and rod-like particles (Figures 4.16 - 4.19, 4.22 and 4.23). Bulk XRD and FTIR analysis highlighted the presence of $CaCO_3$ in the sol-gel HA prepared at 500 °C (Figures 4.6 and 4.11). At 700 °C, XRD showed a HA sample containing notable amounts of alternate calcium phosphate based phases; β-tricalcium phosphate and dicalcium phosphate anhydrate, as well as traces of calcium oxide (Figure 4.7). Bulk analysis of the Ca/P ratio by XRF and LA-ICP-MS confirmed deviations away from the stoichiometric target, 1.67 for the non-pure HA samples (Table 4.2).

A new low-fluence TEM-EDX technique has been demonstrated, which is able to highlight particle to particle compositional variability (Figure 4.27). Hydrothermally produced HA had a near-stoichiometric Ca/P content; TEM-EDX revealed an average Ca/P ratio of 1.61 (S.D = 0.17), with no detection of Ca-rich particles (Figure 4.29b and Table 4.2). The sol-gel method produced particles for which TEM-EDX, at the particle level, indicated average Ca/P ratios in close

agreement with the stoichiometric target, 1.67 (Figure 4.29c and d, and Table 4.2). However a small, but significant, fraction of particles with much higher Ca/P ratios were detected. The sol-gel powders displayed average Ca/P ratios of 1.72 for 500 °C (S.D = 0.38) and 1.65 for 700 °C (S.D = 0.35). The Sigma-Aldrich powder displayed a similar level of compositional consistency to the hydrothermal 'in-house' sample, but the powder was deficient in calcium with a Ca/P ratio of only 1.45 (S.D = 0.16), Figure 4.29a and Table 4.2.

Overall, the work demonstrates the importance of applying a combination of bulk and particle-level analytical techniques (XRD, XRF, FTIR, LA-ICP-MS, SEM and TEM-EDX) to adequately characterise nano-hydroxyapatite powders. Individual characterisation techniques have identified secondary phases in the sol-gel powders that are likely to have important bearings on the performance of the powders in applications such as implant coatings [252]. Literature shows that β-TCP can demonstrate good biocompatibility properties and its less stable nature, in comparison to HA, causes faster biodegradation which can promote the growth of new bone when utilised as a graft material, however there are still questions as to whether β-TCP possesses superior bone formation properties than HA [253-256]. Similarly, dicalcium phosphate has shown promise as a cell culture scaffold for bone regeneration [257, 258] and has also been used as an implant coating material that later is converted to HA [247]. Calcium oxide is undesired in HA coatings due to its high reactivity in aqueous environments [82, 259].

Hydroxyapatite is one of the most widely used synthetic calcium phosphate ceramics for bio-applications due to its greater compositional similarities with bone and its higher stability in aqueous media in comparison to alternate calcium phosphates [11]. The individual characterisation techniques utilised here highlight

the hydrothermal synthesis method as the preferred technique for the production of a single phase and near-stoichiometric HA nanopowder.

Hydroxyapatite is primarily utilised in bulk, non-load bearing applications, as there remains concerns over the exposure of nanoparticle HA with regards to particle size and shape. Consequently, careful consideration of nanoparticle toxicity is required, and this has been explored here (see the appendix - Section 4.5).

Engineering improvements of nanoparticulate HA with particle substitutions can aim to better match the composition of naturally occurring bone, which can often contain ions of, Na^{+}, Mg^{2+}, K^{+}, Cl^{-}, F^{-} and CO_3^{2-} [260]. Ion substitution using, amongst others, Na^{+}, Mg^{2+}, Sr^{2+}, F^{-}, Ag^{-}, Cu^{2+} and Zn^{2+} in synthetic HA has demonstrated various effects with improvements in thermal stability, solubility, textural properties, surface reactivity, osseointegration, bone formation and reduction in bacterial contamination [11, 27, 38, 261-265]. Silicon substitution in HA has also shown increased chemical stability and bioactivity [266-268]. A collaborative study with researchers Mr Adam Qaisar and Miss Rachel Wallace investigated the sol-gel synthesis of nanoparticulate HA modified with either Mg, Sr or Ti; TEM-EDX analysis of the powders showed varying particle sizes with also variability shown in the level of incorporation of each dopant ion into the HA particles [269].

4.5. Appendix

4.5.1. Hydroxyapatite toxicology

Two HA powders, synthesised via the hydrothermal technique at pH 9 and pH 11, have been analysed for potential cytotoxicity to in-vitro cell lines by an undergraduate research group led by Dr Lars Jeuken at the Leeds Faculty of Biological Sciences.

4.5.2. Toxicity assays

Despite sharing a similar chemical composition to that of bone synthetic HA, in nanoparticulate form, has demonstrated damaging effects to muscle cells [270], and pro-inflammatory effects in various pathological conditions including vascular calcification [271] and therefore should not be considered as non-toxic [103]. Increasing uses of HA in biomedical applications, such as for drug delivery [25, 272] as orthopaedic implant coatings [3, 23] and in toothpastes [20, 21, 273] are likely to increase human exposure to nanoparticulate HA and therefore it is essential that the toxic effects are fully understood.

The MTT assay (method outlined in Section 3.4) has been performed to assess the viability of the Caco-2 cell line (intestine cell line to measure response by ingestion), A549 cell line (lung cell line to measure response by inhalation) and SH-SY5Y cell line (brain cell line to measure response of nanoparticles in the blood that may pass the blood-brain barrier), upon exposure to two samples of HA prepared by the hydrothermal method at starting pH 9 and pH 11 respectively. Results are displayed in Figures 4.32 - 4.36.

The Caco-2 cell line shows little affect with exposure to up to 1000 μg ml^{-1} of the hydrothermal HA prepared at pH 11, however a decrease in cell viability is observed with increasing dose of the hydrothermal HA prepared at pH 9 (Figure 4.32). The A549 cell line shows little drop in cell viability with an increasing dose of both pH 9 and pH 11 HA samples (Figures 4.33 and 4.34). The SH-SY5Y cell line does not show a response to doses of the pH 9 HA up to 1000 μg ml^{-1}, however a decrease in cell viability is observed with a high dose (1000 μg ml^{-1}) of the pH 11 HA (Figures 4.35 and 4.36).

Nanoparticle dose can be expressed in terms of total number of particles per 1 μg. By assuming all nanoparticles are perfect cylindrical rods, the volume and subsequent weight of an individual particle can be estimated. Average particles lengths and widths have been measured from 50 measurements of individual particles (in TEM) of both hydrothermal HA samples prepared at pH 9 and pH 11. The theoretical density, ρ, of hydroxyapatite has been obtained from literature as 3.156 g/cm^3 [274]. This calculated data is shown in Table A1.

Using this data, high nanoparticle doses would contain a very large number of individual nanoparticles; 500 μg ml^{-1} can be expressed as ~87,000 particles per ml of the pH 9 HA, and ~135,000 particles per ml of the pH 11 HA. Previous literature has shown that high doses (> 500 μg ml^{-1}) of HA nanoparticles are toxic to other cell lines, likely due to cellular particle load and possible release of calcium [103]; and this is the most likely cause of the effects observed here.

Table A1: Calculated data showing estimated number of nanoparticles per 1 μg**.**

	pH 9 hydrothermal HA	**pH 11 hydrothermal HA**
Average nanoparticle length, from 50 particles (nm)	200.00	129.00
Average nanoparticle width, from 50 particles (nm)	34.00	34.00
Volume of single cylindrical nanoparticle rod (m^3)	1.82×10^{-4}	1.17×10^{-4}
Mass of single nanoparticle (g)	5.74×10^{-6}	3.70×10^{-6}
Estimated number of nanoparticles per 1 μg	174	270

Particle size variation may contribute to the affect observed in both the Caco-2 and SH-SY5Y cell lines; however there is currently little evidence to support this and further research would be required to confirm this hypothesis. Poor dispersion properties of HA due to sedimentation in the cell culture medium have been speculated to be a contributing factor to the decreasing cell viabilities observed at high HA concentrations (by the group at the Leeds Faculty of Biological Sciences) and particle size distribution data of the samples measured by DLS (Figure 4.31) confirms agglomeration of the HA samples in cell culture medium.

Overall the results of HA cytotoxicity indicate promising and expected biocompatibility, but are inconclusive. Only very high doses of HA nanoparticles caused significant drops in cell viability. Further work utilising improved nanoparticle dispersions could investigate the potential effects of particle size more carefully.

4.5.2.1. Caco-2 cell line

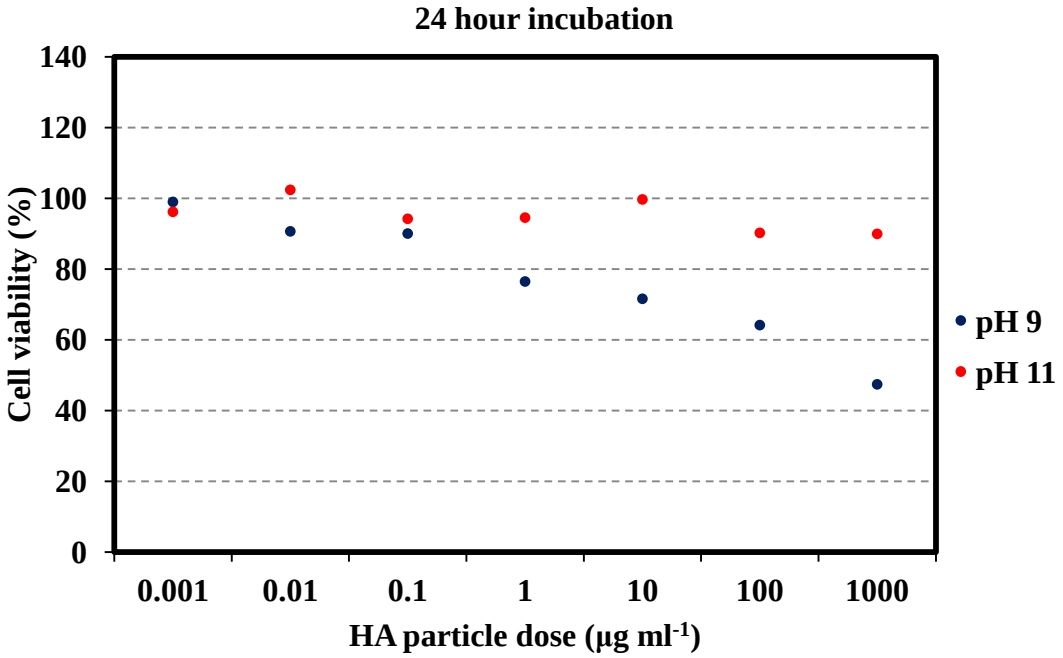

Figure 4.32: MTT assay for the cytotoxicity of varying doses of pH 9 and pH 11 hydrothermal HA particles with 24 hour incubation period using Caco-2 cell line, measured as the percentage cell viability compared to control wells with no particles (G. Dyson).

4.5.2.2. A549 cell line

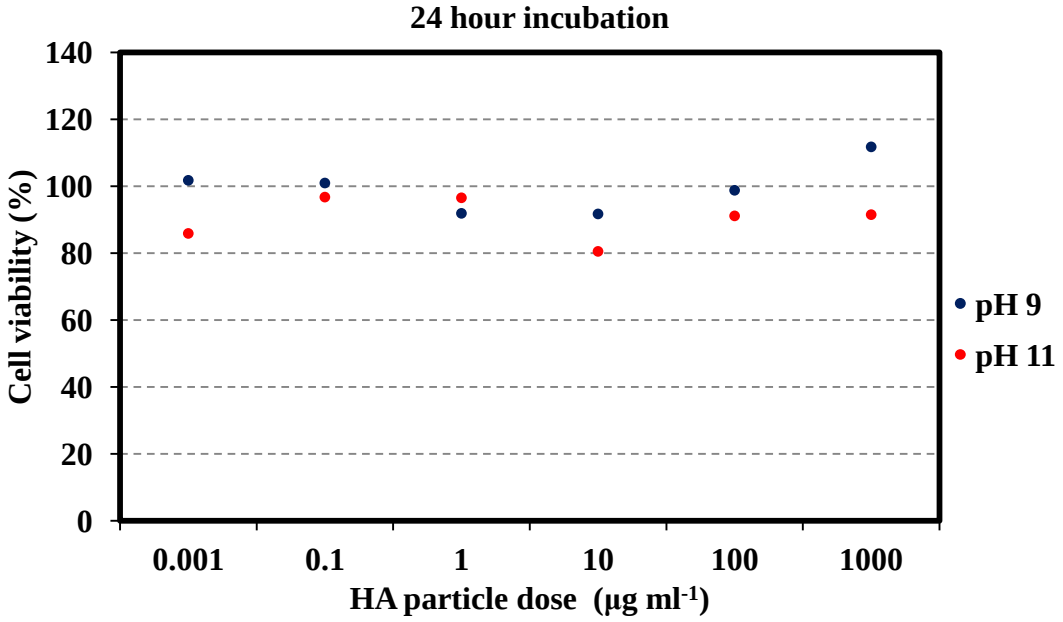

Figure 4.33: MTT assay for the cytotoxicity of varying doses of pH 9 and pH 11 hydrothermal HA particles with 24 hour incubation period using A549 cell line, measured as the percentage cell viability compared to control wells with no particles (E. Horncastle).

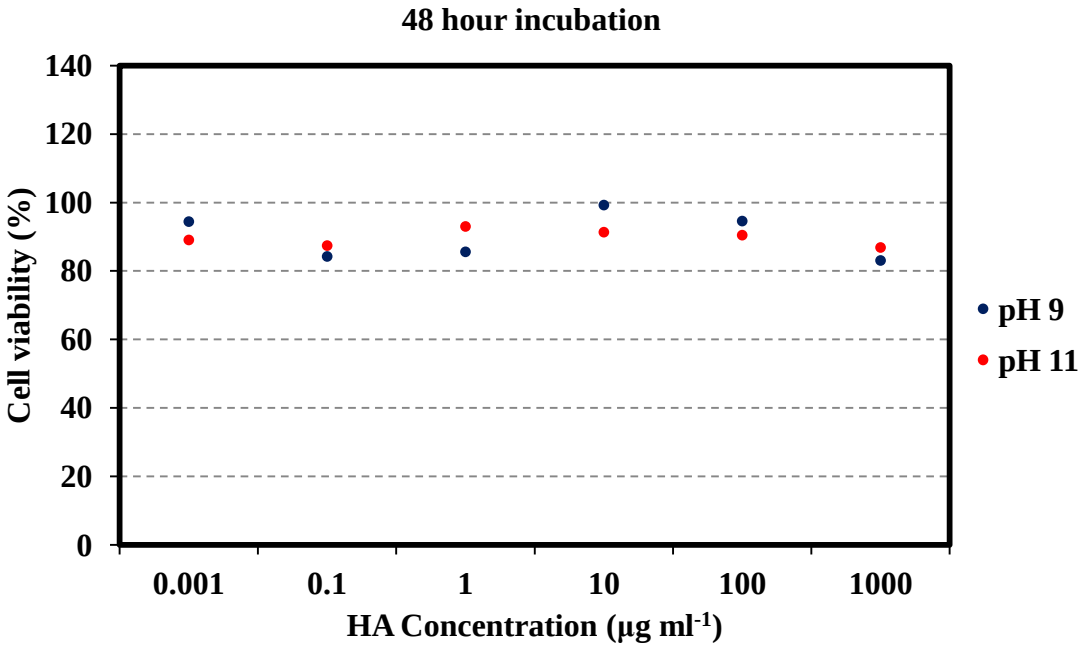

Figure 4.34: MTT assay for the cytotoxicity of varying doses of pH 9 and pH 11 hydrothermal HA particles with 48 hour incubation period using A549 cell line, measured as the percentage cell viability compared to control wells with no particles (E. Horncastle).

4.5.2.3. SH-SY5Y cell line

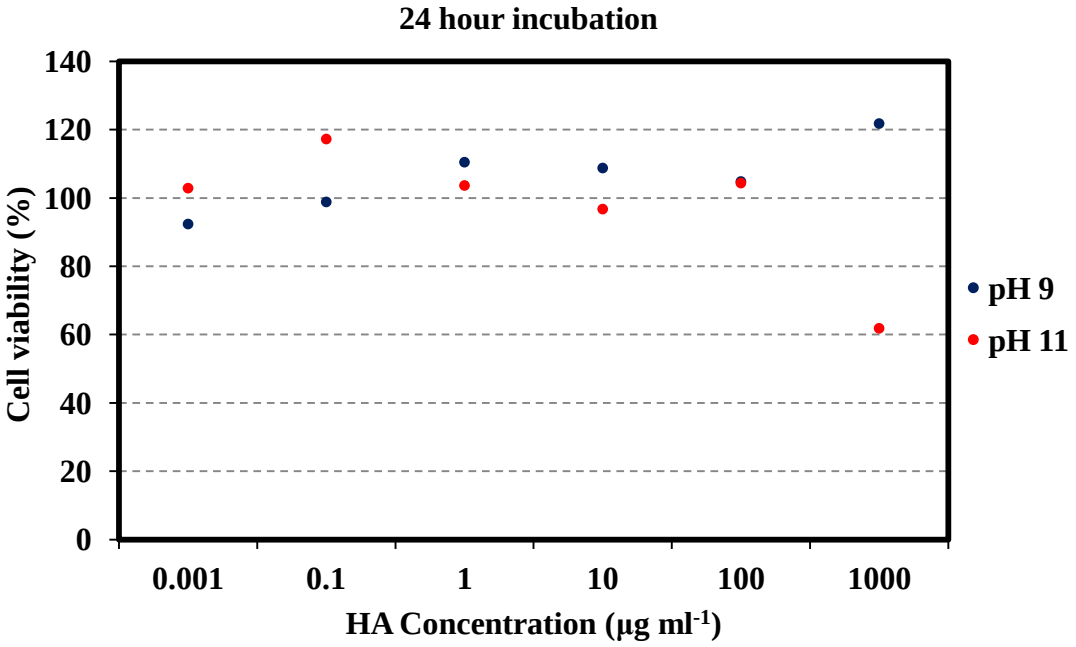

Figure 4.35: MTT assay for the cytotoxicity of varying doses of pH 9 and pH 11 hydrothermal HA particles with 24 hour incubation period using SH-SY5Y cell line, measured as the percentage cell viability compared to control wells with no particles (J. Jones).

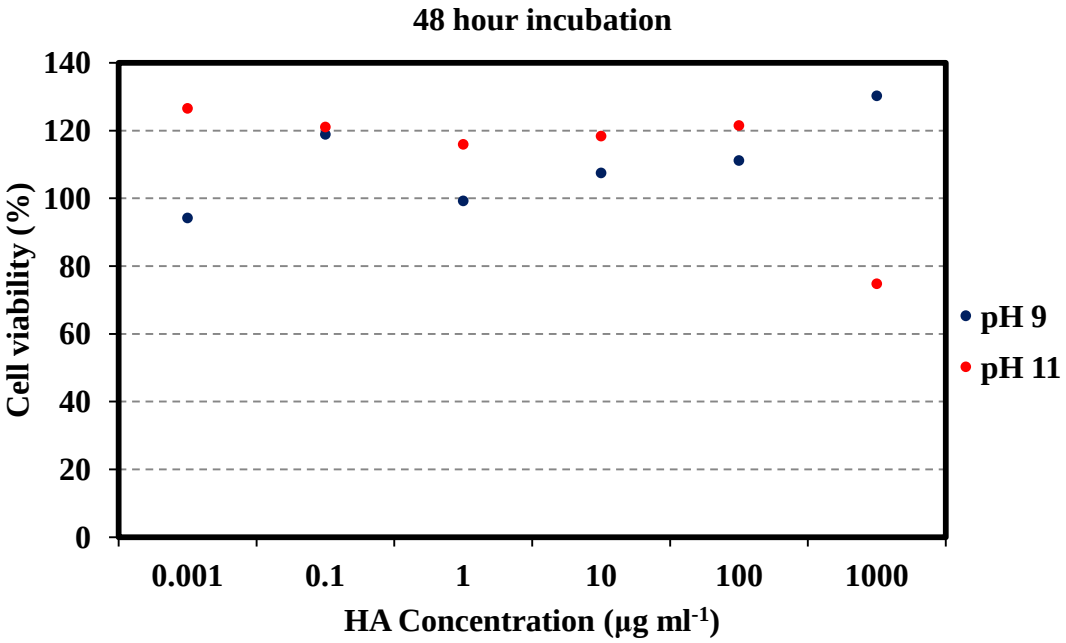

Figure 4.36: MTT assay for the cytotoxicity of varying doses of pH 9 and pH 11 hydrothermal HA particles with 48 hour incubation period using SH-SY5Y cell line, measured as the percentage cell viability compared to control wells with no particles (J. Jones).

4.5.3. XRD peak list data

Table A2: XRD peak list data for the Sigma-Aldrich HA, with ICDD reference file number: 01-074-0566 [37]. $a = b = 9.41$ Å, $c = 6.89$ Å.

Sigma-Aldrich HA			**Hydroxyapatite reference file, ICDD: 074-0566**						
Pos.°2θ	**d-spacing (Å)**	**Relative intensity (%)**	**Pos.°2θ**	**d-spacing (Å)**	**Relative intensity (%)**	**h**	**k**	**l**	**Δ°2θ**
10.877	8.1476	15.17	10.832	8.1614	17.00	1	0	0	-0.045
21.854	4.0738	6.58	21.762	4.0807	6.50	2	0	0	-0.092
22.874	3.8848	8.51	22.858	3.8875	6.30	1	1	1	-0.016
25.845	3.4445	37.74	25.883	3.4395	35.70	0	0	2	0.038
28.103	3.1726	8.42	28.131	3.1695	8.80	1	0	2	0.028
28.971	3.0795	18.52	28.921	3.0847	16.00	2	1	0	-0.050
31.804	2.8114	100.00	31.766	2.8147	100.00	2	1	1	-0.038
32.183	2.7791	55.76	32.195	2.7781	51.50	1	1	2	0.012
32.954	2.7159	58.52	32.897	2.7205	61.30	3	0	0	-0.057
34.058	2.6303	19.60	34.063	2.6299	21.00	2	0	2	0.005
39.861	2.2597	20.42	39.791	2.2636	20.50	1	3	0	-0.070
42.047	2.1472	6.00	41.986	2.1502	5.60	1	3	1	-0.061
46.729	1.9424	29.94	46.694	1.9437	28.10	2	2	2	-0.035
48.120	1.8894	10.86	48.081	1.8908	12.20	1	3	2	-0.039
49.473	1.8409	31.70	49.490	1.8403	31.30	2	1	3	0.017
50.555	1.8040	15.07	50.475	1.8066	16.10	3	2	1	-0.080
51.348	1.7779	11.51	51.255	1.7810	11.60	1	4	0	-0.093
52.125	1.7533	12.18	52.075	1.7548	11.70	4	0	2	-0.050
53.137	1.7223	16.59	53.220	1.7198	14.00	0	0	4	0.083
55.922	1.6429	5.35	55.863	1.6445	5.90	3	2	2	-0.059
60.037	1.5398	5.45	59.925	1.5424	4.30	2	4	0	-0.112
61.677	1.5027	6.84	61.571	1.5050	3.20	2	4	1	-0.106
63.060	1.4730	8.11	62.982	1.4747	7.90	5	0	2	-0.078
63.959	1.4545	6.50	63.998	1.4537	7.40	3	0	4	0.039
64.196	1.4496	8.23	64.165	1.4503	9.30	3	2	3	-0.031
65.114	1.4314	6.98	65.000	1.4337	6.90	5	1	1	-0.114
75.539	1.2577	5.61	75.622	1.2565	4.50	2	1	5	0.083
77.027	1.2370	5.62	77.021	1.2371	5.00	1	4	4	-0.006
77.246	1.2341	7.07	77.174	1.2350	4.40	5	1	3	-0.072
78.301	1.2201	7.51	78.179	1.2217	5.60	2	5	2	-0.122

Table A3: XRD peak list data for pH 11 hydrothermal HA, with ICDD reference file number: 01-074-0566 [37]. $a = b = 9.45$ Å, $c = 6.89$ Å.

pH 11 hydrothermal HA			**Hydroxyapatite reference file, ICDD: 074-0566**						
Pos. °2θ	**d-spacing (Å)**	**Relative intensity (%)**	**Pos. °2θ**	**d-spacing (Å)**	**Relative intensity (%)**	**h**	**k**	**l**	**Δ°2θ**
10.801	8.1845	15.59	10.832	8.1614	17.00	1	0	0	0.031
21.733	4.0859	7.76	21.762	4.0807	6.50	2	0	0	0.029
22.828	3.8925	8.57	22.858	3.8875	6.30	1	1	1	0.030
25.849	3.4440	41.28	25.883	3.4395	35.70	0	0	2	0.034
28.098	3.1732	9.81	28.131	3.1695	8.80	1	0	2	0.033
28.895	3.0875	18.01	28.921	3.0847	16.00	2	1	0	0.026
31.739	2.8170	100.00	31.766	2.8147	100.00	2	1	1	0.027
32.164	2.7808	62.02	32.195	2.7781	51.50	1	1	2	0.031
32.871	2.7225	57.07	32.897	2.7205	61.30	3	0	0	0.026
34.032	2.6322	21.88	34.063	2.6299	21.00	2	0	2	0.031
39.870	2.2648	16.15	39.791	2.2636	20.50	1	3	0	-0.079
41.962	2.1513	5.19	41.986	2.1502	5.60	1	3	1	0.024
46.669	1.9447	26.19	46.694	1.9437	28.10	2	2	2	0.025
48.056	1.8918	10.17	48.081	1.8908	12.20	1	3	2	0.025
49.460	1.8413	33.09	49.490	1.8403	31.30	2	1	3	0.030
50.454	1.8073	13.06	50.475	1.8066	16.10	3	2	1	0.021
51.235	1.7816	9.30	51.255	1.7810	11.60	1	4	0	0.020
52.052	1.7556	10.59	52.075	1.7548	11.70	4	0	2	0.023
53.185	1.7208	19.52	53.220	1.7198	14.00	0	0	4	0.035
61.673	1.5028	6.60	61.704	1.5021	5.00	1	2	4	0.031
62.963	1.4751	6.26	62.982	1.4747	7.90	5	0	2	0.019
63.969	1.4542	8.44	63.998	1.4537	7.40	3	0	4	0.029
64.142	1.4507	9.26	64.165	1.4503	9.30	3	2	3	0.023
64.985	1.4340	5.34	65.000	1.4337	6.90	5	1	1	0.015
75.591	1.2569	5.27	75.622	1.2565	4.50	2	1	5	0.031
76.998	1.2374	5.50	77.021	1.2371	5.00	1	4	4	0.023
77.158	1.2353	5.77	77.174	1.2350	4.40	5	1	3	0.016

Table A4: XRD peak list data for 500 °C sol-gel HA, with ICDD reference file number: 01-074-0566 [37] and single calcite peak, ICDD reference file number: 00-005-0586 [221].
Lattice parameters for HA phase: $a = b = 9.41$ Å, $c = 6.89$ Å

500 °C sol-gel HA			Pattern Assignment							
Pos. °2θ	**d-spacing (Å)**	**Relative intensity (%)**	**ICDD Reference file**	**Pos. °2θ**	**d-spacing (Å)**	**Relative intensity (%)**	**h**	**k**	**l**	**Δ°2θ**
10.877	8.1476	15.03	HA #74-0566	10.832	8.1614	17.00	1	0	0	-0.045
21.799	4.0738	7.71	HA #74-0566	21.762	4.0807	6.50	2	0	0	-0.037
22.874	3.8848	8.67	HA #74-0566	22.858	3.8875	6.30	1	1	1	-0.016
25.845	3.4445	34.90	HA #74-0566	25.883	3.4395	35.70	0	0	2	0.038
28.103	3.1726	8.26	HA #74-0566	28.131	3.1695	8.80	1	0	2	0.028
28.971	3.0795	18.34	HA #74-0566	28.921	3.0847	16.00	2	1	0	-0.050
29.397	3.0359	16.81	$CaCO_3$ #05-0586	29.406	3.0350	100.00	1	0	4	0.009
31.804	2.8114	100.00	HA #74-0566	31.766	2.8147	100.00	2	1	1	-0.038
32.183	2.7791	50.74	HA #74-0566	32.195	2.7781	51.50	1	1	2	0.012
32.954	2.7159	58.15	HA #74-0566	32.897	2.7205	61.30	3	0	0	-0.057
34.058	2.6303	19.88	HA #74-0566	34.063	2.6299	21.00	2	0	2	0.005
39.861	2.2597	21.52	HA #74-0566	39.791	2.2636	20.50	1	3	0	-0.070
42.047	2.1472	5.69	HA #74-0566	41.986	2.1502	5.60	1	3	1	-0.061
46.729	1.9424	29.37	HA #74-0566	46.694	1.9437	28.10	2	2	2	-0.035
48.120	1.8894	11.46	HA #74-0566	48.081	1.8908	12.20	1	3	2	-0.039
49.473	1.8409	32.10	HA #74-0566	49.490	1.8403	31.30	2	1	3	0.017
50.555	1.8040	15.63	HA #74-0566	50.475	1.8066	16.10	3	2	1	-0.080
51.348	1.7779	11.19	HA #74-0566	51.255	1.7810	11.60	1	4	0	-0.093
52.125	1.7533	12.18	HA #74-0566	52.075	1.7548	11.70	4	0	2	-0.050
53.137	1.7223	8.02	HA #74-0566	53.220	1.7198	14.00	0	0	4	0.083
55.922	1.6429	5.50	HA #74-0566	55.863	1.6445	5.90	3	2	2	-0.059
61.677	1.5027	6.87	HA #74-0566	61.571	1.5050	3.20	2	4	1	-0.106
63.060	1.4730	10.27	HA #74-0566	62.982	1.4747	7.90	5	0	2	-0.078
63.959	1.4545	6.77	HA #74-0566	63.998	1.4537	7.40	3	0	4	0.039
64.196	1.4496	7.64	HA #74-0566	64.165	1.4503	9.30	3	2	3	-0.031
65.114	1.4314	7.41	HA #74-0566	65.000	1.4337	6.90	5	1	1	-0.114
77.027	1.2370	5.67	HA #74-0566	77.021	1.2371	5.00	1	4	4	-0.006
77.246	1.2341	7.22	HA #74-0566	77.174	1.2350	4.40	5	1	3	-0.072
78.301	1.2201	7.53	HA #74-0566	78.179	1.2217	5.60	2	5	2	-0.122

Table A5: XRD peak list data for 700 °C sol-gel HA, with reference patterns for HA (ICDD reference file number: 01-074-0566 [9]), β-TCP (ICDD reference file number: 04-008-8714 [232]), DCPA (ICDD reference file number: 04-012-8346 [225]) and CaO (ICDD reference file number: 04-003-7161 [226]). Lattice parameters for HA phase: $a = b = 9.45$ Å, $c = 6.89$ Å

700 °C sol-gel HA			Pattern Assignment							
Pos. °2θ	**d-spacing (Å)**	**Relative intensity (%)**	**ICDD Reference file**	**Pos. °2θ**	**d-spacing (Å)**	**Relative intensity (%)**	**h**	**k**	**l**	**Δ°2θ**
10.800	8.1854	15.78	HA #74-0566	10.832	8.1614	17.00	1	0	0	0.032
10.826	8.1653	18.98	TCP #04-008-8714	10.863	8.1382	11.60	0	1	2	0.037
13.582	6.5144	20.15	TCP #04-008-8714	13.618	6.4971	17.00	1	0	4	0.036
16.806	5.2711	3.29	HA #74-0566	16.842	5.2599	4.60	1	0	1	0.036
16.936	5.2309	23.30	TCP #04-008-8714	16.974	5.2195	20.80	1	1	0	0.038
21.733	4.0860	7.40	HA #74-0566	21.762	4.0807	6.50	2	0	0	0.029
21.787	4.0760	13.82	TCP #04-008-8714	21.824	4.0691	11.70	0	2	4	0.037
25.736	3.4588	26.34	TCP #04-008-8714	25.773	3.4540	24.40	1	0	10	0.037
25.840	3.4452	21.80	HA #74-0566	25.883	3.4395	35.70	0	0	2	0.043
26.129	3.4076	4.01	TCP #04-008-8714	26.167	3.4028	3.70	2	1	1	0.038
26.445	3.3677	8.71	DCPA #04-012-8346	26.360	3.3784	92.10	0	0	2	-0.085
26.459	3.3660	9.46	TCP #04-008-8714	26.497	3.3612	7.90	1	2	2	0.038
26.534	3.3566	9.22	DCPA #04-012-8346	26.547	3.3550	92.50	2	0	0	0.013
27.386	3.2540	6.02	TCP #04-008-8714	27.423	3.2497	5.30	1	1	9	0.037
27.739	3.2134	18.94	TCP #04-008-8714	27.777	3.2091	51.90	2	1	4	0.038
28.090	3.1741	3.78	HA #74-0566	28.131	3.1695	8.80	1	0	2	0.041
28.678	3.1091	20.52	DCPA #04-012-8346	28.518	3.1274	23.70	-1	-1	2	-0.160
28.896	3.0874	6.38	HA #74-0566	28.921	3.0847	16.00	2	1	0	0.025
28.902	3.0867	6.35	DCPA #04-012-8346	28.842	3.0930	5.10	0	-2	1	-0.060
29.582	3.0173	12.49	TCP #04-008-8714	29.620	3.0135	12.40	3	0	0	0.038
30.525	2.9251	23.07	DCPA #04-012-8346	30.241	2.9530	100.00	-1	2	0	-0.284
30.985	2.8838	40.65	TCP #04-008-8714	31.023	2.8804	100.00	0	2	10	0.038
31.738	2.8171	100.00	HA #74-0566	31.766	2.8147	100.00	2	1	1	0.028
32.157	2.7813	54.71	HA #74-0566	32.195	2.7781	51.50	1	1	2	0.038
32.387	2.7621	20.21	DCPA #04-012-8346	32.463	2.7558	34.40	2	0	1	0.076
32.399	2.7611	21.67	TCP #04-008-8714	32.436	2.7580	19.90	1	2	8	0.037
32.872	2.7224	52.22	HA #74-0566	32.897	2.7205	61.30	3	0	0	0.025
32.955	2.7158	5.74	TCP #04-008-8714	32.993	2.7127	7.50	3	0	6	0.038
33.440	2.6775	5.35	TCP #04-008-8714	33.477	2.6746	5.90	1	1	12	0.037
34.027	2.6327	8.88	HA #74-0566	34.063	2.6299	21.00	2	0	2	0.036
34.296	2.6126	20.70	TCP #04-008-8714	34.334	2.6098	69.20	2	2	0	0.038
34.982	2.5629	5.79	TCP #04-008-8714	35.019	2.5603	3.90	0	1	14	0.037
35.065	2.5570	10.20	TCP #04-008-8714	35.104	2.5543	6.30	2	2	3	0.039
35.533	2.5245	12.16	TCP #04-008-8714	35.570	2.5219	11.50	2	1	10	0.037
37.290	2.4094	4.92	TCP #04-008-8714	37.329	2.4070	7.70	2	2	6	0.039
37.428	2.4009	3.78	CaO #04-003-7161	37.345	2.4060	100.00	2	0	0	-0.083
37.776	2.3795	3.06	TCP #04-008-8714	37.814	2.3772	4.70	3	1	5	0.038
39.770	2.2647	17.87	HA #74-0566	39.791	2.2636	20.50	1	3	0	0.021
39.789	2.2636	3.11	TCP #04-008-8714	39.825	2.2617	9.70	1	0	16	0.036
40.030	2.2506	5.37	TCP #04-008-8714	40.067	2.2486	2.60	1	1	15	0.037
40.118	2.2458	4.05	TCP #04-008-8714	40.156	2.2438	1.40	0	4	2	0.038
40.956	2.2018	4.95	TCP #04-008-8714	41.054	2.1968	9.90	2	1	13	0.098
41.633	2.1676	11.42	TCP #04-008-8714	41.670	2.1657	9.50	3	0	12	0.037
43.386	2.0839	4.61	TCP #04-008-8714	43.424	2.0822	3.40	1	3	10	0.038

43.516	2.0780	5.93	TCP #04-008-8714	43.552	2.0764	4.20	0	0	18	0.036
43.636	2.0726	4.82	TCP #04-008-8714	43.676	2.0708	2.30	3	2	1	0.040
43.833	2.0637	7.01	HA #74-0566	43.876	2.0618	4.50	1	1	3	0.043
43.847	2.0631	7.22	TCP #04-008-8714	43.885	2.0614	4.80	2	3	2	0.038
44.457	2.0362	7.69	TCP #04-008-8714	44.496	2.0345	7.40	0	4	8	0.039
44.684	2.0264	5.98	TCP #04-008-8714	44.723	2.0247	3.60	3	2	4	0.039
45.260	2.0019	6.68	TCP #04-008-8714	45.297	2.0004	6.30	2	2	12	0.037
45.288	2.0008	6.28	HA #74-0566	45.330	1.9990	3.50	2	0	3	0.042
46.534	1.9500	3.28	TCP #04-008-8714	46.573	1.9485	1.80	1	4	3	0.039
46.667	1.9448	30.69	HA #74-0566	46.694	1.9437	28.10	2	2	2	0.027
46.905	1.9355	9.62	TCP #04-008-8714	46.943	1.9340	22.20	4	0	10	0.038
47.914	1.8970	6.61	TCP #04-008-8714	47.953	1.8956	13.00	2	3	8	0.039
48.055	1.8918	12.67	HA #74-0566	48.081	1.8908	12.20	1	3	2	0.026
48.318	1.8821	13.79	TCP #04-008-8714	48.357	1.8807	11.30	1	4	6	0.039
49.452	1.8416	35.71	HA #74-0566	49.490	1.8403	31.30	2	1	3	0.038
49.749	1.8313	4.85	TCP #04-008-8714	49.784	1.8301	3.70	0	1	20	0.035
50.233	1.8148	5.20	TCP #04-008-8714	50.271	1.8135	4.40	3	2	10	0.038
50.457	1.8072	6.04	HA #74-0566	50.475	1.8066	16.10	3	2	1	0.018
50.572	1.8034	4.34	TCP #04-008-8714	50.683	1.7997	4.30	2	2	15	0.111
51.187	1.7832	6.72	TCP #04-008-8714	51.226	1.7819	3.90	4	1	9	0.039
51.239	1.7815	6.93	HA #74-0566	51.255	1.7810	11.60	1	4	0	0.016
51.396	1.7764	6.15	TCP #04-008-8714	51.434	1.7752	6.80	0	5	4	0.038
51.549	1.7715	5.37	TCP #04-008-8714	51.586	1.7703	1.00	2	3	11	0.037
52.051	1.7556	3.96	HA #74-0566	52.075	1.7548	11.70	4	0	2	0.024
52.944	1.7281	29.29	TCP #04-008-8714	52.979	1.7270	24.40	2	0	20	0.035
53.169	1.7213	30.58	HA #74-0566	53.220	1.7198	14.00	0	0	4	0.051
53.518	1.7109	9.23	TCP #04-008-8714	53.554	1.7098	7.90	3	0	18	0.036
53.688	1.7059	5.79	TCP #04-008-8714	53.724	1.7048	1.40	2	1	19	0.036
54.326	1.6873	6.60	TCP #04-008-8714	54.365	1.6862	5.50	5	0	8	0.039
54.435	1.6842	3.98	HA #74-0566	54.484	1.6828	1.00	1	0	4	0.049
54.474	1.6831	5.24	TCP #04-008-8714	54.561	1.6806	1.80	3	2	13	0.087
55.021	1.6676	4.90	TCP #04-008-8714	55.058	1.6666	3.00	4	1	12	0.037
56.009	1.6405	4.06	TCP #04-008-8714	56.111	1.6378	3.30	1	2	20	0.102
56.455	1.6286	3.14	TCP #04-008-8714	56.494	1.6276	2.20	0	5	10	0.039
57.337	1.6057	3.57	TCP #04-008-8714	57.378	1.6046	4.20	3	3	9	0.041
57.531	1.6007	2.78	TCP #04-008-8714	57.570	1.5997	2.70	5	1	4	0.039
59.415	1.5544	6.32	TCP #04-008-8714	59.439	1.5538	7.30	5	1	7	0.024
59.523	1.5518	5.13	TCP #04-008-8714	59.561	1.5509	6.70	3	2	16	0.038
59.703	1.5476	6.62	TCP #04-008-8714	59.739	1.5467	1.20	4	1	15	0.036
60.259	1.5346	4.10	TCP #04-008-8714	60.298	1.5337	2.40	1	5	8	0.039
61.454	1.5076	3.76	TCP #04-008-8714	61.494	1.5067	3.70	2	3	17	0.040
61.661	1.5030	3.15	HA #74-0566	61.704	1.5021	5.00	1	2	4	0.043
62.965	1.4750	3.31	HA #74-0566	62.982	1.4747	7.90	5	0	2	0.017
63.289	1.4682	4.88	TCP #04-008-8714	63.309	1.4678	3.90	1	2	23	0.020
63.958	1.4545	3.25	HA #74-0566	63.998	1.4537	7.40	3	0	4	0.040
64.139	1.4508	3.69	HA #74-0566	64.165	1.4503	9.30	3	2	3	0.026
64.991	1.4338	3.11	HA #74-0566	65.000	1.4337	6.90	5	1	1	0.009
66.188	1.4108	6.33	TCP #04-008-8714	66.229	1.4100	4.70	5	2	6	0.041
66.388	1.4070	4.14	HA #74-0566	66.412	1.4066	2.10	1	4	3	0.024
72.322	1.3055	3.01	TCP #04-008-8714	72.359	1.3049	2.80	1	5	17	0.037
73.396	1.2890	3.89	TCP #04-008-8714	73.435	1.2884	2.20	5	3	2	0.039
75.273	1.2615	4.42	TCP #04-008-8714	75.311	1.2609	3.40	4	2	20	0.038
78.173	1.2217	4.30	HA #74-0566	78.179	1.2217	5.60	2	5	2	0.006
78.218	1.2212	4.30	TCP #04-008-8714	78.253	1.2207	1.70	3	5	10	0.035

Table A6: XRD peak list data for Sigma-Aldrich HA calcined 700 °C, with reference patterns for HA (ICDD reference file number: 01-074-0566 [9]) and β-TCP (ICDD reference file number: 04-008-8714 [232]). Lattice parameters for HA phase: $a = b = 9.48$ Å, $c = 6.89$ Å

Sigma-Aldrich HA at 700 °C			**Pattern Assignment**							
Pos. °2θ	**d-spacing (Å)**	**Relative intensity (%)**	**ICDD Reference file:**	**Pos. °2θ**	**d-spacing (Å)**	**Relative intensity (%)**	**h**	**k**	**l**	**Δ°2θ**
10.771	8.2070	11.89	HA #74-0566	10.832	8.161	17.00	1	0	0	0.061
21.697	4.0930	7.35	HA #74-0566	21.762	4.081	6.50	2	0	0	0.065
22.797	3.8980	7.71	HA #74-0566	22.858	3.888	6.30	1	1	1	0.061
25.830	3.4460	32.80	HA #74-0566	25.883	3.440	35.70	0	0	2	0.053
28.076	3.1760	10.27	HA #74-0566	28.131	3.170	8.80	1	0	2	0.055
28.855	3.0920	19.04	HA #74-0566	28.921	3.085	16.00	2	1	0	0.066
31.005	2.9090	5.94	β-TCP #04-008-8714	31.023	2.880	100.00	0	2	10	0.018
31.701	2.8200	100.00	HA #74-0566	31.766	2.815	100.00	2	1	1	0.065
32.138	2.7830	58.87	HA #74-0566	32.195	2.778	51.50	1	1	2	0.057
32.829	2.7260	59.70	HA #74-0566	32.897	2.721	61.30	3	0	0	0.068
34.004	2.6340	22.85	HA #74-0566	34.063	2.630	21.00	2	0	2	0.059
35.388	2.5340	5.56	HA #74-0566	35.455	2.530	3.90	3	0	1	0.067
39.136	2.3000	5.69	HA #74-0566	39.197	2.297	5.00	2	1	2	0.061
39.720	2.2670	21.20	HA #74-0566	39.791	2.264	20.50	1	3	0	0.071
41.917	2.1540	6.49	HA #74-0566	41.986	2.150	5.60	1	3	1	0.069
43.821	2.0640	5.22	HA #74-0566	43.876	2.062	4.50	1	1	3	0.055
46.310	1.9590	8.70	HA #74-0566	46.381	1.956	0.70	4	0	1	0.071
46.629	1.9460	27.41	HA #74-0566	46.694	1.944	28.10	2	2	2	0.065
48.015	1.8930	12.22	HA #74-0566	48.081	1.891	12.20	1	3	2	0.066
48.513	1.8750	6.45	HA #74-0566	48.586	1.872	4.00	2	3	0	0.073
49.432	1.8420	29.29	HA #74-0566	49.490	1.840	31.30	2	1	3	0.058
50.403	1.8090	15.61	HA #74-0566	50.475	1.807	16.10	3	2	1	0.072
51.180	1.7830	11.89	HA #74-0566	51.255	1.781	11.60	1	4	0	0.075
52.007	1.7570	12.57	HA #74-0566	52.075	1.755	11.70	4	0	2	0.068
53.171	1.7210	13.75	HA #74-0566	53.220	1.720	14.00	0	0	4	0.049
55.793	1.6460	5.32	HA #74-0566	55.863	1.645	5.90	3	2	2	0.070
59.846	1.5440	5.09	HA #74-0566	59.925	1.542	4.30	2	4	0	0.079
61.494	1.5070	5.36	HA #74-0566	61.571	1.505	3.20	2	4	1	0.077
61.649	1.5030	5.84	HA #74-0566	61.704	1.502	5.00	1	2	4	0.055
62.908	1.4760	7.39	HA #74-0566	62.982	1.475	7.90	5	0	2	0.074
63.942	1.4550	9.21	HA #74-0566	63.998	1.454	7.40	3	0	4	0.056
64.098	1.4520	9.14	HA #74-0566	64.165	1.450	9.30	3	2	3	0.067
64.921	1.4350	6.75	HA #74-0566	65.000	1.434	6.90	5	1	1	0.079
76.956	1.2380	6.14	HA #74-0566	77.021	1.237	5.00	1	4	4	0.065
77.100	1.2360	5.98	HA #74-0566	77.174	1.235	4.40	5	1	3	0.074
78.098	1.2230	5.16	HA #74-0566	78.179	1.222	5.60	2	5	2	0.081

Table A7: XRD peak list data for Sigma-Aldrich HA calcined 800 °C, with reference patterns for HA (ICDD reference file number: 01-074-0566 [9]) and β-TCP (ICDD reference file number: 04-008-8714 [232]). Lattice parameters for HA phase: $a = b = 9.46$ Å, $c = 6.89$ Å

Sigma-Aldrich HA at 800 °C			Pattern Assignment							
Pos. °2θ	**d-spacing (Å)**	**Relative intensity (%)**	**ICDD Reference file:**	**Pos. °2θ**	**d-spacing (Å)**	**Relative intensity (%)**	**h**	**k**	**l**	**Δ°2θ**
10.788	8.1940	15.97	HA #74-0566	10.832	8.1614	17.00	1	0	0	0.044
10.821	8.1691	18.44	β-TCP #04-008-8714	10.863	8.1382	11.60	0	1	2	0.042
13.573	6.5187	20.27	β-TCP #04-008-8714	13.618	6.4971	17.00	1	0	4	0.045
16.937	5.2307	24.12	β-TCP #04-008-8714	16.974	5.2195	20.80	1	1	0	0.037
21.718	4.0888	8.30	HA #74-0566	21.762	4.0807	6.50	2	0	0	0.044
21.785	4.0763	14.12	β-TCP #04-008-8714	21.824	4.0691	11.70	0	2	4	0.039
25.715	3.4617	30.76	β-TCP #04-008-8714	25.773	3.4540	24.40	1	0	10	0.058
25.840	3.4452	21.76	HA #74-0566	25.883	3.4395	35.70	0	0	2	0.043
26.134	3.4070	5.78	β-TCP #04-008-8714	26.167	3.4028	3.70	2	1	1	0.033
26.463	3.3655	8.09	β-TCP #04-008-8714	26.497	3.3612	7.90	1	2	2	0.034
27.372	3.2557	7.33	β-TCP #04-008-8714	27.423	3.2497	5.30	1	1	9	0.051
27.741	3.2132	61.06	β-TCP #04-008-8714	27.777	3.2091	51.90	2	1	4	0.036
28.878	3.0893	5.72	HA #74-0566	28.921	3.0847	16.00	2	1	0	0.043
29.589	3.0166	12.93	β-TCP #04-008-8714	29.620	3.0135	12.40	3	0	0	0.031
30.970	2.8851	100.00	β-TCP #04-008-8714	31.023	2.8804	100.00	0	2	10	0.053
31.722	2.8184	35.07	HA #74-0566	31.766	2.8147	100.00	2	1	1	0.044
32.152	2.7818	20.15	HA #74-0566	32.195	2.7781	51.50	1	1	2	0.043
32.393	2.7616	26.30	β-TCP #04-008-8714	32.436	2.7580	19.90	1	2	8	0.043
32.853	2.7240	23.24	HA #74-0566	32.897	2.7205	61.30	3	0	0	0.044
32.956	2.7157	24.64	β-TCP #04-008-8714	32.993	2.7127	7.50	3	0	6	0.037
33.419	2.6791	6.71	β-TCP #04-008-8714	33.477	2.6746	5.90	1	1	12	0.058
34.020	2.6332	9.47	HA #74-0566	34.063	2.6299	21.00	2	0	2	0.043
34.305	2.6119	67.98	β-TCP #04-008-8714	34.334	2.6098	69.20	2	2	0	0.029
34.952	2.5651	6.25	β-TCP #04-008-8714	35.019	2.5603	3.90	0	1	14	0.067
35.073	2.5565	10.00	β-TCP #04-008-8714	35.104	2.5543	6.30	2	2	3	0.031
35.522	2.5252	12.47	β-TCP #04-008-8714	35.570	2.5219	11.50	2	1	10	0.048
37.293	2.4092	9.61	β-TCP #04-008-8714	37.329	2.4070	7.70	2	2	6	0.036
37.782	2.3792	5.82	β-TCP #04-008-8714	37.814	2.3772	4.70	3	1	5	0.032
39.747	2.2660	18.46	HA #74-0566	39.791	2.2636	20.50	1	3	0	0.044
39.755	2.2655	18.73	β-TCP #04-008-8714	39.825	2.2617	9.70	1	0	16	0.070
40.002	2.2521	7.05	β-TCP #04-008-8714	40.067	2.2486	2.60	1	1	15	0.065
41.620	2.1682	10.58	β-TCP #04-008-8714	41.670	2.1657	9.50	3	0	12	0.050
43.475	2.0799	6.26	β-TCP #04-008-8714	43.552	2.0764	4.20	0	0	18	0.077
43.832	2.0638	6.47	HA #74-0566	43.876	2.0618	4.50	1	1	3	0.044

43.860	2.0625	6.88	β-TCP #04-008-8714	43.885	2.0614	4.80	2	3	2	0.025
44.460	2.0361	7.16	β-TCP #04-008-8714	44.496	2.0345	7.40	0	4	8	0.036
44.695	2.0259	5.90	β-TCP #04-008-8714	44.723	2.0247	3.60	3	2	4	0.028
45.251	2.0023	6.10	β-TCP #04-008-8714	45.297	2.0004	6.30	2	2	12	0.046
45.286	2.0008	6.06	HA #74-0566	45.330	1.9990	3.50	2	0	3	0.044
46.547	1.9495	8.38	β-TCP #04-008-8714	46.573	1.9485	1.80	1	4	3	0.026
46.651	1.9454	12.02	HA #74-0566	46.694	1.9437	28.10	2	2	2	0.043
46.904	1.9355	24.83	β-TCP #04-008-8714	46.943	1.9340	22.20	4	0	10	0.039
47.919	1.8969	15.33	β-TCP #04-008-8714	47.953	1.8956	13.00	2	3	8	0.034
48.038	1.8925	13.10	HA #74-0566	48.081	1.8908	12.20	1	3	2	0.043
48.328	1.8818	13.25	β-TCP #04-008-8714	48.357	1.8807	11.30	1	4	6	0.029
49.447	1.8418	10.36	HA #74-0566	49.490	1.8403	31.30	2	1	3	0.043
49.705	1.8328	7.15	β-TCP #04-008-8714	49.784	1.8301	3.70	0	1	20	0.079
50.234	1.8148	5.88	β-TCP #04-008-8714	50.271	1.8135	4.40	3	2	10	0.037
50.432	1.8081	7.16	HA #74-0566	50.475	1.8066	16.10	3	2	1	0.043
50.555	1.8040	6.14	β-TCP #04-008-8714	50.683	1.7997	4.30	2	2	15	0.128
51.192	1.7830	7.91	β-TCP #04-008-8714	51.226	1.7819	3.90	4	1	9	0.034
51.211	1.7824	8.09	HA #74-0566	51.255	1.7810	11.60	1	4	0	0.044
51.411	1.7759	10.22	β-TCP #04-008-8714	51.434	1.7752	6.80	0	5	4	0.023
51.548	1.7715	5.98	β-TCP #04-008-8714	51.586	1.7703	1.00	2	3	11	0.038
52.903	1.7293	24.23	β-TCP #04-008-8714	52.979	1.7270	24.40	2	0	20	0.076
53.176	1.7211	8.03	HA #74-0566	53.220	1.7198	14.00	0	0	4	0.044
53.489	1.7117	8.64	β-TCP #04-008-8714	53.554	1.7098	7.90	3	0	18	0.065
53.654	1.7069	5.86	β-TCP #04-008-8714	53.724	1.7048	1.40	2	1	19	0.070
54.335	1.6871	5.80	β-TCP #04-008-8714	54.365	1.6862	5.50	5	0	8	0.030
59.428	1.5540	9.60	β-TCP #04-008-8714	59.439	1.5538	7.30	5	1	7	0.011
59.510	1.5521	11.29	β-TCP #04-008-8714	59.561	1.5509	6.70	3	2	16	0.051
59.693	1.5478	6.13	β-TCP #04-008-8714	59.739	1.5467	1.20	4	1	15	0.046

Table A8: XRD peak list data for pH 9 hydrothermal HA for cytotoxicity analysis, with ICDD reference file number: 01-074-0566 [37]. $a = b = 9.48$ Å, $c = 6.88$ Å.

pH 9 hydrothermal HA for cytotoxicity analysis			**Hydroxyapatite reference file, ICDD: 074-0566**						
Pos. °2θ	**d-spacing (Å)**	**Relative intensity (%)**	**Pos. °2θ**	**d-spacing (Å)**	**Relative intensity (%)**	**h**	**k**	**l**	**Δ°2θ**
10.793	8.2106	14.59	10.832	8.1614	17.00	1	0	0	0.039
16.820	5.2798	4.45	16.842	5.2599	4.60	1	0	1	0.022
18.797	4.7288	3.19	18.817	4.7120	2.30	1	1	0	0.020
21.748	4.0934	6.33	21.762	4.0807	6.50	2	0	0	0.014
22.848	3.8987	8.05	22.858	3.8875	6.30	1	1	1	0.010
25.353	3.5189	2.76	25.357	3.5097	2.30	2	0	1	0.004
25.886	3.4477	33.66	25.883	3.4395	35.70	0	0	2	-0.003
28.139	3.1766	8.23	28.131	3.1695	8.80	1	0	2	-0.008
28.924	3.0921	17.13	28.921	3.0847	16.00	2	1	0	-0.003
31.776	2.8208	100	31.766	2.8147	100.00	2	1	1	-0.010
32.129	2.7837	57.76	32.195	2.7781	51.50	1	1	2	0.066
32.824	2.7263	66.15	32.897	2.7205	61.30	3	0	0	0.073
34.084	2.6349	21.93	34.063	2.6299	21.00	2	0	2	-0.021
35.474	2.5348	3.84	35.455	2.5298	3.90	3	0	1	-0.019
39.230	2.3003	4.98	39.197	2.2965	5.00	2	1	2	-0.033
39.819	2.2676	17.86	39.791	2.2636	20.50	1	3	0	-0.028
42.021	2.1538	4.68	41.986	2.1502	5.60	1	3	1	-0.035
43.925	2.0648	3.71	43.876	2.0618	4.50	1	1	3	-0.049
45.382	2.0018	3.39	45.330	1.9990	3.50	2	0	3	-0.052
46.427	1.9591	7.72	46.381	1.9561	0.70	4	0	1	-0.046
46.745	1.9466	24.07	46.694	1.9437	28.10	2	2	2	-0.051
48.135	1.8935	10.74	48.081	1.8908	12.20	1	3	2	-0.054
48.637	1.8752	4.10	48.586	1.8724	4.00	2	3	0	-0.051
49.553	1.8427	27.55	49.490	1.8403	31.30	2	1	3	-0.063
50.532	1.8092	13.04	50.475	1.8066	16.10	3	2	1	-0.057
51.313	1.7835	9.43	51.255	1.7810	11.60	1	4	0	-0.058
52.055	1.7555	11.97	52.075	1.7548	11.70	4	0	2	0.020
53.299	1.7216	11.18	53.220	1.7198	14.00	0	0	4	-0.079
55.838	1.6452	5.49	55.863	1.6445	5.90	3	2	2	0.025
57.061	1.6128	4.13	57.134	1.6109	3.70	3	1	3	0.073
60.006	1.5443	4.01	59.925	1.5424	4.30	2	4	0	-0.081
61.636	1.5036	6.11	61.571	1.5050	3.20	2	4	1	-0.065
61.659	1.5068	6.06	61.704	1.5021	5.00	1	2	4	0.045
62.902	1.4763	8.77	62.982	1.4747	7.90	5	0	2	0.080
63.929	1.4551	9.23	63.998	1.4537	7.40	3	0	4	0.069
64.107	1.4551	10.96	64.165	1.4503	9.30	3	2	3	0.058
64.917	1.4353	7.7	65.000	1.4337	6.90	5	1	1	0.083
71.509	1.3183	4.13	71.596	1.3169	3.70	4	3	1	0.087
72.144	1.3082	3.27	72.232	1.3069	2.80	5	2	0	0.088
73.931	1.2810	4.13	74.012	1.2798	3.80	2	4	3	0.081
75.553	1.2575	4.53	75.622	1.2565	4.50	2	1	5	0.069
75.999	1.2512	2.97	76.085	1.2500	2.40	3	4	2	0.086
76.944	1.2382	6.48	77.021	1.2371	5.00	1	4	4	0.077
77.092	1.2362	7.42	77.174	1.2350	4.40	5	1	3	0.082
78.323	1.2228	3.73	78.179	1.2217	5.60	2	5	2	-0.144

Table A9: XRD peak list data for pH 11 hydrothermal HA for cytotoxicity analysis, with ICDD reference file number: 01-074-0566 [37]. $a = b = 9.49$ Å, $c = 6.90$ Å.

pH 11 hydrothermal HA for cytotoxicity analysis			**Hydroxyapatite reference file, ICDD: 074-0566**						
Pos. °2θ	**d-spacing (Å)**	**Relative intensity (%)**	**Pos. °2θ**	**d-spacing (Å)**	**Relative intensity (%)**	**h**	**k**	**l**	**Δ°2θ**
10.850	8.1476	16.17	10.832	8.1614	17.00	1	0	0	-0.018
21.799	4.0738	8.05	21.762	4.0807	6.50	2	0	0	-0.037
22.874	3.8848	8.51	22.858	3.8875	6.30	1	1	1	-0.016
25.845	3.4445	37.74	25.883	3.4395	35.70	0	0	2	0.038
28.103	3.1726	8.42	28.131	3.1695	8.80	1	0	2	0.028
28.971	3.0795	18.52	28.921	3.0847	16.00	2	1	0	-0.050
31.804	2.8114	100.00	31.766	2.8147	100.00	2	1	1	-0.038
32.183	2.7791	55.76	32.195	2.7781	51.50	1	1	2	0.012
32.954	2.7159	58.52	32.897	2.7205	61.30	3	0	0	-0.057
34.058	2.6303	19.60	34.063	2.6299	21.00	2	0	2	0.005
39.861	2.2597	20.42	39.791	2.2636	20.50	1	3	0	-0.070
42.047	2.1472	6.00	41.986	2.1502	5.60	1	3	1	-0.061
43.837	2.0636	4.75	43.876	2.0618	4.50	1	1	3	0.039
45.296	2.0004	4.00	45.330	1.9990	3.50	2	0	3	0.034
46.729	1.9424	29.94	46.694	1.9437	28.10	2	2	2	-0.035
48.120	1.8894	10.86	48.081	1.8908	12.20	1	3	2	-0.039
49.473	1.8409	31.70	49.490	1.8403	31.30	2	1	3	0.017
50.555	1.8040	15.07	50.475	1.8066	16.10	3	2	1	-0.080
51.348	1.7779	11.51	51.255	1.7810	11.60	1	4	0	-0.093
52.117	1.7535	11.59	52.075	1.7548	11.70	4	0	2	-0.042
53.160	1.7215	13.71	53.220	1.7198	14.00	0	0	4	0.060
55.915	1.6431	5.13	55.863	1.6445	5.90	3	2	2	-0.052
60.037	1.5398	5.45	59.925	1.5424	4.30	2	4	0	-0.112
61.655	1.5031	6.89	61.571	1.5050	3.20	2	4	1	-0.084
61.677	1.5027	6.84	61.704	1.5021	5.00	1	2	4	0.027
63.060	1.4730	8.11	62.982	1.4747	7.90	5	0	2	-0.078
63.959	1.4545	6.50	63.998	1.4537	7.40	3	0	4	0.039
64.196	1.4496	8.23	64.165	1.4503	9.30	3	2	3	-0.031
65.114	1.4314	6.98	65.000	1.4337	6.90	5	1	1	-0.114
74.074	1.2789	4.93	74.012	1.2798	3.80	2	4	3	-0.062
75.539	1.2577	5.61	75.622	1.2565	4.50	2	1	5	0.083
77.027	1.2370	5.62	77.021	1.2371	5.00	1	4	4	-0.006
77.246	1.2341	7.07	77.174	1.2350	4.40	5	1	3	-0.072
78.301	1.2201	7.51	78.179	1.2217	5.60	2	5	2	-0.122

4.5.4. XRF compositional data

Table A10: Full XRF data for four HA samples.

	Sigma Aldrich HA	**pH 11 Hydrothermal HA**	**500 °C sol-gel HA**	**700 °C sol-gel HA**
	Concentration (wt%)	Concentration (wt%)	Concentration (wt%)	Concentration (wt%)
SiO_2	<0.006	<0.062	0.062	<0.062
TiO_2	0.033	<0.006	<0.012	<0.006
Al_2O_3	0.008	<0.041	<0.012	<0.041
Fe_2O_3	0.133	<0.005	<0.011	<0.005
Mn_3O_4	0.019	0.011	0.020	0.015
MgO	<0.005	<0.007	<0.017	<0.007
CaO	49.645	55.019	55.422	52.370
Na_2O	0.154	<0.008	<0.021	<0.008
K_2O	<0.003	<0.004	<0.010	<0.004
P_2O_5	41.875	41.345	38.291	45.224
SO_3	0.115	0.037	0.044	0.035
V_2O_5	<0.002	0.005	<0.008	<0.004
Cr_2O_3	<0.003	0.008	<0.010	<0.005
SrO	0.043	0.011	0.020	0.014
ZrO_2	0.018	0.005	0.031	0.013
BaO	<0.004	<0.008	<0.017	<0.008
NiO	<0.002	<0.002	<0.005	<0.002
CuO	<0.002	<0.002	<0.004	<0.002
ZnO	0.012	<0.001	<0.003	<0.001
PbO	0.009	0.017	0.029	0.016
HfO_2	0.014	0.007	<0.009	0.004
F	<0.085	0.000	<0.020	0.000
LOI	5.600	1.576	5.844	2.114
Total	97.679	98.041	99.763	99.806

Laboratory notes:

1. Major elements determined on fused glass beads prepared from dried powders. Sample to flux ratio 1:10, 100% Lithium tetraborate flux (Fluxana FX-X100) results quoted as component oxide weight percent, re-calculated to include LOI.
2. Samples analysed on University of Leicester, Department of Geology PANalytical Axios Advanced XRF spectrometer using WROXI analytical package.
3. LOI determined on powders previously dried overnight at 105 °C. Samples ignited for 90 mins at 950 °C in air ventilated electric muffle furnace.
4. Results below limit of detection quoted as less than the limit of detection (<LLD)
5. Low total for pH 11 hydrothermal HA, but not enough sample to repeat LOI determination or make another bead. LOI does seem lower than for other samples.

4.5.5. LA-ICP-MS compositional data

Table A11: LA-ICP-MS composition summary for all four HA samples and Bonemeal standard reference material.

Sample Name	Na_{23} (wt% x 10^{-8})	Mg_{24} (wt% x 10^{-4})	K_{39} (wt% x 10^{-6})	Ca_{44} (wt%)	Ca_{44} (at.% x 10^{-2})	P_{31} (wt%)	P_{31} (at.% x 10^{-2})	Ca/P	Ca/P Avg
Sigma-Aldrich HA	15.973	1.057	1.947	0.697	1.584	0.303	0.977	1.620	1.64 ± 0.03
	17.299	1.048	2.090	0.704	1.601	0.296	0.953	1.680	
	16.859	1.068	1.857	0.701	1.592	0.299	0.966	1.650	
	16.657	1.068	1.667	0.693	1.575	0.307	0.990	1.590	
	16.469	1.049	1.914	0.701	1.594	0.299	0.963	1.650	
pH 11 hydrothermal HA	2.806	3.925	1.700	0.700	1.592	0.299	0.965	1.650	1.65 ± 0.02
	2.882	3.401	1.668	0.701	1.594	0.298	0.962	1.660	
	2.810	4.297	1.757	0.697	1.584	0.303	0.976	1.620	
	2.889	3.961	1.606	0.705	1.601	0.295	0.952	1.680	
	2.856	4.542	1.671	0.699	1.590	0.300	0.968	1.640	
500 °C sol-gel HA	2.776	2.675	91.977	0.729	1.658	0.270	0.872	1.900	1.84 ± 0.09
	1.588	2.548	40.053	0.709	1.611	0.291	0.939	1.720	
	1.965	2.437	46.146	0.720	1.637	0.280	0.902	1.810	
	2.055	2.416	41.642	0.734	1.668	0.266	0.857	1.950	
	2.209	2.534	32.859	0.720	1.637	0.279	0.901	1.820	
700 °C sol-gel HA	3.395	2.525	25.230	0.702	1.597	0.297	0.959	1.670	1.66 ± 0.02
	3.163	2.568	21.158	0.700	1.590	0.300	0.968	1.640	
	2.977	2.360	16.460	0.700	1.591	0.300	0.967	1.640	
	2.332	2.120	18.460	0.703	1.599	0.296	0.956	1.670	
	2.922	2.454	25.930	0.706	1.605	0.294	0.947	1.690	
Bonemeal NIST1486 Standard	1.437	0.211	1.683	0.725	1.647	0.275	0.888	1.860	1.86 ± 0.01
	1.586	0.205	1.726	0.725	1.647	0.275	0.888	1.850	
	1.611	0.199	1.677	0.725	1.649	0.275	0.886	1.860	
	1.685	0.206	1.837	0.726	1.650	0.274	0.884	1.870	
	1.748	0.205	1.700	0.724	1.645	0.276	0.891	1.850	

Chapter 5. Results & discussion - Calcium oxide nanosorbents for CO_2 sequestration

Preface

The worldwide obligation to reduce anthropogenic CO_2 emissions has led to large interest being generated in the development of technologies for carbon capture and storage (CCS). The technique for CO_2 capture currently considered the most commercially viable is amine scrubbing, which was first successfully trialled on gas and coal power stations on a small scale in the early 1980's [119]. The technique captures CO_2 for geological storage by regenerating the solvent by stripping with water vapour at 100 °C to 120 °C [119] however, due to various operational (e.g. corrosion) and environmental disadvantages, there is a drive to develop greener and more cost-effective methods [120]. Alternate technologies include absorption with soluble carbonate, adsorption with activated carbon and capture using an ionic liquid [121, 122], but these are not easily applied at temperatures above 500 °C, which would be necessary for incorporation into coal power plants where temperature conditions for coal combustion (and therefore CO_2 emission) are typically in the range 550 – 750 °C [108, 122-124]. One effective method for CO_2 sequestration, at a higher temperature range (550 – 950 °C), is to use a solid metal oxide such as CaO (e.g. calcined limestone) and nanoparticulate CaO based powder sorbents are well recognised as materials for effective high-capacity capture and storage of CO_2 [125-129]. Calcium acetate hydrate, CaAc ($Ca(CH_3COO)_2 \cdot xH_2O$), powder has been previously highlighted as an effective precursor for the formation of nanoparticulate CaO which can be utilised for optimum sequestration of CO_2 gas [123, 128, 275].

Although the costs of these nano-powder sorbents may prevent their utilisation in large scale operations, information gained from research on model CaO nano-powder sorbents will help understand the fundamental issues concerning carbonations and decarbonation.

Calcium acetate hydrate reportedly thermally decomposes (in an N_2 atmosphere) in a step-wise fashion, by an initial release of water (between 100-200°C), and then decomposition of acetate to form an intermediate calcium carbonate ($CaCO_3$) phase (between 350-450 °C), which ultimately decomposes to form fine nanoparticulate CaO (at ~750 °C) [141, 275]. This resultant CaO product exists as a more open (not fully-sintered) structure in comparison to CaO formed by the decomposition of alternate calcium-based precursors, such as calcium nitrate tetrahydrate ($Ca(NO_3)_2 \cdot 4H_2O$), calcium hydroxide ($Ca(OH)_2$) and calcium carbonate ($CaCO_3$) and therefore, due to the larger exposed surface area available for reaction, offers a higher amount of carbonation conversion for the sequestration of CO_2 [128, 275].

Modification of powder CaO sorbents using dopant and second-phase materials have been highlighted as means for improving CO_2-capture performance, with zirconia (ZrO_2) and mayenite ($Ca_{12}Al_{14}O_{33}$) both recognised as effective materials for such improvement [130, 276, 277]. These ‘spacer’ powders aim to improve the regenerability of the CaO sorbents during multicycle CO_2 capture by acting as barriers against the sintering of CaO during decarbonation (at 800 °C), limiting CaO particle growth and maintaining higher particle surface areas for the subsequent carbonation reaction.

Work in this Chapter aims to firstly analyse the step-wise decomposition of CaAc to identify the key microstructural changes that lead to the reported formation

of an open structured CaO sorbent by characterisation at the bulk and nanoparticle level.

Secondly, nanoscale analysis of the carbonation process of the CaO sorbent will be carried out to identify the growth mechanism of calcium carbonate, $CaCO_3$, and subsequently any densification and sintering during the continuous decarbonation/carbonation multicycle process.

Finally, modifications of the optimum CaO sorbent will be prepared using particle spacer materials (yttria stabilised zirconia, calcium zirconate and mayenite), and analysed for potential further improvement in multicycle durability. The main concept here is to use yttria stabilised zirconia to extend beyond passive ‘spacers’ by utilising its phase transformation from tetragonal to monoclinic (at ~550 °C) between sorbent carbonation and decarbonation to induce micro stresses and crack to provide active ‘spacers’.

Nanoparticle analysis by electron microscopy will be used to highlight the microstructural effects of particle spacers on the CaO sorbent, which ultimately may lead to improving the overall sorbent performance for CO_2 capture.

5.1. Hydroxyapatite as a sorbent for CO_2 capture

As previously discussed in Section 4.2.2, the decomposition of synthetic HA can begin at ~600 °C, and with increasing temperature (> 700 °C), proceeds by the following reaction to produce β-TCP and CaO [227, 228]:

$$Ca_{10}(PO_4)_6(OH)_2\ (s) \rightarrow 3Ca_3(PO_4)_2\ (s) + CaO\ (s) + H_2O\ (g) \qquad (5.1)$$

Naturally occurring hydroxyapatite contains carbonate ions (CO_3^{2-}) that have substituted on hydroxyl ion (OH^-) sites [38], and the HA samples previously prepared in house by the sol-gel synthesis route similarly exhibited contaminants of carbonate and also CaO (see Section 4.2.2, Figure 4.6 and 4.7). This therefore presents a possibility for the use of HA as a high temperature sorbent for the capture of CO_2 gas, following the reaction:

$$CaO\ (s) + CO_2\ (g) \rightarrow CaCO_3\ (s) \qquad (5.2)$$

A preliminary experiment has investigated the CO_2 uptake capability of synthetic HA was by thermogravimetric analysis (TGA) using a Shimadzu TGA-50 thermobalance. The HA samples previously prepared by the sol-gel route (calcined at 500 and 700 °C) and hydrothermal method (at pH 11), and also the commercial HA powder (Sigma-Aldrich) have been heated from 20 to 1000 °C at a constant heating rate of 20 °C min^{-1} in a fixed a CO_2 atmosphere (flow rate = 50 ml min^{-1}). Results are displayed in Figure 5.1 and it is observed that no significant weight gain due to uptake of CO_2 is observed by any of the HA samples in these conditions.

In fact weight loss (6.5%) was observed in the Sigma-Aldrich sample, which may be due to loss of H_2O. The in-house prepared samples showed negligible changes in weight percentage (all < 2.5%) with the pH 11 hydrothermal HA showing a < 2% decrease in mass up to 600 °C, and then a minor gain of < 1% up to

1000 °C. Such small changes may be erroneous and caused by drift by the TGA instrument. The sol-gel sample prepared at 500 °C showed no notable weight decrease up to 900 °C, after which a 2.5% decrease in weight was observed up to 1000 °C, which may be the start of HA decomposition to β-TCP. Similarly the sol-gel HA prepared at 700 °C showed no notable weight change up to 900 °C, with a < 1% weight decrease observed up to 1000 °C, which again which may be the start of HA decomposition to β-TCP.

It can be ultimately concluded that HA is not effective for the capture of CO_2, at this temperature range, and consequently will not be pursued further here for the production of powder sorbents for CO_2.

.

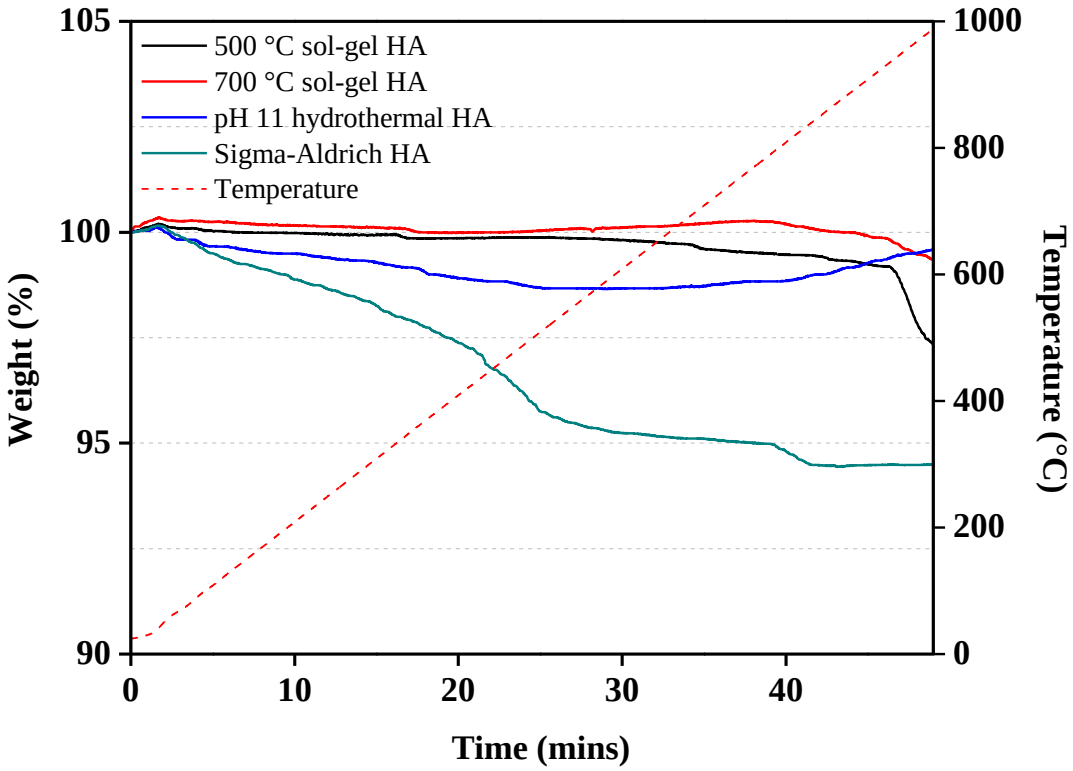

Figure 5.1: Thermogravimetric analysis of the CO_2 uptake capability of HA samples prepared by the sol-gel method (calcined at 500 °C and 700 °C), the hydrothermal method (at pH 11) and commercial HA powder (Sigma-Aldrich). Temperature raised from 20 – 1000 °C at (20 °C min^{-1}) under constant CO_2 atmosphere (50 ml min^{-1} flow rate).

5.2. As received calcium acetate hydrate

The thermal decomposition of a commercial calcium acetate hydrate, CaAc powder ($Ca(CH_3COO)_2 \cdot xH_2O$; value of x unreported by supplier), Acros Organics, 99%, extra pure) has been analysed using thermogravimetric analysis (TGA) with evolved gases analysed by Fourier transform infrared spectroscopy (FTIR). The development of the phases formed during this process have been analysed by XRD, SEM and TEM.

5.2.1. XRD analysis

The X-ray powder diffraction pattern for the CaAc, powder is shown in Figure 5.2a. Sharp peaks suggest a high degree of crystallinity, and a prevalence of high-intensity peaks at low 2θ values indicates large unit cell parameters. Analysis of the peak data using X'pert HiScore software shows the sample was best matched to calcium acetate hydrate, $Ca(CH_3COO)_2 \cdot 0.5H_2O$ (ICDD ref: 00-019-0199); this reference pattern suggests a crystal structure where one water molecule is shared between every two calcium acetate molecules [278]. The crystallographic parameters (space group and Miller indices) are unreported by the reference pattern for this material.

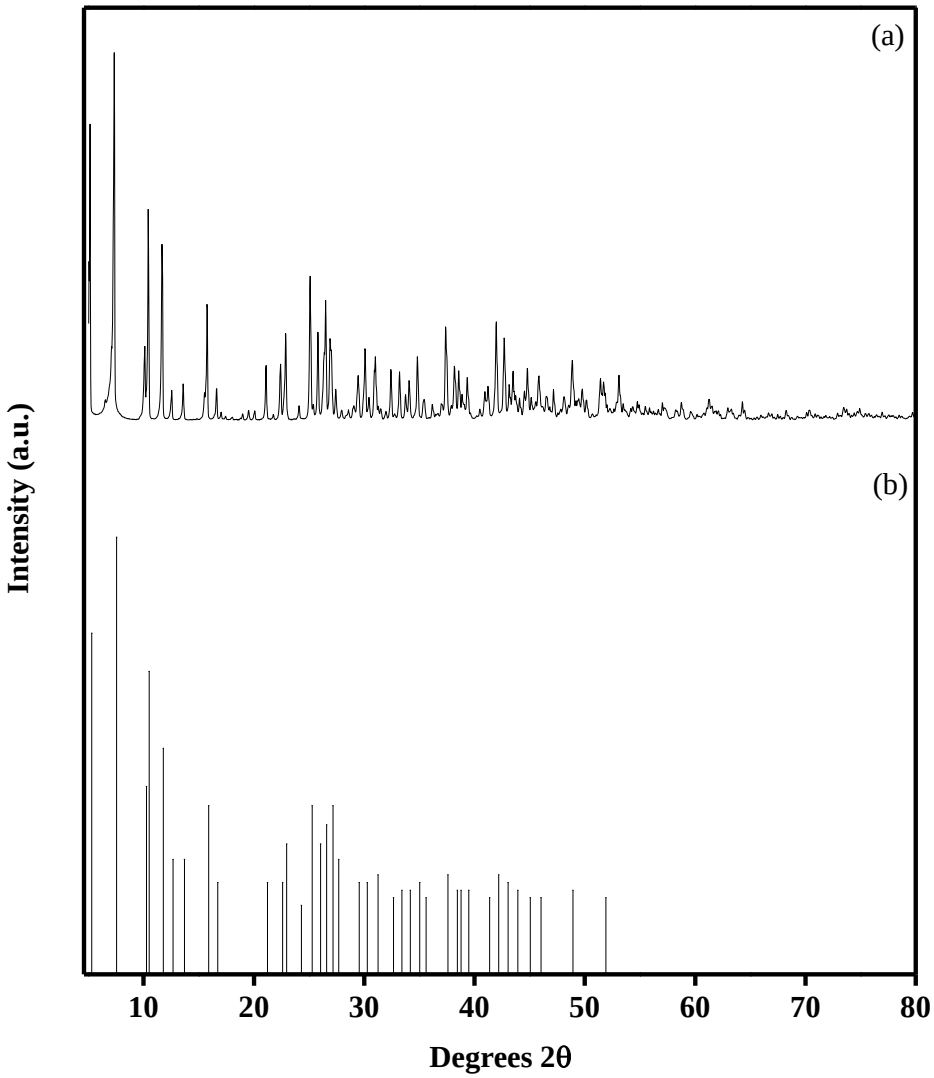

Figure 5.2: (a) XRD pattern for as received calcium acetate hydrate powder. Pattern is in close agreement with (b) calcium acetate hydrate, $Ca(CH_3COO)_2 \cdot 0.5H_2O$, ICDD ref: 00-019-0199 [279]. Full peak data in the appendix, Table A12. Note: Reference provides peak data in the 2θ range 5 - 52°, with Miller indices not provided.

5.2.2. Particle analysis by SEM and TEM

Particle analysis of the as received CaAc powder has been carried out by SEM and TEM, with images and a selected area electron diffraction pattern (SAED) shown in Figures 5.3 and 5.4. Particle size information was obtained by manually measuring the dimensions of 50 particles (imaged by TEM) using Gatan's Digital Micrograph software, Figure 5.5.

Analysis by SEM (Figure 5.3a-c) shows that the as received CaAc powder consists of very large (> 50 μm), elongated and flake-like aggregates of lath shaped primary particles. At high magnification (Figure 5.3c), the aggregate appears disrupted with the presence of much smaller lath shaped particles (typically 1 μm in length) observed on the surface.

Analysis by TEM (Figure 5.4) shows individual lath shaped particles of CaAc, with measurements of 50 individual particles imaged by TEM (Figure 5.5) showing lengths ranging from < 0.5 μm to > 5 μm with the greatest proportion of particles existing in the range 1 - 1.5 μm; aspect ratios varied greatly from 1.3 to 65.4, with an average of 8.1. The selected area electron diffraction (SAED) pattern of a CaAc particle is shown in Figure 5.4c, and no sharp rings are observed. This does not agree with the previous XRD pattern (Figure 5.2) where sharp intense diffraction peaks were observed, indicating a highly crystalline structure. It is assumed that CaAc may have undergone alteration under the electron beam or vacuum of the TEM; but this result is not considered to present any bearing on the remainder of this study.

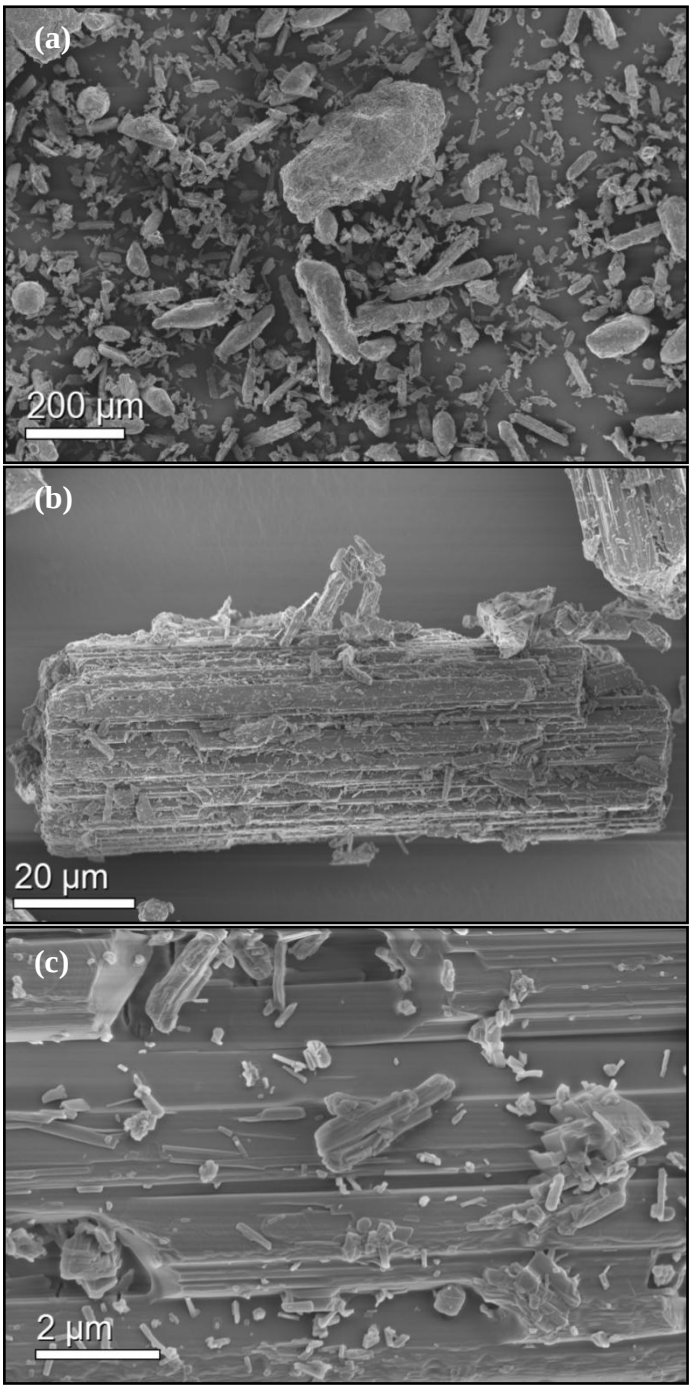

Figure 5.3: (a & b) Low magnification SEM images of as received commercial calcium acetate hydrate showing large (> 50 µm), elongated and flake-like aggregates of lath shaped primary particles and (c) high magnification SEM image of as received commercial calcium acetate hydrate showing smaller lath shaped particles (typically 1 µm in length) observed on the surface of a larger aggregate, (Figure 5.3b).

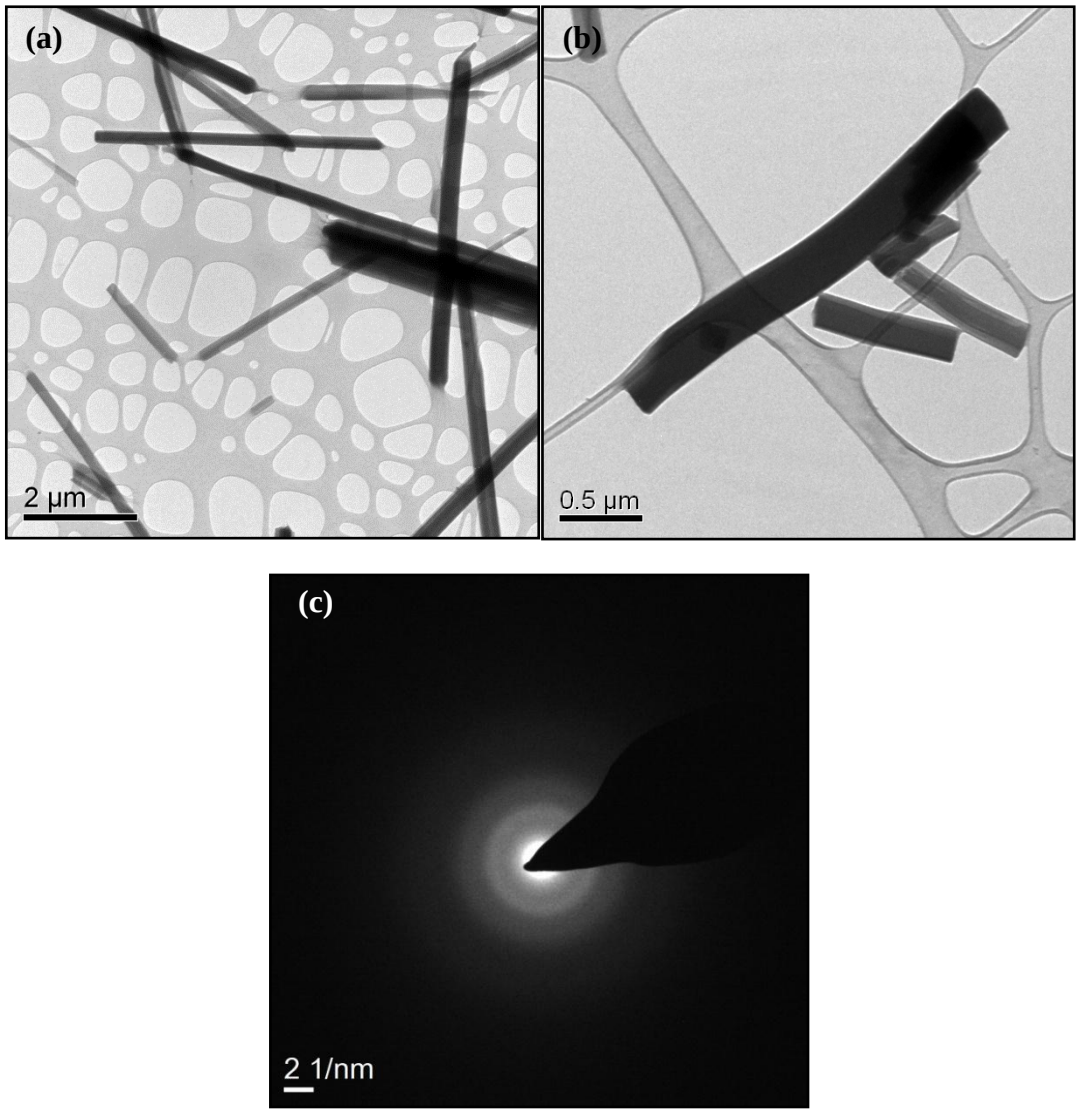

Figure 5.4: (a & b) Bright field TEM images of as received commercial calcium acetate hydrate showing individual lath-shaped primary particles (c) shows selected area diffraction pattern for image (b), no sharp rings may suggest alteration of the material under the electron beam or vacuum of the TEM.

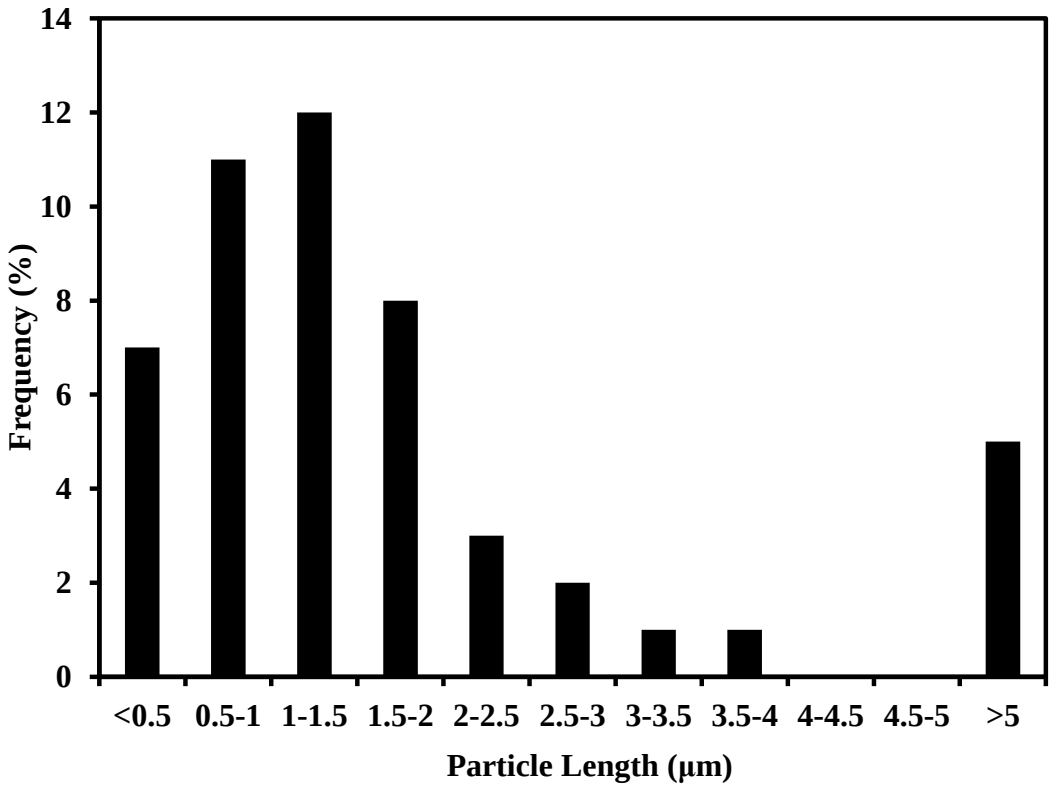

Figure 5.5: Distribution of particle lengths (50 individual particles) measured from TEM images of the as received calcium acetate hydrate powder.

5.3. Thermal decomposition of CaAc analysed by thermogravimetric analysis (TGA), and evolved-gas analysis by Fourier transform infrared spectroscopy (FTIR)

The thermal decomposition and evolved-gas analysis of the as received CaAc has been analysed by a Stanton Redcroft TGH-1000 TGA instrument connected to a Thermo Scientific Nicolet iS10 FTIR spectrometer running OMNIC processing software and fitted with an attenuated total reflection (ATR) accessory. A 15 mg sample of CaAc was decomposed by heating from 20 to 1000 °C at a constant heating rate of 20 °C min^{-1}, under a N_2 atmosphere (50 ml min^{-1}). Figure 5.6 displays TGA data from the decomposition of CaAc in N_2 from 20 - 1000 °C.

Table 5.1 highlights the percentage mass loss across three given temperature ranges; 150 - 240 °C, 400 - 520 °C and 650 - 765 °C. Expected percentage mass loss values are also presented in Table 5.1 for $CaAc{\cdot}0.5H_2O$. FTIR spectra were recorded every 30 seconds (10 °C), and are displayed in Figures 5.7 and 5.8. In the temperature region 150 – 240 °C, where water loss is predicted, no infrared absorption due to evolved gases was detected‡‡.

The data here (Figure 5.6) shows that by 765 °C CaAc has decomposed to CaO with an overall percentage mass loss of 65.5%. The process occurs firstly via an initial two-stage mass loss of water molecules, the first at ~150 - 200 °C, and the second at ~200 - 240 °C, with a total percentage mass loss of 5% (equivalent to a xH_2O molar loss = 0.45) [141]. This is in close agreement with the previous XRD reference pattern which reports $CaAc{\cdot}0.5H_2O$. This process follows the proposed reaction:

‡‡ From discussion with Dr Adrian Cunliffe (Energy Research Institute), this is a common occurrence in hydrated species.

$$Ca(CH_3COO)_2 \cdot 0.45H_2O \rightarrow Ca(CH_3COO)_2 + 0.45H_2O \quad (5.3)$$

Between ~400 - 520 °C, previous work indicates that the dehydrated CaAc breaks down to form calcite ($CaCO_3$) with the release of acetone (C_3H_6O), with a total percentage mass loss of 34.5% between 400 °C and 500 °C [141]. The formation of $CaCO_3$ within this temperature is confirmed by X-ray diffraction in Sections 5.3.1 and 5.4. This decomposition of dehydrated CaAc to calcite and acetone follows the reaction:

$$Ca(CH_3COO)_2 \rightarrow CaCO_3 + C_3H_6O \quad (5.4)$$

This decomposition to the calcium carbonate phase occurs via a two-step process and this has previously been attributed to the melting of the calcium acetate [280]. Melting subsequently slows down the rate of decomposition and occurs at ~440 °C on Figure 5.6. Figure 5.7a highlights the FTIR spectra for absorption by acetone, detected in the temperature region 415 – 520 °C. Experimental data (red) and best-matched reference data (purple) for acetone absorption, collected using OMNIC processing software, are shown. Figure 5.7b shows the changing intensity of the strongest peak due to carbonyl (C=O) stretching mode, commonly associated with acetone absorption (in the wavenumber region 1650 – 1850 cm^{-1}), with the progression of CaAc decomposition from 20 – 1000 °C in N_2 [281]. It is observed that absorbance due to the carbonyl group of acetone first begins at 415 °C, with the peak reaching a maxima at 455 °C. A second, less intense, maxima is also observed at 498 °C, with no further absorbance beyond 520 °C. This loss of acetone coincides with the significant weight loss observed by TGA (Figure 5.6) in the temperature region 400 – 500 °C. Despite TGA showing a two-step decomposition in this temperature region, only infrared absorption due to acetone was detected by FTIR analysis of evolved gases. This supports the previous work suggesting that this change in decomposition rate is cause by melting of the calcium acetate [280].

The calcium carbonate then decomposes to form calcium oxide from ~650 °C to completion at ~765 °C [141]:

$$CaCO_3 \rightarrow CaO + CO_2 \quad (5.5)$$

Figure 5.8a highlights the FTIR spectra associated with carbon dioxide absorption, detected in the region 600 – 800 °C. Experimental data (red) and best-matched reference data (purple) for CO_2 absorption, collected using OMNIC processing software are shown. Figure 5.8b shows the changing intensity of the strongest peak due to the antisymmetric stretching mode of carbonate (C-O), commonly associated with CO_2 absorption (in the wavenumber region 2300 – 2400 cm^{-1}), with the progression of CaAc decomposition from 20 – 1000 °C in N_2 [282].

Significant absorbance due to the carbonate stretching mode is first observed at 600 °C, with the peak reaching a maxima at 775 °C. A sharp decrease is seen beyond this temperature with no carbonate absorption detected after 800 °C; from the TGA curve (Figure 5.6), this suggests the full decomposition of the intermediate $CaCO_3$ phase to CaO, which is subsequently confirmed by X-ray diffraction in Sections 5.3.1 and 5.4. Only infrared absorption due to the CO_2 carbonate group was detected in this temperature region.

Overall, the data presented here are in good agreement with previous reports for this material [141, 275, 278].

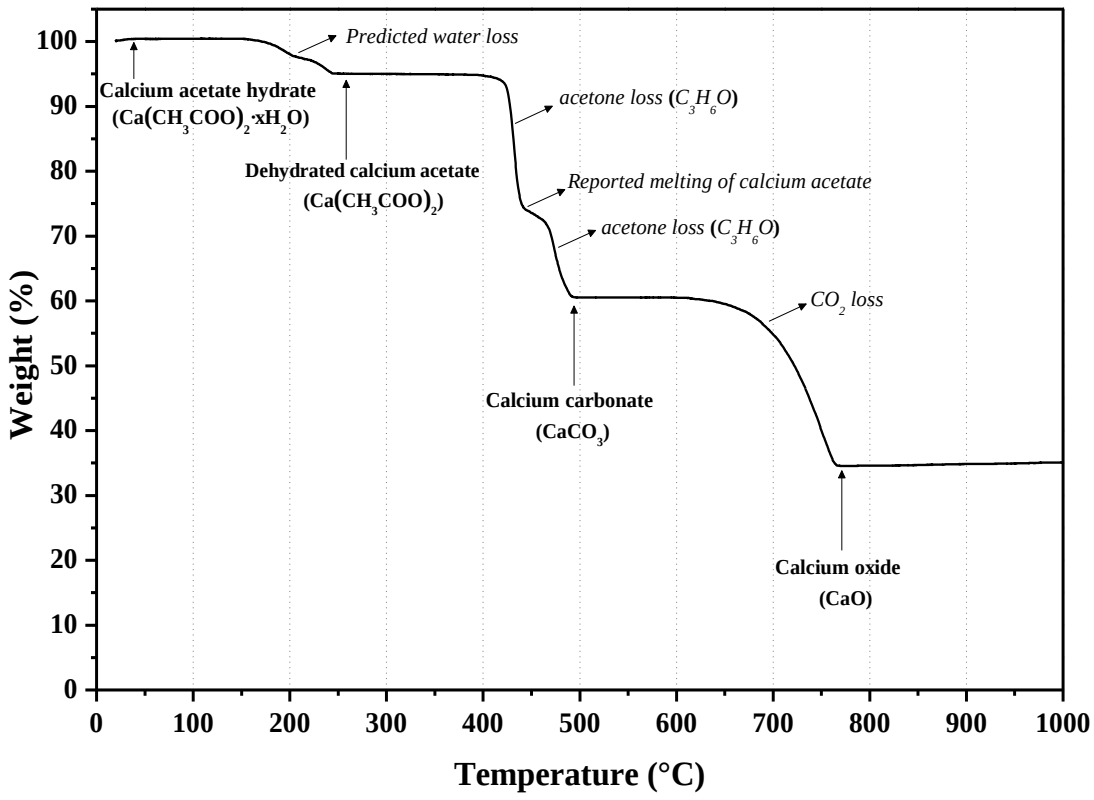

Figure 5.6: TGA data for the thermal decomposition of calcium acetate hydrate from 20 – 1000 °C in N_2. Temperature ramp = 20 °C min^{-1}.

Table 5.1: Percentage mass loss for thermal decomposition of CaAc by TGA, with expected percentage mass loss values for $CaAc \cdot 0.5H_2O$.

Temp (°C)	Measured mass loss (%)	Expected mass loss (%) for $CaAc \cdot 0.5H_2O$
~150-240	5.0	5.7
~400-500	34.5	34.7
~650-765	26.0	26.3
Total Loss =	65.5	66.7

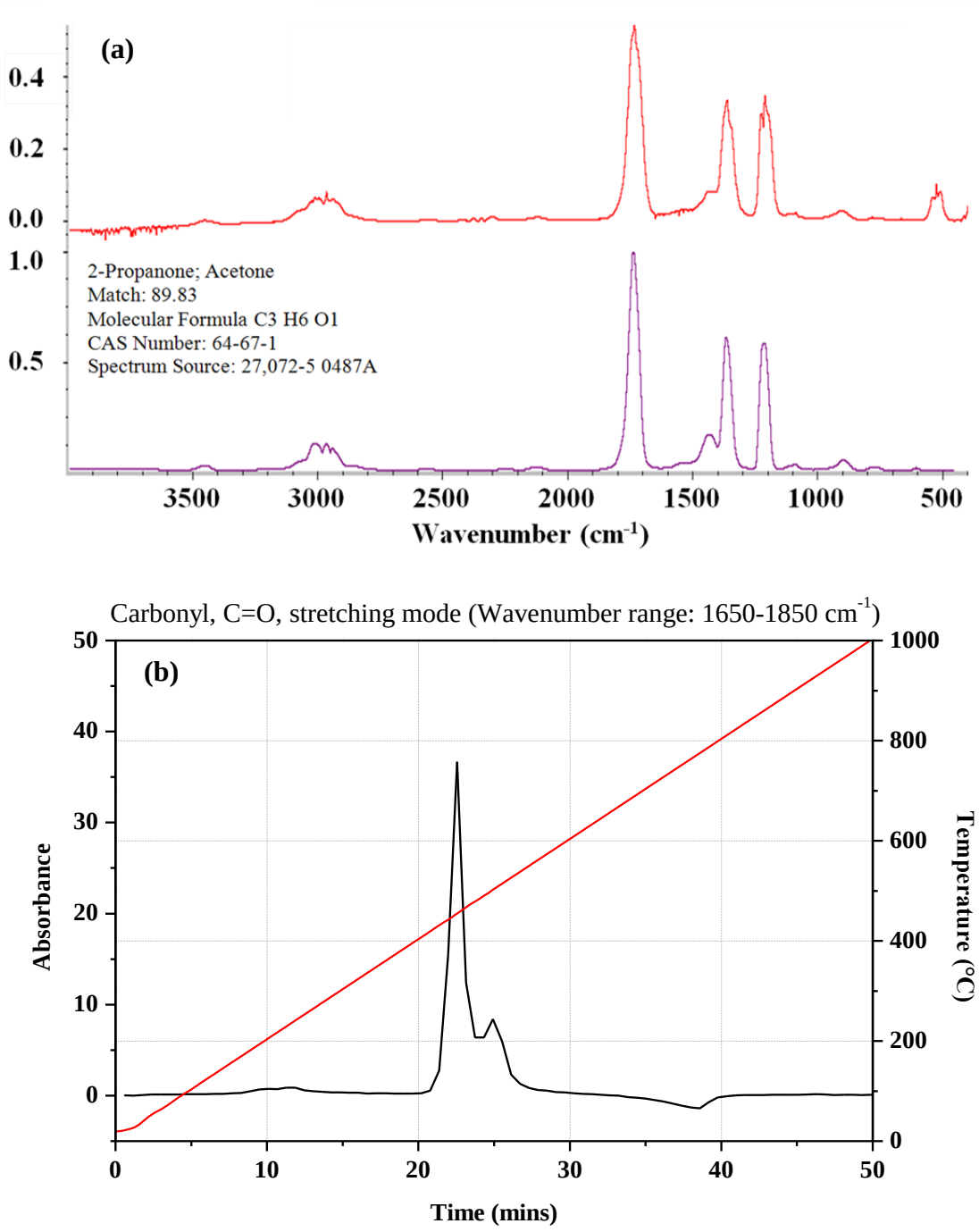

Figure 5.7: TGA/FTIR data for gases evolved during the decomposition of CaAc with (a) pattern (red) assigned to acetone, with reference pattern for acetone (purple) and (b) development of the most intense carbonyl group peak due to acetone absorbance, in the region 1650-1850 cm^{-1}, with decomposition of CaAc from 20 – 1000 °C in N_2.

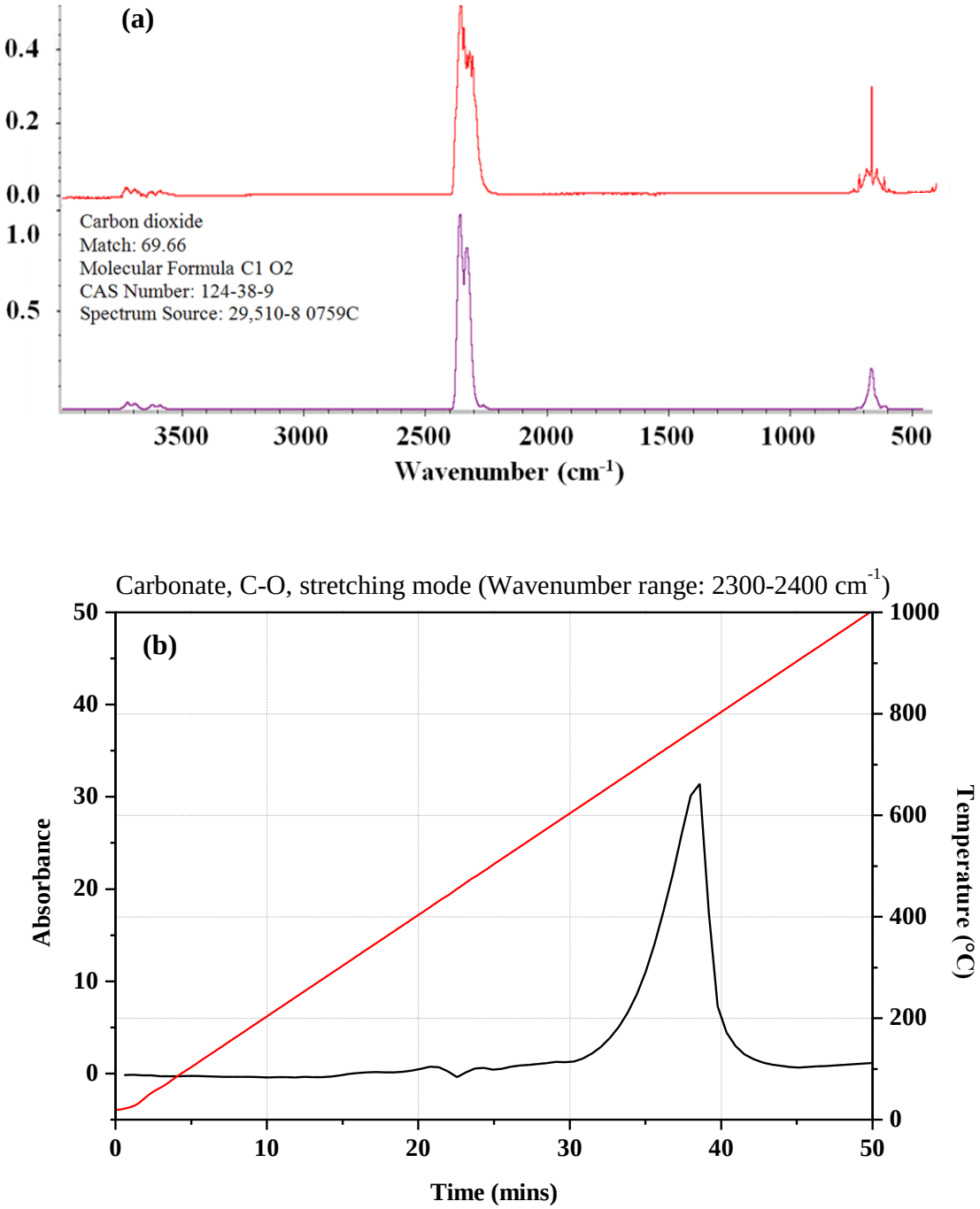

Figure 5.8: TGA/FTIR data for gases evolved during the decomposition of CaAc with (a) pattern (red) assigned to carbon dioxide (CO_2), with reference pattern (purple) and (b) development of the most intense CO_2 group peak, in the region 2300-2400 cm^{-1}, with decomposition of CaAc from 20 – 1000 °C in N_2.

5.3.1. XRD & TEM analysis

Analysis of the CaO, derived from TGA decomposition of CaAc at 800 °C, has been carried out by XRD and TEM. An additional sample has also been prepared by the TGA decomposition of CaAc up to at 500 °C (following the previously outlined TGA conditions), which will be also be analysed by XRD and TEM. Figure 5.9 and Figure 5.10 show XRD patterns of CaAc samples decomposed by TGA (at 20 °C min^{-1} in N_2) up to 500 °C and 800 °C respectively with no dwell time. Furnace cooling is carried out by an external Shimadzu BLW-50 cooling blower. The N_2 supply is not removed until the chamber is cool and opened for removal of the sample. Figure 5.9 shows the presence of two polymorphic forms of calcium carbonate; calcite and vaterite, formed upon decomposition of CaAc at 500 °C by TGA. Higher intensity diffraction peaks were observed to calcite, suggesting a dominant phase here, with only low intensity peaks observed due to vaterite. Calcite exhibits a rhombohedral crystal structure ($a = b = 4.99$ Å, $c = 17.06$ Å) and is recognised as more thermodynamically stable at room temperature. Vaterite exhibits a hexagonal crystal structure ($a = b = 4.13$ Å, $c = 8.49$ Å) and is considered to be a metastable polymorph of calcium carbonate which can often contain disordered carbonate molecules which lead to partial occupancy of carbonate in the structure [283-285]. Vaterite is also seen as a precursor of calcite, which, when initially crystallised from amorphous calcium carbonate, will transform to calcite by a dissolution and reprecipitation mechanism [286]. A report by de Leeuw and Parker explains that vaterite can exist in different morphologies including spheres comprising of needle-like units, ellipsoids or disklike crystals [283].

After decomposition of CaAc at 800 °C by TGA, peaks due to CaO were mainly observed in the XRD pattern (Figure 5.10), with also small broad peaks due

to calcium hydroxide ($Ca(OH)_2$), and a single peak (at $2\theta = 29.6°$) indexed to the 100% peak of calcite ($CaCO_3$). The $Ca(OH)_2$ and calcite peaks can be attributed to the reactive nature of CaO on exposure to air (atmospheric moisture and CO_2), and this is most likely (despite care during handling) during storage, and unavoidable during sample preparation for analysis [287]. Such rapid hydration and carbonation, of the CaO sorbent can be attributed to the large pore volume and high surface area of the nano particulate CaO product formed by the decomposition of calcium acetate hydrate, properties which similarly make CaO, produced by decomposition of CaAc, a superior powder sorbent (in relation to CaO formed by alternate calcium precursors) for CO_2 capture [123, 128, 275, 278].

Figure 5.12 displays TEM images that show the morphologies of the products formed by TGA decomposition of CaAc at 500 °C and 800 °C (with immediate cooling upon reaching desired temperatures).

The products of TGA decomposition of CaAc at 500 °C (which contains both vaterite and calcite phases from XRD, Figure 5.9) are shown by bright field TEM images and SAED patterns in Figures 5.11 and 5.12. Figure 5.11a displays polycrystalline vaterite, which is observed to consist of a branched network of long needle-like particles, reaching up ~1 μm in length. The corresponding SAED pattern (Figure 5.11b) confirms only a vaterite phase, with no diffraction spots due to calcite observed.

The calcite form of calcium carbonate, also produced by CaAc decomposition at 500 °C by TGA, is shown in Figure 5.11c, with the calcite phase confirmed by the corresponding SAED pattern in Figure 5.11d. No diffraction spots due to vaterite were observed. Calcite does not show the same branched structure as the vaterite; the material is seen to exist as large thin sheet-like structures. A small amount of

porosity within the sheets was evident which may be due to loss of CO_2 or may be a result of air trapped during recrystallisation from the melting calcium acetate, which occurs at 440 °C (Figure 5.6) [280].

The product of TGA decomposition of CaAc at 800 °C (which, displayed mainly CaO, with small amounts of $Ca(OH)_2$ and calcite, by XRD, Figure 5.10) is shown by a bright field TEM image and SAED pattern in Figure 5.12a-c. Figure 5.12a shows highly sintered agglomerates of fine plate-like particles (typical size < 150 nm); selected area electron diffraction (Figure 5.12b) confirms diffraction due to CaO, $Ca(OH)_2$ and $CaCO_3$. Figure 5.12c shows the presence of nanopores within the particles, these are typically < 10 nm. Individual particles after TGA decomposition at 800 °C are smaller than those formed after decomposition at 500 °C, however there is a significant amount of sintering evident.

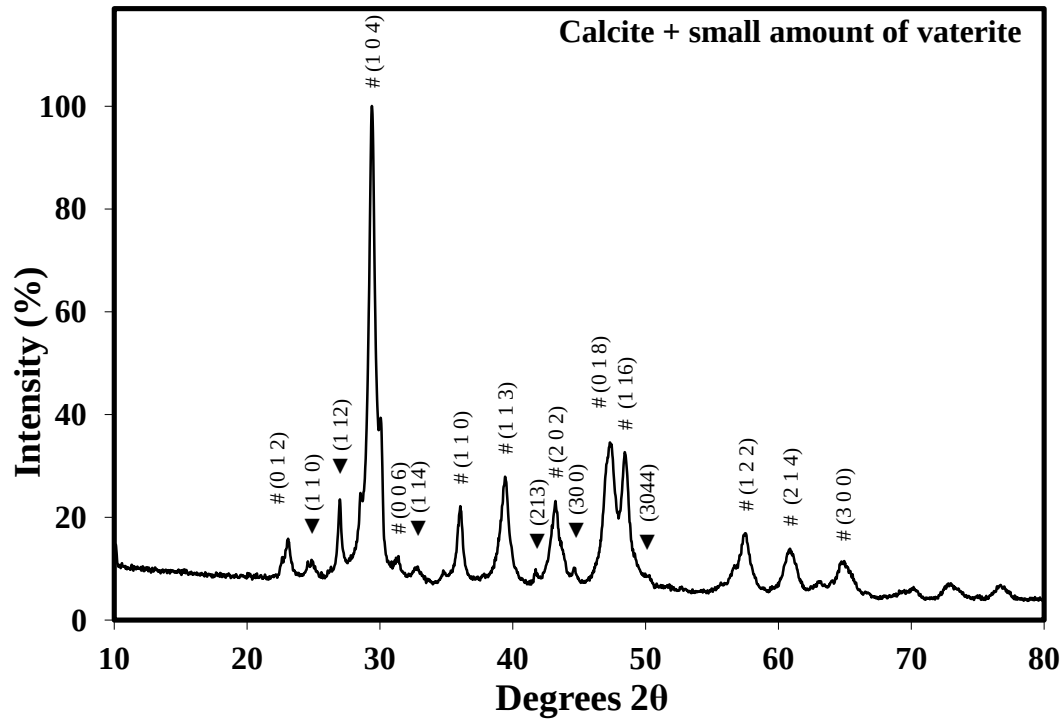

Figure 5.9: XRD pattern for CaAc sample decomposed by TGA from room temperature to 500 °C (at 20 °C min^{-1}) with no dwell time. '#' denotes indexed peaks of calcite, $CaCO_3$, ICDD ref: 00-005-0586 [221]. '▼' denotes indexed peaks of vaterite, $CaCO_3$, ICDD ref: 00-033-0268 [288]. Full peak list available in the appendix, Table A13.

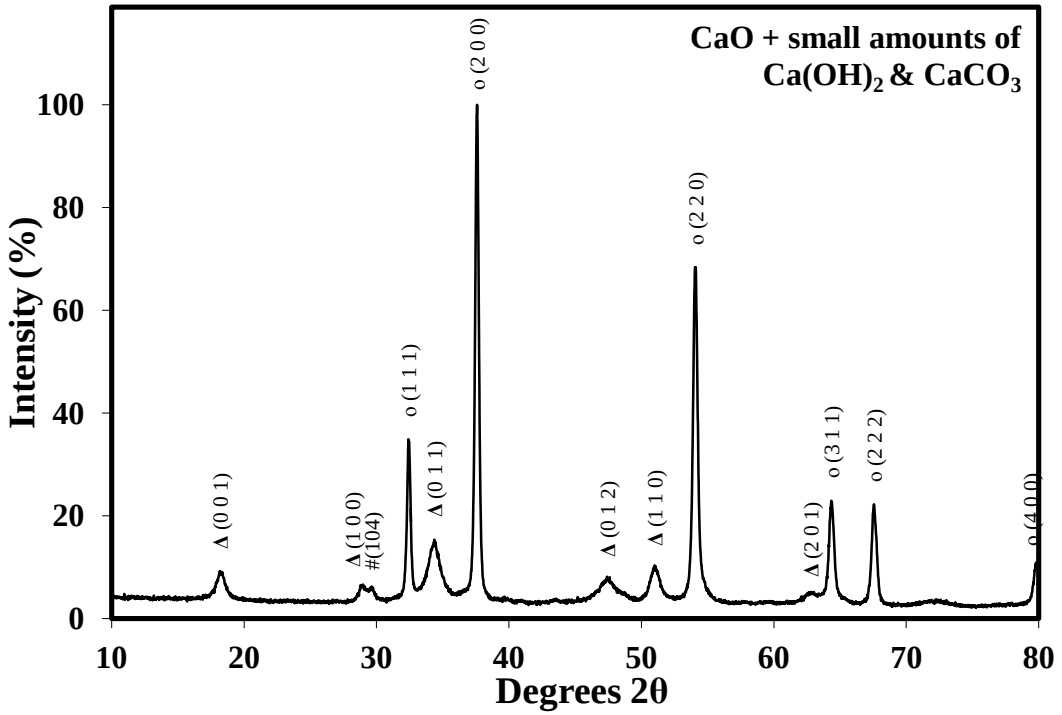

Figure 5.10: XRD pattern for CaAc sample decomposed by TGA from room temperature to 800 °C (at 20 °C min^{-1}) with no dwell time. '○' denotes indexed peaks of calcium oxide, CaO, ICDD ref: 04-003-7161 [226]. 'Δ' denotes indexed peaks of calcium hydroxide $Ca(OH)_2$, ICDD ref: 01-084-1263 [289]. '#' denotes indexed peaks of calcite, $CaCO_3$, ICDD ref: 00-005-0586 [221]. Full peak list available in the appendix, Table A14.

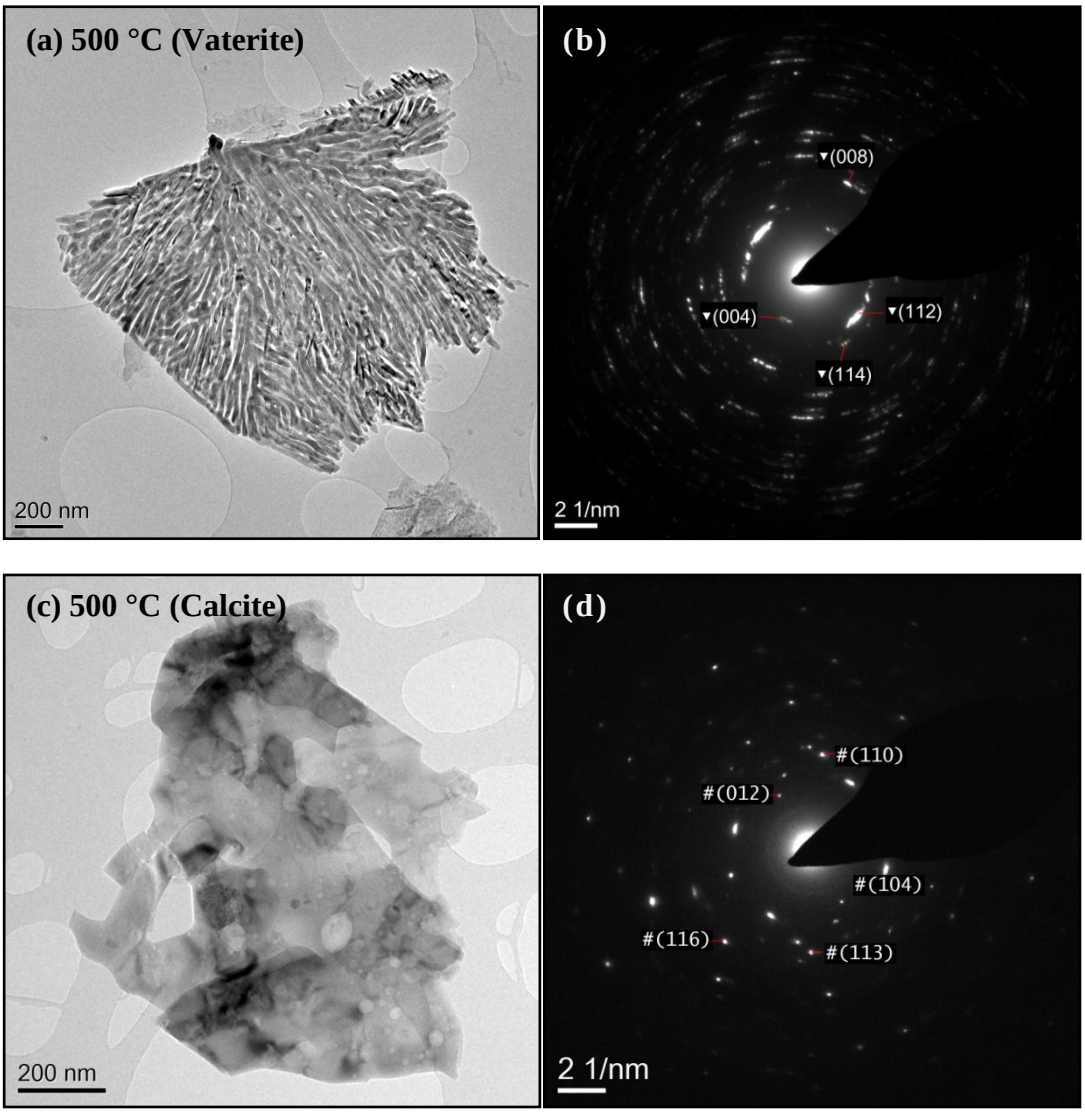

Figure 5.11: Bright field TEM images and SAED patterns of (a & b) Vaterite $CaCO_3$ '▼' (ICDD ref: 00-033-0268) [288]) and (c & d) Calcite $CaCO_3$ '#' (ICDD ref: 00-005-0586 [221]) both formed from by TGA decomposition of CaAc at 500 °C. Labels of SAED pattern correspond to spots on diffraction rings.

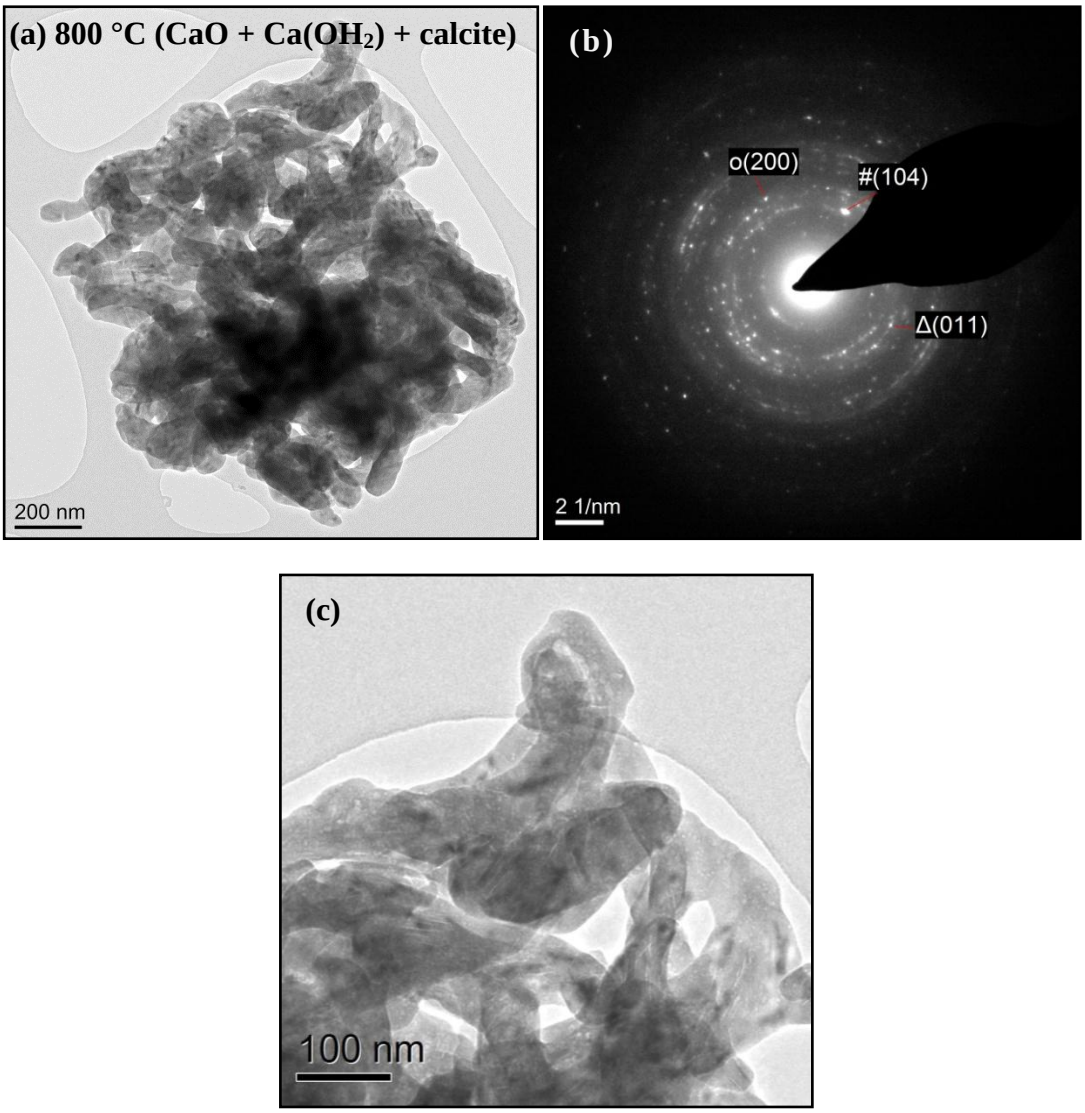

Figure 5.12: (a) Bright field TEM image and (b) corresponding SAED pattern of the CaO formed by decomposition of CaAc by TGA at 800 °C. SAED pattern shows diffraction rings due to CaO 'o' (ICDD ref: 04-003-7161 [226]), $Ca(OH)_2$ 'Δ' (ICDD ref: 01-084-1263 [289]) and calcite $CaCO_3$ '#' (ICDD ref: 00-005-0586 [221]), labels correspond to spots on diffraction rings. (c) shows higher magnification image of (a) highlighting presence of nanopores within the particles.

5.4. *In-situ* hot-stage X-ray diffraction

The decomposition process of CaAc has also been studied using a Philips/PANalytical X'pert diffractometer fitted with an *in-situ* heating stage. A sample of CaAc was heated at a rate of 20 °C min^{-1} in 100 °C intervals, up to 800 °C, and was held for ~1 hour at each temperature (100, 200, 300, 400, 500, 600, 700 and 800 °C) to allow for X-ray analysis. X-ray diffraction patterns are presented in Figure 5.13 and it must firstly be noted that all diffraction patterns contain a low-intensity peak at °2θ = 7.06, which is a recognised peak due to X-ray scatter from the oven-stage of the X-ray diffractometer[§§].

The XRD data here (Figure 5.13) show that the calcium acetate hydrate firstly decomposes into a poorly-crystalline compound at 200 °C. Some detectable peaks in the low 2θ region (< 15° 2θ) can be assigned to crystalline CaAc (ICDD ref: 00-019-0199 [279]) and dehydrated CaAc, $Ca(CH_3COO)_2$ (ICDD ref: 00-019-0198 [279]), with the remainder of the XRD pattern showing no identifiable reflections. Overall this suggests an incomplete breakdown of the CaAc phase into an amorphous compound.

After decomposition at 300 °C, the XRD pattern can be assigned to dehydrated CaAc, (ICDD ref: 00-019-0198 [279]), where the significant difference, in comparison to the as received CaAc, is observed in the region of interplanar lattice spacing's of 5 - 10° (2θ). This is most likely due to the loss in the amount of water co-ordinated to the calcium acetate molecules [278].

Subsequent decomposition at 400 °C leads to the formation of calcite, $CaCO_3$ (ICDD ref: 00-005-0586 [221]). The vaterite phase, previously observed by CaAc

[§§] From discussion with Dr Tim Comyn (Institute for Materials Research).

decomposition by TGA, was not detected here, and this is likely due to the extended temperature hold that allows for X-ray analysis, converting any vaterite phase into the more stable calcite phase.

After decomposition at 600 °C a mixture of calcite and CaO (ICDD ref: 04-003-7161 [226]) is observed, with the higher intensity peaks due to the calcite phase and low intensity peaks due to CaO, this indicates the start of the breakdown of calcite. After decomposition at 700 °C only peaks due to CaO are observed, indicating full decomposition of the intermediate calcite phase to CaO. No change from this pure CaO phase is observed after decomposition at 800 °C.

There is a greater time for phase decomposition and formation under the hot-stage XRD heating conditions, and subsequently phases such as $CaCO_3$ and CaO are formed at slightly lower temperatures than those produced with a faster heating rate, by TGA, overall indicating a kinetically limited transformation. A pure calcite phase is observed after decomposition at 400 °C in the hot-stage XRD whereas, by TGA, full decomposition to the calcite phase is complete at 520 °C. Similarly, single phase CaO is observed after decomposition at 700 °C in the hot-stage XRD whereas, by TGA, full decomposition to the CaO phase is complete at 765 °C.

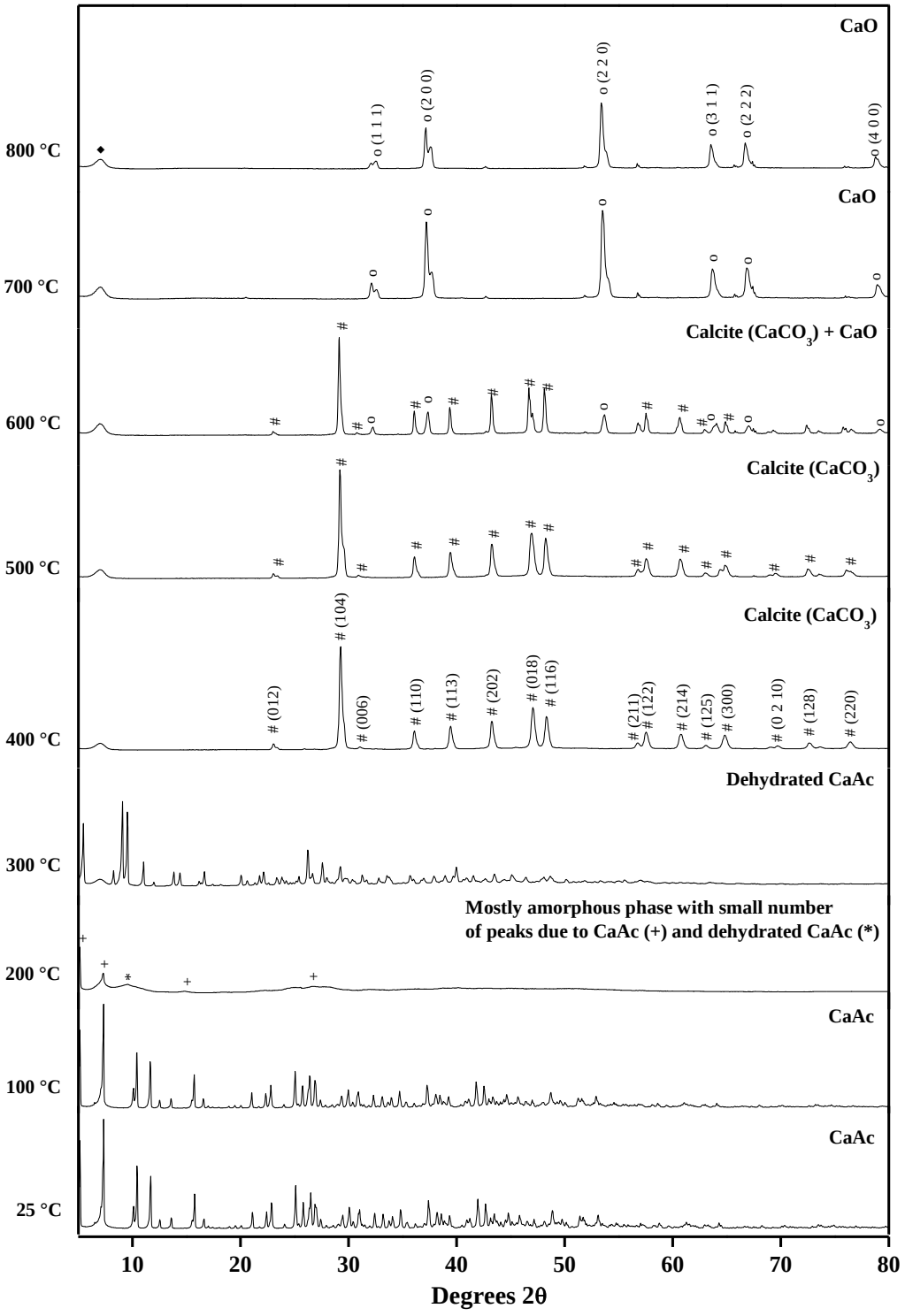

Figure 5.13: Hot-stage XRD patterns for decomposition of calcium acetate hydrate in air. Patterns at 25 °C and 100 °C are in close agreement with calcium acetate hydrate ($Ca(CH_3COO)_2 \cdot 0.5H_2O$), ICDD ref: 00-019-0199 [279]. Pattern at 200 °C shows a small number of peaks that can be assigned to crystalline calcium acetate hydrate '+' ($Ca(CH_3COO)_2 \cdot 0.5H_2O$), ICDD ref: 00-019-0199 [279] and a single peak due to dehydrated calcium acetate '*' ($Ca(CH_3COO)_2$), ICDD ref: 00-019-0198 [279]. Pattern at 300 °C is in close agreement with dehydrated calcium acetate ($Ca(CH_3COO)_2$), ICDD ref: 00-019-0198 [279]. Patterns at 400 °C and 500 °C, and peaks labelled 'C' at 600 °C are indexed to calcite, ($CaCO_3$), ICDD ref: 00-005-0586 [221]. Patterns at 700 and 800 °C, and peaks labelled 'o' at 600 °C are indexed to calcium oxide (CaO) ICDD ref: 04-003-7161 [226]. Peak at 7.06 °2θ, labelled '♦', corresponds to a recognised instrumental peak from the XRD-oven apparatus (from discussion with Dr T Comyn). Full peak list available in the appendix Tables A15 - A22.

5.4.1. TEM analysis

To reproduce the stages of CaAc decomposition observed at various temperatures by hot-stage XRD, three samples of CaAc have been decomposed in a furnace by heating from room temperatures to 200 °C, 500 °C and 800 °C (at 20 °C min^{-1}, in air) respectively, and held for 1 hour. Samples were immediately removed from the furnace after 1 hour and left to cool. These samples were then analysed by TEM with data shown in Figure 5.14a-f.

At 200 °C (Figure 5.14a), observed particles appear as broken laths of CaAc (typical length = 1-5 μm). Broad rings shown by SAED (Figure 5.14b) suggest an amorphous phase, which is in agreement with the previous hot-stage XRD pattern (Figure 5.13).

At 500 °C (Figure 5.14c and d), calcite ($CaCO_3$) is observed, with no indication of vaterite previously observed following TGA decomposition (Figure 5.12a). Particles display a similar sheet like morphology to the calcite by TGA decomposition (Figure 5.12c), with a small amount of porosity also visible, which may be due to release of CO_2. The sheet structure here appears more broken than that shown by TGA decomposition, with smaller particles evident (typically < 200 nm).

At 800 °C (Figure 5.14c) CaO is observed, with $Ca(OH)_2$ and calcite ($CaCO_3$). Particles displayed larger and more heavily sintered agglomerates in relation to the CaO formed by TGA decomposition (Figure 5.12e). There is also now a significant amount of porosity evident, which was not observed in the CaO formed by TGA decomposition. This may be due to a higher amount of sintering entrapping CO_2 or air between the particles.

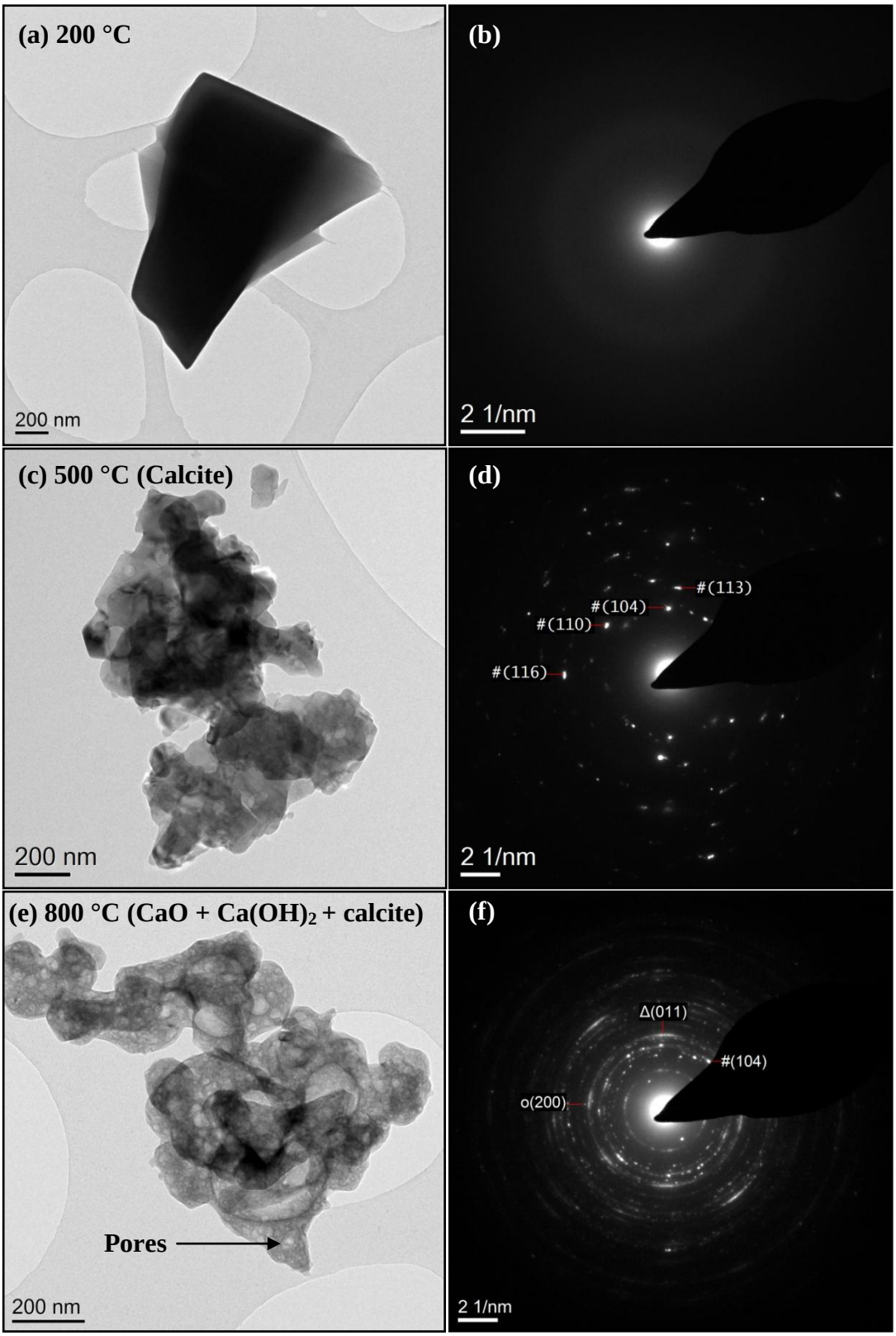

Figure 5.14: Bright field TEM images of and SAED patterns of (a & b) CaAc heated to 200 °C held for 1 hour (c & d) CaAc heated to 500 °C (Calcite, $CaCO_3$) and held for 1 hour, and (e & f) CaAc heated to 800 °C (CaO) and held for 1 hour, SAED (f) confirms CaO phase 'o', with rings due to $Ca(OH)_2$ 'Δ' and $CaCO_3$ '#'.

5.5. CO_2 sequestration using a CaO sorbent produced by decomposition of CaAc

5.5.1. Maximum CO_2 uptake capacity of CaO sorbents

The CO_2 uptake capability of CaO produced by decomposition of calcium acetate hydrate, was measured by thermogravimetric analysis (TGA). A sample of CaAc was decomposed in a TGA under an N_2 atmosphere (rotameter controlled flow rate = 50 ml min^{-1}) to 800 °C (at 20 °C min^{-1}), replicating the conditions of Section 5.3. Upon reaching 800 °C, the chamber temperature was dropped to 650 °C and the gas stream was switched to CO_2 at a rotameter controlled flow rate of 50 ml min^{-1} (regulator pressure of the CO_2 cylinder = 2 bar). The carbonation step was held for 15 minutes, before the gas stream was switched back to N_2 gas, while the furnace cooled to room temperature.

Results of this test are shown in Figure 5.15 and it is observed that the uptake of CO_2 by CaO occurs by a two-stage process: the first is a rapid process, following a linear growth rate that suggests no solid-state diffusion involving particle growth; a 50% mass increase due to conversion of CaO to $CaCO_3$ occurred in 28 seconds. This linear region is thought to be a surface reaction between the solid CaO nanoparticles, and CO_2 gas.

The second phase of carbonation at 650 °C, showed a non-linear mass increase from 50 to 71.73%, due to further conversion of CaO to $CaCO_3$. This second phase of carbonation proceeds as a slower, solid-state diffusion controlled process whereby CaO conversion continues by CO_2 diffusion through the growing product layer [140]. The overall percentage mass increase of CaO to $CaCO_3$ can be represented in terms of a molar conversion ratio χ, where;

$$\chi = \frac{\text{mol } CO_2 \text{ uptake}}{\text{starting mol CaO}} \quad (5.6)$$

Thus a total molar conversion ratio of 0.92 was obtained after 15 minutes of carbonation at 650 °C. This result is in good agreement with a previous report on the uptake of CO_2 by a CaO nanopowder sorbent produced by the thermal decomposition of CaAc, where Lu *et al* (2006) observed a 90% conversion of CaO to $CaCO_3$ after 10 minutes of carbonation (at various carbonation temperatures between 550-800 °C) [128].

The previous sample was decomposed by TGA at 800 °C with zero dwell time, and so to observe whether a prolonged decomposition time hold had an effect on the overall carbonation conversion (due to possible sintering), a second sample was analysed and held at 800 °C for 1 hour prior to carbonation for a further 15 minutes. These data are displayed in Figure 5.16 and show only a slightly smaller overall percentage mass conversion of CaO to $CaCO_3$, of 71.6%, with a total molar conversion ratio, χ, of 0.91 after 15 minutes of carbonation. The kinetics of the carbonation reaction was comparable to the previous sample (with a zero decomposition dwell time at 800 °C) and this unexpected result suggests that the particle sintering observed with a calcination temperature hold at 800 °C (Figure 5.14e), has no effect on the overall performance of the sorbent for the subsequent carbonation step at 650 °C. Henceforth all subsequent carbonation experiments do not utilise a hold time for calcination.

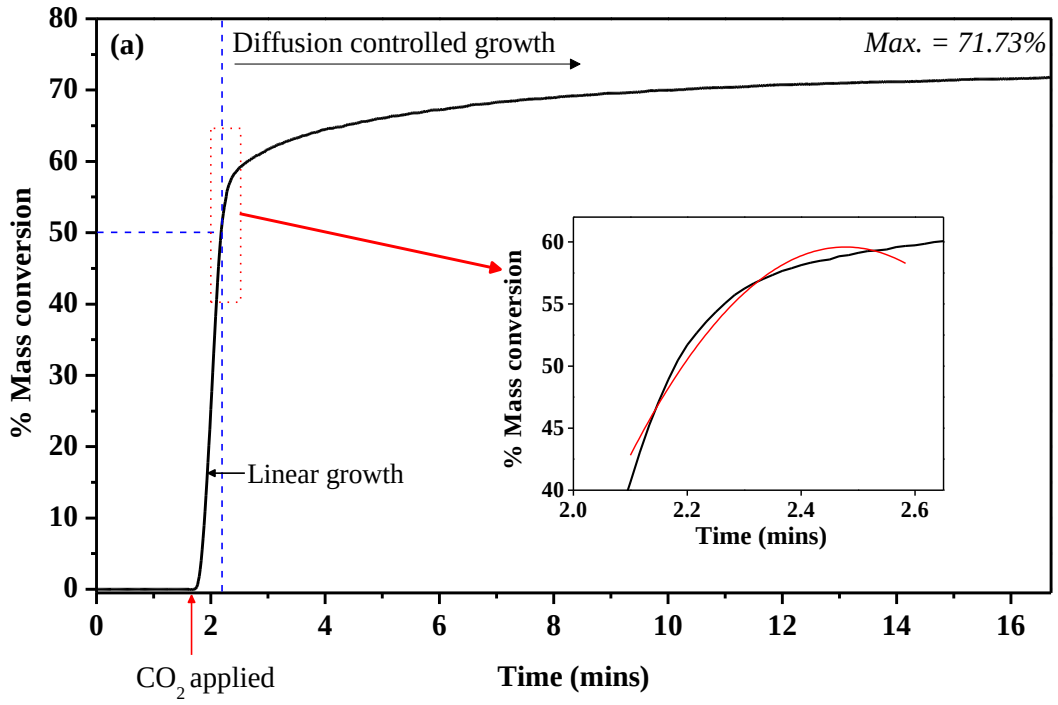

Figure 5.15: CO_2 uptake of CaO (from CaAc) at 650 °C for 15 minutes by TGA. Starting mass = 6.08 g (starting mass% = 0). Final mass = 10.45 g (final CaO to $CaCO_3$ mass conversion% = 71.73). CaO formed by thermal decomposition of CaAc at 800 °C, in N_2, (by TGA) with no dwell time; chamber temperature was then dropped to 650 °C, and CO_2 gas applied for 15 minutes. Insert shows best polynomial fit to curved region of graph (start of solid-state diffusion controlled growth)

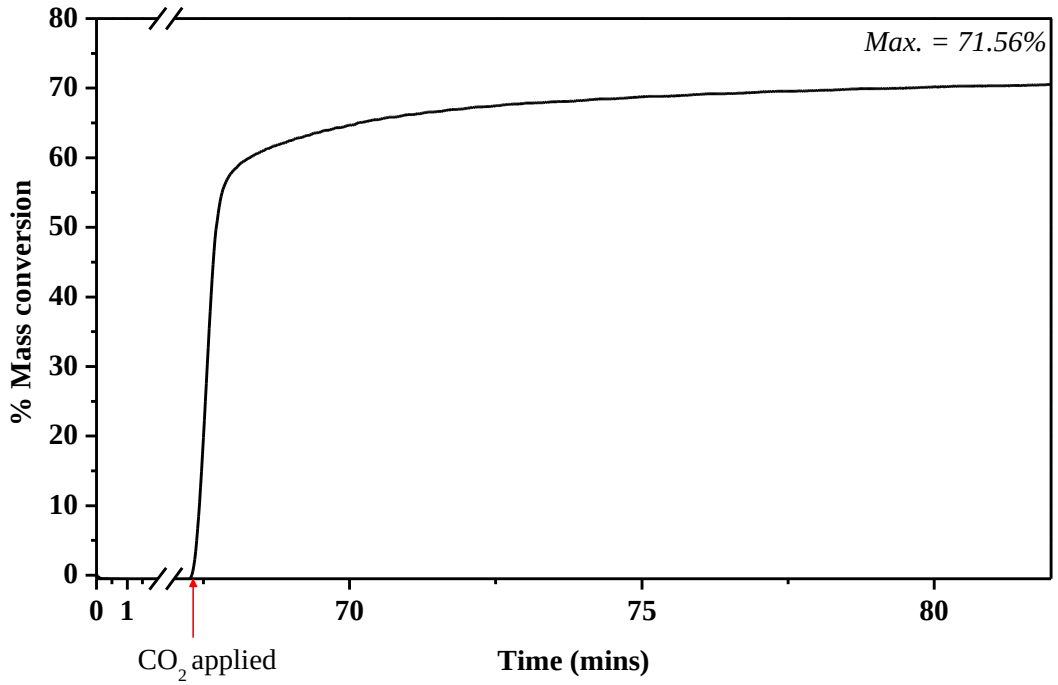

Figure 5.16: CO_2 uptake of CaO at 650 °C for 15 minutes by TGA. Starting mass = 6.39 g. Final mass = 10.96 g (final CaO to $CaCO_3$ mass conversion% = 71.56). CaO formed by thermal decomposition of CaAc at 800 °C, in N_2, (by TGA) with a dwell time of 60 minutes; chamber temperature was then dropped to 650 °C and CO_2 gas applied for 15 minutes.

Analysis of the final carbonated product (Figure 5.15) has been carried out by XRD, SEM and TEM. Figure 5.17 displays the XRD pattern for the carbonated CaO sorbent, with data showing diffraction peaks due to calcite, $CaCO_3$ (ICDD ref: 00-005-0586 [221]) and secondary peaks due to CaO (ICDD ref: 04-003-7161 [226]), confirming an incomplete carbonation at 650 °C for 15 minutes (χ = 0.91). Diffraction peaks for both calcite and CaO are sharp, suggesting good crystallinity.

From SEM analysis (Figures 5.18 - 5.20), the carbonated product appears as large, micron-sized agglomerates that are comprised of well sintered polygonal components (typically > 200 nm) with many particle boundaries meeting at equilibrium angles i.e. 120°. Figure 5.20a shows an SEM image of the initial CaO sorbent produced by the thermal decomposition of CaAc at 800 °C by TGA, with Figure 5.20b showing the sorbent after 15 minutes of carbonation at 650 °C, at the same scale. The CaO sorbent (Figure 5.20a) shows small (< 200 nm) particles which appear lightly sintered, there are also several large pores (typically > 200 nm) observed within the structure. After carbonation at 650 °C (Figure 5.20b), a dense structure consisting of larger (> 200 nm) polygonal particles is observed, with no major porosity. Although not measured by BET analysis (due to small sample sizes produced by TGA), the particle surface area observed by SEM images is significantly decreased upon carbonation.

Overall growth of the individual carbonated particles appears limited by a large amount of particle densification. From TGA data (Figure 5.15), carbonation does not appear to completely stop after 15 minutes of carbonation, suggesting that CO_2 gas is penetrating through this product layer and that there remains unreacted CaO sorbent with the structure, as was confirmed by XRD (Figure 5.17).

Analysis by bright field TEM imaging and SAED (Figure 5.21b) shows the sintered particles are composed of crystals of calcite; SAED did not detect CaO in this instance despite previous detection, in the bulk material, by XRD (Figure 5.17).

Previous work has solely attributed the loss of CO_2 capture capacity of CaO sorbents to the particle sintering of the sorbent during calcination (decarbonation) [136], however we observe here significant particle densification due to the crystal growth of calcite during carbonation, and therefore a loss of particle surface area which may also contribute to the incomplete conversion of CaO to $CaCO_3$.

The formation of a carbonate product layer upon carbonation has previously been studied using micro-sized CaO sorbents; Mess *et al* (1999) described a recrystallised product layer of sintered polygonal crystals of $CaCO_3$ with a uniform thickness [290]. Abanades and Alvarez (2003) additionally suggest that the carbonation reaction stops due to lack of useful porosity for $CaCO_3$ to grow into, rather than the sealing of the outer product layer by the sintered $CaCO_3$ particles, a result which would be expected due to lattice expansion upon carbonation, with a decrease in density from CaO (ρ = 3.35 g cm^{-3}) to $CaCO_3$ (ρ = 2.71 g cm^{-3}) [147].

The carbonation of a nano-sized CaO sorbent has not been comprehensively studied and from TEM analysis here (Figure 5.21) a product layer is not observed as $CaCO_3$ crystals show no detection of CaO by SAED (Figure 5.21b), suggesting carbonation has extended to the core of the particles. The densification of $CaCO_3$ during carbonation may provide an additional factor that affects the overall CO_2 capture capability and regenerability of CaO nano-sorbents used in multi-cycle CO_2 capture.

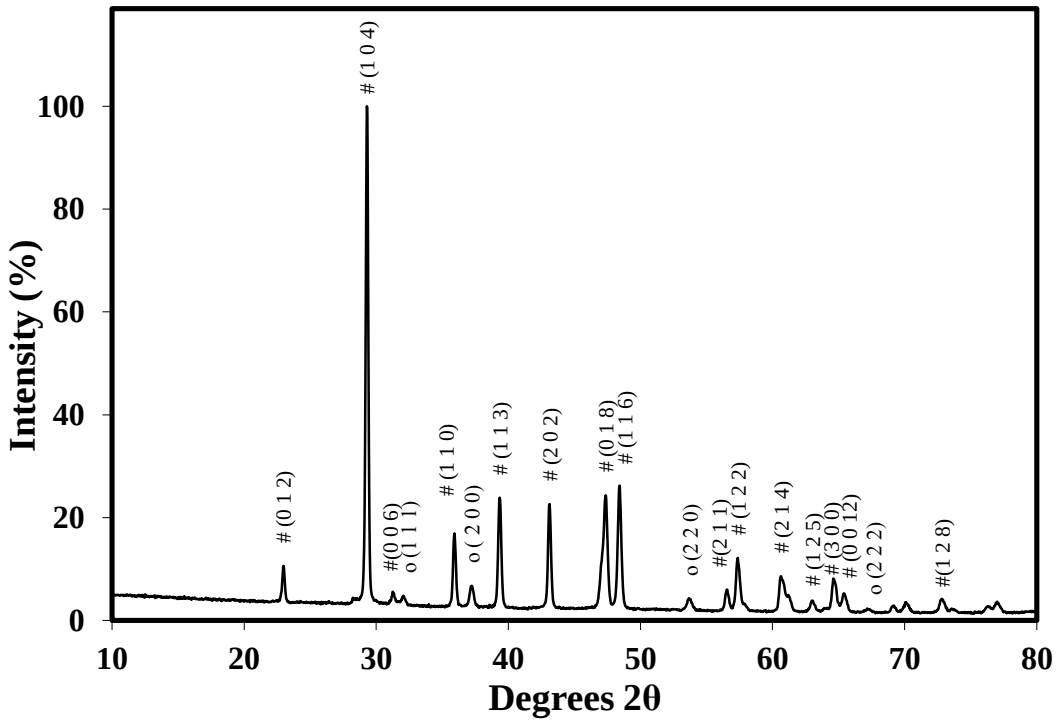

Figure 5.17: XRD pattern for CaAc decomposed at 800 °C and carbonated at 650 °C by TGA for 15 minutes. '#' denotes peaks indexed to calcite, $CaCO_3$, ICDD ref: 00-005-0586 [291], '○' denotes peaks indexed calcium oxide, CaO, ICDD ref: 04-003-7161 [226]. Full peak list available in the appendix Table A23.

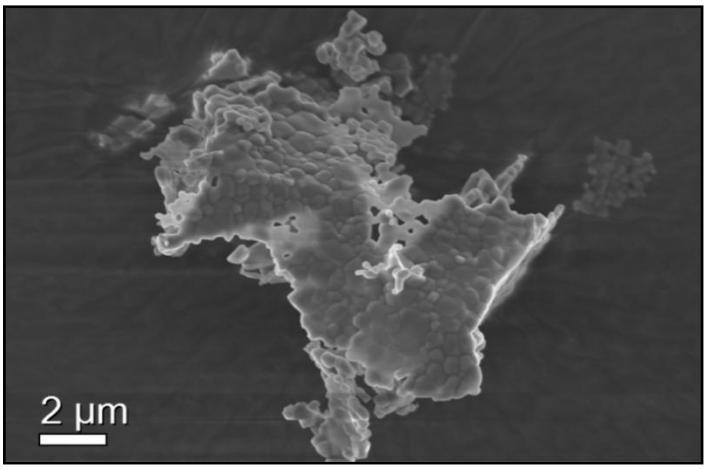

Figure 5.18: Low magnification SEM images of the CaO sorbent after maximum CO_2 pickup at 650 °C by TGA.

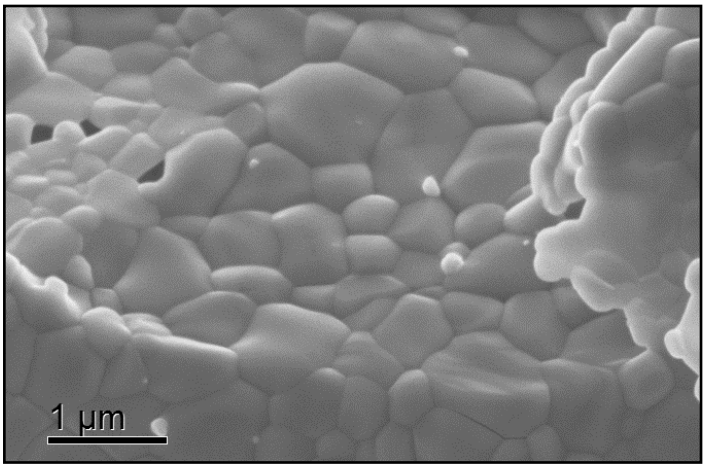

Figure 5.19: Low magnification SEM images of the CaO sorbent after maximum CO_2 pickup at 650 °C by TGA.

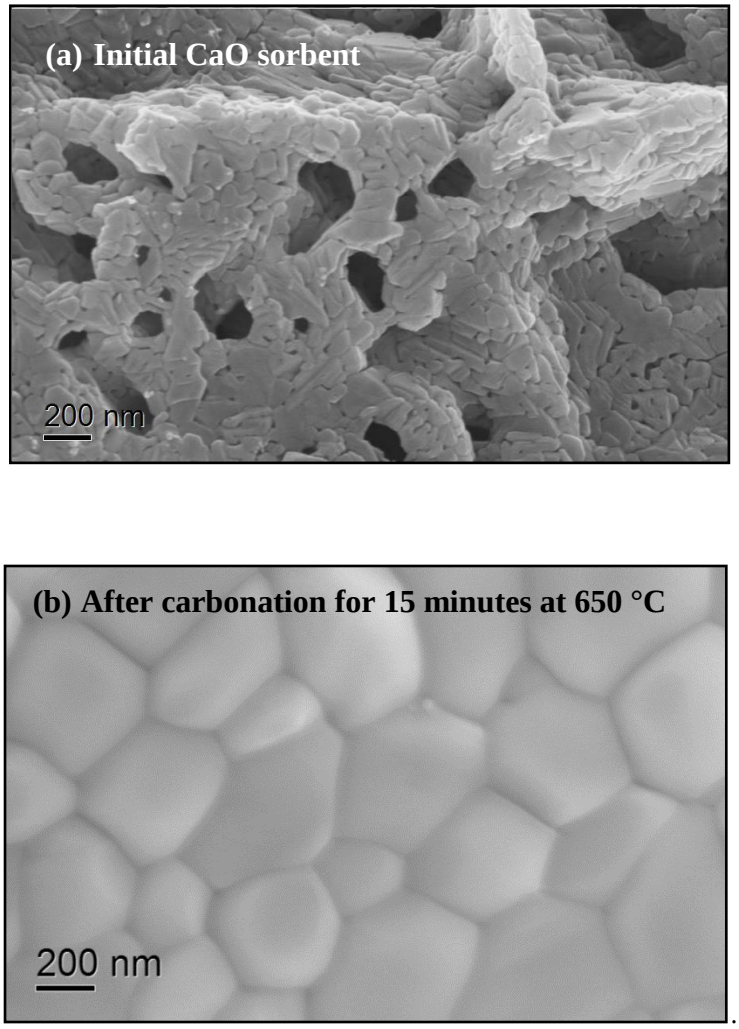

Figure 5.20: High magnification SEM images of (a) initial CaO sorbent produced by decomposition of CaAc at 800 °C by TGA and (b) the CaO sorbent after CO_2 pickup at 650 °C for 15 minutes by TGA.

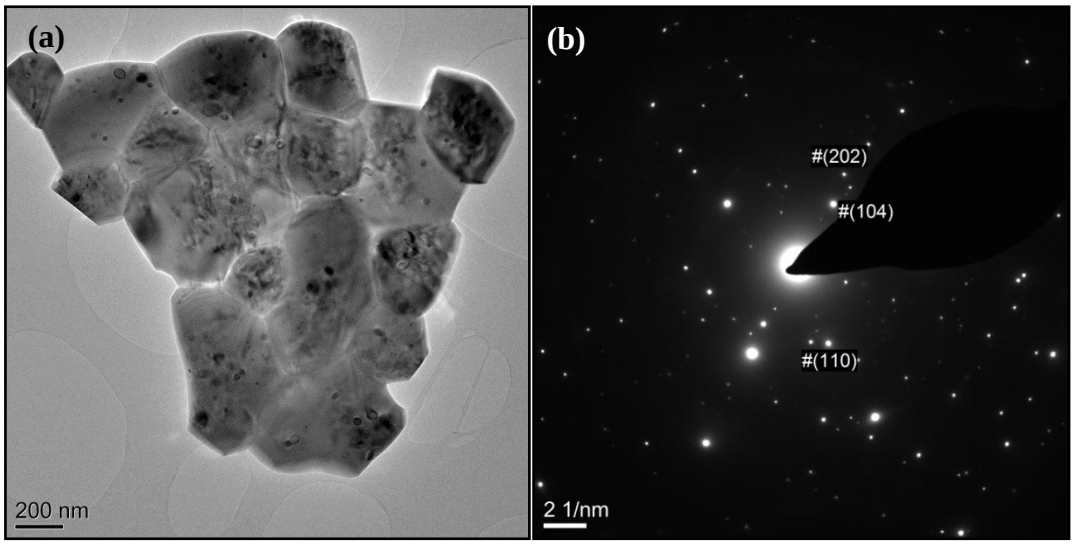

Figure 5.21: (a) Bright field TEM image showing the CaO sorbent after 15 minutes of CO_2 pickup at 650 °C by TGA, with (b) corresponding selected area diffraction pattern showing diffraction spots due to calcite ($CaCO_3$), labels correspond to spots. The apparent carbonation extends to the core of the particles.

5.5.2. Multiple CO_2 carbonation-calcination cycles

The regenerability of carbonated CaO has been investigated by a multi-cycle carbonation and de-carbonation process using a Shimadzu TGA-50 thermobalance. A starting sample of CaAc was decomposed under an N_2 atmosphere (rotameter controlled flow rate = 50 ml min^{-1}) to 800 °C (heating rate = 20 °C min^{-1}), following the process previously outlined in Section 5.3. For carbonation, the chamber temperature was dropped to 650 °C before a 50 ml min^{-1} flow rate of CO_2 was applied and carbonation was carried out for 5 minutes. Subsequent decarbonation then took place under N_2 at 800 °C; this cycle was repeated a total of 9 times, with the final sample left in the carbonated state for analysis (10^{th} carbonation stage).

The TGA data from the multi-cycle process are shown in Figure 5.23 with CaO to $CaCO_3$ conversion data for the first 9 complete cycles, displayed in Table 5.2. The data here show that the initial capacity of the CaO powder sorbent is equivalent to a mass increase due to CO_2 uptake of 71.2% after the first cycle of carbonation for 5 minutes (previously analysis of sorbent carbonation for 15 minutes showed a CO_2 uptake of 71.7 mass%, χ = 0.91) however after each successive regenerative heat treatment this value significantly declines, reaching 46.4% mass increase after 9 cycles. A decrease in the molar conversion ratio, χ, is observed from χ = 0.89 in the first cycle, to χ = 0.57 after 9 cycles. This is typical of the loss of CaO durability reported elsewhere, e.g. Liu *et al* (2009) report a ~40% decrease in the conversion of CaO to $CaCO_3$ after 9 cycles (carbonation cycles at 650 °C for 30 min) [137] and Siliban *et al* (1992) report a ~20% decrease in the conversion of CaO to $CaCO_3$ after 5 carbonation cycles (carbonation cycles at 750 °C for ~40 minutes) [275]; both using a CaO sorbent produced from CaAc decomposition.

An enlarged chart showing the first three complete cycles of this process is displayed in Figure 5.24. The first three cycles here show molar conversion ratios, χ, of 0.89, 0.81 and 0.76 respectively. From cycle 1 to cycle 2, the largest decrease in overall carbonation conversion between consecutive carbonation/decarbonation cycles is observed, 4.8%. The shape of the curves is also seen to alter after the first cycle: as previously discussed, $CaCO_3$ growth due to CO_2 uptake on a CaO particle surface is initially a rapid, linear process and this is observed in the first cycle to be significantly more pronounced than in subsequent cycles. Continuation of $CaCO_3$ growth is then controlled by the slower diffusion of CO_2 through the $CaCO_3$ product layer. A schematic showing the initial linear growth of $CaCO_3$ particles and then diffusion controlled growth of $CaCO_3$ particle, on the surface of a CaO nanosorbents particle, during carbonation is presented in Figure 5.22.

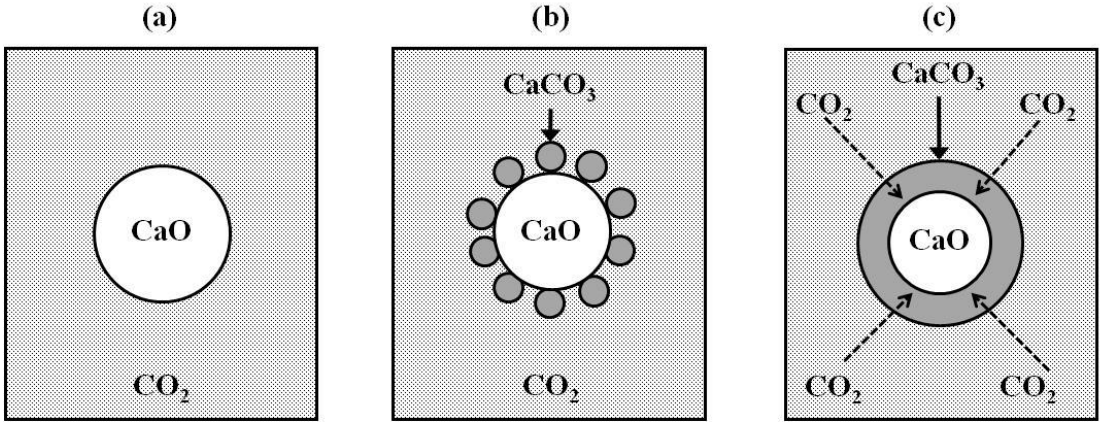

Figure 5.22: Basic schematic showing the carbonation process where (a) displays the initial CaO nanoparticle in a CO_2 atmosphere, at time = 0 (b) shows the rapid linear growth of $CaCO_3$ particles on the surface of the CaO particle and (c) continued slow growth of the $CaCO_3$ particles by the diffusion of CO_2 gas through the carbonate product layer.

The areas of the three curves marked '*' in Figure 5.24 signify the approximate end of the rapid linear growth (straight-line) region and subsequent onset of solid-state diffusion controlled growth (curved region). It is observed that this begins much later in the first cycle with diffusion controlled growth contributing to a much lower proportion of conversion in comparison to subsequent cycles. This suggests that the initial CaO sorbent is more dispersed and porous than the sorbents produced by successive decarbonations, which are likely to have lower particle surface areas and hence recarbonations are more diffusion controlled, in relative terms. Subsequent analysis of multiple decarbonated stages of the cycling process by SEM (Figure 5.28a-h) support this, however measurements of surface area were found to be unreliable here due to the insufficient sample amounts generated by TGA decomposition[***].

From Figure 5.24 is it observed that mass increase due to carbonation continues for ~2.0 mins per cycle after the CO_2 supply is removed, an effect consistent across all carbonation cycles. This is likely to be caused by residual CO_2 gas in the chamber that remains as the N_2 gas supply is reapplied. This uptake continues as chamber temperature increases from 650 °C to 690 °C, and decarbonation then occurs beyond this temperature.

Sample decarbonation occurs as the chamber temperature increases from 690 °C (heating rate = 20 °C min^{-1}) and is completed by 780 °C, taking 4.5 mins. Complete decarbonation to CaO is observed at each cycle.

[***] From discussion with Dr Adrian Cunliffe (Energy Research Institute)

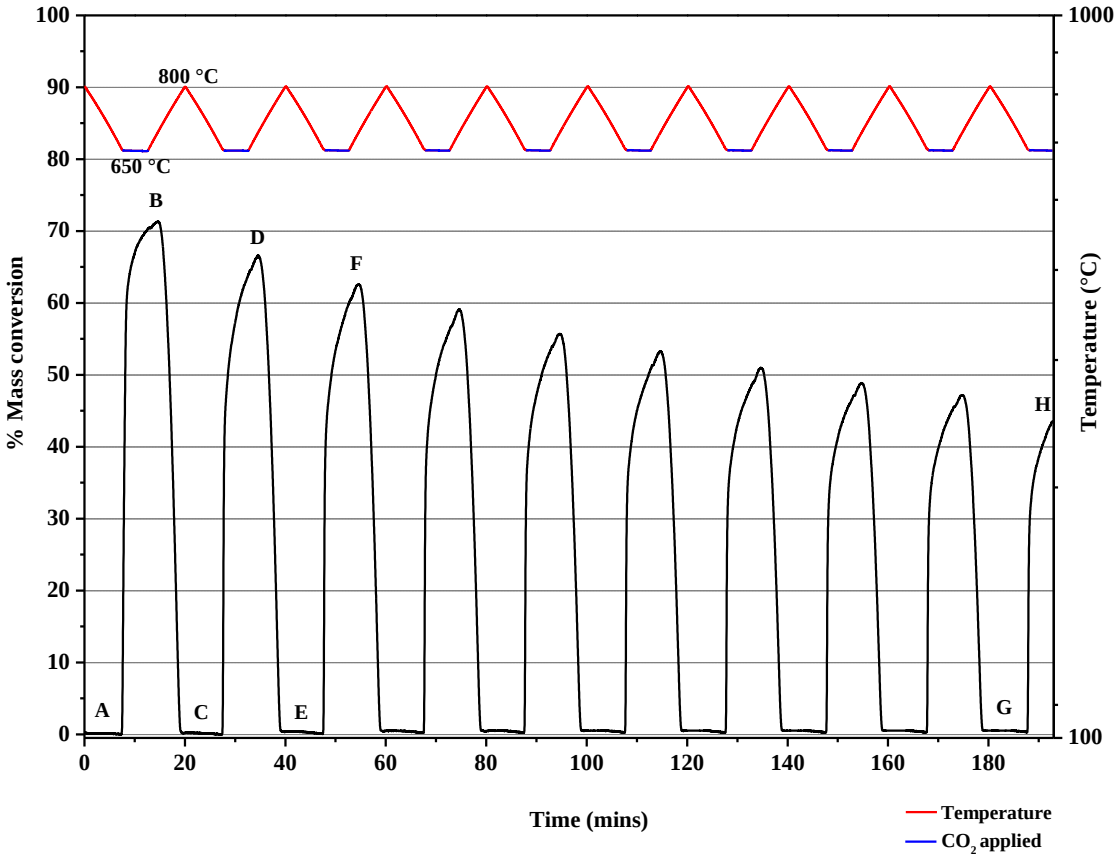

Figure 5.23: Degradation in CO_2 capture capacity for CaO produced via decomposition of calcium acetate hydrate ($Ca(CH_3COO)_2 \cdot xH_2O$) at 800 °C. Y-axis (left) displayed as percentage mass change due to uptake of CO_2. Y-axis (right) displays temperature in log-scale (°C): the red coloured temperature plot indicates N_2 conditions; the blue coloured temperature curve regions indicate the application of CO_2, at 650 °C, for carbonation. Samples have been reproduced at points A-H for more detailed analysis, see Section 5.5.3.

Table 5.2: CaO to $CaCO_3$ conversion data calculated for first 9 complete cycles. With decarbonation carried out at 800 °C (in 100% N_2) with no dwell time, and carbonation carried out at 650 °C (in 100% CO_2) for 5 minutes.

Cycle No.	**1**	**2**	**3**	**4**	**5**	**6**	**7**	**8**	**9**
% mass change to CO_2 uptake	71.21	66.37	60.96	58.21	55.04	52.51	50.11	47.92	46.39
Molar conversion ratio, χ	0.89	0.81	0.76	0.71	0.68	0.64	0.62	0.59	0.57

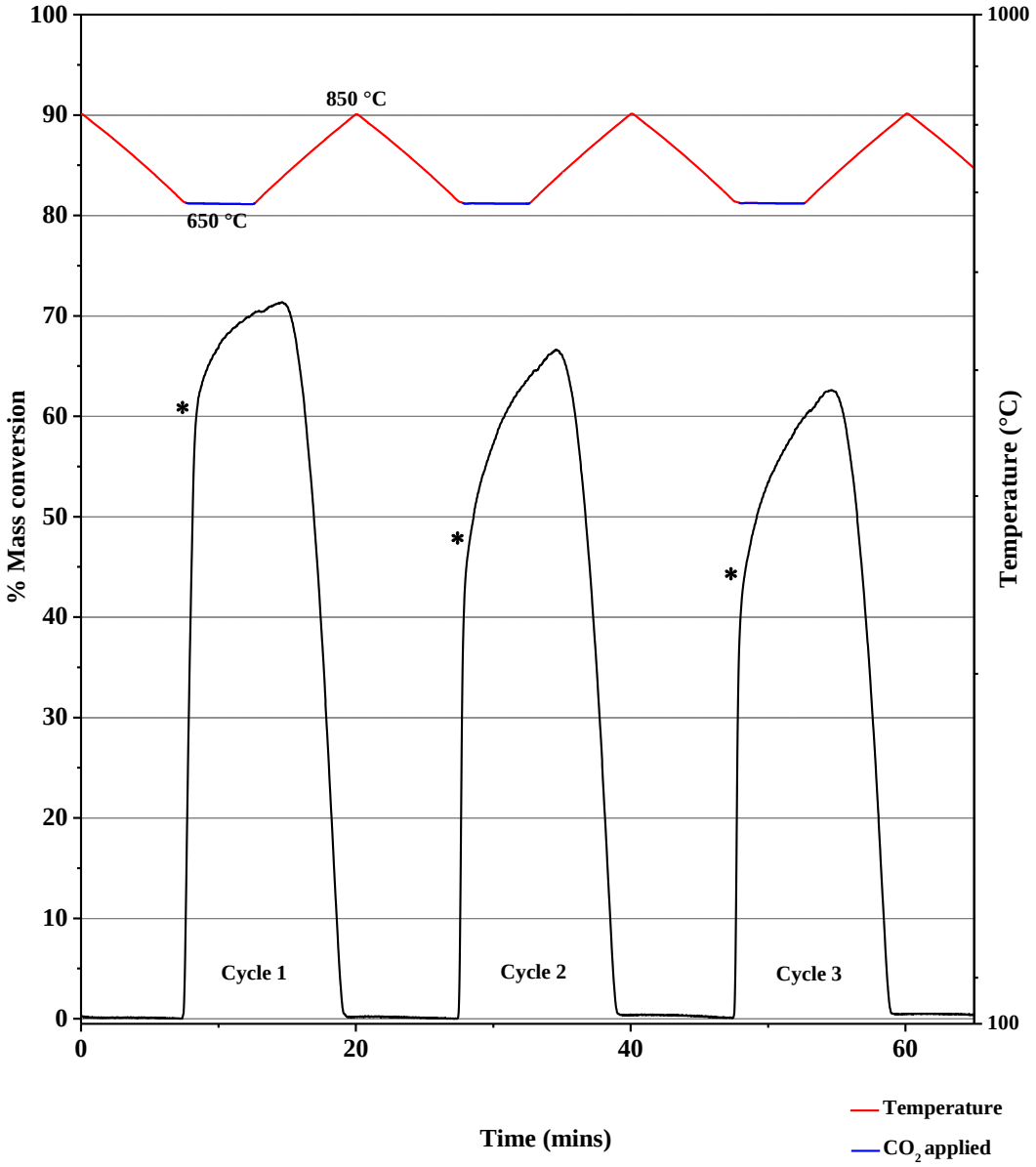

Figure 5.24: Enhancement of Figure 5.23 showing first three CO_2 capture cycles CaO produced via decomposition of calcium acetate hydrate ($Ca(CH_3COO)_2 \cdot xH_2O$) at 800 °C with no dwell time**.** Y-axis (left) displayed as percentage mass change due to uptake of CO_2. Y-axis (right) displays temperature in log-scale (°C): the red coloured temperature plot indicates N_2 conditions; the blue coloured temperature curve regions indicate the application of CO_2, at 650 °C, for carbonation. '*' signifies the approximate end of the region of rapid linear growth ('straight-line') and subsequent onset of diffusion controlled growth.

5.5.3. Structural analysis

To observe the causes for the reduction in carbonation conversion with progressive cycles at the particle level, repetitions of the multi-cycle process have been carried out by TGA and terminated after specific periods to produce samples at specific stages. Samples were collected after various post-decarbonation and post-carbonation steps and have been labelled A-H on Figure 5.23, where:

A = Initial decomposition of CaAc to 800 °C;

B = after 1st carbonation cycle at 650 °C;

C = after 2nd decarbonation at 800 °C;

D = after 2nd carbonation cycle at 650 °C ;

E = after 3rd decarbonation at 800 °C;

F = after 3rd carbonation cycle at 650 °C;

G = after 9th decarbonation at 800 °C;

H = after 10th carbonation cycle at 650 °C

Each sample was analysed by XRD, SEM and TEM. Sample A has been previously analysed in Section 5.3.1.

X-ray diffraction patterns for samples A-H are displayed in Figure 5.25. Carbonated samples (B, D, F and H) show sharp diffraction peaks due to $CaCO_3$, calcite (ICDD ref: 00-005-0586 [291]) and minor peaks due to CaO (ICDD ref: 04-003-7161 [226]). The relative intensity of the $CaCO_3$ diffraction peaks are observed to decrease with progressive CO_2 cycles, further confirming a lower conversion of CaO to $CaCO_3$ with progressive cycles of carbonation.

Figure 5.26 displays the measured changes in relative intensity of $CaCO_3$ to CaO (I_{CaCO3}/I_{CaO}) with progressing cycles of carbonation, as measured using maximum intensity peaks for $CaCO_3$ (104) and CaO (200) from XRD plots (Figure 5.25) for the 1st, 2nd, 3rd and 10th carbonation stages (samples, B, D, F and H respectively). These data show how the amount of $CaCO_3$ present in the sample, after carbonation, decreases with progressing cycles, as the amount of uncarbonated CaO sorbent increases. From Figure 5.26 it is observed that the largest decrease in sorbent carbonation is observed between the first two cycles, as the $CaCO_3$/CaO ratio decreases from 10.9 to 5.7. After the third cycles the $CaCO_3$/CaO decreases to 3.5, and after 10 cycles, 1.3.

X-ray diffraction patterns for decarbonated samples, C and E (Figure 5.25) show sharp diffraction peaks due to CaO (ICDD ref: 04-003-7161 [226]) plus low intensity broad diffraction peaks due to $Ca(OH)_2$ (ICDD ref: 01-084-1263 [289]). The diffraction peaks of $Ca(OH)_2$ have increasing intensity with progressive decarbonations, and sample 'G' (after the 9th decarbonation at 800 °C) displays a near single $Ca(OH)_2$ phase with only small traces of CaO. In addition, the $Ca(OH)_2$ crystallite size is significantly smaller than the CaO or $CaCO_3$. These results suggest a rise in instability of the CaO sorbent upon progressive decarbonations, subsequently making the crystallite sizes smaller and material more vulnerable to hydration. This contradicts the previous model using micro sized powder sorbents where a decrease in sorbent surface area, due to particle densification, is expected with progressive decarbonations (see Figure 2.7) [151]. Analysis by SEM and TEM will investigate this further. All samples here were collected from the TGA and stored in a desiccator, however exposure to air is unavoidable in this process and during XRD sample preparation and analysis.

Low magnification SEM images of samples A-H (Figure 5.27a-h) show that the large elongated and aggregated particle morphology observed previously from the as received CaAc (Figure 5.3) is maintained throughout the carbonation and decarbonation cycles. Higher magnification SEM images and TEM images of samples A-H and shown in Figure 5.28a-h (for decarbonated samples A, C, E and G) and Figure 5.29a-h (for carbonated samples B, D, F and H), and reveal more notable microstructural changes, during multicycle capture.

Analysis by SEM and TEM of the initial CaO sorbent produced by TGA decomposition of CaAc at 800 °C (sample A) and the subsequent 2^{nd}, 3^{rd} and 9^{th} decarbonated samples, C, E and G show a decreasing crystallite size, as observed in the TEM, with an overall increasing agglomerate size and decreasing porosity observed in the SEM with successive decarbonations. This suggests an increase in crystallite densification with progressive decarbonations.

The initial CaO sorbent, sample A (Figure 5.28a and b) shows small (< 200 nm) sintered crystallites within an agglomerated structure containing several large pores (typically > 200nm). Analysis of sample C, Figure 5.28c and d, (after the 2^{nd} decarbonation at 800 °C), shows a smaller overall crystallite size (< 100 nm) from TEM (Figure 5.28d), but an overall structure of larger agglomerates with increased densification and less porosity than the initial CaO sorbent (sample A, Figure 5.28a). After the 3^{rd} decarbonation at 800 °C, sample E, TEM (Figure 5.28g) shows a further decrease in crystallite size (~ < 50nm) and large crystallite densification. From SEM (Figure 5.28e) an increase in overall agglomerate size and notable further reduction in porosity is observed. After the 9^{th} decarbonation cycle at 800 °C, sample G, SEM and TEM (Figure 5.28g and h) show further crystallite densification with only small amounts of porosity evident; XRD of this sample (Figure 5.25)

shows a dominant $Ca(OH)_2$ phase, with only traces of CaO detected. Significant broadening of the $Ca(OH)_2$ peaks suggests a very fine crystallite size, but these proved difficult to distinguish in SEM and TEM images due to large densification. Porosity loss may be the result of expansion upon hydration, which is expected from the decreasing density of CaO (3.34 g cm^{-3}) to $Ca(OH)_2$ (2.24 g cm^{-3}). The effects of a large amount of sorbent hydration, as shown by XRD (Figure 5.25), are likely to complicate the interpretation of these results and their comparison to the other decarbonated samples (A, C and E). Selected area electron diffraction data for sample G (see the appendix Figure 5.58) shows diffraction rings only due to $Ca(OH)_2$ with no spots detected due to CaO, and surface hydration is likely to effect the porosity of the sorbent. Reasons for the observed differences in the decarbonated samples between SEM and TEM are unclear and the structural effects of sorbent hydration require and require further investigation. Although unconfirmed, potential water contamination in the methanol used for TEM sample dispersion, prior to drop-casting onto the support film, may be a contributing factor toward further hydration.

To address the issue of sorbent hydration, a TEM based technique has been developed using an Environmental heating cell (E-cell) to analyse the carbonation and decarbonation steps under vacuum, minimising exposure to air. Results are displayed in Sections 5.5.4 and 5.5.5.

Images from SEM and TEM of the 1^{st}, 2^{nd}, 3^{rd} and 10^{th} carbonated samples B, D, F and H (Figure 5.29a-h) all show similar microstructural characteristics, with heavily sintered crystals of $CaCO_3$ forming in the size range of ~100 - 400 nm. Images from SEM and TEM are in good agreement. Expansion on carbonation of the first CaO sorbent (sample A) is likely to be the cause of the loss in porosity seen after subsequent decarbonation stages, and with progressing sorbent crystallite

densification upon decarbonation this is likely to contribute to the overall decay in carbonation conversion with progressive cycles, as observed by TGA (Figure 5.23) and XRD (Figures 5.25 and 5.26).

Table 5.3 subsequently displays average particle sizes for samples A-H, as measured across 25 individual particles per sample, using SEM micrographs. This data suggests that sorbent particle size gradually increases with progressing decarbonation stages (samples A, C, E and G), with the initial CaO sorbent, sample A, showing an average particle size of 145 ± 36 nm, which rises to 170 ± 65 nm after the 2^{nd} decarbonation at 800 °C (sample C), 204 ± 59 nm after the 3^{rd} decarbonation at 800 °C (sample E), and to 230 ± 51 nm after the 9^{th} decarbonation at 800 °C (sample G). It should be noted that the particle sizes measurements for the decarbonated samples are likely to be affected by unavoidable hydration of the sorbents at room temperature.

With progressive decarbonations, TEM analysis shows a decrease in the overall crystallite size of the CaO sorbent; with SEM highlighting increasing agglomeration, densification and decrease in observed porosity. This densification inhibits the amount of carbonation on subsequent carbonation cycles, as is confirmed by the decreasing relative peak intensity ratio of $CaCO_3$ to CaO (I_{CaCO_3}/I_{CaO}) measured from XRD (Figure 5.25) with progressive carbonations (Figure 5.26).

The 1^{st}, 2^{nd} 3^{rd} and 10^{th} carbonated samples (samples B, D, F and H respectively) show a gradual decrease in average particle size, with the largest particle size of 374 ± 120 nm observed after the first carbonation (sample B), decreasing to 340 ± 132 nm and 324 ± 91 nm after successive carbonations (samples D and F respectively); however values for these samples B, D and F all fit into each

range of standard deviation. The average particle size observed after the 10^{th} carbonation then decreases to 242 ± 97 nm.

Overall, an expansion of particle size is observed upon each carbonation, which would be expected due to the lower density (ρ) of $CaCO_3$ (2.71 g cm^{-1}) compared to CaO (3.34 g cm^{-1}). This expansion leads to the large crystal densification of $CaCO_3$ observed here (Figure 5.29).

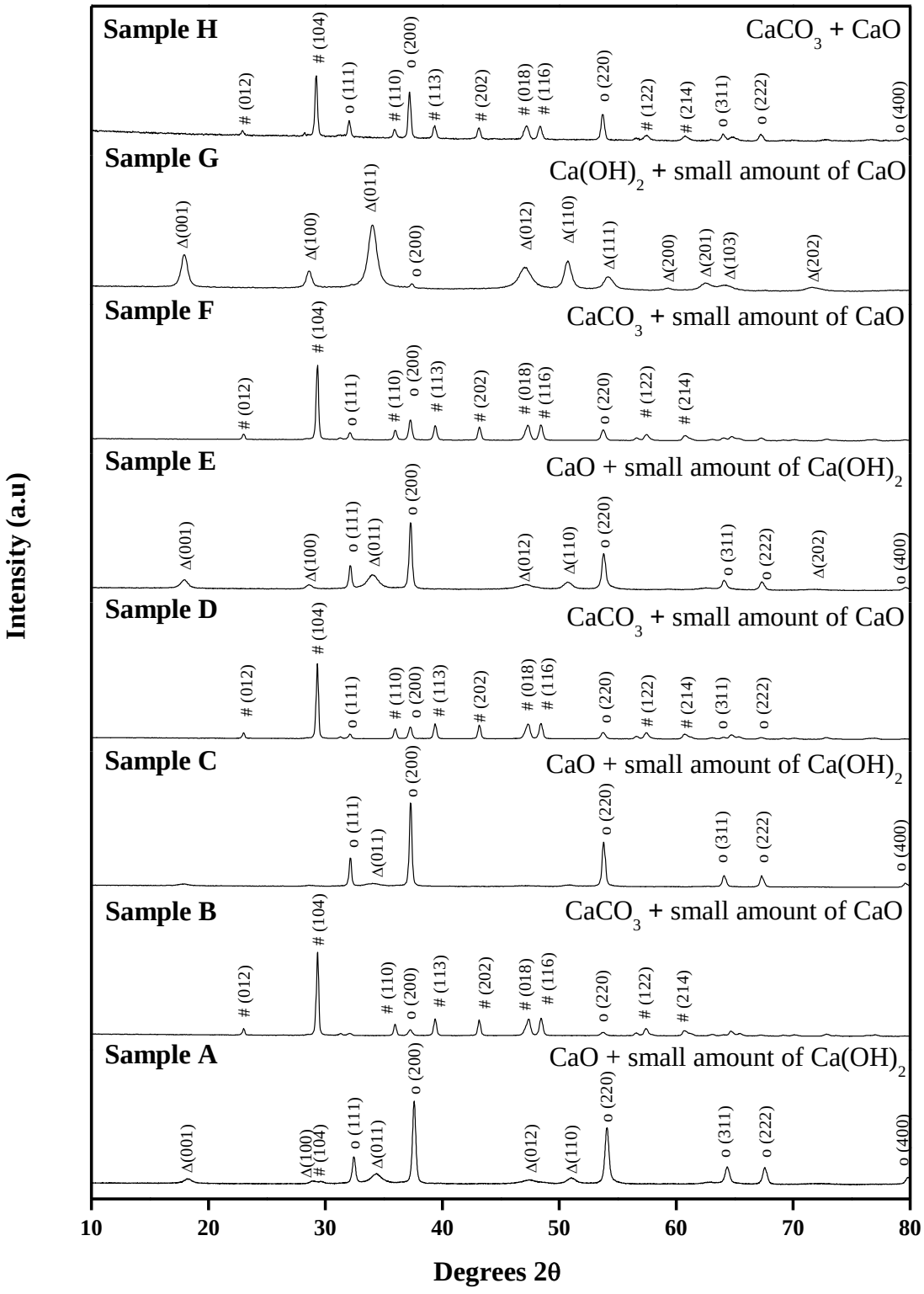

Figure 5.25: XRD pattern for multicycle carbonation/decarbonation samples A to H. '#' denotes peaks indexed to calcite, $CaCO_3$, ICDD ref: 00-005-0586 [291], '○' denotes peaks indexed to calcium oxide, CaO, ICDD ref: 04-003-7161 [226], 'Δ' denotes peaks indexed to calcium hydroxide $Ca(OH)_2$, ICDD ref: 01-084-1263 [289]. Full peak data available in the appendix Tables A14 and A24 - A30.

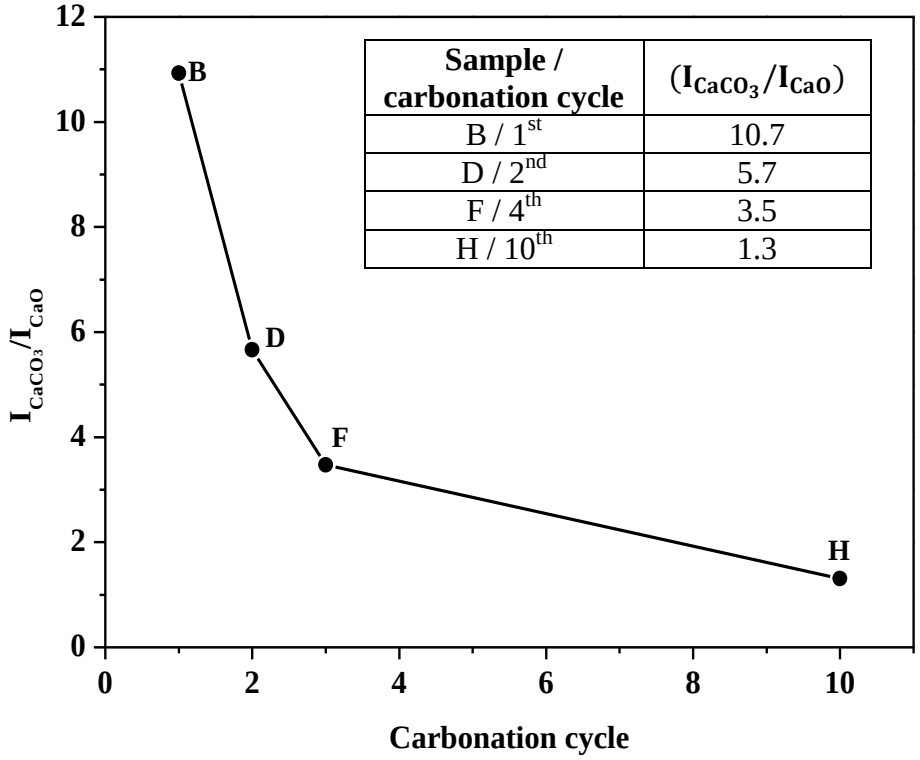

Figure 5.26: Change in relative intensities of $CaCO_3$ to CaO (I_{CaCO3}/I_{CaO}) with progressing cycles of carbonation, measured using maximum intensity peaks for $CaCO_3$ (104) and CaO (200) from XRD plots for the 1st, 2nd, 3rd and 10th carbonation stages (samples, B, D, F and H respectively).

Low mag SEM images of all multicycle carbonated and decarbonated samples A – H.

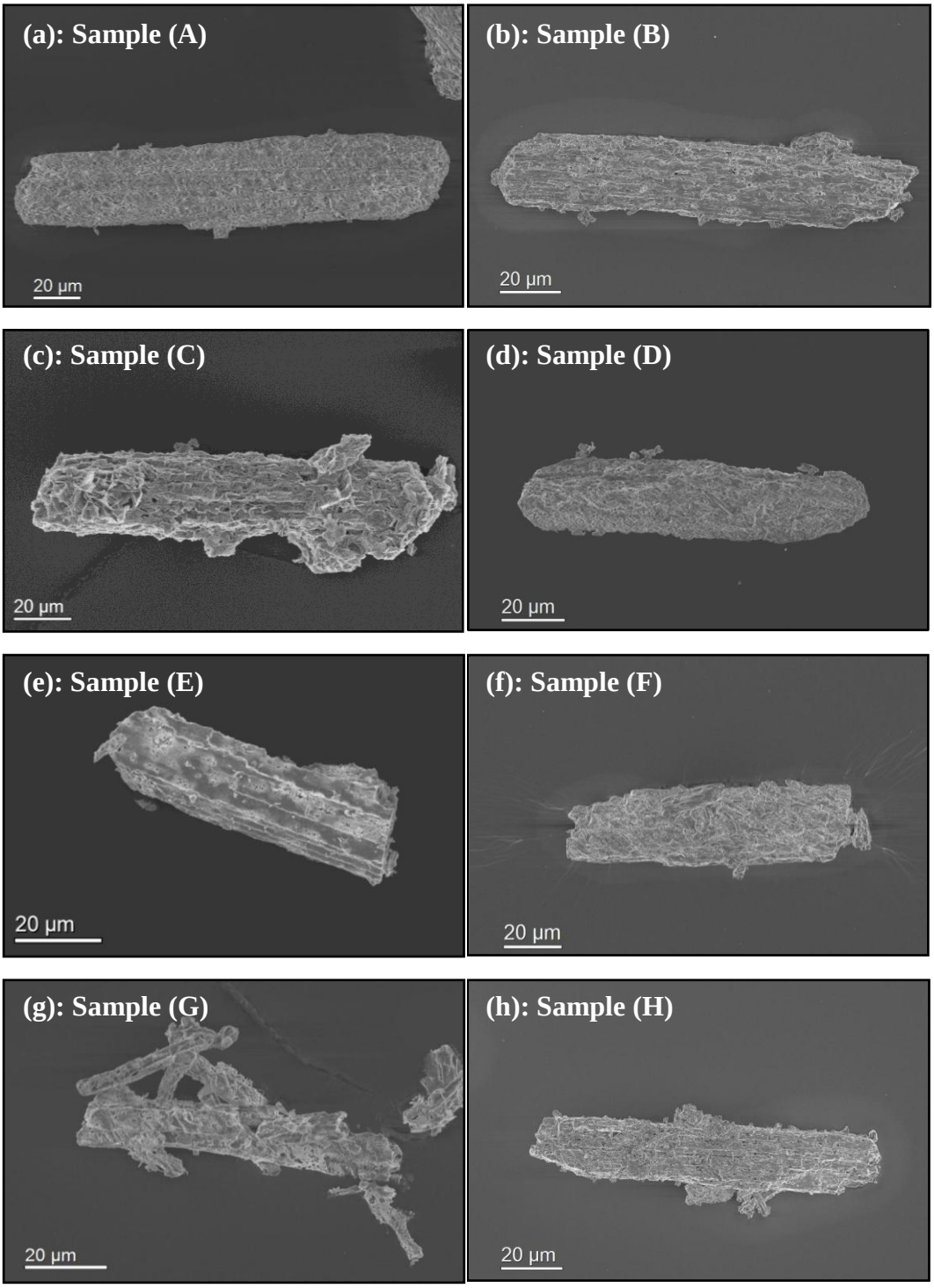

Figure 5.27: Low magnification SEM image of multicycle samples A-H.

High mag SEM and TEM images of decarbonated samples A, C, E & G

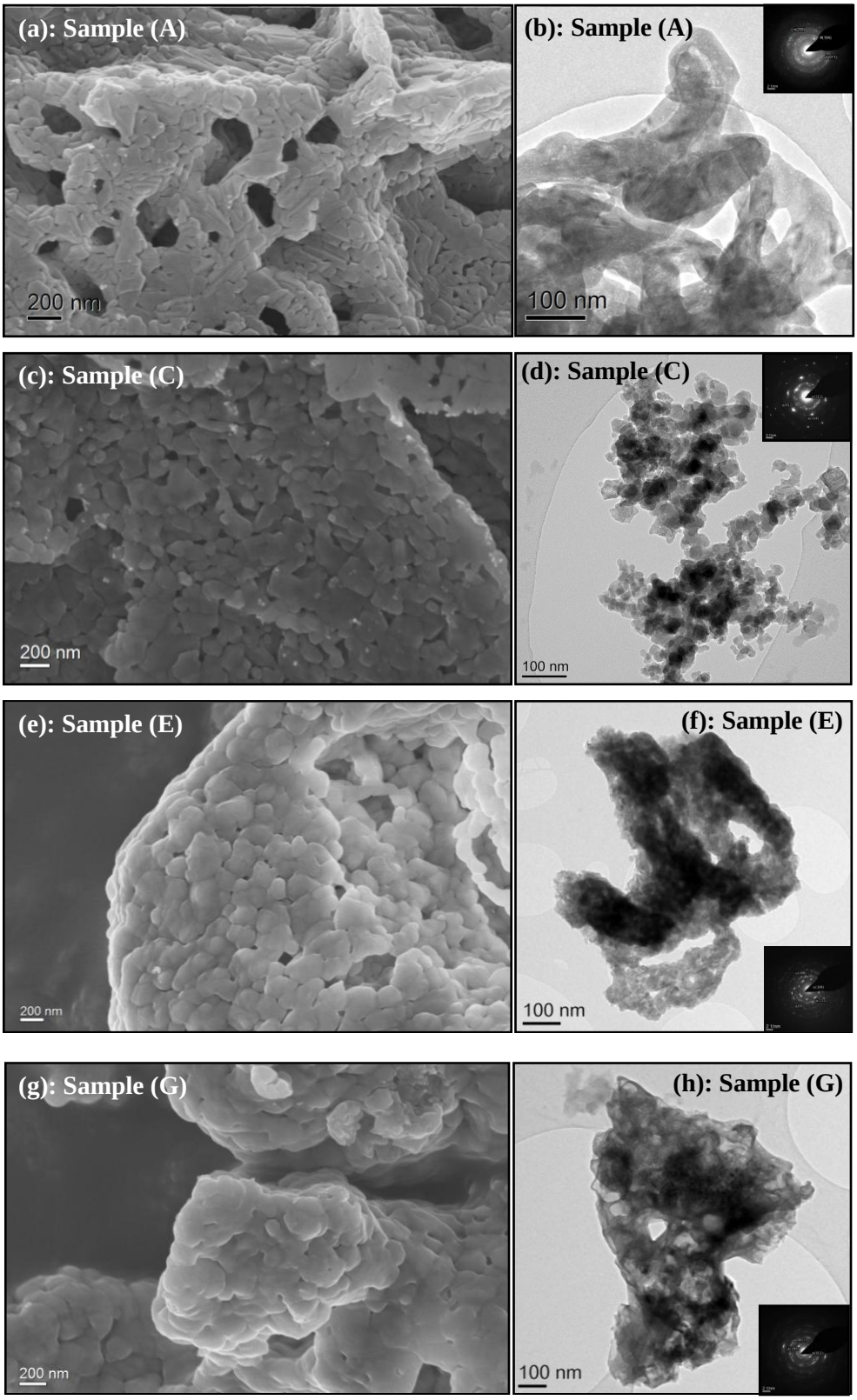

Figure 5.28: High magnification SEM images with bright field TEM image and SAED pattern insert of decarbonated samples A, C, E and G. SAED's show for sample A: diffraction due to CaO, $Ca(OH)_2$ and calcite, $CaCO_3$. Samples C and E indexed to CaO and $Ca(OH)_2$. Sample G indexed to only $Ca(OH)_2$. Larger SAED images for samples A, C, E & G displayed in the appendix Figures 5.54, 5.56 amd 5.58.

High mag SEM and TEM images of carbonated samples B, D, F & H

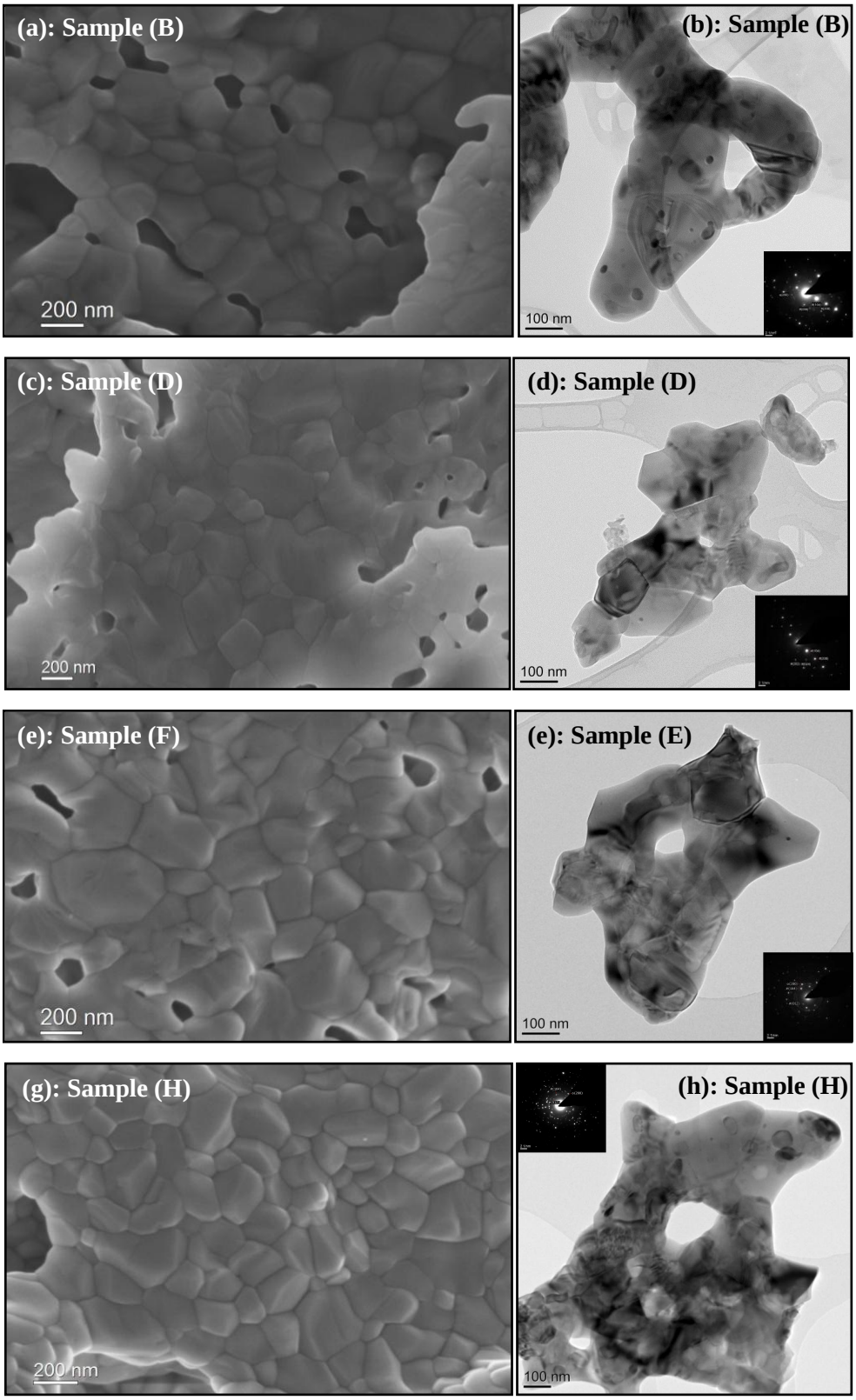

Figure 5.29: High magnification SEM images with bright field TEM image and SAED pattern insert of carbonated samples B, D, F and H. SAED's show for sample and D, diffraction only due to calcite, $CaCO_3$. Samples B, F and H are indexed to both calcite, $CaCO_3$ and CaO. Larger SAED images displayed in the appendix, Figures 5.53, 5.55, 5.57 and 5.59.

Table 5.3: Average particle size and standard deviation (measured across 25 individual particles per sample using SEM micrograph images) and estimated crystallite size (measured from TEM images) of decarbonated samples (A, C, E & G).

Decarbonated Samples	**Average particle size, nm (measured across 25 particles from SEM images)**	**Estimated crystallite size, nm (measured from TEM images)**
A - Initial CaO sorbent	145 ± 36	< 150
C - after 2nd decarbonation	170 ± 65	~40
E - after 3rd decarbonation	204 ± 59	~30
G - after 9th decarbonation	230 ± 51	-

Table 5.4: Average crystal size, and standard deviation (measured across 25 individual particles per sample using SEM micrograph images) of carbonated samples (B, D, F & H).

Carbonated Samples	**Average crystal size, nm (measured across 25 particles from SEM images)**
B – after 1st carbonation cycle	374 ± 120
D - after 2nd carbonation cycle	340 ± 132
F - after 3rd carbonation cycle	324 ± 91
H - after 10th carbonation cycle	242 ± 97

5.5.4. Hot-stage TEM analysis of decarbonation

To examine how the carbonated product is decomposed (decarbonated) back to CaO, a carbonated CaO powder sample has been analysed in the TEM using a water cooled Gatan Single Tilt Heating Holder with SmartSet Hotstage Controller. This holder allows for the *in-situ* decomposition of the sample under vacuum, removing the risk of sorbent-hydration. A sample of CaO carbonated for 5 minutes by TGA (Sample 'B' in Figure 5.23) was drop cast onto a silicon nitride (SiN) support membrane and heated gradually from room temperature to 800 °C and held at 10 °C temperature intervals to allow for imaging. Bright field TEM images taken at selected temperatures (room temperature, 200, 500, 600, 610 and 800 °C) are shown in Figure 5.30. Due to the process being carried out under vacuum, the temperature for decomposition is lower than those previously reported by TGA and hot-stage XRD decomposition.

Results here show that up to 500 °C (Figure 5.30a-c) the material remained as dense crystals of calcite, typically 200 nm in size. Decomposition of the calcite crystals was first observed at 600 °C (Figure 5.30d) and the expected loss of CO_2 was mostly complete by 610 °C (Figure 5.30e)†††. Some remaining areas of $CaCO_3$ subsequently broke down as the temperature increased to ~700 °C with no further structural changes then observed in the material up to the maximum temperature, 800 °C (Figure 5.30f). A higher magnification image of the sample at 800 °C (Figure 5.30g) shows that the CaO product appears as aggregates of very fine

††† Selected area electron diffraction was not carried out to confirm the decomposition to CaO phase here due to the instability of particles on the silicon nitride support film with rising temperature. From preliminary experiments, rising temperature caused many particles to 'jump' off the film, and this effect was commonly observed when the TEM was set into diffraction mode.

crystallites, with some observed nano-porosity. Crystallites are roughly < 50 nm in size however exact measurements of the crystallites proved difficult due to significant densification. Most notably during this decomposition, the original outline of the starting $CaCO_3$ particles is maintained upon decarbonation.

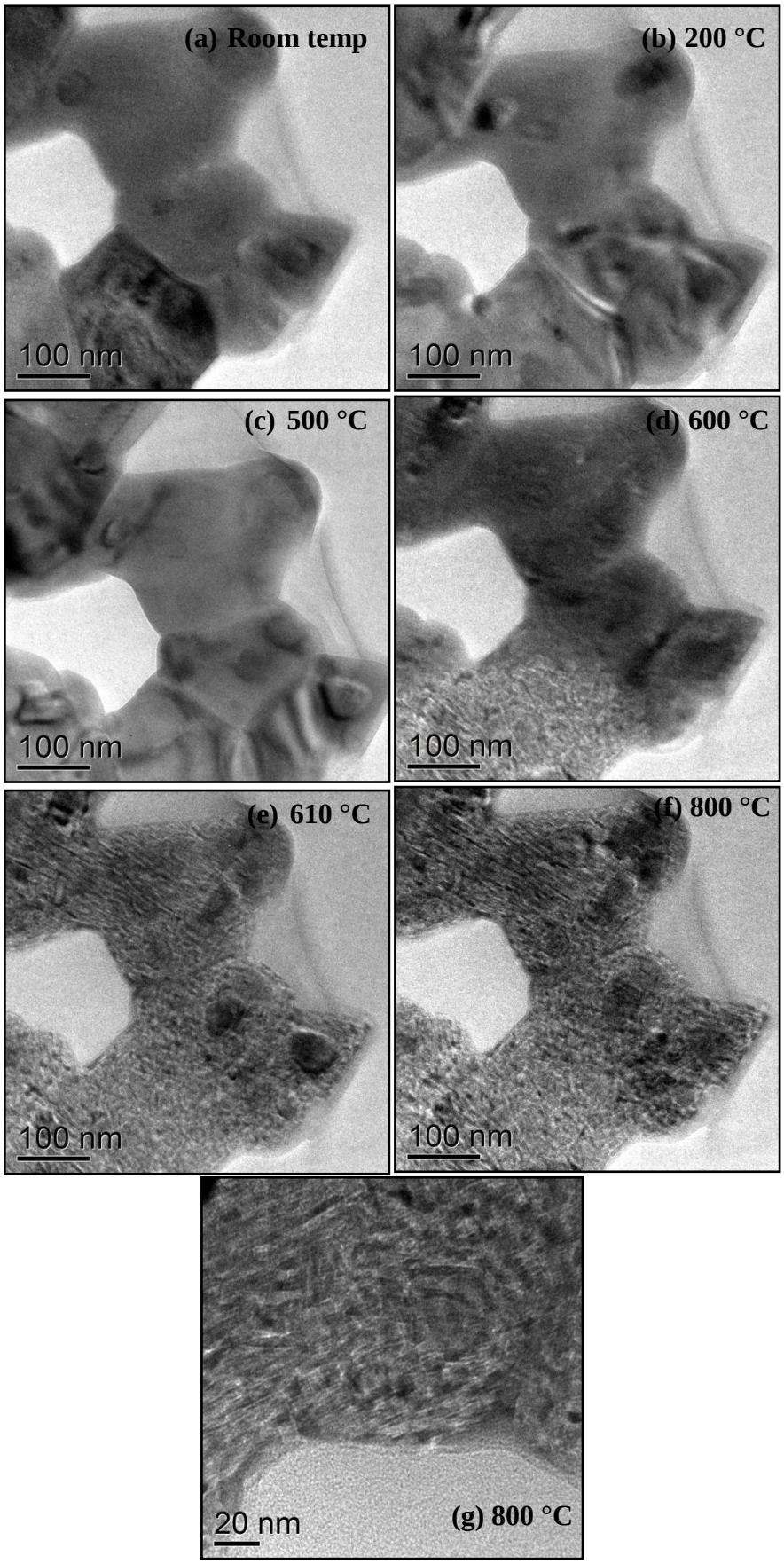

Figure 5.30: Bright field TEM images of sample D (CaO after 1st carbonation) decomposed using an *in-situ* heating stage in the TEM. Decomposition of $CaCO_3$ begins at 600 °C and is mostly complete by 610 °C.

5.5.5. Analysis of the CO_2 multicycle process using an *ex-situ* environmental-cell (E-cell) TEM technique

To analyse the effects of CO_2 looping cycles at the particle level without risk of sorbent hydration, a FEI Tecnai F20 FEG-TEM with a *ex-situ* Gatan Environmental heating cell (E-cell) has been used. The E-cell allows for a sample to be loaded into a gas or vacuum environment, with controllable temperature, before being transferred into the TEM without exposure to air, thus eliminating potential hydration of the nanoparticulate CaO. A CaO sorbent has been prepared by decomposition of CaAc at 500 °C in a furnace, to produce calcium carbonate ($CaCO_3$)‡‡‡. This was drop cast onto a silicon nitride (SiN) support membrane (Agar Scientific). Calcination of the $CaCO_3$ to CaO was carried out under vacuum, using an Edwards RV8 vacuum pump (lowest achievable vacuum pressure = ~10^{-3} Pa), from room temperature to 800 °C at ~20 °C min^{-1}. Carbonation of the CaO sorbent was carried out at 650 °C for 5 min. A CO_2 flow rate of 50 ml min^{-1}, previously used by TGA, was unachievable here due to the sealed chamber of the cell; therefore the chamber was filled to a 0.5 bar pressure of CO_2 during carbonation. This was considered the highest achievable gas pressure that did not force the release of the chamber seal.

Results of the E-cell multicycle experiment are shown in Figures 5.33 - 5.38, with a reference image of multicycle CO_2 capture by TGA (Figure 5.32) included to show the comparative stages of carbonation and decarbonation using the E-cell. Figure 5.33a shows the starting $CaCO_3$ as sheet-like particles formed by the decomposition of CaAc at 500 °C by TGA. Selected area electron diffraction

‡‡‡ Using the as received CaAc powder as the starting material in the E-cell was avoided due to the previously observed alteration of the material under the electron beam (see Figure 5.4).

(Figure 5.33c) confirms only a calcite phase, with no vaterite detected. This sheet-like form of calcite has previously been discussed in Section 5.3, however the particle here (Figure 5.33a) suggests that melting during acetate decomposition or perhaps an effect of the dispersion in methanol for TEM sample preparation may have resulted in this particle shape. Future work is required to investigate this further.

Figure 5.34 shows the first E-cell decomposition of the starting acetate material, forming CaO; the images show the outline shape of the original material is maintained, however the sheet-like structure has broken down to form fine crystallites, observed to be < 70 nm in size. Selected area electron diffraction (Figure 5.34c) confirms a CaO phase, with also diffracted rings due to $Ca(OH)_2$ indicating some sorbent hydration and an imperfect vacuum within the E-cell chamber.

The first carbonation stage at 650 °C is shown in Figure 5.35; with growth of round crystals of calcium carbonate observed with varying size range (20 – 650 nm). Where the starting CaO sorbent was observed to be thickest, large (up to 650 nm) rounded crystals of $CaCO_3$ form and become densified; some pores are evident between particles as highlighted in Figure 5.35b. Porosity observed upon carbonation using the E-cell is unexpected as previous analysis by SEM and TEM of a CaO sorbent carbonated by TGA (Figures 5.20 and 5.21) did not show the formation of pores upon carbonation. The formation of pores upon carbonation using the E-cell may be a result of the sample being fixed to the support film, which would limit particle growth in all directions and perhaps also generate differential stresses between crystals during growth. Further work is required to comprehensively assess the formation of pores upon carbonation.

Towards the edges of the particle (Figure 5.35b), where the initial CaO sorbent appeared finer; smaller (~20 - 100 nm) individual crystals of $CaCO_3$ form upon carbonation. Figure 5.35c shows the corresponding SAED pattern, confirming both $CaCO_3$ and CaO phases, suggesting an incomplete carbonation of the starting CaO sorbent, as would be expected from previous the analysis of sorbent mass conversion during carbonation by TGA (Figure 5.15).

The 2nd decarbonation at 800 °C is shown in Figure 5.36, and it is observed that the resulting CaO shows significantly different morphology to the starting CaO sorbent (Figure 5.34) with the rounded particle structure created upon carbonation, maintained, with an observed crystal size range of 20 – 600 nm. Selected area electron diffraction (Figure 5.36c) confirms this phase as CaO, with also a some spots detected due to $Ca(OH)_2$, indicating some sorbent hydration. A maximum particle size of 600 nm indicates particle shrinkage upon carbonation causing an increase in particle densification and a reduction in porosity (Figure 5.36b); with the pore highlighted previously in Figure 5.35 observed to have now closed. Most notably here it is observed that the fine aggregated CaO observed previously by hot-stage decomposition in the TEM (Figure 5.30), was not observed here using the E-cell. Reasons for this are unclear, however the difference in vacuum level for each decarbonation may have an effect, with previous decarbonation *in-situ* in the TEM taking place under a significantly higher vacuum (typically 10^{-5} Pa) than that used in *ex-situ* E-cell experiment (lowest pressure = ~10^{-3} Pa). This caused a much faster rate of decomposition by the hot-stage TEM, where structural changes due to decarbonation were first observed at 600 °C. Table 5.5 highlights the different conditions for carbonation and decarbonation for the TGA, hot-stage TEM (decarbonation only) and E-cell techniques.

The sample after the 2nd carbonation at 650 °C is shown by Figure 5.37. Here greater particle densification upon carbonation is observed in comparison to the 1st carbonation cycle (Figure 5.40) with fewer and larger particles evident (up to 880 nm); some pores are evident between the carbonate particles (Figure 5.40b) despite the previously decarbonated sample (Figure 5.36) showing no observable pores. Smaller (< 100 nm) particles are still evident towards to edge of the sample however they are slightly larger in size (typically 50 – 100 nm) and in smaller quantity than after the 1st carbonation cycle (Figure 5.35). Figure 5.37c shows the corresponding SAED pattern confirms $CaCO_3$ and CaO phases.

After the 3rd decarbonation at 800 °C (Figure 5.38), all pores between particles are observed to have closed due to further sintering and particle shrinkage. Particles of CaO are typically 50 - 840 nm in size which is larger than after the previous decarbonation step (Figure 5.36). Figure 5.38c shows the corresponding SAED pattern confirming a CaO phase and some $Ca(OH)_2$.

Upon each decarbonation cycle at 800 °C, small (< 50 nm) rod and square shaped particles were observed covering the entire surface of the sample grid, Figure 5.39. Spot EDX (Figure 5.39c) of an isolated area of these particle confirmed the presence of Mo, which may be caused by possible sputtering of the E-cell furnace at this temperature§§§. Sharp diffraction rings in the SAED pattern (Figure 5.39b) confirms these particles as crystalline, however these have not been assigned to a specific material phase; corresponding diffraction rings detected in the previous decarbonation steps of the E-cell multicycle experiment, Figures 5.36 and 5.38, have been ignored as these particles are considered contaminants. However, for the

§§§ From discussion with Dr Mike Ward (Leeds Electron Microscopy and Spectroscopy Centre)

development of the E-cell technique, future work will investigate the exact origin of these particles.

Table 5.5: Summary of carbonation and decarbonation conditions for multicycle CO_2 capture by TGA, hot-stage TEM (decarbonation only) and the E-cell techniques.

Method for multicycle CO_2 capture	**Carbonation conditions**	**Decarbonation conditions**
TGA	650 °C in CO_2 (2 bar pressure providing a flow rate of 50 ml min^{-1}) for 5 minutes	800 °C in N_2 (2 bar pressure providing a flow rate of 50 ml min^{-1}). No dwell time
Hot-stage TEM	-	800 °C under TEM vacuum (typically 10^{-5} Pa). No dwell time
E-Cell	650 °C in CO_2 (0.5 bar pressure) for 5 minutes	800 °C under rotary vacuum (lowest pressure = ~10^{-3} Pa). No dwell time

Table 5.6 summarises the structural observations of the CaO sorbent through the multicycle carbonation and decarbonation cycles using the E-cell. Overall, these results are in good agreement with Lysikov *et al's* [151] model for the multicycle process, shown in Figure 5.31, showing an increasingly sintered 'skeleton' of CaO upon decarbonation. This model was previously discussed in Section 2.5.2.1 (Figure 2.7).

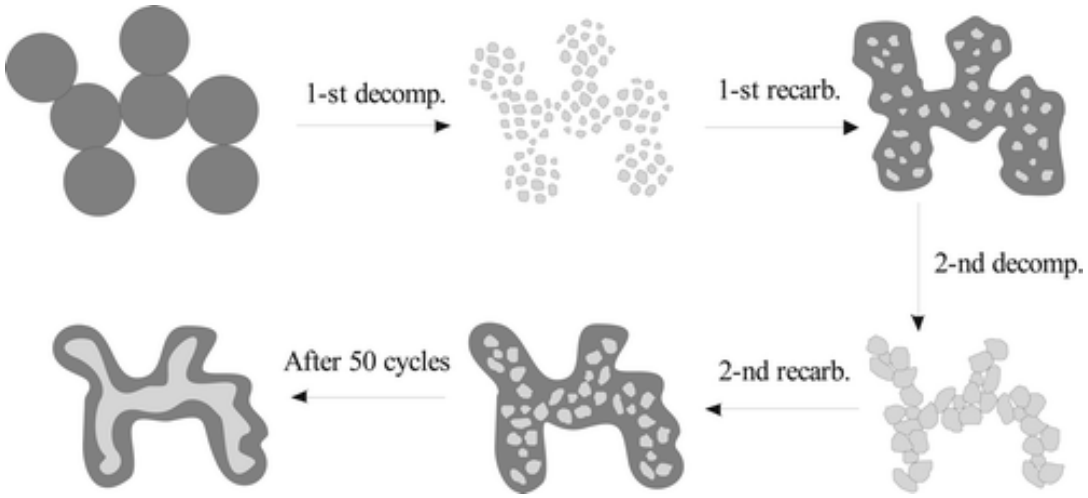

Figure 5.31: The multicycle CO_2 capture process on the textural transformation of the CaO sorbent. The $CaCO_3$ phase is shown by dark grey, and CaO is shown by light grey [151, 154].

Table 5.6: Summary of structural observations of a CaO sorbent analysed during multicycle carbonation and decarbonation using the E-cell technique.

Sample	Observations
Figure 5.33**:** Starting $CaCO_3$, formed by furnace decomposition of CaAc at 500 °C	Sheet-like structure of $CaCO_3$, ~5 μm in size.
Figure 5.34: Initial CaO sorbent formed by E-cell decomposition of starting $CaCO_3$ at 800 °C.	Very fine (< 70 nm) crystallites of CaO. $Ca(OH)_2$ detected by SAED, indicating some sorbent hydration.
Figure 5.35: 1st carbonation to $CaCO_3$ at 650 °C.	Particle growth of densified crystals of $CaCO_3$. Some observed pores (~150 nm). $CaCO_3$ crystal size range 20 nm – 650 nm. CaO detected by SAED, indicating incomplete conversion to $CaCO_3$, From equivalent TGA cycle stage : $\chi = 0.89$.
Figure 5.36: 2nd decarbonation to CaO at 800 °C.	CaO crystals maintain previous structure observed in Figure 5.35. Particle contraction has closed observed pore. CaO crystal size range 20 nm – 600 nm. $Ca(OH)_2$ detected by SAED, indicating some sorbent hydration****.
Figure 5.37: 2nd carbonation to $CaCO_3$ at 650 °C.	Larger densified crystals of $CaCO_3$ formed, compared to 1st carbonated sample (Figure 5.35) Some observed porosity (~70 nm). $CaCO_3$ crystal size range 50 nm – 880 nm. SAED detected some diffraction spots due to CaO, consistent with incomplete conversion. From equivalent TGA cycle stage: $\chi = 0.81$.
Figure 5.38: 3rd decarbonation to CaO at 800 °C.	Small shrinkage of CaO crystals upon decarbonation. Heavily densified with no observed porosity CaO crystal size range 50 nm – 840 nm CaO and some $Ca(OH)_2$ detected by SAED, indicating sorbent hydration****.

**** Small (< 20nm) Mo-based contaminant particles also detected due to possible sputtering of E-cell furnace filament (see Figure 5.39).

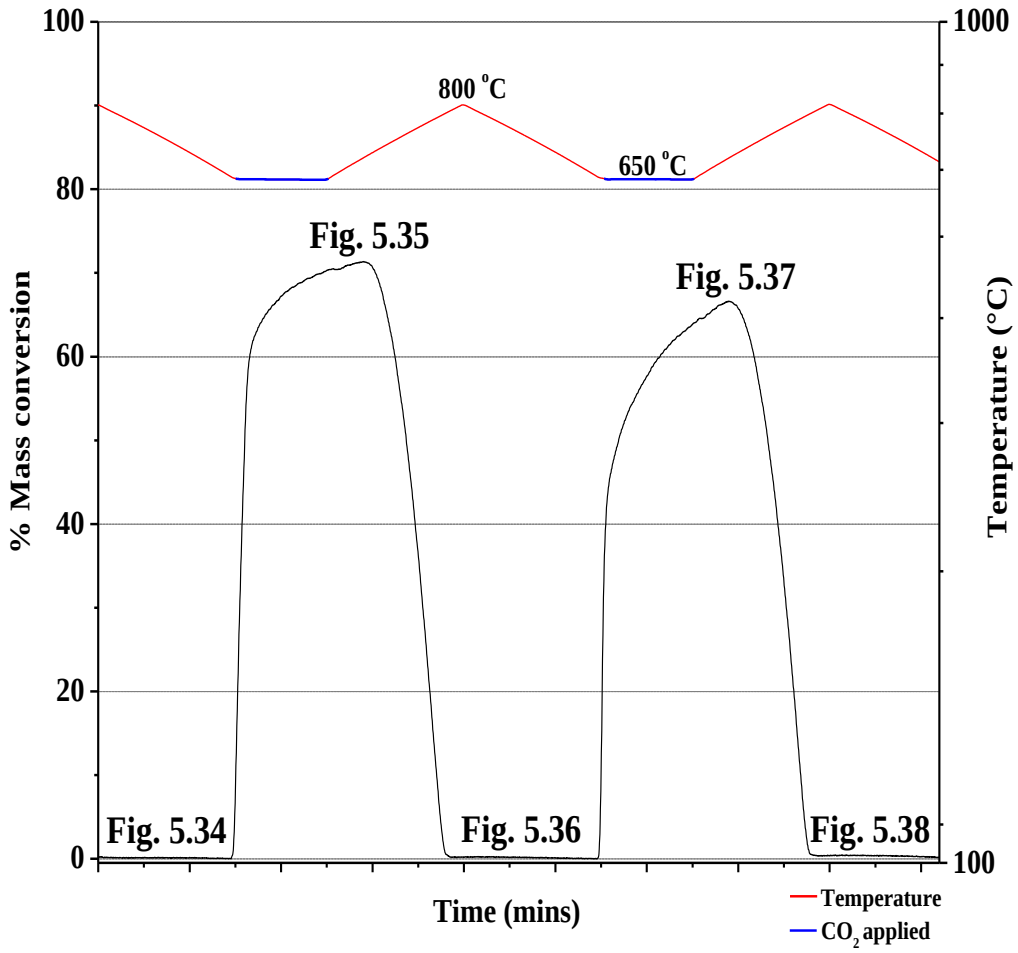

Figure 5.32: Multicycle carbonation and decarbonation of a CaO sorbent as measured previously by TGA in Section 5.5.2. This shows comparative conditions used for the TEM based E-cell analysis of the multicycle capture process, where labels correspond to Figure 5.34 - 5.38.

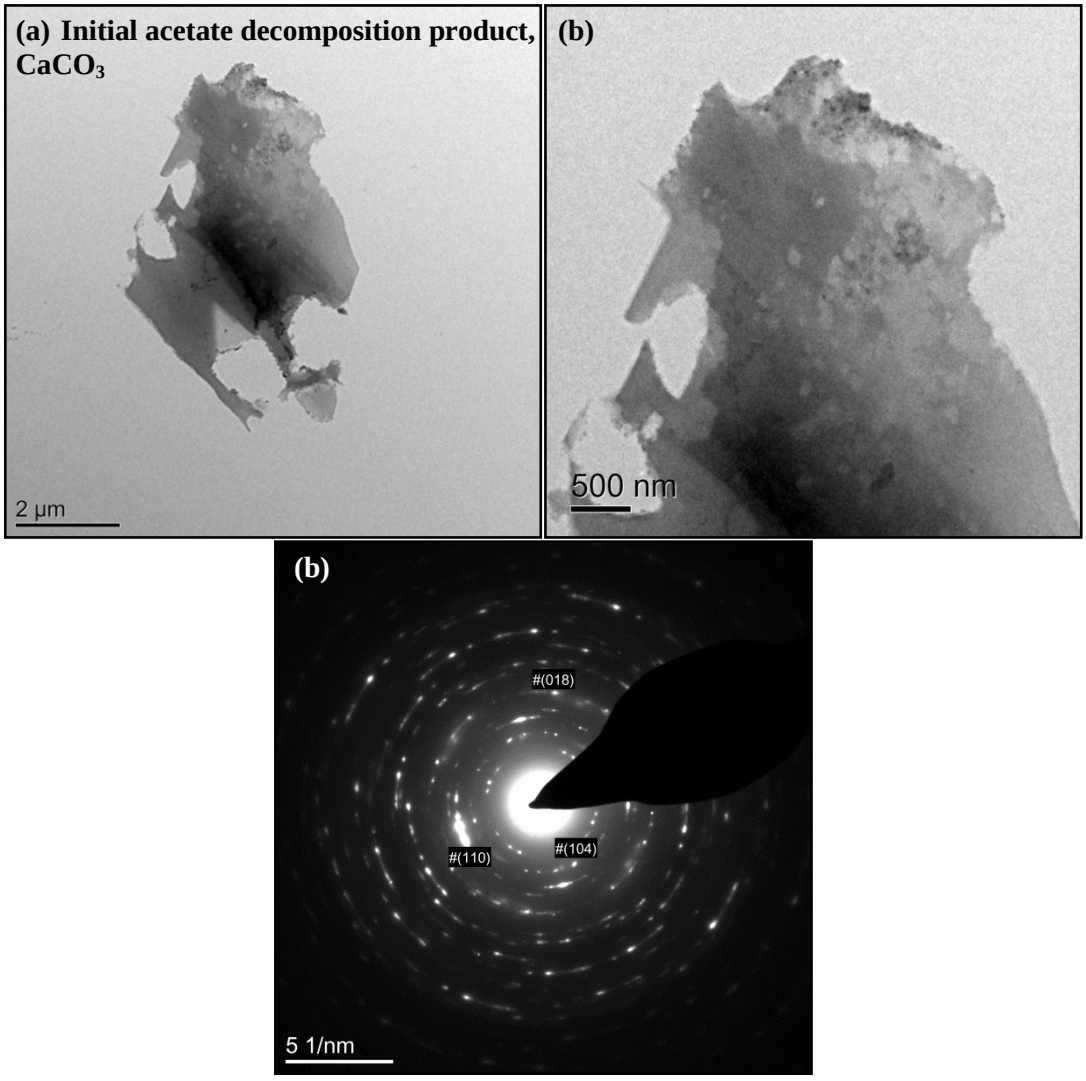

Figure 5.33: Bright field TEM image showing multicycle carbonation and decarbonation of CaO formed upon decomposition of CaAc carried out using the ex-sit E-cell technique: (a & b) initial $CaCO_3$ formed by decomposition of CaAc at 500 °C by TGA with (c) SAED pattern for (a) with all diffraction rings corresponding $CaCO_3$ '#' (ICDD ref: 00-005-0586 [291]).

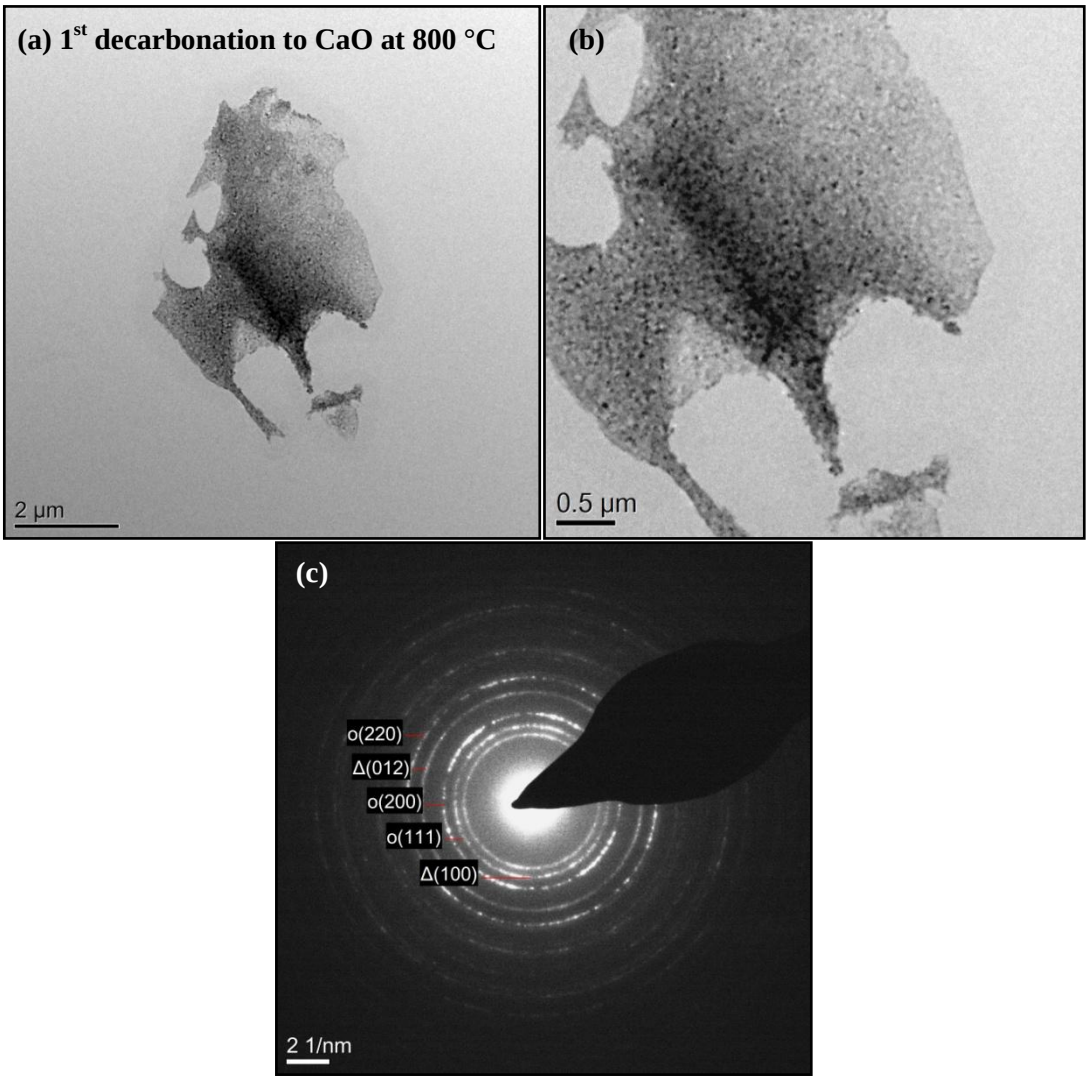

Figure 5.34: Bright field TEM image showing multicycle carbonation and decarbonation of CaO formed upon decomposition of CaAc carried out using the ex-sit E-cell technique: (a & b) 1st calcination at 800 °C using the E-cell with (c) corresponding SAED pattern for (a) showing rings indexed to CaO 'o' (ICDD ref: 04-003-7161 [226]) and $Ca(OH)_2$ 'Δ' (ICDD ref: 01-084-1263 [289]). Diffraction only due to these phases is detected with labels assigned to rings.

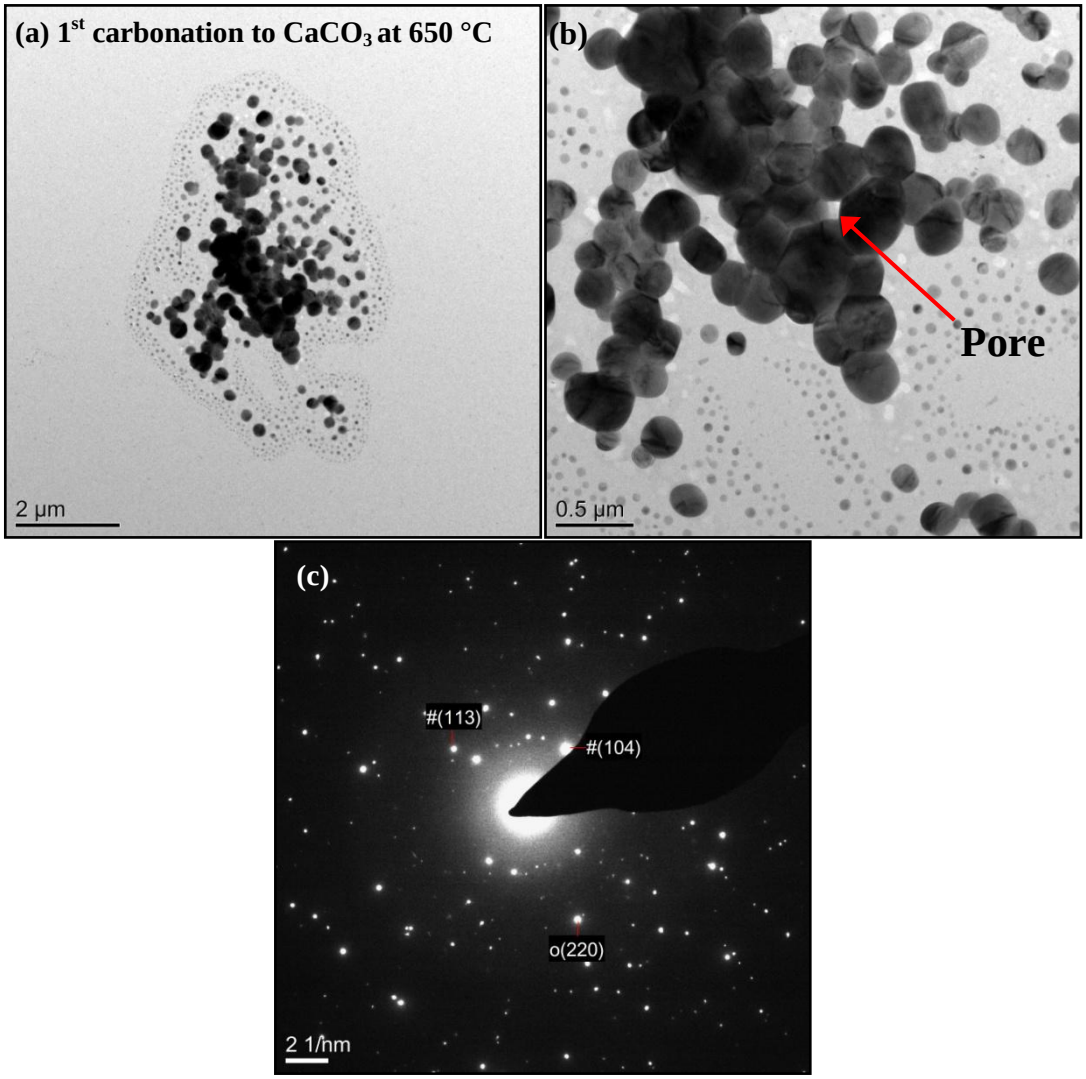

Figure 5.35: Bright field TEM images showing multicycle carbonation and decarbonation of CaO formed upon decomposition of CaAc carried out using the ex-sit E-cell technique: (a & b) first carbonation at 650 °C for 5 mins to form $CaCO_3$ with (c) orresponding SAED pattern for (a) showing spots indexed to $CaCO_3$ '#' (ICDD ref: 00-005-0586 [291]) and CaO 'o' (ICDD ref: 04-003-7161 [226]). Diffraction only due to these phases is detected with labels assigned to spots on rings.

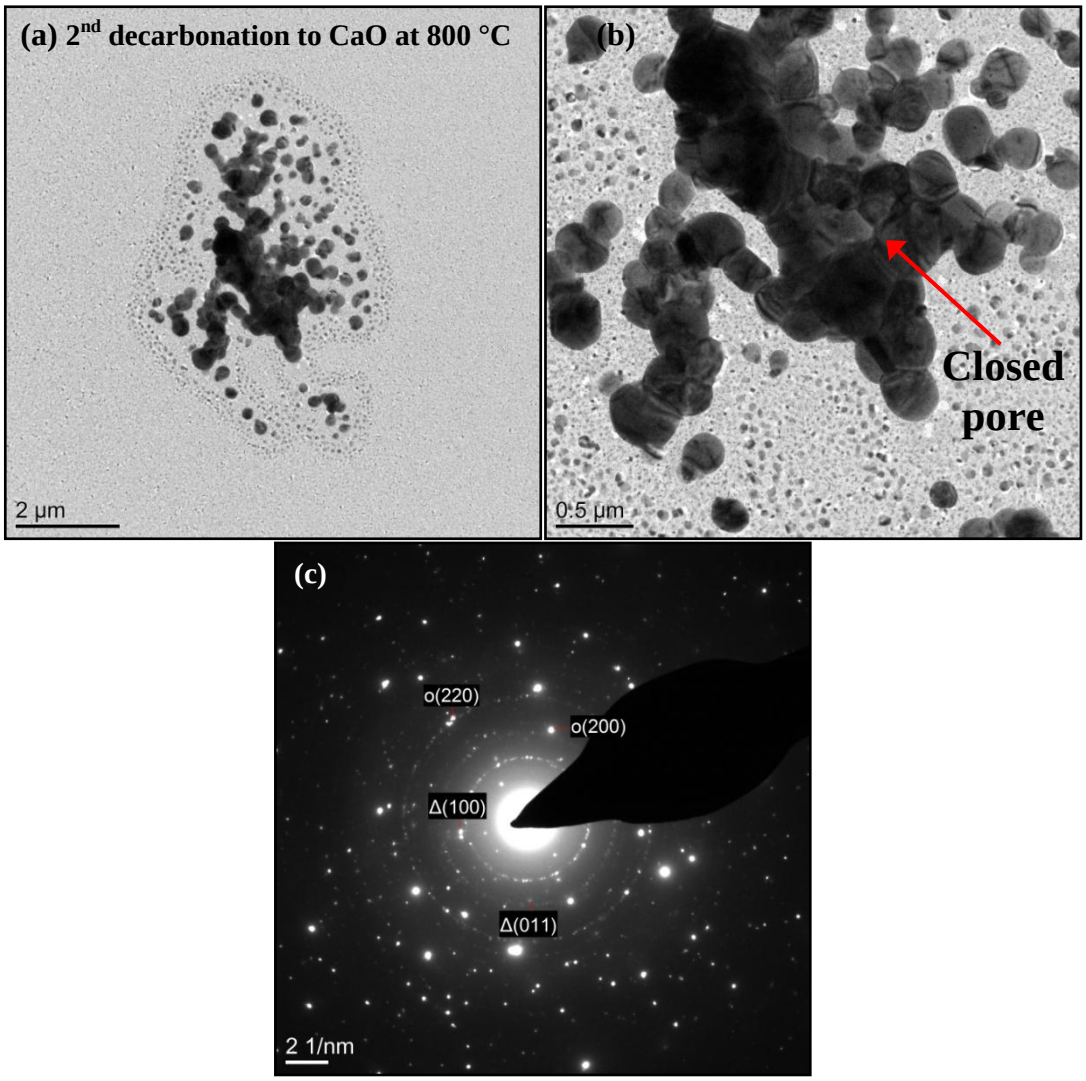

Figure 5.36: Bright field TEM images showing multicycle carbonation and decarbonation of CaO formed upon decomposition of CaAc carried out using the ex-sit E-cell technique: (a & b) 2nd decarbonation at 800 °C to CaO with (c) corresponding SAED pattern for (a) showing rings indexed to CaO 'o' (ICDD ref: 04-003-7161 [226]). Diffraction due to these phases is detected with labels assigned to spots rings. Rings (unlabelled) are also detected that match contaminant Mo-based particles analysed in Figure 5.39.

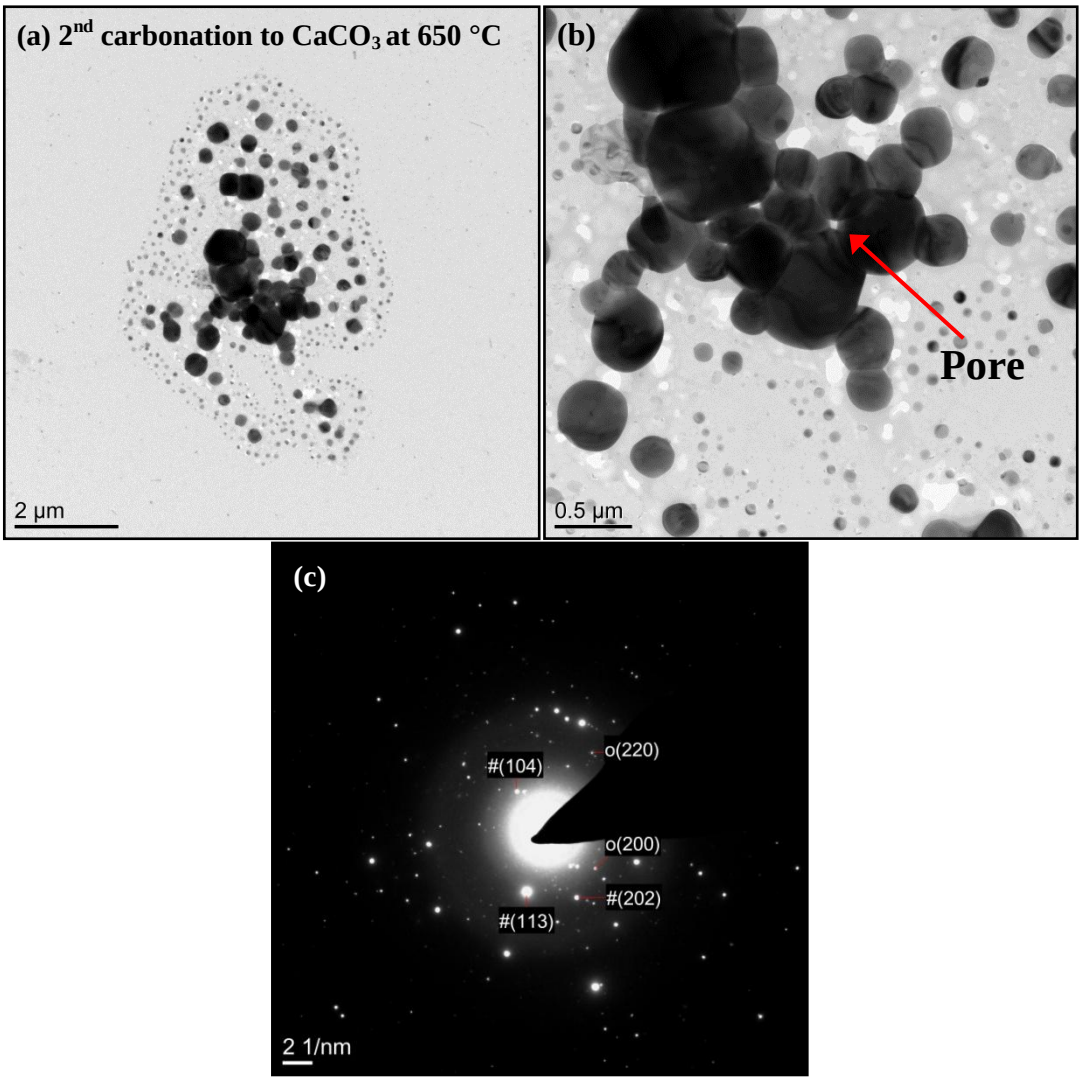

Figure 5.37: Bright field TEM images showing multicycle carbonation and decarbonation of CaO formed upon decomposition of CaAc carried out using the ex-sit E-cell technique: (a & b) 2nd carbonation at 650 °C for 5 mins with (m) corresponding SAED pattern for (a) showing spots indexed to $CaCO_3$ '#' (ICDD ref: 00-005-0586 [291]) and CaO 'o' (ICDD ref: 04-003-7161 [226]). Diffraction only due to these phases is detected with labels assigned to spots on rings.

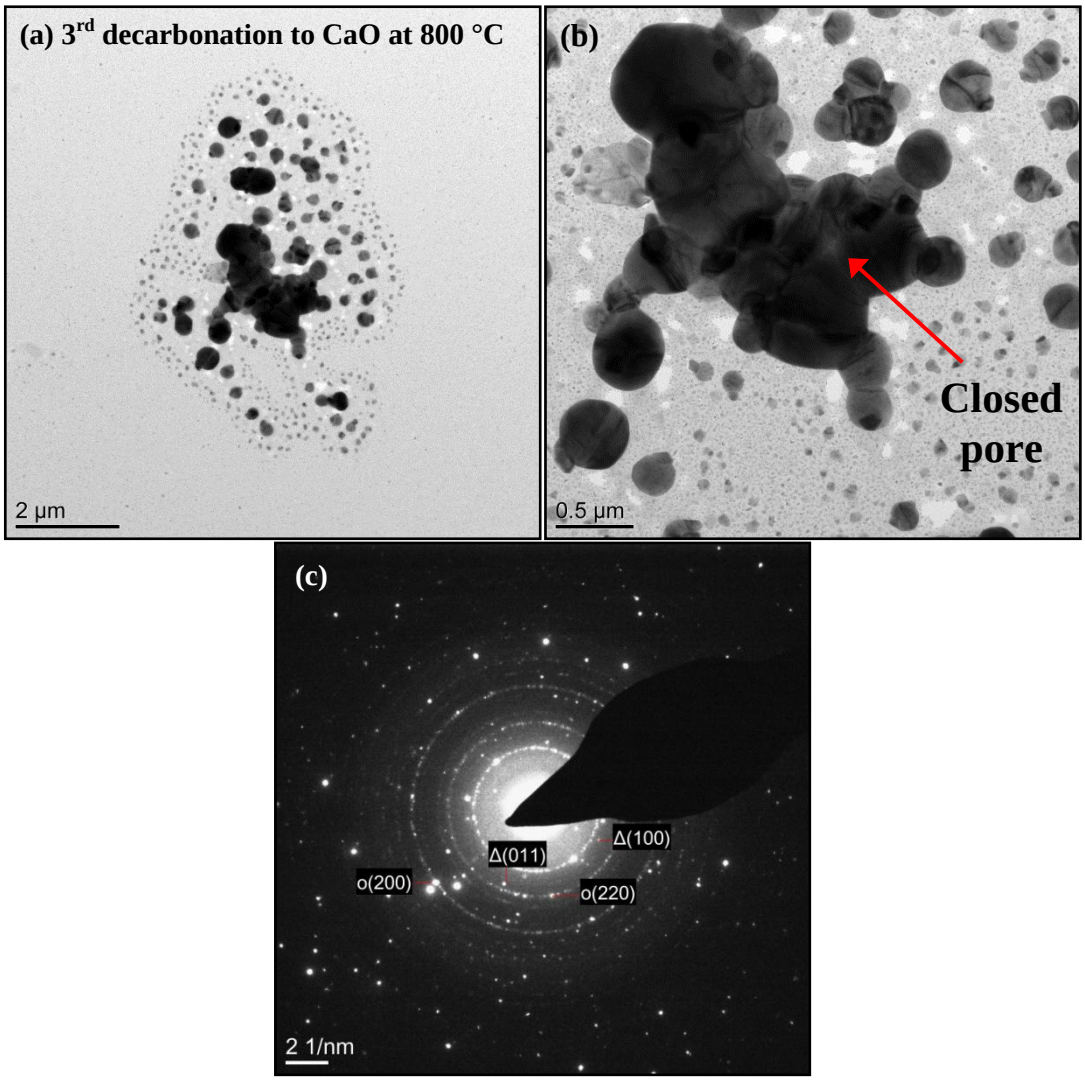

Figure 5.38: Bright field TEM images showing multicycle carbonation and decarbonation of CaO formed upon decomposition of CaAc carried out using the ex-sit E-cell technique: (a & b) 3rd decarbonation at 800 °C with (c) corresponding SAED pattern for (a) showing spots indexed to CaO 'o' (ICDD ref: 04-003-7161 [226]). Diffraction due to these phases is detected with labels assigned to spots rings. Rings (unlabelled) are also detected that match contaminant Mo-based particles analysed in Figure 5.39.

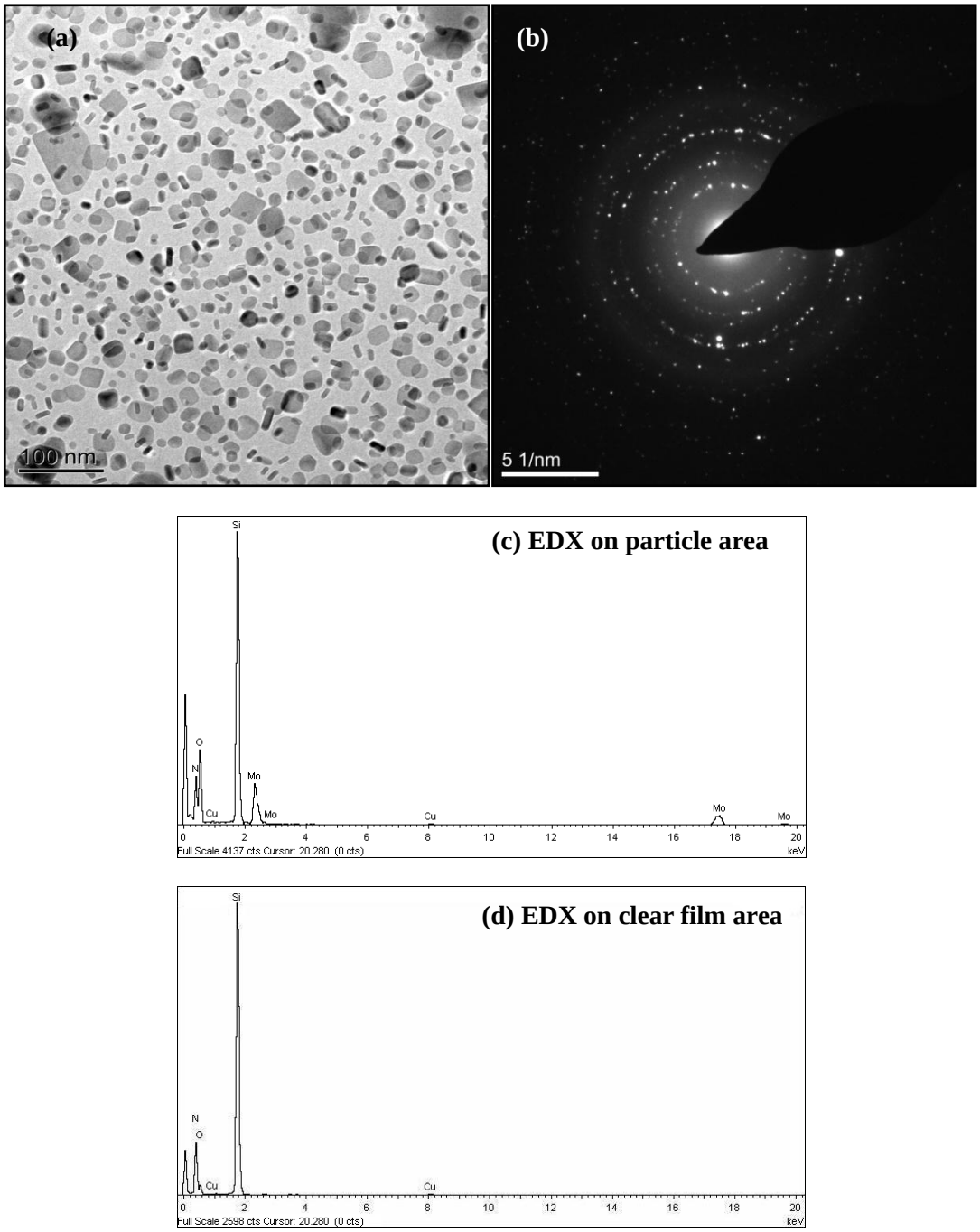

Figure 5.39: (a) Small (< 50nm) contamination particles containing Mo, with unassigned SAED pattern insert (b). Particles formed upon decarbonation at 800 °C during E-cell experiment. (c) EDX spectrum taken over an isolated area of particles in (a) confirming presence of Mo (large Si peak is attributed to the SiN film on the TEM grid). (d) EDX of a particle-free area of the SiN support film.

5.6. Particle spacer materials for modification of CaO sorbents for CO_2 sequestration

Sorbent-spacer blend materials have been prepared with the aim of reducing the decline in CO_2 capture capability with increasing carbonation/decarbonation cycles. It is proposed that the addition of spacer materials could reduce the amount of particle densification observed upon carbonation and subsequent decarbonation during multicycle CO_2 capture, and subsequently retain the sorbent CO_2 capture capability with progressive cycles.

Zirconia-based sorbent additives have demonstrated high performance and stability in multicycle CO_2 capture capability [276]. Resistance to sintering at high temperatures has been demonstrated using $CaZrO_3$, which acts as an inert barrier that prevents CaO particle sintering [277]. Here, the use of partially stabilised zirconia (PSZ) particles, as an additive to CaO powder sorbents, aims to utilise a phase transformation upon cooling (after decarbonation) that may trigger micro-cracking of any sintered CaO-zirconia sorbent, opening inter-particle pores and increasing the sorbent surface area for subsequent carbonation.

Four zirconia-based spacer blend materials have been synthesised here and calcined at 800 °C, with a 70:30 wt% CaO:spacer in the final calcined product. A commercial yttria stabilised zirconia, YSZ (5.4% yttria, Goodfellow) was mixed with CaAc using a pestle and mortar (Sample 1). Similarly, CaAc was also mixed by the same method using a YSZ prepared via a hydrothermal route, (as previously outlined in Section 3.9.4; Sample 2).

Two further samples have been produced using CaAc (sample 3) and $Ca(OH)_2$ (sample 4) precursors which have been individually co-precipitated with $Zr(NO_3)_2$ and NH_4OH, forming $CaO:CaZrO_3$ in the final calcined product. Subsequent X-ray diffraction also revealed a small precipitation of ZrO_2 in the blend prepared using CaAc (see Section 5.6.1).

Mayenite ($Ca_{12}Al_{14}O_{33}$) has also been outlined as an effective material for the enhancement of multicycle CO_2 capture due to its ability to inhibit sintering by providing a stable framework [130, 292]. A 75:25 wt% CaO:Mayenite blend (sample 5) has been provided courtesy of Dr Roger Molinder of the Energy Research Institute, University of Leeds, as prepared according to the solution preparation route outlined in reference [190]. This sorbent blend will also be analysed here for its multicycle CO_2 capture capability.

All five sorbent spacer materials are outlined in Table 5.7.

Table 5.7: CaO:spacer materials for CO_2 capture.

Sample Number	CaO precursor	Spacer material	Preparation method	CaO:spacer (wt%)	CaO:spacer (vol%)
1	**CaAc**	YSZ (Goodfellow, 5.4 wt% yttria)	Mixed by pestle and mortar grinding with a small inclusion of ethanol	70:30	80:20
2	**CaAc**	Hydrothermally prepared YSZ (hYSZ)	Mixed by pestle and mortar grinding with a small inclusion of ethanol	70:30	80:20
3	**CaAc**	$CaZrO_3$ + small formation of ZrO_2	Solution precipitation using $Zr(NO_3)_2$ + NH_4OH precursors.	70:30 (25% $CaZrO_3$ + 5% ZrO_2)	79:21 (18% $CaZrO_3$ + 3% ZrO_2)
4	**$Ca(OH)_2$**	$CaZrO_3$	Solution precipitation using $Zr(NO_3)_2$ + NH_4OH precursors.	70:30	84:16
5	**CaO**	Mayenite ($Ca_{12}Al_{14}O_{33}$)	Solution precipitation method outlined by [190].	75:25	72:28

Preliminary analysis of the commercial YSZ and the hydrothermally prepared YSZ (hYSZ) has been carried out by XRD and TEM, with data shown in Figure 5.40 and Figure 5.41 respectively. X-ray diffraction patterns for the commercial YSZ and the hYSZ are shown in Figure 5.40. The commercial YSZ shows diffraction peaks indexed due to tetragonal yttrium zirconium oxide (ICDD ref: 04-008-7255 [293]) and also monoclinic zirconium oxide, ZrO_2 (ICDD ref: 04-013-4343 [294]). Diffraction peaks are sharp suggesting a well crystallised phase, which is confirmed by subsequent selected area electron diffraction in the TEM, Figure 5.41. TEM imaging of the commercial YSZ powder (Figure 5.41) shows large

crystals (typically 200 - 500 nm), with selected area electron diffraction confirming crystalline tetragonal zirconium yttrium oxide.

The X-ray diffraction pattern for the hYSZ shows diffraction peaks indexed to cubic zirconium yttrium oxide (ICDD ref: 01-077-2112 [295]), as would be expected for 15.6 wt% Y_2O_3-ZrO_2, significant line broadening here can be attributed to a small crystallite size, which, calculated using the Scherrer formula is approximately 5 – 6 nm. TEM imaging (Figure 5.41) confirms a small crystallite size, with particles typically < 10 nm. These results are in good agreement with previously data reported for YSZ synthesised by this hydrothermal route [169]. TEM images (Figure 5.41) show the differences in particle size between the commercial YSZ and the hYSZ, with the commercial YSZ showing larger particles (typically 200 - 500 nm), and the hYSZ showing nanosized single crystals (typically < 10 nm), as expected from this preparation route [169].

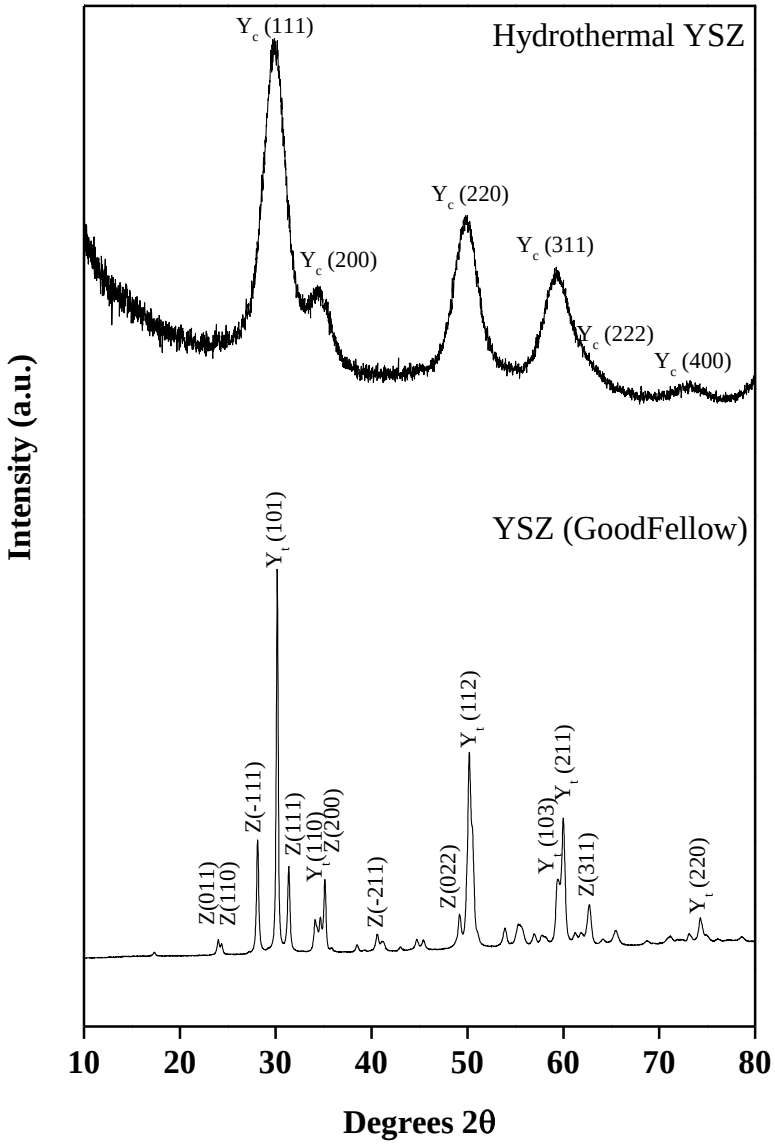

Figure 5.40: XRD patterns for commercial YSZ (Goodfellow) and hydrothermally produced YSZ (hYSZ). Peaks labelled 'Y_c' are indexed to cubic zirconium yttrium oxide, ICDD ref: 01-077-2112 [295]. Peaks labelled 'Y_t' are indexed to tetragonal zirconium yttrium oxide, ICDD ref: 04-008-7255 [293]. Peaks labelled 'Z' denote monoclinic zirconium oxide, ZrO_2, ICDD ref: 04-013-4343 [294]. Full peak data in the appendix, Tables A31 and A32.

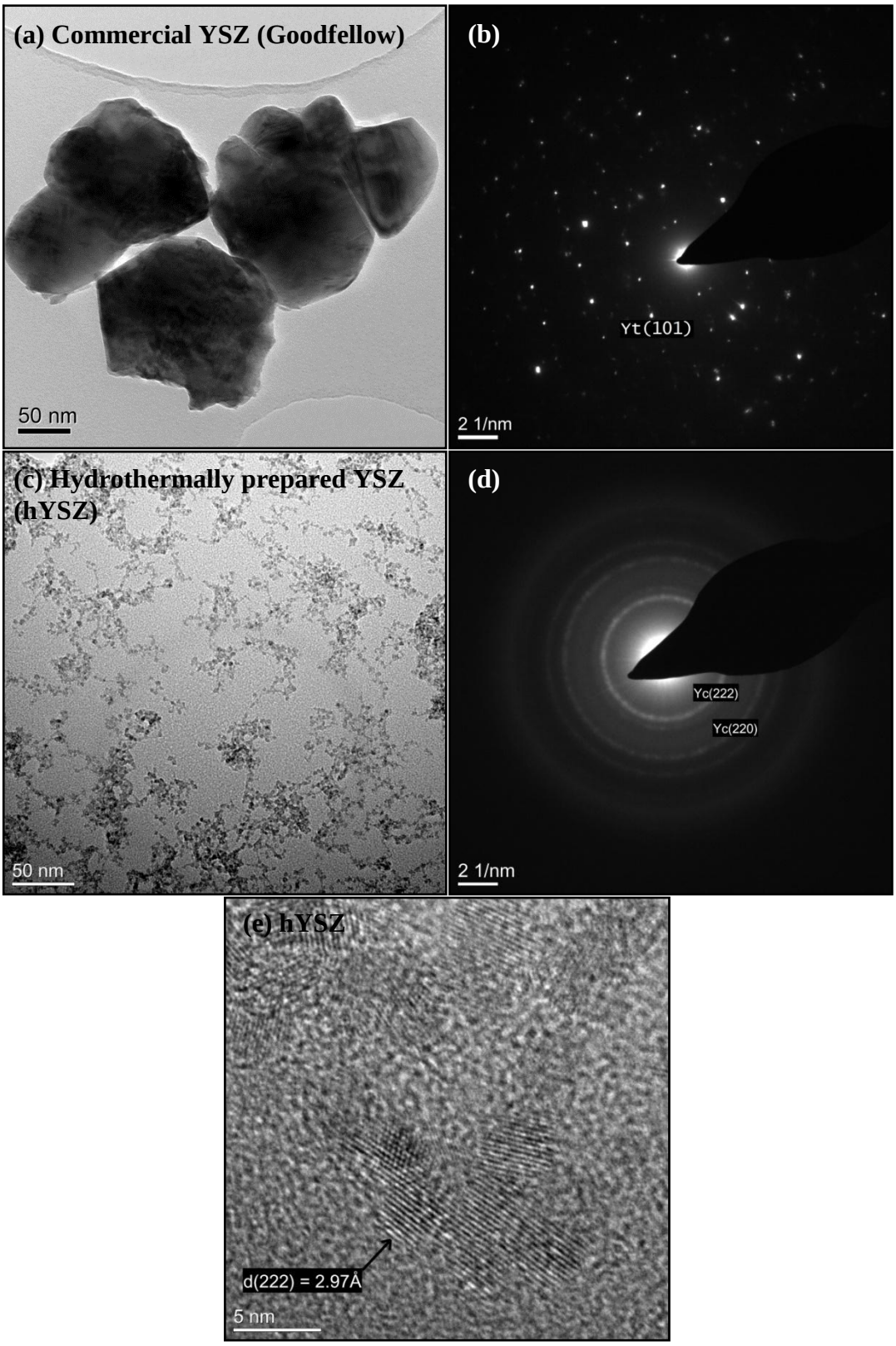

Figure 5.41: Bright field TEM image of (a) commercial YSZ (Goodfellow) with (b) SAED showing diffraction spots due to tetragonal YSZ. (c) shows bright field TEM image of YSZ prepared by a hydrothermal method (hYSZ) with (d) SAED showing diffraction rings due to cubic YSZ (ICDD ref: 01-077-2112 [295]). (e) shows HRTEM image of the hYSZ confirming < 5 nm crystallite size and d-spacing indexed to the cubic YSZ (222) plane.

5.6.1. X-ray diffraction analysis of CaO:spacer materials

X-ray diffraction patterns for all CaO:spacer materials (samples 1-5) calcined at 800 °C are shown in Figure 5.42. Sample 1 (CaO + YSZ) shows sharp diffraction peaks of calcium oxide (ICDD ref: 04-003-7161 [226]) and zirconium yttrium oxide (ICDD ref: 01-070-4428 [296]). Faint peaks due to $Ca(OH)_2$, (ICDD ref: 01-084-1263 [289]) are evident, suggesting a small amount of hydration of CaO.

The XRD pattern for sample 2 (CaO + hYSZ) show sharp diffraction peaks due to CaO (ICDD ref: 04-003-7161 [226]) with small broad diffraction peaks due to $Ca(OH)_2$, (ICDD ref: 01-084-1263 [289]) caused by hydration of the oxide. Small broad diffraction peaks for cubic zirconium yttrium oxide, (ICDD ref: 01-077-2112 [295]) are observed.

The XRD pattern for sample 3 (Zr-doped CaO: from a CaAc precursor) displays sharp diffraction peaks due to CaO (ICDD ref: 04-003-7161 [226]) along with small broad diffraction peaks due to zirconium oxide, ZrO_2 (ICDD ref: 04-013-4343 [294]) and also small diffraction sharp diffraction peaks due to calcium zirconium oxide, $CaZrO_3$, (ICDD ref: 04-010-6398 [297]).

The XRD pattern for sample 4 (Zr-doped CaO: from a $Ca(OH)_2$ precursor) displays sharp diffraction peaks due to CaO (ICDD ref: 04-003-7161 [226]) with also diffraction peaks due to calcium zirconium oxide, $CaZrO_3$, (ICDD ref: 04-010-6398 [297]). Diffraction peaks due to ZrO_2 were not observed.

The XRD pattern for sample 5 (CaO:Mayenite) displays sharp diffraction peaks due to CaO (ICDD ref: 04-003-7161 [226]) with small broad diffraction peaks due to $Ca(OH)_2$, ICDD ref: 01-084-1263 [289]. Sharp diffraction peaks due to mayenite ($Ca_{12}A_{14}O_{33}$) are also observed 04-014-8825 [298].

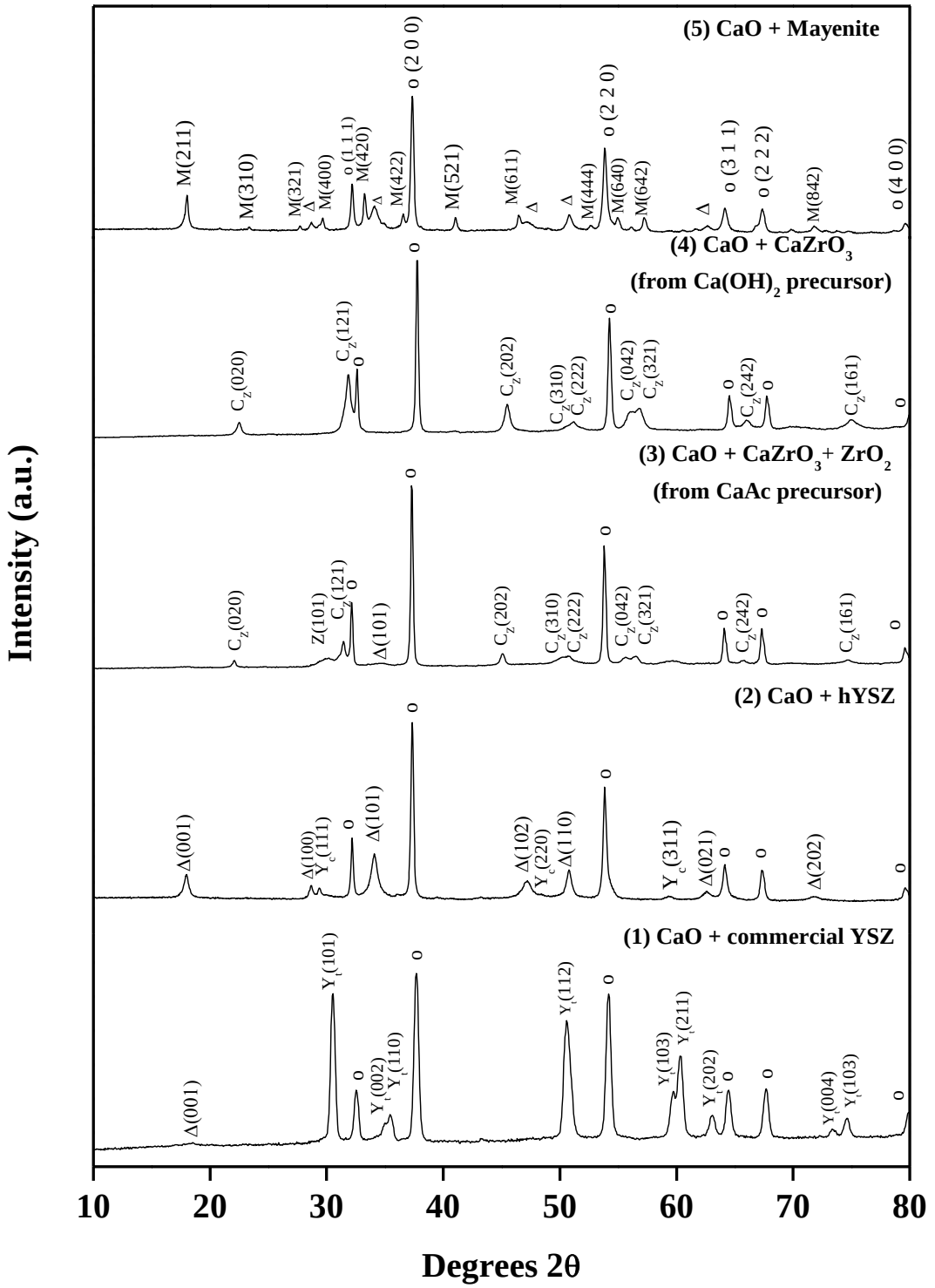

Figure 5.42: XRD patterns for CaO:spacer material samples 1-5, where (1) shows CaO:YSZ, (2) shows CaO:hYSZ, (3) shows CaO precipitated with $Zr(NO_3)_2$, using a CaAc precursor, (4) shows CaO precipitated with $Zr(NO_3)_2$, using a $Ca(OH)_2$ precursor and (5) shows CaO:Mayenite ($Ca_{12}Al_{14}O_{33}$). Peaks labelled 'M' are indexed to mayenite, $Ca_{12}Al_{14}O_{33}$, ICDD ref: 04-014-8825 [298]. Peaks labelled 'o' are indexed to calcium oxide, CaO, ICDD ref: 04-003-7161 [226]. Peaks labelled 'Δ' are indexed to calcium hydroxide, $Ca(OH)_2$, ICDD ref: 01-084-1263 [289]. Peaks labelled 'Y_t' are indexed to tetragonal zirconium yttrium oxide, ICDD ref: 04-008-7255 [293]. Peaks labelled 'Y_c' are indexed to cubic zirconium yttrium oxide, ICDD ref: 01-077-2112 [295]. Peaks labelled 'Z' denote zirconium oxide, ZrO_2, ICDD ref: 04-013-4343 [294]. Peaks labelled 'C_Z' are indexed to calcium zirconium oxide, $CaZrO_3$, ICDD ref: 04-010-6398 [297]. Full peak list data available in the appendix, Tables A33 to A37.

5.6.2. CO_2 carbonation-calcination cycles using CaO-spacer materials

The previously prepared CaO-spacer material blends have been analysed by TGA for their regenerability using the multicycle CO_2 capture process, following the procedure previously outlined in Section 5.5.2. Results are displayed in Figure 5.43 with full molar conversion, χ, data shown in Table 5.8. Data for the previously analysed unmodified CaAc are included for comparative purposes.

The results here show that none of the CaO:spacer blend materials provide a superior performance with regards to overall CO_2 capture, over the first 9 cycles, than the single, unmodified CaO sorbent. However the single CaO sorbent displays the largest decrease in χ (0.32) of all samples after 9 cycles. The CaAc:hYSZ powder provided the highest overall molar conversion values of all blend materials (0.83 in the first cycle, falling to 0.52 after 9 cycles), however the amount of decay closely matched that of the initial raw sorbent (0.31) and so it can be assumed that the spacer material has had little to no affect on restricting progressive sorbent sintering.

The remaining CaO:blend materials all showed lower molar conversion values per cycle, however the overall decay over 9 cycles was notably lower with CaAc:YSZ, CaAc:$CaZrO_3$:ZrO_2, CaO:Mayenite and $Ca(OH)_2$:$CaZrO_3$ showing decreases of 0.17, 0.20, 0.12 and 0.10 respectively. These results suggest, most significantly with regards to powder blends synthesised using CaAc, that sorbent sintering is possibly being restricted by the presence of the spacer materials as the cycle by cycle decay in overall CO_2 uptake is lower than that for the raw CaAc produced CaO sorbent. Cycle analysis using the E-cell TEM technique will be carried out using these blends to investigate this potential effect further.

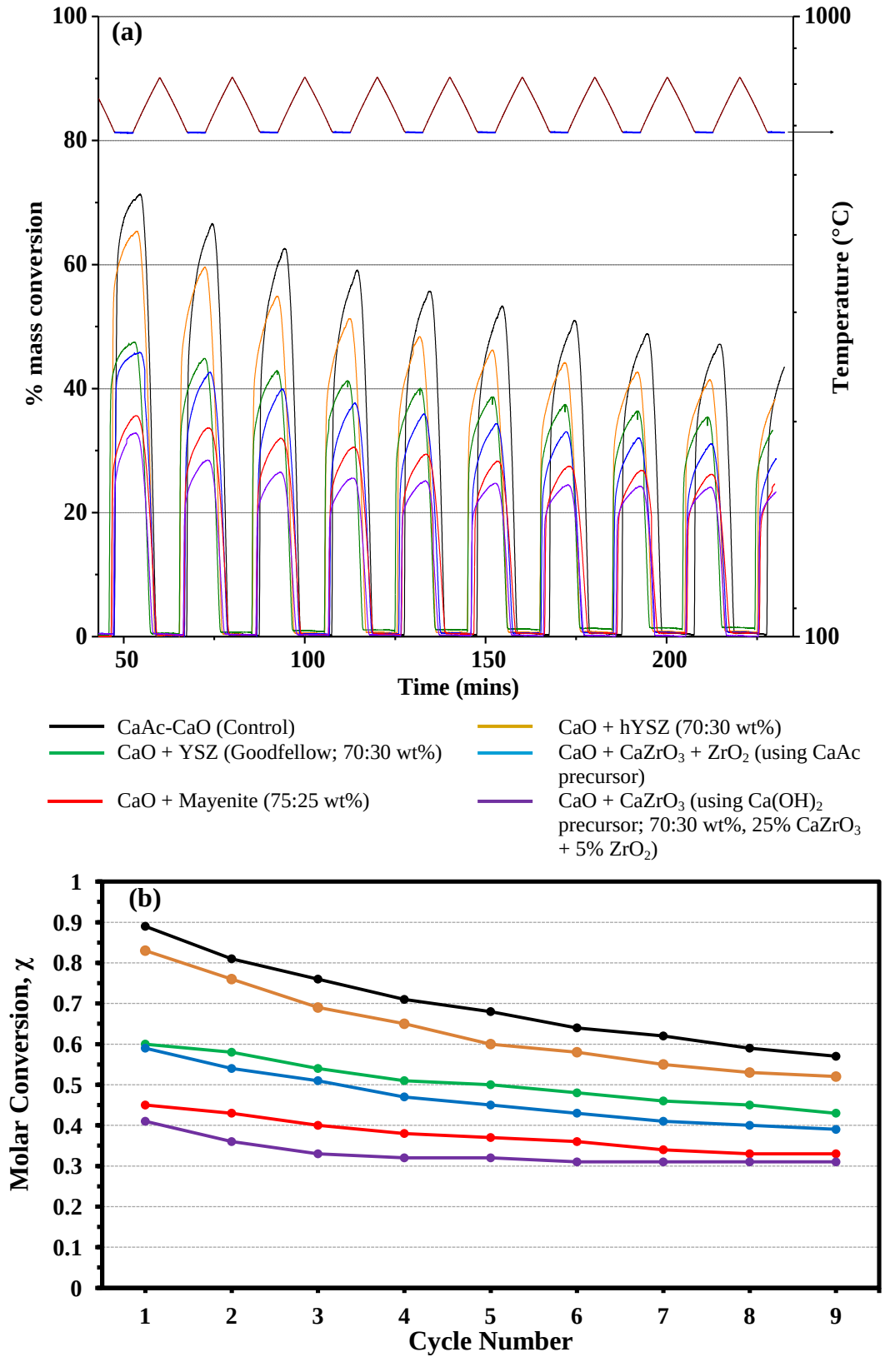

Figure 5.43: (a) Degradation in CO_2 capture capacity for as received CaAc and CaO:spacer material blends using multicycle CO_2 capture by TGA. Decomposition of starting material, and subsequent carbonated sorbents took place at 800 °C under N_2. Carbonation took place at 650 °C for 5 mins. 0% carbonation conversion indicates fully calcined material (CaO + spacer) produced via decomposition of calcium acetate hydrate ($Ca(CH_3COO)_2 \cdot xH_2O$) at 800 °C. (b) displays molar conversion data per cycle for each sample.

Table 5.8: CaO to $CaCO_3$ molar conversion data for as received CaAc and CaO:spacer material blends.

		Cycle Number								
Sample		**1**	**2**	**3**	**4**	**5**	**6**	**7**	**8**	**9**
CaAc	Conversion due to uptake (mass%)	71.21	66.37	60.96	58.21	55.04	52.51	50.11	47.92	46.39
	Molar conversion ratio, χ	0.89	0.81	0.76	0.71	0.68	0.64	0.62	0.59	0.57
CaO + hYSZ	Conversion due to uptake (mass%)	65.35	59.55	58.56	51.28	48.35	46.19	44.20	42.61	41.43
	Molar conversion ratio, χ	0.83	0.76	0.69	0.65	0.60	0.58	0.55	0.53	0.52
CaO + YSZ (Goodfellow)	Conversion due to uptake (mass%)	47.46	44.85	42.26	40.24	39.00	37.43	36.24	35.00	34.04
	Molar conversion ratio, χ	0.60	0.58	0.54	0.51	0.50	0.48	0.46	0.45	0.43
CaO + $CaZrO_3$ + small amount of ZrO_2 (using CaAc precursor)	Conversion due to uptake (mass%)	55.12	53.90	52.89	52.02	51.35	50.78	50.28	49.90	49.55
	Molar conversion ratio, χ	0.59	0.54	0.51	0.47	0.45	0.43	0.41	0.40	0.39
CaO-Mayenite	Conversion due to uptake (mass%)	35.63	33.65	31.98	30.52	29.43	28.31	27.47	26.82	26.16
	Molar conversion ratio, χ	0.45	0.43	0.40	0.38	0.37	0.36	0.34	0.33	0.33
CaO + $CaZrO_3$ (using $Ca(OH)_2$ precursor)	Conversion due to uptake (mass%)	32.83	28.44	26.51	25.56	25.11	24.73	24.45	24.26	24.11
	Molar conversion ratio, χ	0.41	0.36	0.33	0.32	0.32	0.31	0.31	0.31	0.31

5.6.3. E-cell analysis of CaO:YSZ sorbent/ spacer blend

The E-cell technique in the TEM, previously described in Section 3.8.1.2, has been applied using the CaO:YSZ sorbent/spacer material synthesised in Section 3.9.2. Results of the E-cell multicycle experiment are shown in Figures 5.44 - 5.46.

Figure 5.44a and b show bright field TEM images of the CaO:YSZ powder after the first decomposition at 800 °C using the E-cell. Selected area electron diffraction (Figure 5.44c) confirms diffraction spots for tetragonal YSZ (ICDD ref: 04-008-7255 [293]) and a small number of spots due to the most intensely diffracting plane (200) of CaO (ICDD ref: 04-003-7161 [226]).

Figure 5.44a and b display a large cluster of particles ~100 – 300 nm in size; these were confirmed by SAED and spot EDX as particles of YSZ, agreeing with the previous TEM analysis on the material (Figure 5.41). Pores between particles are observed up to ~150 nm in size. A higher magnification image of the CaO:YSZ blend is shown in Figure 5.44b, and shows the presence of a fine layer of crystallites intimately mixed between the larger YSZ particles. Spot EDX of these crystallites confirmed a strong detection of calcium and oxygen, and similarly the SAED pattern (Figure 5.44c) displayed some diffraction spots due to CaO, and it is therefore assumed that this fine layer of particles is CaO.

The sample after the first carbonation at 650 °C is shown in Figure 5.45a and c with respective SAED patterns shown in Figure 5.45b and d, which confirmed the YSZ phase along with diffraction spots due to $CaCO_3$. From Figure 5.45a it is observed that the porosity between the particles within the bulk area of the sample, seen previously in Figure 5.44a, have closed. Rounded, sintered particles of $CaCO_3$ are now observed, most noticeable at the edge of the bulk area, and also non-sintered round crystals of $CaCO_3$ observed surrounding the bulk area, these are displayed in

Figure 5.45c and confirmed at calcite by the SAED pattern in Figure 5.45e. Differentiation between YSZ particles and $CaCO_3$ particles can be made by the difference in mass-thickness contrast, where the $CaCO_3$ are notably lighter, and smaller.

The sample after the 2nd decarbonation at 800 °C, using the E-cell, is shown in Figure 5.46a-c, and more porosity is now observed in the bulk material, in comparison to the previously carbonated sample, Figure 5.45. These pores are of a similar size to those observed in the previously decarbonated sample (Figure 5.44), typically up to 150 nm, however they are fewer in number and the sample is more dense. Compared to the previous E-cell experiment using the unmodified CaO sorbent (Figure 5.36), decarbonation here appears to shows less sorbent densification.

The SAED pattern (Figure 5.46b) shows diffraction spots due reflections of the most intense planes of YSZ and CaO phases. The distribution of calcium and zirconium within the sample is highlighted by (k-shell) EDX mapping in Figure 5.47, acquired by scanning-TEM (STEM).

Small particles (< 50 nm) containing Mo were again detected as in the previous E-Cell experiment (see Figure 5.39); these are considered contaminants likely to be caused by sputtering from the E-cell furnace at high temperature, and are ignored here.

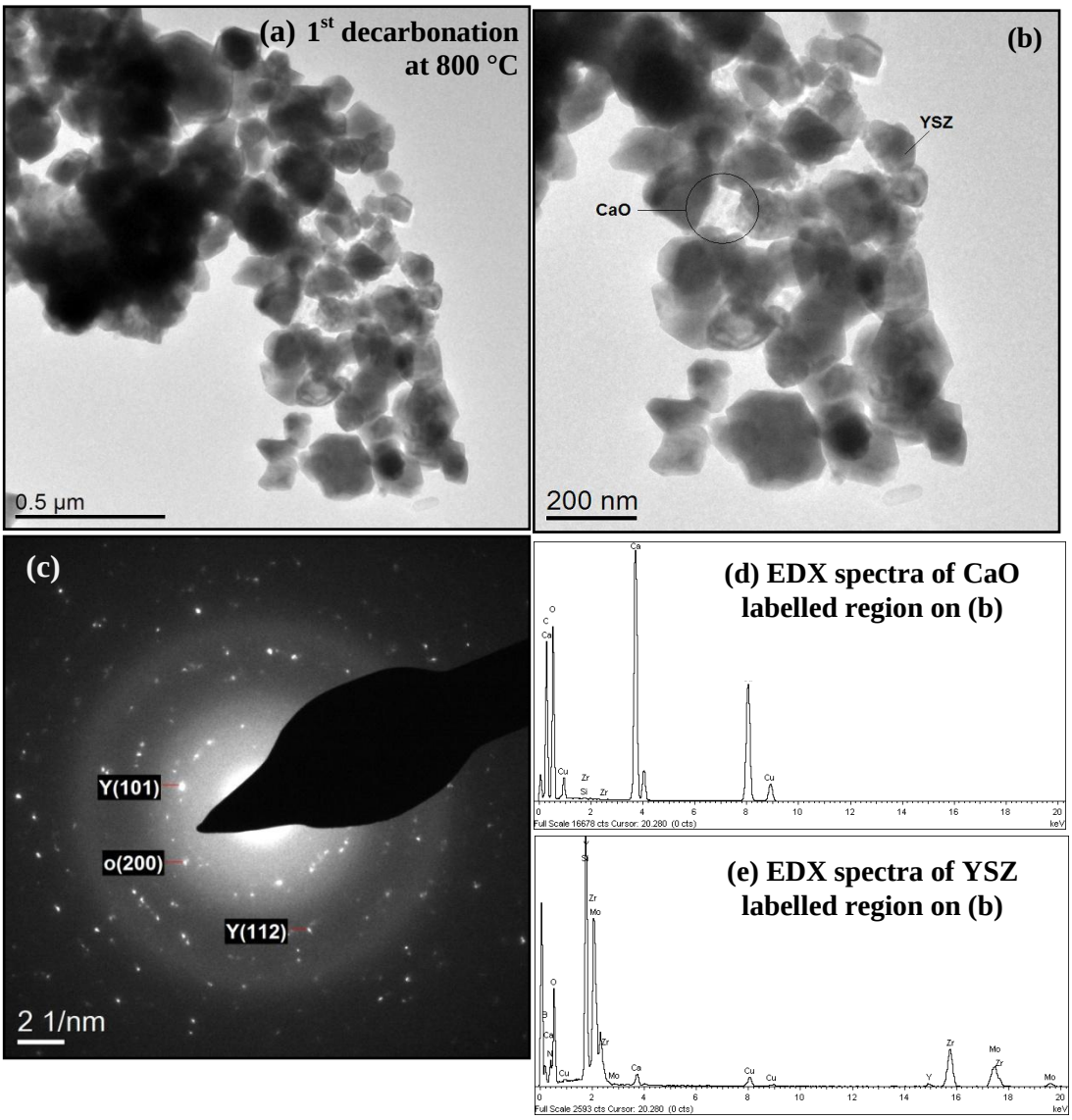

Figure 5.44: (a & b) Bright field TEM images showing CaO+YSZ after 1st decomposition at 800 °C (during E-cell multicycle CO_2 capture technique) with (c) SAED pattern confirming electron diffraction spots due to tetragonal YSZ 'Y' (ICDD ref: 04-008-7255 [293]) and CaO 'o' (ICDD ref: 04-003-7161 [226]). Rings only due to these phases are detected with labels assigned to spots on rings. (d) and (e) show corresponding EDX patterns for areas of CaO and YSZ labelled on (b). Presence of Mo attributed to sputtering of the E-cell furnace at 800 °C.

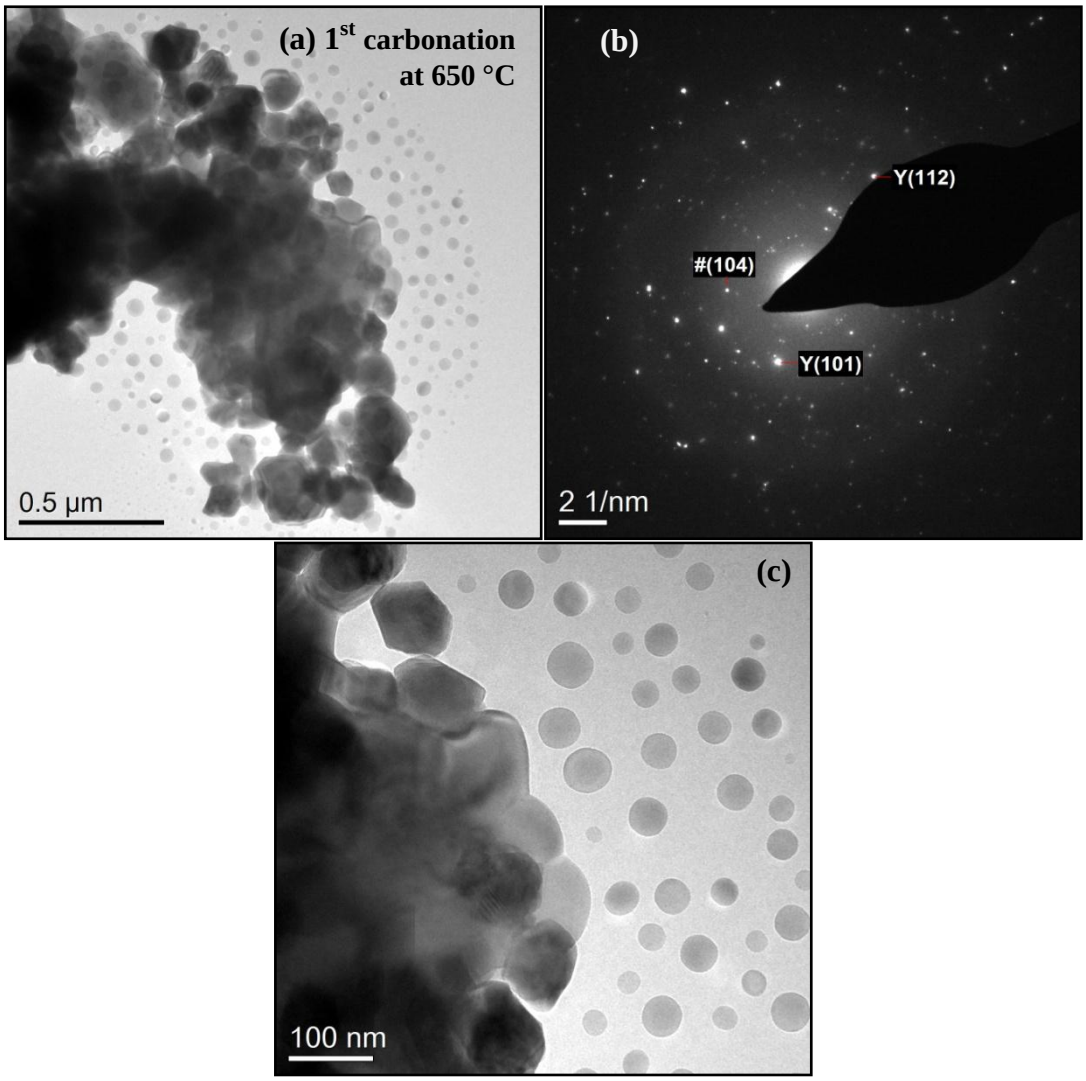

Figure 5.45: (a & c) Bright field TEM images showing CaO+YSZ after 1st carbonation at 650 °C using E-cell multicycle CO_2 capture technique, with (b) respective SAED pattern showing diffraction spots due to tetragonal YSZ 'Y' and $CaCO_3$ '#' (ICDD ref: 00-005-0586 [291]). Rings only due to these phases are detected with labels assigned to spots on rings.

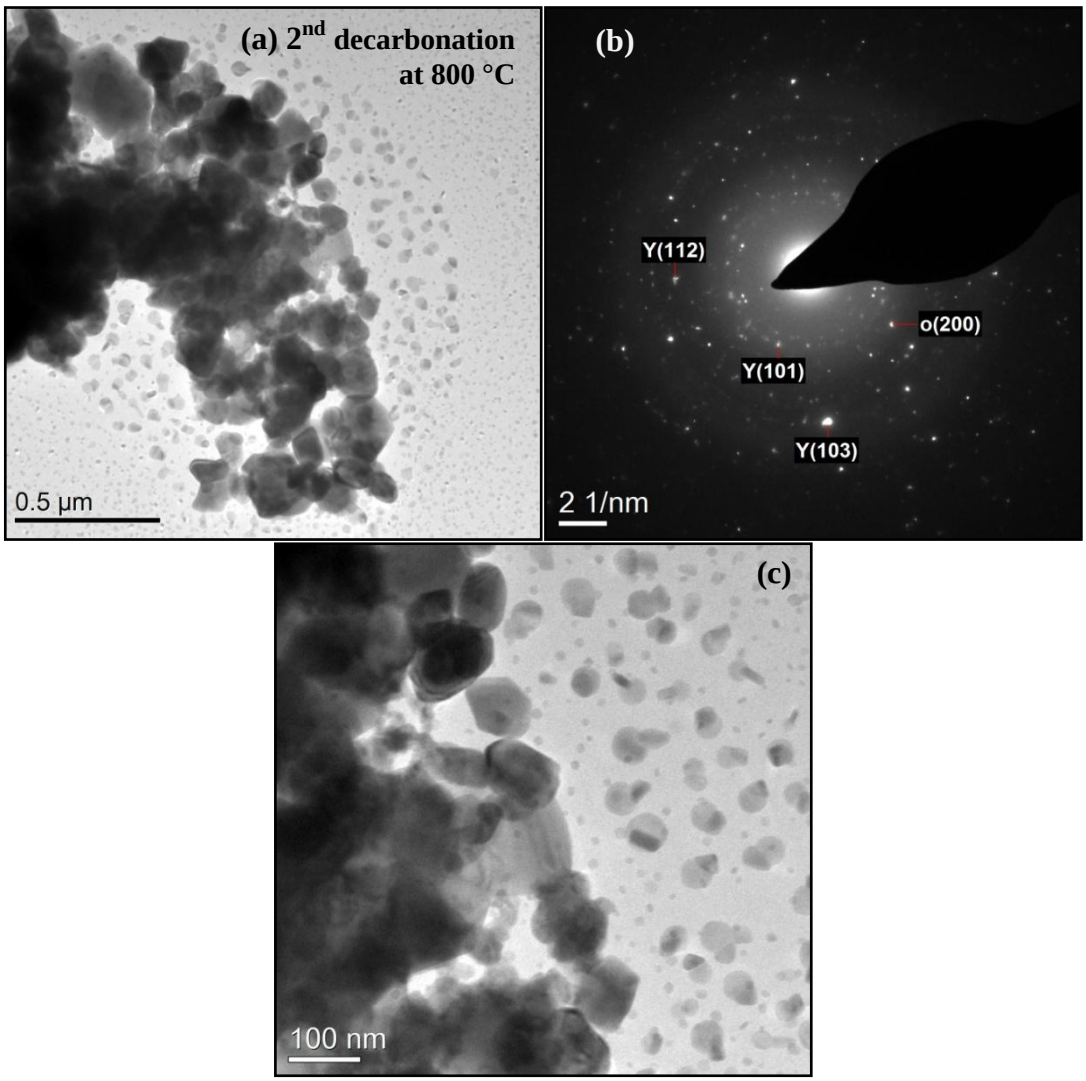

Figure 5.46: (a & c) Bright field TEM images showing CaO+YSZ after 2nd decarbonation at 800 °C using E-cell multicycle CO_2 capture technique, with (c) SAED pattern for (a) d) showing diffraction spots due to tetragonal YSZ 'Y' (ICDD ref: 04-008-7255 [293]) and CaO 'o' (ICDD ref: 04-003-7161 [226]). Rings only due to these phases are detected with labels assigned to spots on rings.

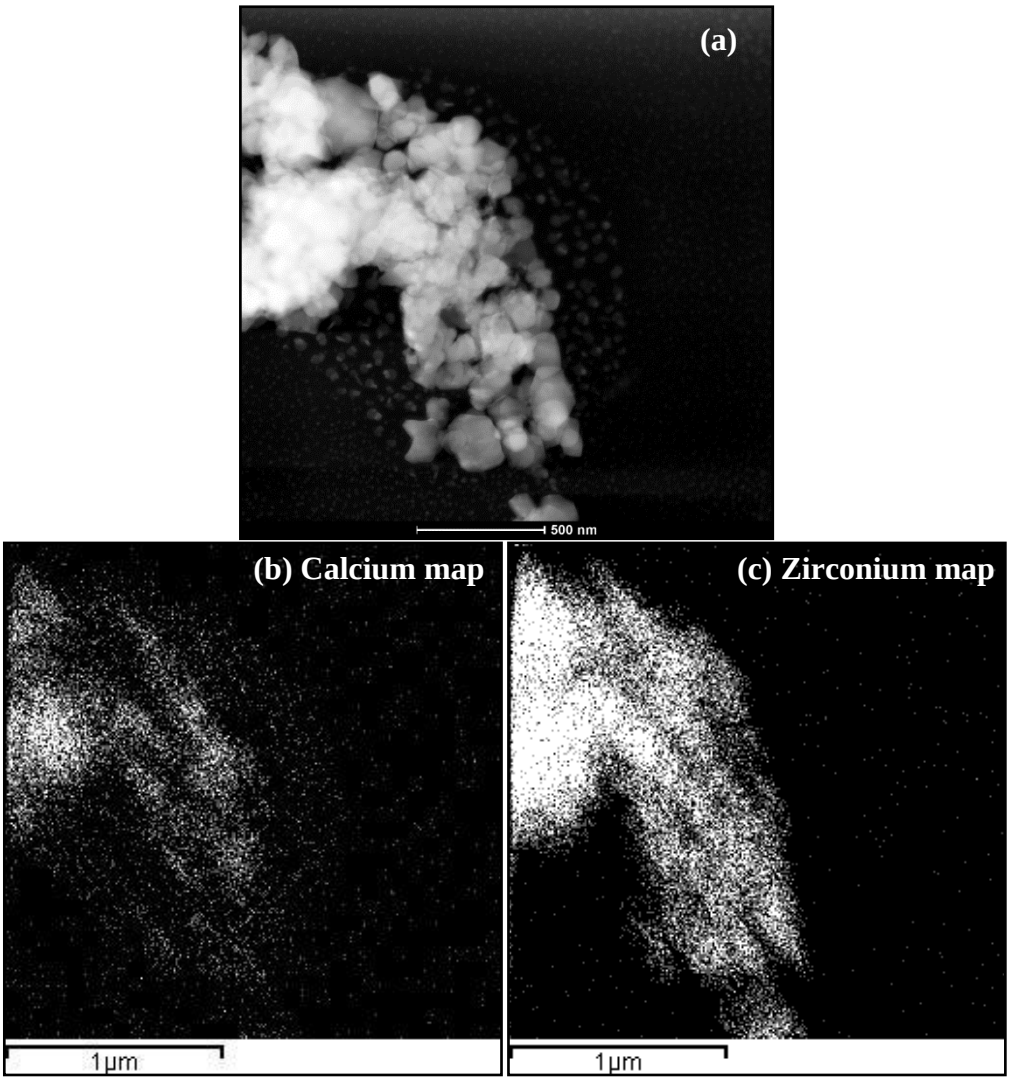

Figure 5.47: (a) STEM image showing CaO+YSZ after 2nd decarbonation at 800 °C using E-cell multicycle CO_2 capture technique, with EDX distribution maps for (b) calcium and (c) zirconium.

5.7. Discussion and final summary

This work has analysed the formation of a nanoparticulate CaO powder sorbent produced by the thermal decomposition of calcium acetate hydrate (CaAc) [299]. The capability for CO_2 capture using the CaO sorbent was investigated by thermogravimetric analysis (Figure 5.15 and Figure 5.23) with the morphological changes, at the nanoscale during carbonation and recarbonation, analysed by TEM. The regenerability of the CaO sorbent over multicycle carbonation and decarbonation cycles was also analysed by TGA (Figure 5.23). A high initial CO_2 capture capacity (molar conversion, χ, of CaO to $CaCO_3$ = 0.89) of the sorbent was followed by a significant decline after progressive cycles (χ = 0.57 after 9 cycles).

Microstructural analysis of decarbonated and carbonated samples at different cycle numbers of the multicycle CO_2 capture process (produced and monitored by TGA, Figure 5.23) by SEM and TEM are shown in Figures 5.27 to 5.29. Data shows crystal growth and expansion of $CaCO_3$ upon carbonation, leading to large amounts of crystal densification and sintering of $CaCO_3$ (Figure 5.29).

With progressive decarbonations, XRD and TEM analysis (Figures 5.25 and 5.28b, d, f and h) show the formation of increasing amounts of $Ca(OH)_2$ and a decrease in the overall crystallite size of the sorbent; with SEM (Figure 5.28a, c, e and g) highlighting increasing agglomeration, densification and a decrease in observed porosity. This densification inhibits the amount of carbonation on subsequent carbonation cycles, as is confirmed by the decreasing relative peak intensity ratio of the $CaCO_3$ to CaO principle reflexions (I_{CaCO_3}/I_{CaO}) measured by XRD (Figure 5.25 and 5.26). The analysis of the decarbonated samples by XRD, SEM and TEM is likely to have been significantly affected by varying amounts of uncontrolled sorbent hydration during storage, sample preparation and analysis.

The hydration of CaO has been modelled by Manzano *et al* (2012), who report an increasing displacement of Ca atoms with increasing hydration, and a dramatic change of surface structure due the adsorption of water monolayers and the formation of $Ca(OH)_2$ [132]. Figure 5.48 shows Manzano *et al's* model for CaO hydration [132], the model shows how Ca and O atoms in the first layer become distorted and, as water dissociates, hydrogen atoms penetrate further into the crystal forming hydroxyl groups in the second layer of CaO, leading to further displacement of Ca and O atoms in the second layer [132]. Manzano *et al* report a very short time, in the scale of nanoseconds, for the reaction to occur (hydration of CaO {001}) at room temperature and this rate is dependent on the levels of water in the surrounding atmosphere. It is a reasonable assumption that this effect has led to the significant structural differences observed between CaO sorbents produced in this study; varying levels of hydration could have occurred with uncontrolled water vapour exposure during storage, sample preparation and analysis, and even due to the varying vacuum levels between the E-cell and hot-stage TEM techniques.

This model also complements further research by Molinder *et al* (2012) who showed the growth of a $Ca(OH)_2$ shell around a nanoparticulate CaO core, following regeneration after carbonation [300]. This nanoscale core-shell structure generates strain in the $Ca(OH)_2$ lattice which led to particle fracture and the formation of smaller crystallites [300]. This description is consistent with the broad XRD peaks of the $Ca(OH)_2$ (Figure 5.25) observed in this work, and the small crystallite size of the decarbonated sorbents observed by TEM (Figure 5.28b, d, f and h). On the positive side, the likely fracturing of CaO nanoparticles due to hydration may offer improved regenerability of powder sorbents during multicycle CO_2 capture [300]. However this needs to be evaluated further since hydration will not have occurred during the TGA runs.

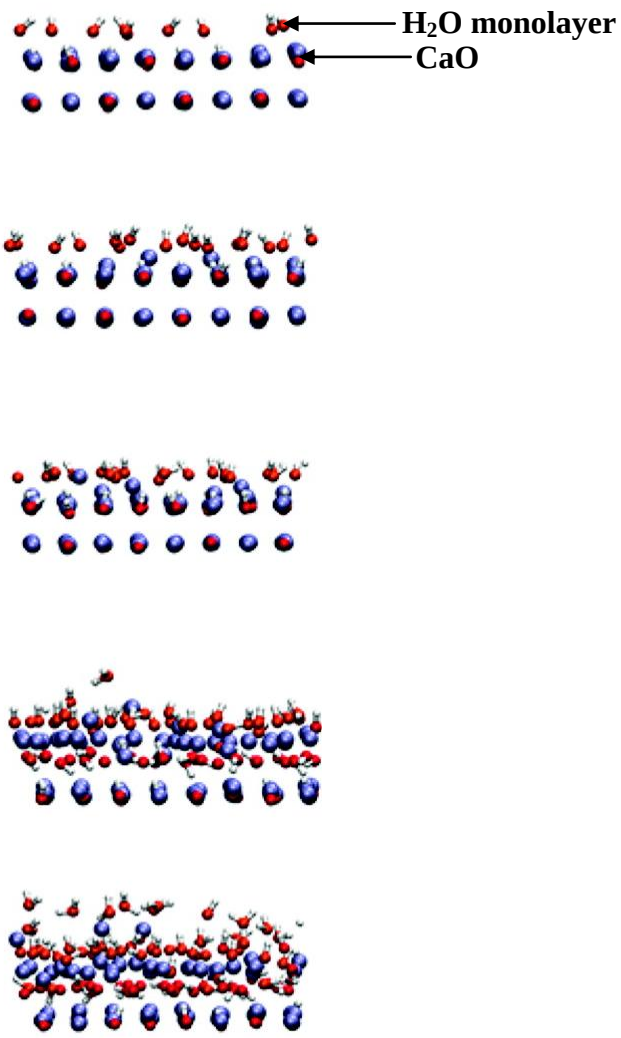

Figure 5.48: Molecular dynamics of increasing hydration of CaO by H_2O. Ca atoms = blue, O atoms = red, H atoms = white [132].

To study the rate of hydration for this study, a supplementary experiment has been carried out by TGA: a sample of CaAc was firstly decomposed (in N_2 at 800 °C), then carbonated (at 650 °C) and decarbonated (in N_2 at 800 °C), completing one capture complete cycle and forming a final CaO product. This CaO sample (starting mass = 4.55 mg) was then left in the TGA in air (flow rate 50 ml min^{-1}) for 4 hours, and a mass increase of 3.12% (mass = 4.69 mg) was observed. The sample was then removed from the TGA and left exposed to atmospheric conditions overnight (17 hours) on a lab workbench; the initial and final mass of the sample were recorded using a balance, with results showing a total mass increase of 39.85% (final mass =

6.30 mg). This corresponds to a molar conversion ratio for hydration, χ_h, of 1.20, where:

$$\chi_h = \frac{\text{mol } H_2O \text{ uptake}}{\text{starting mol CaO}} \quad (5.7)$$

These results are presented in Figure 5.49 and a full conversion to CaO upon decarbonation is indicated at 800 °C, prior to hydration being carried out.

X-ray diffraction of the resulting material (Figure 5.50) was measured 1 hour after the final balance measurement, with $Ca(OH)_2$ shown as the dominant phase and only small peaks due to CaO observed. Peaks assigned to $Ca(OH)_2$ are broad, indicating a fine crystallite size. A small intensity peak due to $CaCO_3$ is also observed, suggesting some pick-up of atmospheric CO_2; this result is likely to explain the > 1 molar conversion ratio, χ_h, for hydration. These results highlight the reactivity of nanoparticulate CaO when exposed to atmospheric gases.

TEM imaging was carried out within 1 hour of a sample being removed from the TGA (and stored in a desiccator) after the single carbonation/decarbonation cycle (Figure 5.51a), and then also of a sample exposed in air by TGA and then left overnight on a lab-bench (Figure 5.51b). For TEM sample preparation, both powder samples were simply dry-cast onto a TEM support film to avoid potential hydration if dispersed in less than 100% alcohol. The sample immediately removed from the TGA after decarbonation is assumed to be pure or near pure CaO based on the TGA mass loss during decarbonation (Figure 5.49). Imaging by TEM of this sample (Figure 5.51a) shows dense faceted crystals which are typically 100 – 200 nm in size.

The XRD pattern of the sample left out overnight (Figure 5.50) shows a dominant $Ca(OH)_2$ phase, with broad peaks indicating a fine crystallite size. By TEM (Figure 5.51b) only dense aggregates with significant diffraction contrast

within the particles were detected, which suggests polycrystalline $Ca(OH)_2$ particles or heavily strained $Ca(OH)_2$ particles are formed. Compared to the unhydrated sample (Figure 5.51a), the original particles appear more distorted and less faceted when hydrated, a result which is in good agreement with Manzano *et al's* model and Molinder *et al's* description for CaO hydration (Figure 5.48) [132, 300]. This is also consistent with the previously hydrated sorbents analysed by TEM in this study (Figure 5.28).

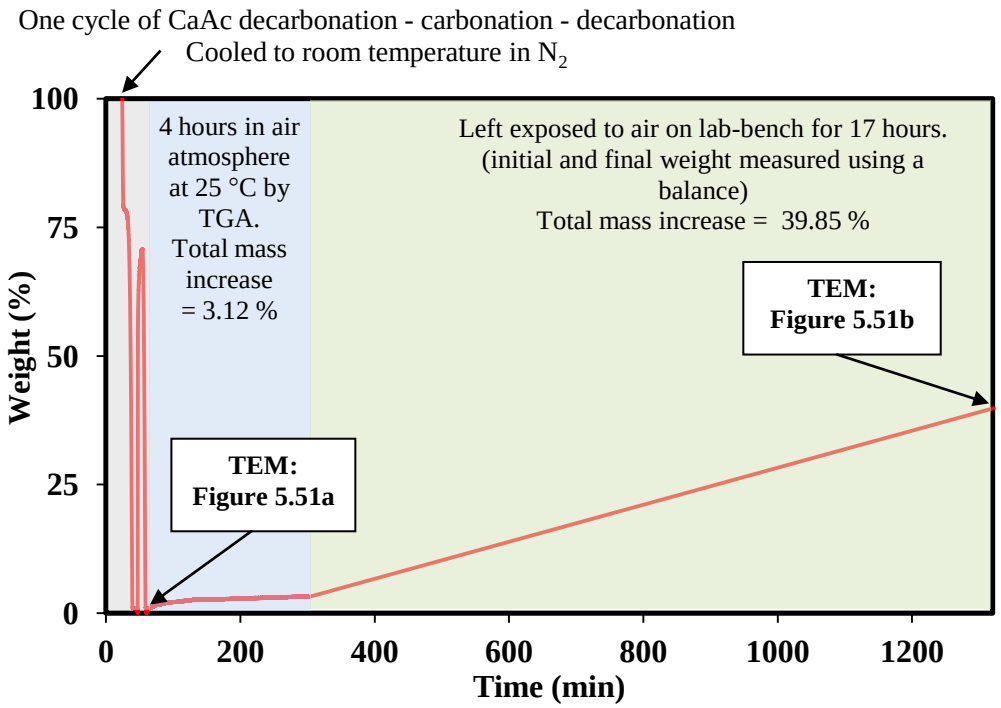

Figure 5.49: Mass increase of a decarbonated CaO sorbent due to hydration. With grey highlighted area showing a single carbonation/decarbonation cycle carried out by TGA (decarbonation in N_2). Blue highlighted area shows mass increase of sorbent exposed at room temperature to air atmosphere for 4 hours by TGA. Green highlighted area shows mass increase when left overnight (17 hours) on a lab workbench and exposed to atmospheric conditions.

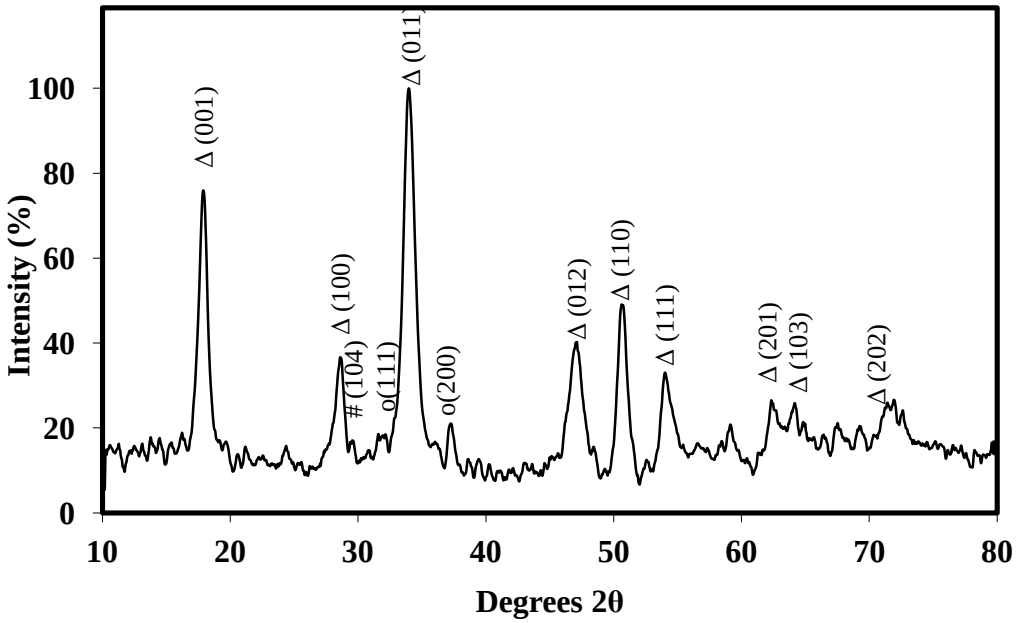

Figure 5.50: XRD pattern for CaAc sample carbonated and decarbonated by TGA, exposed to air by TGA, and finally left exposed to atmospheric conditions on a lab workbench overnight. XRD analysis was carried out 1 hour after final weight measurement of the sample. 'Δ' denotes indexed peaks of calcium hydroxide $Ca(OH)_2$, (ICDD ref: 01-084-1263 [289]), '○' denotes indexed peaks of calcium oxide, CaO (ICDD ref: 04-003-7161 [226]). '#' denotes indexed peak of calcite, $CaCO_3$, (ICDD ref: 00-005-0586 [221]). Full peak list available in the appendix, Table A38.

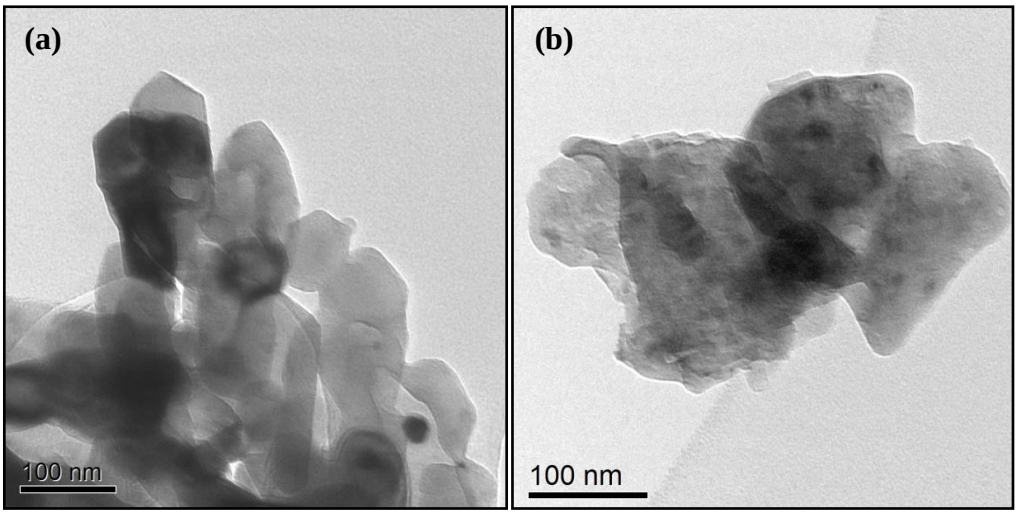

Figure 5.51: Bright field TEM images showing powder sorbent after (a) previous single carbonation/decarbonation cycle (assumed to be CaO based on TGA measurement) and (b) a further 4 hour air exposure at room temperature by TGA, followed by exposure to atmospheric conditions overnight (17 hours) on a lab workbench (see Figure 5.49). TEM image of sample recorded 24 hours later, shown to be $Ca(OH)_2$ by XRD (Figure 5.50).

Problems with hydration of the CaO sorbent at ambient conditions led to the development of an *ex-situ* analytical technique using an environmental heating cell (E-cell) in the TEM, for the analysis of the CO_2 multicycle capture system (Figure 5.34). This technique allows for the analysis of a powder sorbent after progressive stages of carbonation and decarbonation, with minimal exposure to air. Analysis of the CaO-CO_2 powder looping system using the E-cell showed the formation of a densified 'skeleton' of CaO after only 2 decarbonation cycles, with this result consistent with the model of textural changes of a CaO sorbent (produced by initial decomposition of $CaCO_3$) presented by Lysikov *et al* [151] (Figure 5.31).

Minimalisation of sorbent hydration using the E-cell technique presented significantly different results to the decarbonated samples previously observed by SEM and TEM analysis (Figure 5.28) taken after particular stages of the multicycle CO_2 capture by TGA. These samples however were exposed to air during storage and analysis, while those left in the TGA were not. These extracted samples (Figure 5.28), showed that particle densification was observed by SEM however a decrease

in crystallite size was observed by TEM with progressive decarbonations, consistent with reported particle fracture due to induced strain upon hydration [300]. The rate of CaO hydration on exposure to air has subsequently been highlighted in Figure 5.49, but also potential water contamination in the methanol used for TEM sample preparation could also be considered as a contributing factor toward further sorbent hydration, and may perhaps contribute to the notable differences observed between SEM and TEM images of the decarbonated samples, however this is unconfirmed. More importantly, the *ex-situ* TEM decarbonation result is more likely to be a true reflection of the decarbonated structures in the TGA.

In-situ decarbonation of a carbonated sorbent using a hot-stage in the TEM (Figure 5.30), showed the decomposition of $CaCO_3$ into a fine crystallite structure of CaO, with particles observed to be ~ < 50 nm in size. This result contradicts both the previous analysis of decarbonation stages by SEM and TEM analysis (Figure 5.28), where sorbent hydration had occurred, and also the decarbonation result presented using the E-cell (Figures 5.33 - 5.38), where only small amounts of sorbent hydration had occurred. This may be attributed to the difference in the vacuum and heating rate used for each technique; under high vacuum (~10^{-5} Pa in the TEM compared to ~10^{-3} Pa in the E-cell, at best) decomposition of $CaCO_3$ was more rapid and occurred at a lower temperature (~600 °C) than the other methods (which decarbonate $CaCO_3$ at 800 °C). Results of the E-cell showed small amounts of sorbent hydration however it would be expected that using the *in-situ* hot-stage in the TEM, the risk of sorbent hydration would be zero.

In final summary, the capacity for CO_2 capture of CaO nanoparticles degrades rapidly with multiple sorption-desorption cycles. With slow, low-vacuum decarbonation (by *ex-situ* TEM) a densified ‘skeleton’ of CaO forms, consistent with the drop in capture capacity observed by TGA. With rapid, high vacuum

decarbonation, a fine CaO crystallite structure forms (by *in-situ* TEM). By storage in atmospheric conditions (extracted XRD, SEM and TEM) a fine $Ca(OH)_2$ crystallite structure forms. Both of these ultra-fine structures should be re-assessed for CO_2 capture capacity with the potential for $Ca(OH)_2$ formation during hydrogen steam reforming being a likely application for the latter.

The *ex-situ* E-cell technique for the analysis of the multicycle carbonation and decarbonation process provides a valuable new tool in the field of CO_2 capture. The technique allows for the structural changes of powder sorbents to be observed for the first time at the nanolevel, upon progressing capture cycles, and due to the minimal risk for sorbent hydration, is therefore probably the closest microstructural match to what is occurring in the TGA.

This research in powder CaO sorbents has contributed to the awarding of a new EPSRC grant (Ref: EP/J014702/1) for Dr Steven J Milne, who aims to develop the understanding of the relationship between sorbent microstructure and CO_2 capture capacity and durability. Further research will aim to improve the multicycle durability of powder sorbents investigate by steam reforming and also by the development of new sorbent powder blends with additives which offset sintering during carbonation and which are beneficial to inhibiting densification during de-carbonation.

5.8. Appendix

5.8.1. Selected area electron diffraction patterns from Section 5.5.3

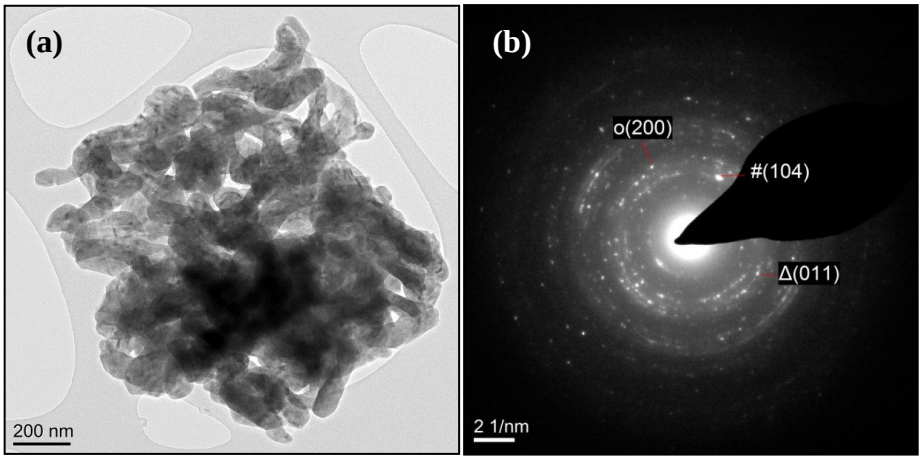

Figure 5.52: (a) Bright field TEM image and corresponding selected area electron diffraction pattern (b) for Sample A: first calcination of CaAc at 800 °C. SAED shows diffraction due to CaO ('o') ICDD ref: 04-003-7161 [226], $Ca(OH)_2$ ('Δ'), ICDD ref: 01-084-1263 [289] and calcite, $CaCO_3$ ('#'), ICDD ref: 00-005-0586 [291]. Rings only due to these phases are detected with labels assigned to spots on rings.

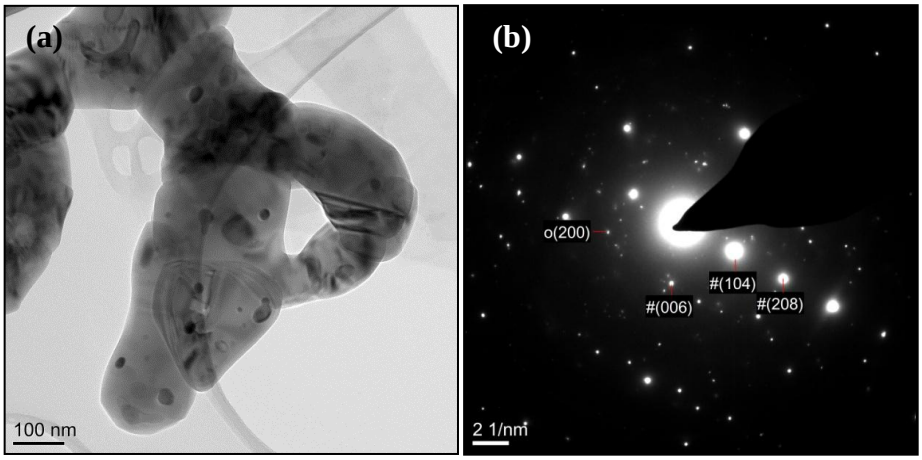

Figure 5.53: (a) Bright field TEM image and corresponding selected area electron diffraction pattern (b) for Sample B: after 1st carbonation at 650 °C. SAED shows diffraction spots due to calcite ('#'), ICDD ref: 00-005-0586 [291] and CaO ('o'), ICDD ref: 04-003-7161 [226]. Diffraction only due to $CaCO_3$ and CaO phases are detected with labels assigned to spots.

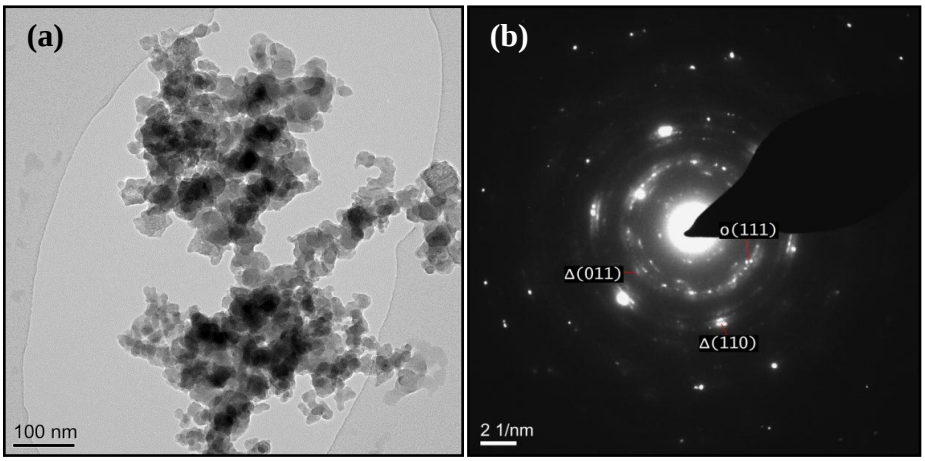

Figure 5.54: (a) Bright field TEM image and corresponding selected area electron diffraction pattern (b) for Sample C: after 2nd decarbonation at 800 °C. SAED shows pattern due to CaO ('o'), ICDD ref: 04-003-7161 [226] and $Ca(OH)_2$ ('Δ'), ICDD ref: 01-084-1263 [289]. Rings only due to these phases are detected with labels assigned to spots on rings.

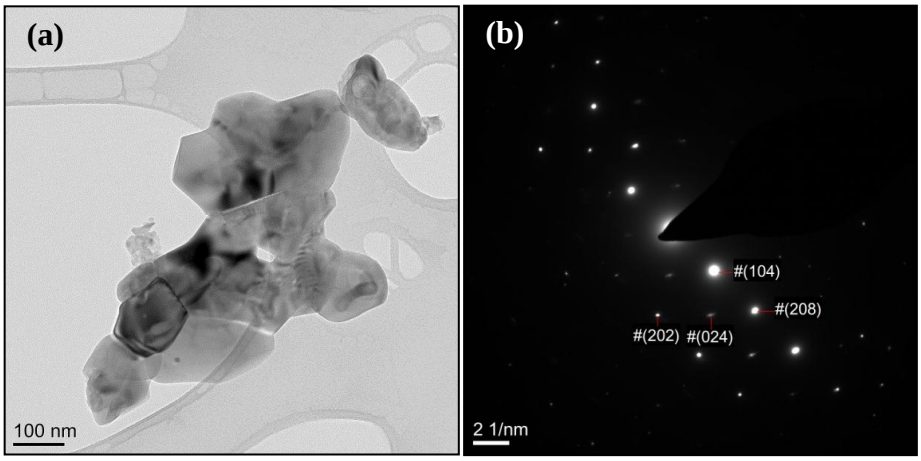

Figure 5.55: (a) Bright field TEM image and corresponding selected area electron diffraction pattern (b) for Sample D: after 2nd carbonation at 650 °C. SAED shows pattern due to only calcite phase ('#'), ICDD ref: 00-005-0586 [291]. Rings only due to the $CaCO_3$ phase are detected with label assigned to spot on rings.

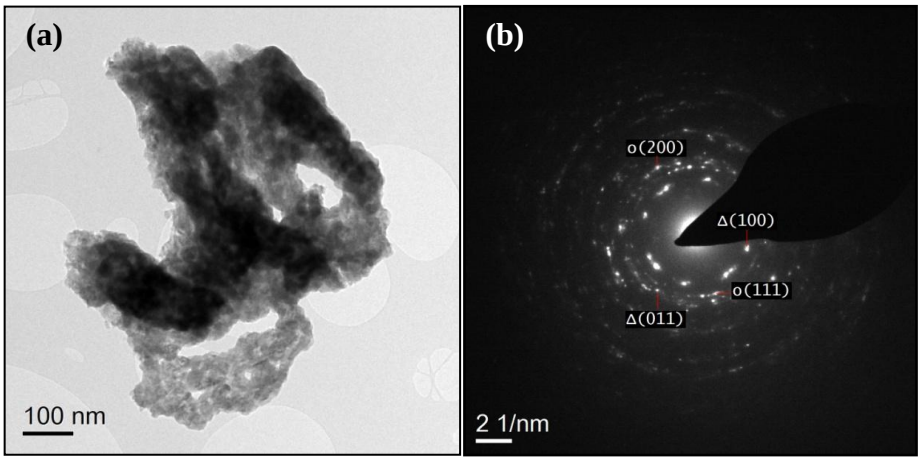

Figure 5.56: (a) Bright field TEM image and corresponding selected area electron diffraction pattern (b) for Sample E: after 3rd decarbonation at 800 °C. SAED shows pattern due to CaO ('o'), ICDD ref: 04-003-7161 [226] and $Ca(OH)_2$ ('Δ'), ICDD ref: 01-084-1263 [289]. Rings only due to these phases are detected with labels assigned to spots on rings.

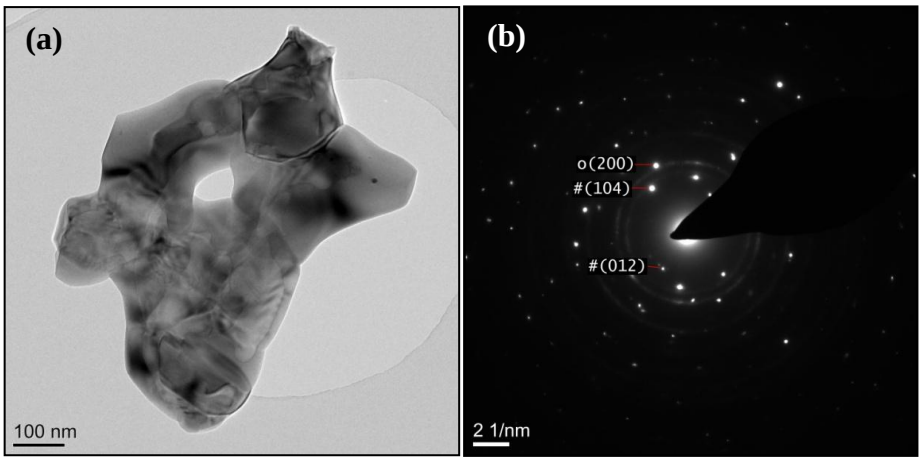

Figure 5.57: (a) Bright field TEM image and corresponding selected area electron diffraction pattern (b) for Sample F: after 3rd carbonation at 650 °C. SAED shows pattern due to calcite ('#'), ICDD ref: 00-005-0586 [291] and CaO ('o'), ICDD ref: 04-003-7161 [226]. Rings only due to these phases are detected with labels assigned to spots on rings.

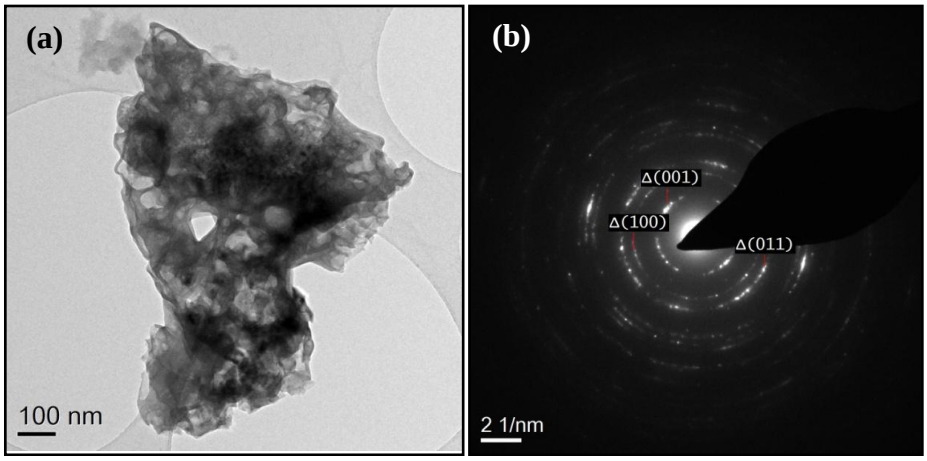

Figure 5.58: (a) Bright field TEM image and corresponding selected area electron diffraction pattern (b) for Sample G: after 9th decarbonation at 800 °C. SAED shows pattern due to $Ca(OH)_2$ ('Δ'), ICDD ref: 01-084-1263 [289]. Rings only due to the $Ca(OH)_2$ phase are detected with label assigned to spot on rings.

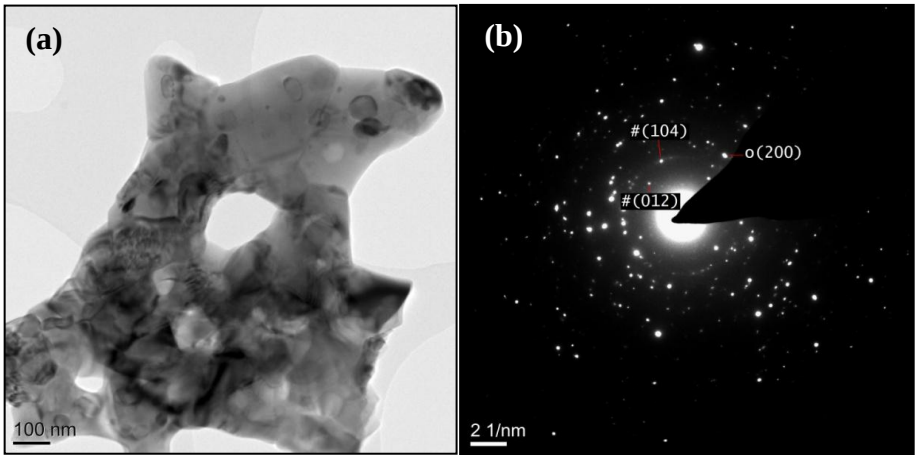

Figure 5.59: (a) Bright field TEM image and corresponding selected area electron diffraction pattern (b) for Sample H: after 10th carbonation at 650 °C. SAED shows pattern due to calcite ('#'), ICDD ref: 00-005-0586 [291] and CaO ('o'), ICDD ref: 04-003-7161 [226]**.** Rings only due to these phases are detected with labels assigned to spots on rings.

5.8.2. XRD peak list data

Table A12: XRD peak list data for as received calcium acetate hydrate, with ICDD reference file number: 00-019-0199 [279].

As received calcium acetate hydrate			Calcium acetate hydrate reference file, ICDD: 00-019-0199				
Pos. °2θ	**d-spacing (Å)**	**Relative intensity (%)**	**Pos. °2θ**	**d-spacing (Å)**	**Relative intensity (%)**	**h k l**	**Δ°2θ**
5.130	17.2135	76.53	5.287	16.700	75.00		0.157
7.319	12.0694	100.00	7.550	11.700	100.00		0.231
10.078	8.7704	19.62	10.278	8.600	35.00		0.200
10.426	8.4778	58.83	10.523	8.400	65.00		0.097
11.673	7.5749	48.43	11.790	7.500	45.00		0.117
12.529	7.0591	8.07	12.672	6.980	16.00		0.143
13.591	6.5099	9.94	13.718	6.450	16.00		0.127
15.496	5.7137	6.81					
15.743	5.6247	33.06	15.898	5.570	30.00		0.155
16.605	5.3347	8.90	16.714	5.300	10.00		0.109
21.094	4.2083	15.37	21.239	4.180	10.00		0.145
22.394	3.9670	15.29	22.607	3.930	10.00		0.213
22.862	3.8868	23.86	22.962	3.870	20.00		0.100
25.089	3.5465	39.95	25.281	3.520	30.00		0.192
25.796	3.4510	24.11					
26.315	3.3840	16.17	26.033	3.420	20.00		-0.282
26.497	3.3612	30.29	26.587	3.350	25.00		0.090
26.869	3.3155	22.16					
27.032	3.2959	17.54	27.165	3.280	30.00		0.133
27.412	3.2511	8.45	27.681	3.220	16.00		0.269
29.445	3.0310	12.17	29.555	3.020	10.00		0.110
30.064	2.9700	19.62	30.273	2.950	10.00		0.209
30.409	2.9371	6.12					
31.014	2.8811	16.08					
32.391	2.7617	14.21					
33.167	2.6989	13.25	33.408	2.680	8.00		0.241
33.723	2.6557	6.96					
34.049	2.6310	10.97	34.196	2.620	8.00		0.147
34.790	2.5766	17.46	35.023	2.560	10.00		0.233
35.394	2.5340	5.42	35.598	2.520	6.00		0.204
37.363	2.4049	25.94					
38.155	2.3568	14.97					
38.544	2.3339	13.53	38.439	2.340	8.00		-0.105
38.838	2.3169	7.05	38.784	2.320	8.00		-0.054
39.311	2.2901	11.91	39.492	2.280	8.00		0.181
40.899	2.2047	7.28					
41.191	2.1898	9.30	41.385	2.180	6.00		0.194
41.917	2.1536	26.71	42.195	2.140	12.00		0.278
42.639	2.1187	23.03					
43.093	2.0974	9.71	43.038	2.100	10.00		-0.055
43.436	2.0817	13.11					
43.723	2.0687	6.51					
44.046	2.0543	5.96	43.917	2.060	8.00		-0.129
44.476	2.0354	7.60					
44.750	2.0236	14.35					
45.094	2.0089	6.23	45.068	2.010	6.00		-0.026
45.503	1.9918	5.03					

45.774	1.9806	12.22					
46.491	1.9518	6.49					
47.114	1.9274	8.27					
48.076	1.8910	6.43					
48.819	1.8640	16.23	48.930	1.860	8.00		0.111
49.362	1.8448	5.32					
49.707	1.8327	8.42					
50.097	1.8194	5.56					
51.348	1.7780	11.05					
51.660	1.7680	10.46	51.911	1.760	6.00		0.251
52.886	1.7298	8.02					
53.039	1.7252	12.28					
61.264	1.5118	5.73					

Table A13: XRD peak list data for as received CaAc decomposed by TGA to 500 °C, with ICDD reference file number for calcite: 00-005-0586 [221] and vaterite: 00-033-0268 [288].

CaAc at 500 °C by TGA			**Pattern Assignment**							
Pos. °2θ	**d-spacing (Å)**	**Relative intensity (%)**	**ICDD ref file**	**Pos. °2θ**	**d-spacing (Å)**	**Relative intensity (%)**	**h**	**k**	**l**	**Δ°2θ**
23.082	3.8501	9.82	Calcite: #00-005-0586	23.022	3.860	12.00	0	1	2	-0.060
24.873	3.5769	5.52	Vaterite: #00-033-0268	24.900	3.573	60.00	1	1	0	0.027
27.032	3.2958	9.64	Vaterite: #00-033-0268	27.048	3.294	100.00	1	1	2	0.016
29.375	3.0381	100.00	Calcite: #00-005-0586	29.406	3.035	100.00	1	0	4	0.031
31.336	2.8523	4.52	Calcite: #00-005-0586	31.418	2.845	3.00	0	0	6	0.082
32.723	2.7345	6.30	Vaterite: #00-033-0268	32.778	2.730	90.00	1	1	4	0.055
35.998	2.4929	13.09	Calcite: #00-005-0586	35.966	2.495	14.00	1	1	0	-0.032
39.404	2.2849	17.17	Calcite: #00-005-0586	39.402	2.285	18.00	1	1	3	-0.002
41.680	2.1670	0.19	Vaterite: #00-033-0268	41.765	2.161	2.00	2	1	3	0.085
43.163	2.0942	13.26	Calcite: #00-005-0586	43.146	2.095	18.00	2	0	2	-0.017
43.735	2.0681	7.57	Vaterite: #00-033-0268	43.849	2.063	60.00	3	0	0	0.114
47.081	1.9287	16.61	Calcite: #00-005-0586	47.124	1.927	5.00	0	2	4	0.043
47.345	1.9185	21.05	Calcite: #00-005-0586	47.490	1.913	17.00	0	1	8	0.145
48.418	1.8785	18.24	Calcite: #00-005-0586	48.514	1.875	17.00	1	1	6	0.096
48.953	1.8592	8.59	Vaterite: #00-033-0268	49.099	1.854	30.00	3	0	4	0.146
57.380	1.6046	7.41	Calcite: #00-005-0586	57.402	1.604	8.00	1	2	2	0.022
60.617	1.5264	5.28	Calcite: #00-005-0586	60.678	1.525	5.00	2	1	4	0.061
60.839	1.5214	5.84	Calcite: #00-005-0586	60.987	1.518	4.00	2	0	8	0.148
64.637	1.4408	4.50	Calcite: #00-005-0586	64.678	1.440	5.00	3	0	0	0.041

Table A14: XRD peak list data for as received CaAc decomposed by TGA to 800 °C, with ICDD reference file number for CaO: 04-003-7161 [226], calcite: 00-005-0586 [221] and $Ca(OH)_2$: 01-084-1263 [289].

CaAc at 800 °C by TGA			Pattern Assignment						
Pos. °2θ	**d-spacing (Å)**	**Relative intensity (%)**	**ICDD ref file**	**Pos. °2θ**	**d-spacing (Å)**	**Relative intensity (%)**	**h**	**k**	**l**	**Δ°2θ**
18.288	4.8472	10.84	$Ca(OH)_2$: #01-084-1263	18.066	4.9063	74.20	0	0	1	-0.222
28.924	3.0842	2.88	$Ca(OH)_2$: #01-084-1263	28.676	3.1104	19.10	1	0	0	-0.248
29.642	3.0382	2.55	Calcite: #00-005-0586	29.406	3.0350	100.00	1	0	4	-0.236
32.415	2.7598	41.85	CaO: #04-003-7161	32.2220	2.7760	41.10	1	1	1	-0.193
34.328	2.6103	12.41	$Ca(OH)_2$: #01-084-1263	34.101	2.6271	100.00	0	1	1	-0.227
37.558	2.3929	100.00	CaO: #04-003-7161	37.377	2.4040	100.00	2	0	0	-0.181
47.325	1.9193	5.40	$Ca(OH)_2$: #01-084-1263	47.144	1.9262	38.60	0	1	2	-0.181
50.689	1.7988	10.21	$Ca(OH)_2$: #01-084-1263	50.798	1.7959	26.20	1	1	0	0.109
54.030	1.6959	51.67	CaO: #04-003-7161	53.891	1.7000	51.20	2	2	0	-0.139
62.819	1.4781	1.30	$Ca(OH)_2$: #01-084-1263	62.606	1.4826	9.80	2	0	1	-0.213
64.304	1.4475	14.23	CaO: #04-003-7161	64.194	1.4500	12.80	3	1	1	-0.110
64.423	1.4451	13.02	$Ca(OH)_2$: #01-084-1263	64.300	1.4480	9.20	1	0	3	-0.123
67.519	1.3862	13.26	CaO: #04-003-7161	67.417	1.3880	13.20	2	2	2	-0.102
79.767	1.2013	5.21	CaO: #04-003-7161	79.710	1.2020	5.00	4	0	0	-0.057

Table A15: XRD peak list data for as received CaAc in hot-stage XRD at 100 °C, with ICDD reference file number: 00-019-0199 [279].

CaAc at 100 °C in hot stage XRD			Calcium acetate hydrate reference file, ICDD: 00-019-0199						
Pos. °2θ	**d-spacing (Å)**	**Relative intensity (%)**	**Pos. °2θ**	**d-spacing (Å)**	**Relative intensity (%)**	**h**	**k**	**l**	**Δ°2θ**
5.124	17.2312	78.14	5.287	16.700	75.00				0.163
6.495	13.5970	5.93							
7.301	12.0983	100.00	7.550	11.700	100.00				0.249
10.066	8.7802	20.91	10.278	8.600	35.00				0.212
10.402	8.4979	69.09	10.523	8.400	65.00				0.121
11.643	7.5947	54.97	11.790	7.500	45.00				0.147
12.510	7.0702	9.36	12.672	6.980	16.00				0.162
13.567	6.5213	11.38	13.718	6.450	16.00				0.151
15.464	5.7255	8.68							
15.698	5.6407	39.29	15.898	5.570	30.00				0.200
16.554	5.3507	10.91	16.714	5.300	10.00				0.160
21.028	4.2214	18.61	21.239	4.180	10.00				0.211
22.323	3.9794	17.00	22.607	3.930	10.00				0.284
22.797	3.8976	26.76	22.962	3.870	20.00				0.165
25.040	3.5534	43.54	25.281	3.520	30.00				0.241
25.726	3.4601	26.17	26.033	3.420	20.00				0.307
26.224	3.3955	18.16	26.587	3.350	25.00				0.363
26.408	3.3723	37.55							
26.884	3.3137	32.81	27.165	3.280	30.00				0.281
27.382	3.2545	9.58	27.681	3.220	16.00				0.299
29.340	3.0417	14.28	29.555	3.020	10.00				0.215
29.961	2.9800	21.27	30.273	2.950	10.00				0.312

30.370	2.9408	6.91					
30.886	2.8928	19.57					
32.282	2.7708	15.26					
33.084	2.7055	13.62	33.408	2.680	8.00		0.324
33.625	2.6632	7.23					
33.942	2.6390	12.46	34.196	2.620	8.00		0.254
34.694	2.5835	19.81	35.023	2.560	10.00		0.329
35.291	2.5412	6.97	35.598	2.520	6.00		0.307
36.027	2.4909	5.62					
36.836	2.4381	5.30					
37.238	2.4127	27.72					
38.032	2.3641	16.35					
38.422	2.3410	15.60	38.439	2.340	8.00		0.017
38.743	2.3224	7.59	38.784	2.320	8.00		0.041
39.214	2.2955	13.50					
40.767	2.2116	8.07					
41.087	2.1951	10.73	41.385	2.180	6.00		0.298
41.774	2.1606	30.95					
42.492	2.1257	25.57	42.195	2.140	12.00		-0.297
42.939	2.1046	10.72	43.038	2.100	10.00		0.099
43.311	2.0874	13.12					
43.666	2.0713	8.01					
44.002	2.0562	7.11	43.917	2.060	8.00		-0.085
44.320	2.0422	9.85					
44.594	2.0303	16.04					
44.980	2.0138	6.13	45.068	2.010	6.00		0.088
45.354	1.9980	6.55					
45.637	1.9863	13.41					
46.333	1.9580	7.84					
46.619	1.9467	5.06					
46.942	1.9340	9.36					
48.007	1.8936	6.84					
48.668	1.8694	18.48	48.930	1.860	8.00		0.262
49.259	1.8484	7.23					
49.537	1.8386	8.88					
49.975	1.8236	6.67					
51.198	1.7828	11.48					
51.574	1.7707	11.24	51.911	1.760	6.00		0.337
52.665	1.7366	6.30					
52.901	1.7294	13.69					
53.284	1.7178	5.54					
54.551	1.6809	6.59					
58.602	1.5740	5.63					
61.059	1.5164	6.35					
64.066	1.4523	5.62					

Table A16: XRD peak list data for as received CaAc in hot-stage XRD at 200 °C, with ICDD reference file number for CaAc: 00-019-0199 and dehydrated CaAc: 00-019-0198 [279].

CaAc at 200 °C in hot-stage XRD			Pattern Assignment					
Pos. °2θ	**d-spacing (Å)**	**Relative intensity (%)**	**ICDD ref file**	**Pos. °2θ**	**d-spacing (Å)**	**Relative intensity (%)**	**h k l**	**Δ°2θ**
5.457	16.1830	76.58	CaAc: 00-019-0199	5.287	16.70	75.00		-0.170
7.341	12.0432	100.00	CaAc: 00-019-0199	7.550	11.70	100.00		0.209
9.720	9.0994	33.02	Dehydrated CaAc: #00-019-0198	9.606	9.20	35.00		-0.114
14.939	5.9302	6.89	Dehydrated CaAc: #00-019-0198	14.827	5.97	6.00		-0.112
22.236	3.9980	5.86	Dehydrated CaAc: #00-019-0198	22.376	3.97	10.00		0.140
25.620	3.4771	22.41	Dehydrated CaAc: #00-019-0198	25.652	3.47	25.00		0.032
26.688	3.3404	27.24	Dehydrated CaAc: #00-019-0198	26.832	3.32	14.00		0.144
28.557	3.1258	15.61	Dehydrated CaAc: #00-019-0198	28.776	3.10	6.00		0.219
30.163	2.9630	8.93	Dehydrated CaAc: #00-019-0198	30.168	2.96	14.00		0.005
31.777	2.8160	4.04	Dehydrated CaAc: #00-019-0198	31.589	2.83	10.00		-0.188
38.851	2.3181	4.62	Dehydrated CaAc: #00-019-0198	39.135	2.30	6.00		0.284

Table A17: XRD peak list data for as received CaAc in hot-stage XRD at 300 °C, with ICDD reference file number for dehydrated CaAc: 00-019-0198 [279].

CaAc at 300 °C in hot stage XRD			Calcium acetate (dehydrated) reference file, ICDD: 00-019-0198				
Pos. °2θ	**d-spacing (Å)**	**Relative intensity (%)**	**Pos. °2θ**	**d-spacing (Å)**	**Relative intensity (%)**	**h k l**	**Δ°2θ**
5.457	16.1830	76.58	5.697	15.5000	30.00		0.240
6.953	12.7023	8.08					
8.249	10.7105	18.09					
9.064	9.7484	100.00	9.205	9.6000	100.00		0.141
9.530	9.2731	87.46	9.606	9.2000	35.00		0.076
11.021	8.0217	28.68	11.191	7.9000	16.00		0.170
13.822	6.4017	16.79					
14.389	6.1506	15.69	14.827	5.9700	6.00		0.438
16.155	5.4819	5.39					
16.649	5.3205	17.07	16.557	5.3500	6.00		-0.092
20.047	4.4258	12.53	20.165	4.4000	8.00		0.118
20.605	4.3071	6.08	20.885	4.2500	10.00		0.280
21.749	4.0830	12.16	21.605	4.1100	6.00		-0.144

22.126	4.0143	16.37	22.376	3.9700	10.00		0.250
23.328	3.8101	9.67	23.083	3.8500	4.00		-0.245
23.800	3.7356	10.01	23.707	3.7500	8.00		-0.093
24.218	3.6720	6.00	24.299	3.6600	16.00		0.081
25.138	3.5397	5.41					
25.392	3.5048	10.89	25.652	3.4700	25.00		0.260
26.220	3.3961	42.25					
26.658	3.3412	14.23	26.832	3.3200	14.00		0.174
27.565	3.2333	27.22					
27.969	3.1876	9.54	28.037	3.1800	6.00		0.068
28.880	3.0890	6.28	28.776	3.1000	6.00		-0.104
29.227	3.0531	22.39	29.160	3.0600	8.00		-0.067
29.574	3.0181	8.02					
29.879	2.9880	8.06	29.961	2.9800	6.00		0.082
30.330	2.9445	7.17	30.168	2.9600	14.00		-0.162
30.560	2.9229	5.07	30.808	2.9000	8.00		0.248
31.241	2.8607	12.62					
31.649	2.8248	6.61	31.589	2.8300	10.00		-0.060
32.763	2.7313	8.75					
33.523	2.6710	11.75	33.537	2.6700	8.00		0.014
33.751	2.6536	9.56					
33.932	2.6398	5.85					
35.663	2.5156	11.69	35.452	2.5300	6.00		-0.211
35.989	2.4935	7.09					
36.691	2.4474	6.32					
36.936	2.4317	8.29					
37.867	2.3740	10.94					
38.503	2.3362	5.03					
38.898	2.3134	11.47	39.135	2.3000	6.00		0.237
39.631	2.2723	10.33	39.673	2.2700	6.00		0.042
39.939	2.2555	21.67					
40.578	2.2214	6.76	40.416	2.2300	10.00		-0.162
40.865	2.2065	8.80					
41.507	2.1739	11.31	41.385	2.1800	6.00		-0.122
42.621	2.1196	7.67	42.824	2.1100	10.00		0.203
43.455	2.0808	12.97					
44.415	2.0380	6.74	43.917	2.0600	8.00		-0.498
45.044	2.0110	12.10					
46.374	1.9564	9.09					
47.754	1.9030	6.24					
48.041	1.8923	9.28					
48.618	1.8712	10.13					
50.088	1.8197	6.60					
55.485	1.6548	5.55					
57.006	1.6142	5.27					

Table A18: XRD peak list data for as received CaAc in hot-stage XRD at 400 °C, with ICDD reference file number for calcite: 00-005-0586 [221].

CaAc at 400 °C in hot stage XRD			Calcium carbonate (calcite) reference file, ICDD: 00-005-0586						
Pos. °2θ	d-spacing (Å)	Relative intensity (%)	Pos. °2θ	d-spacing (Å)	Relative intensity (%)	h	k	l	Δ°2θ
23.076	3.851	9.16	23.022	3.860	12.00	0	1	2	-0.054
29.271	3.049	100.00	29.406	3.035	100.00	1	0	4	0.135
31.044	2.878	2.19	31.418	2.845	3.00	0	0	6	0.374
36.090	2.487	13.52	35.966	2.495	14.00	1	1	0	-0.124
39.434	2.283	18.47	39.402	2.285	18.00	1	1	3	-0.032
43.251	2.090	14.01	43.146	2.095	18.00	2	0	2	-0.105
47.019	1.931	23.60	47.124	1.927	5.00	0	2	4	0.105
47.100	1.928	24.71	47.490	1.913	17.00	0	1	8	0.390
48.303	1.883	19.98	48.514	1.875	17.00	1	1	6	0.211
56.719	1.622	3.44	56.555	1.626	4.00	2	1	1	-0.164
57.391	1.604	5.67	57.402	1.604	8.00	1	2	2	0.011
57.531	1.601	9.81	58.075	1.587	2.00	1	0	10	0.544
60.642	1.526	6.88	60.678	1.525	5.00	2	1	4	0.036
60.710	1.524	8.30	60.987	1.518	4.00	2	0	8	0.277
60.880	1.520	7.80	61.345	1.510	3.00	1	1	9	0.465
63.030	1.474	1.98	63.060	1.473	2.00	1	2	5	0.030
64.650	1.441	5.64	64.678	1.440	5.00	3	0	0	0.028
64.845	1.437	8.50	65.599	1.422	3.00	0	0	12	0.754
72.613	1.301	2.46	72.870	1.297	2.00	1	2	8	0.257
76.306	1.244	2.36	76.300	1.247	1.00	2	2	0	-0.006

Table A19: XRD peak list data for as received CaAc in hot-stage XRD at 500 °C, with ICDD reference file number for calcite: 00-005-0586 [221].

CaAc at 500 °C in hotstage XRD			Calcium Carbonate (Calcite) reference file, ICDD: 00-005-0586						
Pos. °2θ	d-spacing (Å)	Relative intensity (%)	Pos. °2θ	d-spacing (Å)	Relative intensity (%)	h	k	l	Δ°2θ
23.069	3.8523	9.17	23.022	3.8600	12.00	0	1	2	-0.047
29.226	3.0532	100.00	29.406	3.0350	100.00	1	0	4	0.180
30.932	2.8887	2.24	31.418	2.8450	3.00	0	0	6	0.486
36.109	2.4855	13.68	35.966	2.4950	14.00	1	1	0	-0.143
39.428	2.2836	18.72	39.402	2.2850	18.00	1	1	3	-0.026
43.263	2.0896	14.40	43.146	2.0950	18.00	2	0	2	-0.117
46.882	1.9364	21.71	47.124	1.9270	5.00	0	2	4	0.242
47.084	1.9285	17.44	47.490	1.9130	17.00	0	1	8	0.406
48.239	1.8850	20.66	48.514	1.8750	17.00	1	1	6	0.275
56.747	1.6210	3.61	56.555	1.6260	4.00	2	1	1	-0.192
57.203	1.6091	2.15	57.402	1.6040	8.00	1	2	2	0.199
57.553	1.6002	9.75	58.075	1.5870	2.00	1	0	10	0.522
60.539	1.5282	5.41	60.678	1.5250	5.00	2	1	4	0.139
60.708	1.5243	9.77	60.987	1.5180	4.00	2	0	8	0.279
60.742	1.5236	9.85	61.345	1.5100	3.00	1	1	9	0.603
63.012	1.4740	2.10	63.060	1.4730	2.00	1	2	5	0.048
64.391	1.4457	4.24	64.678	1.4400	5.00	3	0	0	0.287
64.879	1.4360	6.67	65.599	1.4220	3.00	0	0	12	0.720
68.944	1.3610	1.48	69.231	1.3560	1.00	2	1	7	0.287
69.510	1.3512	2.42	70.238	1.3390	2.00	0	2	10	0.728

72.530	1.3022	2.70	72.870	1.2970	2.00	1	2	8	0.340
73.576	1.2863	0.59	73.729	1.2840	1.00	3	0	6	0.153
76.076	1.2501	2.09	76.300	1.2470	1.00	2	2	0	0.224
76.531	1.2438	1.37	77.177	1.2350	2.00	1	1	12	0.646

Table A20: XRD peak list data for as received CaAc in hot-stage XRD at 600 °C, with calcite ($CaCO_3$) ICDD reference file number: 00-005-0586 [221] and CaO ICDD reference file number: 04-003-7161 [226].

CaAc at 600 °C in hotstage XRD			**Pattern Assignment**						
Pos. °2θ	**d-spacing (Å)**	**Relative intensity (%)**	**ICDD ref file**	**Pos. °2θ**	**d-spacing (Å)**	**Relative intensity (%)**	**h**	**k**	**l**	**Δ°2θ**
23.008	3.862	8.99	Calcite: #00-005-0586	23.022	3.860	12.00	0	1	2	0.014
29.124	3.064	100.00	Calcite: #00-005-0586	29.406	3.035	100.00	1	0	4	0.282
30.756	2.905	2.36	Calcite: #00-005-0586	31.418	2.845	3.00	0	0	6	0.662
32.088	2.787	2.52	CaO: #04-003-7161	32.222	2.776	41.10	1	1	1	0.134
36.073	2.488	14.26	Calcite: #00-005-0586	35.966	2.495	14.00	1	1	0	-0.107
37.220	2.414	6.32	CaO: #04-003-7161	37.377	2.404	100.00	2	0	0	0.157
39.366	2.287	19.78	Calcite: #00-005-0586	39.402	2.285	18.00	1	1	3	0.036
43.219	2.092	15.15	Calcite: #00-005-0586	43.146	2.095	18.00	2	0	2	-0.073
46.680	1.944	21.84	Calcite: #00-005-0586	47.124	1.927	5.00	0	2	4	0.444
47.011	1.931	7.32	Calcite: #00-005-0586	47.490	1.913	17.00	0	1	8	0.479
48.115	1.890	22.99	Calcite: #00-005-0586	48.514	1.875	17.00	1	1	6	0.399
53.653	1.707	3.60	CaO: #04-003-7161	53.891	1.700	51.20	2	2	0	0.238
56.718	1.622	3.92	Calcite: #00-005-0586	56.555	1.626	4.00	2	1	1	-0.163
57.518	1.601	10.90	Calcite: #00-005-0586	57.402	1.604	8.00	1	2	2	-0.116
60.371	1.532	3.69	Calcite: #00-005-0586	60.678	1.525	5.00	2	1	4	0.307
60.536	1.528	6.13	Calcite: #00-005-0586	60.987	1.518	4.00	2	0	8	0.451
60.649	1.526	7.40	Calcite: #00-005-0586	61.345	1.510	3.00	1	1	9	0.696
62.934	1.476	2.51	Calcite: #00-005-0586	63.060	1.473	2.00	1	2	5	0.126
63.900	1.456	1.87	CaO: #04-003-7161	64.194	1.450	12.80	3	1	1	0.294
64.056	1.453	5.33	Calcite: #00-005-0586	64.678	1.440	5.00	3	0	0	0.622
64.858	1.437	7.42	Calcite: #00-005-0586	65.599	1.422	3.00	0	0	12	0.741
67.106	1.394	1.04	CaO: #04-003-7161	67.417	1.388	13.20	2	2	2	0.311
68.822	1.363	1.72	Calcite: #00-005-0586	69.231	1.356	1.00	2	1	7	0.409
69.282	1.355	2.85	Calcite: #00-005-0586	70.238	1.339	2.00	0	2	10	0.956
72.381	1.305	3.29	Calcite: #00-005-0586	72.870	1.297	2.00	1	2	8	0.489
73.486	1.288	0.68	Calcite: #00-005-0586	73.729	1.284	1.00	3	0	6	0.243
75.771	1.254	2.59	Calcite: #00-005-0586	76.300	1.247	1.00	2	2	0	0.529
76.516	1.244	1.30	Calcite: #00-005-0586	77.177	1.235	2.00	1	1	12	0.661
79.316	1.207	0.44	CaO: #04-003-7161	79.710	1.202	5.00	4	0	0	0.394

Table A21: XRD peak list data for as received CaAc in hot-stage XRD at 700 °C, with ICDD reference file number: 04-003-7161 [226].

CaAc at 700 °C in hot stage XRD			CaO reference file, ICDD: 04-003-7161						
Pos. °2θ	d-spacing (Å)	Relative intensity (%)	Pos. °2θ	d-spacing (Å)	Relative intensity (%)	h	k	l	Δ°2θ
32.394	2.7615	21.32	32.222	2.7759	41.10	1	1	1	-0.172
37.503	2.3963	87.52	37.377	2.4040	100.00	2	0	0	-0.126
53.857	1.7009	100.00	53.891	1.6999	51.20	2	2	0	0.034
64.048	1.4526	36.42	64.194	1.4497	12.80	3	1	1	0.146
67.235	1.3913	37.64	67.417	1.3880	13.20	2	2	2	0.182
79.368	1.2063	19.56	79.710	1.2020	5.00	4	0	0	0.342

Table A22: XRD peak list data for as received CaAc in hot-stage XRD at 800 °C, with ICDD reference file number: 04-003-7161 [226].

CaAc at 800 °C in hot stage XRD			CaO reference file, ICDD: 04-003-7161						
Pos. °2θ	d-spacing (Å)	Relative intensity (%)	Pos. °2θ	d-spacing (Å)	Relative intensity (%)	h	k	l	Δ°2θ
32.016	2.7933	14.99	32.222	2.7759	41.10	1	1	1	0.206
37.184	2.4160	63.71	37.377	2.4040	100.00	2	0	0	0.193
53.745	1.7042	100.00	53.891	1.6999	51.20	2	2	0	0.146
64.083	1.4519	39.46	64.194	1.4497	12.80	3	1	1	0.111
67.319	1.3898	41.48	67.417	1.3880	13.20	2	2	2	0.098
79.657	1.2027	21.59	79.710	1.2020	5.00	4	0	0	0.053

Table A23: XRD peak list data for CaO after 15 minutes of carbonation by TGA, with ICDD reference file number for Calcite ($CaCO_3$): 00-005-0586 [221] and CaO: 04-003-7161 [226].

CaAc-CaO after 15 minutes carbonation by TGA			Pattern Assignment							
Pos. °2θ	d-spacing (Å)	Relative intensity (%)	ICDD ref file	Pos. °2θ	d-spacing (Å)	Relative intensity (%)	h	k	l	Δ°2θ
22.895	3.8813	9.80	Calcite: #00-005-0586	23.022	3.8600	12.00	0	1	2	0.127
29.209	3.0550	100.00	Calcite: #00-005-0586	29.406	3.0350	100.00	1	0	4	0.197
31.175	2.8667	2.46	Calcite: #00-005-0586	31.418	2.8450	3.00	0	0	6	0.243
31.989	2.7956	2.31	CaO: #04-003-7161	32.222	2.7759	41.10	1	1	1	0.233
35.860	2.5021	13.14	Calcite: #00-005-0586	35.966	2.4950	14.00	1	1	0	0.106
37.137	2.4190	5.33	CaO: #04-003-7161	37.377	2.4040	100.00	2	0	0	0.240
39.279	2.2919	17.10	Calcite: #00-005-0586	39.402	2.2850	18.00	1	1	3	0.123
43.055	2.0992	12.62	Calcite: #00-005-0586	43.146	2.0950	18.00	2	0	2	0.091
46.987	1.9323	6.93	Calcite: #00-005-0586	47.124	1.9270	5.00	0	2	4	0.137
47.247	1.9223	17.27	Calcite: #00-005-0586	47.490	1.9130	17.00	0	1	8	0.243
48.328	1.8818	16.63	Calcite: #00-005-0586	48.514	1.8750	17.00	1	1	6	0.186
53.625	1.7077	2.33	CaO: #04-003-7161	53.891	1.6999	51.20	2	2	0	0.266
56.503	1.6274	2.60	Calcite: #00-005-0586	56.555	1.6260	4.00	2	1	1	0.052
57.334	1.6057	6.94	Calcite: #00-005-0586	57.402	1.6040	8.00	1	2	2	0.068
57.785	1.5943	1.14	Calcite: #00-005-0586	58.075	1.5870	2.00	1	0	10	0.290
60.585	1.5271	3.93	Calcite: #00-005-0586	60.678	1.5250	5.00	2	1	4	0.093
60.803	1.5222	3.69	Calcite: #00-005-0586	60.987	1.5180	4.00	2	0	8	0.184
61.141	1.5145	1.04	Calcite: #00-005-0586	61.345	1.5100	3.00	1	1	9	0.204
62.956	1.4752	1.41	Calcite: #00-005-0586	63.060	1.4730	2.00	1	2	5	0.104
64.626	1.4410	4.22	Calcite: #00-005-0586	64.678	1.4400	5.00	3	0	0	0.052
65.257	1.4286	2.54	Calcite: #00-005-0586	65.599	1.4220	3.00	0	0	12	0.342
67.129	1.3933	0.52	CaO: #04-003-7161	67.417	1.3880	13.20	2	2	2	0.288

69.059	1.3590	0.85	Calcite: #00-005-0586	69.231	1.3560	1.00	1 2 7	0.172
70.006	1.3429	1.37	Calcite: #00-005-0586	70.238	1.3390	2.00	0 2 10	0.232
72.747	1.2989	1.54	Calcite: #00-005-0586	72.870	1.2970	2.00	1 2 8	0.123
76.863	1.2393	1.10	Calcite: #00-005-0586	77.177	1.2350	2.00	1 1 12	0.314

Table A24: XRD peak list data for Cycle Sample B: after 1st carbonation cycle in multicycle CO_2 capture, with ICDD reference file number for Calcite ($CaCO_3$): 00-005-0586 [221] and CaO: 04-003-7161 [226].

Cycle Sample B: after 1st carbonation cycle at 650 °C			**Pattern Assignment**							
Pos. °2θ	**d-spacing (Å)**	**Relative intensity (%)**	**ICDD ref file**	**Pos. °2θ**	**d-spacing (Å)**	**Relative intensity (%)**	**h**	**k**	**l**	**Δ°2θ**
22.986	3.8660	10.93	Calcite: #00-005-0586	23.022	3.8600	12.00	0	1	2	0.036
29.305	3.0452	100.00	Calcite: #00-005-0586	29.406	3.0350	100.00	1	0	4	0.101
35.931	2.4974	12.06	Calcite: #00-005-0586	35.966	2.4950	14.00	1	1	0	0.035
37.223	2.4136	5.36	CaO: #04-003-7161	37.377	2.4040	100.00	2	0	0	0.154
39.352	2.2878	15.10	Calcite: #00-005-0586	39.402	2.2850	18.00	1	1	3	0.050
43.119	2.0963	10.58	Calcite: #00-005-0586	43.146	2.0950	18.00	2	0	2	0.027
47.055	1.9297	5.27	Calcite: #00-005-0586	47.124	1.9270	5.00	0	2	4	0.069
47.349	1.9184	13.48	Calcite: #00-005-0586	47.490	1.9130	17.00	0	1	8	0.141
48.407	1.8789	13.01	Calcite: #00-005-0586	48.514	1.8750	17.00	1	1	6	0.107
53.698	1.7056	2.36	CaO: #04-003-7161	53.891	1.6999	51.20	2	2	0	0.193
57.378	1.6046	4.90	Calcite: #00-005-0586	57.402	1.6040	8.00	1	2	2	0.024
60.631	1.5261	2.73	Calcite: #00-005-0586	60.678	1.5250	5.00	2	1	4	0.047
64.656	1.4404	2.75	Calcite: #00-005-0586	64.678	1.4400	5.00	3	0	0	0.022

Table A25: XRD peak list data for Cycle Sample C: After decarbonation of 1st carbonated product in multicycle CO_2 capture, with ICDD reference file number for CaO: 04-003-7161 [226] and $Ca(OH)_2$: 01-084-1263 [289].

Cycle Sample C: After 2nd decarbonation at 800 °C.			**Pattern Assignment**							
Pos. °2θ	**d-spacing (Å)**	**Relative intensity (%)**	**ICDD ref file**	**Pos. °2θ**	**d-spacing (Å)**	**Relative intensity (%)**	**h**	**k**	**l**	**Δ°2θ**
37.257	2.4115	100.00	CaO: #04-003-7161	37.377	2.4040	100.00	2	0	0	0.120
32.105	2.7857	43.69	CaO: #04-003-7161	32.222	2.7759	41.10	1	1	1	0.117
53.759	1.7038	42.19	CaO: #04-003-7161	53.891	1.6999	51.20	2	2	0	0.132
64.067	1.4523	9.82	$Ca(OH)_2$: #01-084-1263	64.300	1.4476	9.20	1	0	3	0.233
64.053	1.4525	9.66	CaO: #04-003-7161	64.194	1.4497	12.80	3	1	1	0.141
67.275	1.3906	9.33	CaO: #04-003-7161	67.417	1.3880	13.20	2	2	2	0.142
79.553	1.2040	3.07	CaO: #04-003-7161	79.710	1.2020	5.00	4	0	0	0.157

Table A26: XRD peak list data for Cycle Sample D: after 2nd carbonation cycle in multicycle CO_2 capture, with ICDD reference file number for Calcite ($CaCO_3$): 00-005-0586 [221] and CaO: 04-003-7161 [226].

Cycle Sample D: after 2nd carbonation cycle at 650 °C.			Pattern Assignment							
Pos. °2θ	d-spacing (Å)	Relative intensity (%)	ICDD ref file	Pos. °2θ	d-spacing (Å)	Relative intensity (%)	h	k	l	Δ°2θ
22.978	3.8673	9.95	Calcite: #00-005-0586	23.022	3.8600	12.00	0	1	2	0.044
29.287	3.0470	100.00	Calcite: #00-005-0586	29.406	3.0350	100.00	1	0	4	0.119
32.079	2.7879	5.64	CaO: #04-003-7161	32.222	2.7759	41.10	1	1	1	0.143
35.937	2.4970	12.52	Calcite: #00-005-0586	35.966	2.4950	14.00	1	1	0	0.029
37.226	2.4134	12.95	CaO: #04-003-7161	37.377	2.4040	100.00	2	0	0	0.151
39.352	2.2878	16.27	Calcite: #00-005-0586	39.402	2.2850	18.00	1	1	3	0.050
43.127	2.0959	11.63	Calcite: #00-005-0586	43.146	2.0950	18.00	2	0	2	0.019
47.056	1.9296	5.93	Calcite: #00-005-0586	47.124	1.9270	5.00	0	2	4	0.068
47.310	1.9199	15.54	Calcite: #00-005-0586	47.490	1.9130	17.00	0	1	8	0.180
48.393	1.8794	14.97	Calcite: #00-005-0586	48.514	1.8750	17.00	1	1	6	0.121
53.710	1.7052	5.41	CaO: #04-003-7161	53.891	1.6999	51.20	2	2	0	0.181
57.396	1.6041	5.90	Calcite: #00-005-0586	57.402	1.6040	8.00	1	2	2	0.006
60.644	1.5258	3.23	Calcite: #00-005-0586	60.678	1.5250	5.00	2	1	4	0.034
63.992	1.4538	1.23	CaO: #04-003-7161	64.194	1.4497	12.80	3	1	1	0.202
67.210	1.3918	1.15	CaO: #04-003-7161	67.417	1.3880	13.20	2	2	2	0.207

Table A27: XRD peak list data for Cycle Sample E: After decarbonation of 2nd carbonated product in multicycle CO_2 capture, with ICDD reference file number for CaO: 04-003-7161 [226] and $Ca(OH)_2$: 01-084-1263 [289].

Cycle Sample E: After 3rd decarbonation at 800 °C.			Pattern Assignment							
Pos. °2θ	d-spacing (Å)	Relative intensity (%)	ICDD ref file	Pos. °2θ	d-spacing (Å)	Relative intensity (%)	h	k	l	Δ°2θ
17.946	4.9388	23.31	$Ca(OH)_2$: #01-084-1263	18.066	4.9063	74.20	0	0	1	0.120
28.593	3.1194	5.78	$Ca(OH)_2$: #01-084-1263	28.676	3.1106	19.10	1	0	0	0.083
32.100	2.7861	44.56	CaO: #04-003-7161	32.222	2.7759	41.10	1	1	1	0.122
34.007	2.6342	23.76	$Ca(OH)_2$: #01-084-1263	34.101	2.6271	100.00	0	1	1	0.094
37.253	2.4117	100.00	CaO: #04-003-7161	37.377	2.4040	100.00	2	0	0	0.124
47.028	1.9307	8.96	$Ca(OH)_2$: #01-084-1263	47.144	1.9262	38.60	0	1	2	0.116
50.735	1.7980	5.08	$Ca(OH)_2$: #01-084-1263	50.798	1.7959	26.20	1	1	0	0.063
53.758	1.7038	42.15	CaO: #04-003-7161	53.891	1.6999	51.20	2	2	0	0.133
54.284	1.6885	5.20	$Ca(OH)_2$: #01-084-1263	54.356	1.6865	14.30	1	1	1	0.072
64.054	1.4525	10.59	CaO: #04-003-7161	64.194	1.4497	12.80	3	1	1	0.140
64.159	1.4504	9.90	$Ca(OH)_2$: #01-084-1263	64.300	1.4476	9.20	1	0	3	0.141
67.277	1.3906	8.64	CaO: #04-003-7161	67.417	1.3880	13.20	2	2	2	0.140
71.727	1.3148	0.99	$Ca(OH)_2$: #01-084-1263	71.808	1.3136	7.10	2	0	2	0.081
79.557	1.2039	2.83	CaO: #04-003-7161	79.710	1.2020	5.00	4	0	0	0.153

Table A28: XRD peak list data for Cycle Sample F: after 3rd carbonation cycle in multicycle CO_2 capture, with ICDD reference file number for Calcite ($CaCO_3$): 00-005-0586 [221] and CaO: 04-003-7161 [226].

Cycle Sample F: after 3rd carbonation cycle at 650 °C.			Pattern Assignment							
Pos. °2θ	**d-spacing (Å)**	**Relative intensity (%)**	**ICDD ref file**	**Pos. °2θ**	**d-spacing (Å)**	**Relative intensity (%)**	**h**	**k**	**l**	**Δ°2θ**
22.984	3.8664	9.95	Calcite: #00-005-0586	23.022	3.8600	12.00	0	1	2	0.038
29.289	3.0468	100.00	Calcite: #00-005-0586	29.406	3.0350	100.00	1	0	4	0.117
31.242	2.8607	2.22	Calcite: #00-005-0586	31.418	2.8450	3.00	0	0	6	0.176
32.086	2.7873	9.63	CaO: #04-003-7161	32.222	2.7759	41.10	1	1	1	0.136
35.947	2.4963	12.47	Calcite: #00-005-0586	35.966	2.4950	14.00	1	1	0	0.019
37.233	2.4130	22.01	CaO: #04-003-7161	37.377	2.4040	100.00	2	0	0	0.144
39.360	2.2873	15.85	Calcite: #00-005-0586	39.402	2.2850	18.00	1	1	3	0.042
43.137	2.0954	11.73	Calcite: #00-005-0586	43.146	2.0950	18.00	2	0	2	0.009
47.063	1.9294	6.30	Calcite: #00-005-0586	47.124	1.9270	5.00	0	2	4	0.061
47.302	1.9201	15.61	Calcite: #00-005-0586	47.490	1.9130	17.00	0	1	8	0.188
48.395	1.8793	14.81	Calcite: #00-005-0586	48.514	1.8750	17.00	1	1	6	0.119
53.719	1.7049	8.96	CaO: #04-003-7161	53.891	1.6999	51.20	2	2	0	0.172
56.581	1.6253	2.18	Calcite: #00-005-0586	56.555	1.6260	4.00	2	1	1	-0.026
57.410	1.6038	5.77	Calcite: #00-005-0586	57.402	1.6040	8.00	1	2	2	-0.008
57.826	1.5932	1.01	Calcite: #00-005-0586	58.075	1.5870	2.00	1	0	10	0.249
60.655	1.5255	3.22	Calcite: #00-005-0586	60.678	1.5250	5.00	2	1	4	0.023
60.856	1.5210	3.14	Calcite: #00-005-0586	60.987	1.5180	4.00	2	0	8	0.131
61.188	1.5135	2.01	Calcite: #00-005-0586	61.345	1.5100	3.00	1	1	9	0.157
63.022	1.4738	1.15	Calcite: #00-005-0586	63.060	1.4730	2.00	1	2	5	0.038
64.003	1.4536	2.01	CaO: #04-003-7161	64.194	1.4497	12.80	3	1	1	0.191
64.700	1.4396	3.42	Calcite: #00-005-0586	64.678	1.4400	5.00	3	0	0	-0.022
65.282	1.4281	2.05	Calcite: #00-005-0586	65.599	1.4220	3.00	0	0	12	0.317
67.221	1.3916	1.90	CaO: #04-003-7161	67.417	1.3880	13.20	2	2	2	0.196
69.114	1.3580	0.65	Calcite: #00-005-0586	69.231	1.3560	1.00	2	1	7	0.117
70.044	1.3422	1.07	Calcite: #00-005-0586	70.238	1.3390	2.00	0	2	10	0.194
72.795	1.2981	1.17	Calcite: #00-005-0586	72.870	1.2970	2.00	1	2	8	0.075
73.642	1.2853	0.26	Calcite: #00-005-0586	73.729	1.2840	1.00	3	0	6	0.087
76.342	1.2464	0.45	Calcite: #00-005-0586	76.300	1.2470	1.00	2	2	0	-0.042
76.884	1.2390	0.82	Calcite: #00-005-0586	77.177	1.2350	2.00	1	1	12	0.293
79.483	1.2049	0.60	CaO: #04-003-7161	79.710	1.2020	5.00	4	0	0	0.227

Table A29: XRD peak list data for Cycle Sample G: After decarbonation of 9th carbonated product in multicycle CO_2 capture, with ICDD reference file number for CaO: 04-003-7161 [226] and $Ca(OH)_2$: 01-084-1263 [289].

Cycle Sample G: After 9th decarbonation at 800 °C.			Pattern Assignment							
Pos. °2θ	d-spacing (Å)	Relative intensity (%)	ICDD ref file	Pos. °2θ	d-spacing (Å)	Relative intensity (%)	h	k	l	Δ°2θ
17.937	4.9414	97.08	$Ca(OH)_2$: #01-084-1263	18.066	4.9063	74.20	0	0	1	0.129
28.575	3.1213	24.19	$Ca(OH)_2$: #01-084-1263	28.676	3.1106	19.10	1	0	0	0.101
32.201	2.7776	6.42	CaO: #04-003-7161	32.222	2.7759	41.10	1	1	1	0.021
33.986	2.6357	100.00	$Ca(OH)_2$: #01-084-1263	34.101	2.6271	100.00	0	1	1	0.115
37.371	2.4044	7.49	CaO: #04-003-7161	37.377	2.4040	100.00	2	0	0	0.006
46.999	1.9318	37.99	$Ca(OH)_2$: #01-084-1263	47.144	1.9262	38.60	0	1	2	0.145
50.701	1.7991	21.07	$Ca(OH)_2$: #01-084-1263	50.798	1.7959	26.20	1	1	0	0.097
53.934	1.6987	10.03	CaO: #04-003-7161	53.891	1.6999	51.20	2	2	0	-0.043
54.248	1.6896	13.35	$Ca(OH)_2$: #01-084-1263	54.356	1.6865	14.30	1	1	1	0.108
59.279	1.5576	1.79	$Ca(OH)_2$: #01-084-1263	59.376	1.5553	2.10	2	0	0	0.097
62.500	1.4848	6.89	$Ca(OH)_2$: #01-084-1263	62.606	1.4826	9.80	2	0	1	0.106
64.117	1.4512	8.14	CaO: #04-003-7161	64.194	1.4497	12.80	3	1	1	0.077
64.272	1.4481	8.01	$Ca(OH)_2$: #01-084-1263	64.300	1.4476	9.20	1	0	3	0.028
67.508	1.3864	0.28	CaO: #04-003-7161	67.417	1.3880	13.20	2	2	2	-0.091

Table A30: XRD peak list data for Cycle Sample H: after 10th carbonation cycle in multicycle CO_2 capture, with ICDD reference file number for Calcite ($CaCO_3$): 00-005-0586 [221] and CaO: 04-003-7161 [226].

Cycle Sample H: after 10th carbonation cycle at 650 °C.			Pattern Assignment							
Pos. °2θ	d-spacing (Å)	Relative intensity (%)	ICDD ref file	Pos. °2θ	d-spacing (Å)	Relative intensity (%)	h	k	l	Δ°2θ
22.903	3.8798	9.74	Calcite: #00-005-0586	23.022	3.8600	12.00	0	1	2	0.119
29.197	3.0562	100.00	Calcite: #00-005-0586	29.406	3.0350	100.00	1	0	4	0.209
31.120	2.8716	2.58	Calcite: #00-005-0586	31.418	2.8450	3.00	0	0	6	0.298
32.014	2.7934	27.40	CaO: #04-003-7161	32.222	2.7759	41.10	1	1	1	0.208
35.895	2.4998	13.23	Calcite: #00-005-0586	35.966	2.4950	14.00	1	1	0	0.071
37.167	2.4171	64.91	CaO: #04-003-7161	37.377	2.4040	100.00	2	0	0	0.210
39.300	2.2907	16.85	Calcite: #00-005-0586	39.402	2.2850	18.00	1	1	3	0.102
43.090	2.0976	12.28	Calcite: #00-005-0586	43.146	2.0950	18.00	2	0	2	0.056
47.008	1.9315	9.56	Calcite: #00-005-0586	47.124	1.9270	5.00	0	2	4	0.116
47.189	1.9245	16.93	Calcite: #00-005-0586	47.490	1.9130	17.00	0	1	8	0.301
48.318	1.8821	16.04	Calcite: #00-005-0586	48.514	1.8750	17.00	1	1	6	0.196
53.671	1.7063	29.58	CaO: #04-003-7161	53.891	1.6999	51.20	2	2	0	0.220
56.560	1.6258	2.40	Calcite: #00-005-0586	56.555	1.6260	4.00	2	1	1	-0.005
57.388	1.6044	6.42	Calcite: #00-005-0586	57.402	1.6040	8.00	1	2	2	0.014
57.702	1.5964	1.15	Calcite: #00-005-0586	58.075	1.5870	2.00	1	0	10	0.373
60.627	1.5262	3.93	Calcite: #00-005-0586	60.678	1.5250	5.00	2	1	4	0.051
60.779	1.5227	2.97	Calcite: #00-005-0586	60.987	1.5180	4.00	2	0	8	0.208
61.094	1.5156	2.05	Calcite: #00-005-0586	61.345	1.5100	3.00	1	1	9	0.251
62.989	1.4745	1.34	Calcite: #00-005-0586	63.060	1.4730	2.00	1	2	5	0.071
63.968	1.4543	6.96	CaO: #04-003-7161	64.194	1.4497	12.80	3	1	1	0.226
64.696	1.4397	3.90	Calcite: #00-005-0586	64.678	1.4400	5.00	3	0	0	-0.018
65.135	1.4310	2.35	Calcite: #00-005-0586	65.599	1.4220	3.00	0	0	12	0.464
67.190	1.3921	6.79	CaO: #04-003-7161	67.417	1.3880	13.20	2	2	2	0.227
69.071	1.3588	0.75	Calcite: #00-005-0586	69.231	1.3560	1.00	2	1	7	0.160

69.954	1.3437	1.19	Calcite: #00-005-0586	70.238	1.3390	2.00	0	2	10	0.284
72.747	1.2989	1.32	Calcite: #00-005-0586	72.870	1.2970	2.00	1	2	8	0.123
73.622	1.2856	0.28	Calcite: #00-005-0586	73.729	1.2840	1.00	3	0	6	0.107
76.362	1.2461	0.52	Calcite: #00-005-0586	76.300	1.2470	1.00	2	2	0	-0.062
76.771	1.2405	0.91	Calcite: #00-005-0586	77.177	1.2350	2.00	1	1	12	0.406
79.471	1.2050	2.28	CaO: #04-003-7161	79.710	1.2020	5.00	4	0	0	0.239

Table A31: XRD peak list data for hydrothermally prepared YSZ (hYSZ) with ICDD reference file number for cubic zirconium yttrium oxide: 01-077-2112 [295].

Hydrothermally prepared YSZ (hYSZ)			**Zirconium yttrium oxide reference file, ICDD: 01-077-2112**						
Pos. °2θ	**d-spacing (Å)**	**Relative intensity (%)**	**Pos. °2θ**	**d-spacing (Å)**	**Relative intensity (%)**	**h**	**k**	**l**	**Δ°2θ**
29.834	2.9924	100.00	29.970	2.9791	100.00	1	1	1	0.136
34.605	2.5900	47.83	34.743	2.5800	21.60	2	0	0	0.138
49.809	1.8292	62.50	49.953	1.8243	48.20	2	2	0	0.144
59.208	1.5593	51.15	59.355	1.5558	31.90	3	1	1	0.147
62.132	1.4928	35.05	62.278	1.4896	5.30	2	2	2	0.146
73.177	1.2923	27.62	73.330	1.2900	5.40	4	0	0	0.153

Table A32: XRD peak list data for commercial YSZ (Goodfellow) with ICDD reference file number for tetragonal zirconium yttrium oxide, ICDD ref: 04-008-7255 [293] and zirconium oxide (ZrO_2), ICDD ref: 04-013-4343 [294].

Commercial YSZ (Goodfellow)			**Pattern Assignment**							
Pos. °2θ	**d-spacing (Å)**	**Relative intensity (%)**	**ICDD ref file**	**Pos. °2θ**	**d-spacing (Å)**	**Relative intensity (%)**	**h**	**k**	**l**	**Δ°2θ**
23.973	3.7090	4.67	ZrO_2 : #04-013-4343	24.040	3.6988	14.60	0	1	1	0.067
24.330	3.6554	3.76	ZrO_2 : #04-013-4343	24.440	3.6392	10.90	1	1	0	0.110
28.084	3.1748	29.98	ZrO_2 : #04-013-4343	28.171	3.1651	100.00	-1	1	1	0.087
30.131	2.9635	100.00	Yttrium Zirconium Oxide: #04-008-7255	30.177	2.9592	100.00	1	0	1	0.046
31.331	2.8528	20.45	ZrO_2 : #04-013-4343	31.437	2.8434	68.40	1	1	1	0.106
34.073	2.6292	7.35	ZrO_2 : #04-013-4343	34.113	2.6262	20.90	0	0	2	0.040
34.290	2.6130	6.79	ZrO_2 : #04-013-4343	34.400	2.6049	12.40	0	2	0	0.110
34.630	2.5882	8.89	Yttrium Zirconium Oxide: #04-008-7255	34.607	2.5898	8.10	0	0	2	-0.023
35.094	2.5550	17.25	ZrO_2 : #04-013-4343	35.268	2.5428	14.80	2	0	0	0.174
35.103	2.5544	17.52	Yttrium Zirconium Oxide: #04-008-7255	35.172	2.5495	13.40	1	1	0	0.069
40.562	2.2223	3.87	ZrO_2 : #04-013-4343	40.709	2.2146	12.90	-2	1	1	0.147
49.140	1.8526	5.26	ZrO_2 : #04-013-4343	49.229	1.8494	16.80	0	2	2	0.089
49.909	1.8258	11.48	ZrO_2 : #04-013-4343	50.091	1.8196	21.20	2	2	0	0.182
50.153	1.8175	29.71	Yttrium Zirconium Oxide: #04-008-7255	50.170	1.8169	33.70	1	1	2	0.017
50.449	1.8075	21.89	ZrO_2 : #04-013-4343	50.545	1.8043	11.90	-1	2	2	0.096
50.498	1.8059	21.39	Yttrium Zirconium Oxide: #04-008-7255	50.590	1.8028	17.60	2	0	0	0.092
53.847	1.7012	3.21	Yttrium Zirconium Oxide: #04-008-7255	53.799	1.7026	0.10	2	0	1	-0.048
55.263	1.6609	3.28	ZrO_2 : #04-013-4343	55.310	1.6596	8.90	2	2	1	0.047
55.501	1.6544	3.26	ZrO_2 : #04-013-4343	55.501	1.6544	3.26	1	1	-3	0.000
55.561	1.6527	3.14	ZrO_2 : #04-013-4343	55.546	1.6531	5.90	-1	1	3	-0.015

59.342	1.5561	8.89	Yttrium Zirconium Oxide: #04-008-7255	59.296	1.5572	11.60	1	0	3	-0.046
59.608	1.5498	8.28	ZrO_2 : #04-013-4343	59.773	1.5459	8.50	1	3	1	0.165
59.825	1.5447	12.64	ZrO_2 : #04-013-4343	60.004	1.5405	6.40	-3	0	2	0.179
59.957	1.5416	17.45	Yttrium Zirconium Oxide: #04-008-7255	60.043	1.5396	22.10	2	1	1	0.086
62.506	1.4847	3.98	ZrO_2 : #04-013-4343	61.927	1.4972	6.00	-2	1	3	-0.579
62.672	1.4812	5.37	Yttrium Zirconium Oxide: #04-008-7255	62.747	1.4796	5.50	2	0	2	0.075
62.705	1.4805	5.35	ZrO_2 : #04-013-4343	62.756	1.4794	9.00	3	1	1	0.051
68.440	1.3697	0.22	Yttrium Zirconium Oxide: #04-008-7255	68.493	1.3688	0.20	2	1	2	0.053
71.806	1.3136	0.48	ZrO_2 : #04-013-4343	71.836	1.3131	0.80	0	0	4	0.030
74.232	1.2765	2.77	Yttrium Zirconium Oxide: #04-008-7255	74.357	1.2747	4.00	2	2	0	0.125
77.852	1.2260	0.32	Yttrium Zirconium Oxide: #04-008-7255	78.406	1.2187	0.20	1	0	4	0.554

Table A33: XRD peak list data for CaO:Mayenite spacer blend material calcined at 800 °C, with ICDD reference file number for CaO: 04-003-7161 [226] and $Ca(OH)_2$: 01-084-1263 [289] and Mayenite: 04-014-8825 [298].

CaO + Mayenite calcined at 800 °C.			**Pattern Assignment**							
Pos. °2θ	**d-spacing (Å)**	**Relative intensity (%)**	**ICDD ref file**	**Pos. °2θ**	**d-spacing (Å)**	**Relative intensity (%)**	**h**	**k**	**l**	**Δ°2θ**
18.005	4.9227	46.16	Mayenite: #04-014-8825	18.046	4.9116	100.00	2	1	1	0.041
18.023	4.9302	46.14	$Ca(OH)_2$: #01-084-1263	18.066	4.9063	74.20	0	0	1	0.043
27.679	3.2203	8.37	Mayenite: #04-014-8825	27.722	3.2154	23.80	3	2	1	0.043
29.635	3.0120	12.80	Mayenite: #04-014-8825	29.679	3.0077	38.80	4	0	0	0.044
32.160	2.7811	42.75	CaO: #04-003-7161	32.222	2.7759	41.10	1	1	1	0.062
33.233	2.6937	28.47	Mayenite: #04-014-8825	33.277	2.6902	81.60	4	2	0	0.044
34.056	2.6305	20.55	$Ca(OH)_2$: #01-084-1263	34.101	2.6271	100.00	0	1	1	0.045
34.908	2.5682	7.45	Mayenite: #04-014-8825	34.953	2.5650	12.90	3	3	2	0.045
36.516	2.4587	14.93	Mayenite: #04-014-8825	36.561	2.4558	39.50	4	2	2	0.045
36.552	2.4625	15.29	$Ca(OH)_2$: #01-084-1263	36.601	2.4532	0.70	0	0	2	0.049
37.311	2.4081	100.00	CaO: #04-003-7161	37.377	2.4040	100.00	2	0	0	0.066
41.013	2.1989	8.96	Mayenite: #04-014-8825	41.060	2.1965	30.40	5	2	1	0.047
46.446	1.9535	8.71	Mayenite: #04-014-8825	46.495	1.9516	20.20	6	1	1	0.049
47.160	1.9304	8.03	$Ca(OH)_2$: #01-084-1263	47.144	1.9262	38.60	0	1	2	-0.016
50.805	1.7957	5.40	$Ca(OH)_2$: #01-084-1263	50.798	1.7959	26.20	1	1	0	-0.007
53.790	1.7029	47.27	Mayenite: #04-014-8825	53.840	1.7014	5.60	7	1	0	0.050
53.812	1.7022	49.76	CaO: #04-003-7161	53.891	1.6999	51.20	2	2	0	0.079
54.341	1.6869	5.84	$Ca(OH)_2$: #01-084-1263	54.356	1.6865	14.30	1	1	1	0.015
54.945	1.6698	7.33	Mayenite: #04-014-8825	54.994	1.6684	19.50	6	4	0	0.049
57.208	1.6090	6.59	Mayenite: #04-014-8825	57.257	1.6077	23.50	6	4	2	0.049
64.105	1.4515	13.56	CaO: #04-003-7161	64.194	1.4497	12.80	3	1	1	0.089
64.296	1.4512	10.15	$Ca(OH)_2$: #01-084-1263	64.300	1.4476	9.20	1	0	3	0.004
67.327	1.3897	11.61	CaO: #04-003-7161	67.417	1.3880	13.20	2	2	2	0.090

Table A34: XRD peak list data for CaO + $CaZrO_3$ (from a $Ca(OH)_2$ precursor) spacer blend material calcined at 800 °C, with ICDD reference file number for CaO: 04-003-7161 [226] and $CaZrO_3$: 04-010-6398 [297].

CaO + $CaZrO_3$ (from a $Ca(OH)_2$ precursor)			**Pattern Assignment**						
Pos. °2θ	**d-spacing (Å)**	**Relative intensity (%)**	**ICDD ref file**	**Pos. °2θ**	**d-spacing (Å)**	**Relative intensity (%)**	**h**	**k**	**l**	**Δ°2θ**
22.481	3.9517	14.50	$CaZrO_3$: #04-010-6398	22.116	4.0161	51.40	0	2	0	-0.365
31.439	2.8432	15.77	$CaZrO_3$: #04-010-6398	31.013	2.8813	25.60	0	0	2	-0.426
31.828	2.8093	33.92	$CaZrO_3$: #04-010-6398	31.488	2.8389	100.00	1	2	1	-0.340
32.205	2.7773	19.49	$CaZrO_3$: #04-010-6398	31.937	2.8000	23.00	2	0	0	-0.268
32.585	2.7458	45.80	CaO: #04-003-7161	32.222	2.7759	41.10	1	1	1	-0.363
37.733	2.3821	100.00	CaO: #04-003-7161	37.377	2.4040	100.00	2	0	0	-0.356
45.432	1.9947	12.05	$CaZrO_3$: #04-010-6398	45.116	2.0080	36.50	2	0	2	-0.316
50.581	1.8031	2.35	$CaZrO_3$: #04-010-6398	50.167	1.8170	5.90	3	1	0	-0.414
51.101	1.7860	4.81	$CaZrO_3$: #04-010-6398	50.801	1.7958	13.60	2	2	2	-0.300
51.613	1.7694	2.10	$CaZrO_3$: #04-010-6398	50.167	1.8170	5.90	3	1	0	-1.446
54.222	1.6903	49.01	CaO: #04-003-7161	53.891	1.6999	51.20	2	2	0	-0.331
55.857	1.6446	6.37	$CaZrO_3$: #04-010-6398	55.781	1.6467	10.60	0	4	2	-0.076
56.106	1.6379	7.08	$CaZrO_3$: #04-010-6398	56.362	1.6311	9.80	2	4	0	0.256
56.821	1.6190	8.82	$CaZrO_3$: #04-010-6398	56.631	1.6240	21.50	3	2	1	-0.190
64.508	1.4434	12.64	CaO: #04-003-7161	64.194	1.4497	12.80	3	1	1	-0.314
65.986	1.4146	3.31	$CaZrO_3$: #04-010-6398	65.734	1.4194	10.50	2	4	2	-0.252
67.726	1.3824	13.17	CaO: #04-003-7161	67.417	1.3880	13.20	2	2	2	-0.309
74.941	1.2662	3.13	$CaZrO_3$: #04-010-6398	74.727	1.2693	8.20	1	6	1	-0.214
79.784	1.2041	4.25	CaO: #04-003-7161	79.710	1.2020	5.00	4	0	0	-0.074
79.914	1.1994	4.34	$CaZrO_3$: #04-010-6398	79.750	1.2015	1.60	4	2	2	-0.164

Table A35: XRD peak list data for CaO + $CaZrO_3$ + ZrO_2 (from a CaAc precursor) spacer blend material calcined at 800 °C, with ICDD reference file number for CaO: 04-003-7161 [226], $Ca(OH)_2$: 01-084-1263 [289], ZrO_2: 04-013-4343 [294] and $CaZrO_3$: 04-010-6398 [297].

CaO + $CaZrO_3$ + ZrO_2 (from a CaAc precursor)			**Pattern Assignment**						
Pos. °2θ	**d-spacing (Å)**	**Relative intensity (%)**	**ICDD ref file**	**Pos. °2θ**	**d-spacing (Å)**	**Relative intensity (%)**	**h**	**k**	**l**	**Δ°2θ**
22.054	4.0273	6.66	$CaZrO_3$: #04-010-6398	22.116	4.0161	51.40	0	2	0	0.062
29.732	3.0025	3.94	ZrO_2: #04-013-4343	28.710	3.1651	100.00	-1	1	1	-1.022
30.920	2.8897	5.49	$CaZrO_3$: #04-010-6398	31.013	2.8813	25.60	0	0	2	0.093
31.395	2.8471	14.54	$CaZrO_3$: #04-010-6398	31.488	2.8389	100.00	1	2	1	0.093
31.820	2.8100	7.97	$CaZrO_3$: #04-010-6398	31.937	2.8000	23.00	2	0	0	0.117
32.129	2.7837	43.42	CaO: #04-003-7161	32.222	2.7759	41.10	1	1	1	0.093
34.238	2.6186	6.36	$Ca(OH)_2$: #01-084-1263	34.101	2.6271	100.00	0	1	1	-0.137
37.280	2.4100	100.00	CaO: #04-003-7161	37.377	2.4040	100.00	2	0	0	0.097
44.993	2.0132	5.07	$CaZrO_3$: #04-010-6398	45.116	2.0080	36.50	2	0	2	0.123
50.005	1.8208	0.87	$CaZrO_3$: #04-010-6398	50.167	1.8170	5.90	3	1	0	0.162
50.679	1.7999	1.94	$CaZrO_3$: #04-010-6398	50.801	1.7958	13.60	2	2	2	0.122
53.780	1.7032	49.55	CaO: #04-003-7161	53.891	1.6999	51.20	2	2	0	0.111
55.680	1.6494	2.34	$CaZrO_3$: #04-010-6398	55.781	1.6467	10.60	0	4	2	0.101
56.486	1.6278	3.79	$CaZrO_3$: #04-010-6398	56.631	1.6240	21.50	3	2	1	0.145
64.073	1.4521	12.62	CaO: #04-003-7161	64.194	1.4497	12.80	3	1	1	0.121

65.607	1.4219	1.36	$CaZrO_3$: #04-010-6398	65.734	1.4194	10.50	2	4	2	0.127
67.295	1.3902	13.24	CaO: #04-003-7161	67.417	1.3880	13.20	2	2	2	0.122
74.619	1.2208	1.19	$CaZrO_3$: #04-010-6398	74.727	1.2693	8.20	1	6	1	0.108
79.562	1.2039	5.30	CaO: #04-003-7161	79.710	1.2020	5.00	4	0	0	0.148
79.570	1.2038	5.36	$CaZrO_3$: #04-010-6398	79.750	1.2015	1.60	4	2	2	0.180

Table A36: XRD peak list data for CaO (from a CaAc precursor) + hydrothermally prepared YSZ (hYSZ) spacer blend material calcined at 800 °C, with ICDD reference file number for CaO: 04-003-7161 [226], $Ca(OH)_2$: 01-084-1263 [289] and cubic zirconium yttrium oxide, ICDD ref: 01-077-2112 [295].

CaO (from a CaAc precursor) + hydrothermally prepared YSZ (hYSZ)			**Pattern Assignment**							
Pos. °2θ	**d-spacing (Å)**	**Relative intensity (%)**	**ICDD ref file**	**Pos. °2θ**	**d-spacing (Å)**	**Relative intensity (%)**	**h**	**k**	**l**	**Δ°2θ**
18.011	4.9212	19.33	$Ca(OH)_2$: #01-084-1263	18.066	4.9063	74.20	0	0	1	0.055
28.643	3.1140	5.27	$Ca(OH)_2$: #01-084-1263	28.676	3.1106	19.10	1	0	0	0.033
30.073	2.9692	3.59	Cubic YSZ #01-077-2112	29.970	2.9791	100.00	1	1	1	-0.103
32.158	2.7812	42.46	CaO: #04-003-7161	32.222	2.7759	41.10	1	1	1	0.064
34.056	2.6304	28.83	$Ca(OH)_2$: #01-084-1263	34.101	2.6271	100.00	0	1	1	0.045
35.116	2.5534	2.54	Cubic YSZ #01-077-2112	34.743	2.5800	21.60	2	0	0	-0.373
36.522	2.4583	2.02	$Ca(OH)_2$: #01-084-1263	36.601	2.4532	0.70	0	0	2	0.079
37.308	2.4083	100.00	CaO: #04-003-7161	37.377	2.4040	100.00	2	0	0	0.069
47.074	1.9289	11.11	$Ca(OH)_2$: #01-084-1263	47.144	1.9262	38.60	0	1	2	0.070
49.969	1.8237	1.97	Cubic YSZ #01-077-2112	49.953	1.8243	48.20	2	2	0	-0.016
50.767	1.7970	7.29	$Ca(OH)_2$: #01-084-1263	50.798	1.7959	26.20	1	1	0	0.031
53.805	1.7024	49.04	CaO: #04-003-7161	53.891	1.6999	51.20	2	2	0	0.086
54.315	1.6876	6.20	$Ca(OH)_2$: #01-084-1263	54.356	1.6865	14.30	1	1	1	0.041
56.091	1.6383	0.40	$Ca(OH)_2$: #01-084-1263	56.199	1.6354	1.10	0	0	3	0.108
59.344	1.5561	0.56	Cubic YSZ #01-077-2112	59.355	1.5558	31.90	3	1	1	0.011
59.939	1.5420	0.82	$Ca(OH)_2$: #01-084-1263	59.376	1.5553	2.10	2	0	0	-0.563
62.553	1.4837	2.85	Cubic YSZ #01-077-2112	62.278	1.4896	5.30	2	2	2	-0.275
62.567	1.4834	2.85	$Ca(OH)_2$: #01-084-1263	62.606	1.4826	9.80	2	0	1	0.039
64.095	1.4517	14.28	CaO: #04-003-7161	64.194	1.4497	12.80	3	1	1	0.099
64.161	1.4504	14.03	$Ca(OH)_2$: #01-084-1263	64.300	1.4476	9.20	1	0	3	0.139
67.316	1.3898	11.86	CaO: #04-003-7161	67.417	1.3880	13.20	2	2	2	0.101
71.747	1.3145	1.81	$Ca(OH)_2$: #01-084-1263	71.808	1.3136	7.10	2	0	2	0.061
72.485	1.3029	0.47	Cubic YSZ #01-077-2112	73.330	1.2900	5.40	4	0	0	0.845
74.265	1.2761	0.13	$Ca(OH)_2$: #01-084-1263	77.807	1.2266	1.00	0	0	4	3.542
79.047	1.2104	0.61	$Ca(OH)_2$: #01-084-1263	79.143	1.2092	1.80	1	1	3	0.096
79.588	1.2035	4.58	CaO: #04-003-7161	79.710	1.2020	5.00	4	0	0	0.122

Table A37: XRD peak list data for CaO (from a CaAc precursor) + commercial YSZ (Goodfellow) spacer blend material calcined at 800 °C, with ICDD reference file number for CaO: 04-003-7161 [226], $Ca(OH)_2$: 01-084-1263 and tetragonal zirconium yttrium oxide, ICDD ref: 04-008-7255 [293].

CaO (from a CaAc precursor) + commercial YSZ (Goodfellow)			Pattern Assignment						
Pos. °2θ	**d-spacing (Å)**	**Relative intensity (%)**	**ICDD ref file**	**Pos. °2θ**	**d-spacing (Å)**	**Relative intensity (%)**	**h**	**k**	**l**	**Δ°2θ**
18.555	4.7781	2.13	$Ca(OH)_2$: #01-084-1263	18.066	4.9063	74.20	0	0	1	-0.489
28.874	3.0897	1.55	$Ca(OH)_2$: #01-084-1263	28.676	3.1106	19.10	1	0	0	-0.198
30.505	2.9281	100.00	Yttrium Zirconium Oxide: #04-008-7255	30.177	2.9592	100.00	1	0	1	-0.328
32.519	2.7512	37.66	CaO: #04-003-7161	32.222	2.7759	41.10	1	1	1	-0.297
34.386	2.6060	4.54	$Ca(OH)_2$: #01-084-1263	34.101	2.6271	100.00	0	1	1	-0.285
34.979	2.5631	11.40	Yttrium Zirconium Oxide: #04-008-7255	34.607	2.5898	8.10	0	0	2	-0.372
35.466	2.5291	15.32	Yttrium Zirconium Oxide: #04-008-7255	35.172	2.5495	13.40	1	1	0	-0.294
37.208	2.4146	9.04	$Ca(OH)_2$: #01-084-1263	36.601	2.4532	0.70	0	0	2	-0.607
37.661	2.3866	90.87	CaO: #04-003-7161	37.377	2.4040	100.00	2	0	0	-0.284
43.301	2.0878	0.97	Yttrium Zirconium Oxide: #04-008-7255	42.965	2.1034	0.90	1	0	2	-0.336
47.590	1.9092	1.50	$Ca(OH)_2$: #01-084-1263	47.144	1.9262	38.60	0	1	2	-0.446
50.481	1.8065	37.99	Yttrium Zirconium Oxide: #04-008-7255	50.170	1.8169	33.70	1	1	2	-0.311
50.842	1.7945	29.20	Yttrium Zirconium Oxide: #04-008-7255	50.590	1.8028	17.60	2	0	0	-0.252
50.841	1.7945	29.26	$Ca(OH)_2$: #01-084-1263	50.798	1.7959	26.20	1	1	0	-0.043
54.054	1.6952	42.01	Yttrium Zirconium Oxide: #04-008-7255	53.799	1.7026	0.10	2	0	1	-0.255
54.126	1.6931	49.59	CaO: #04-003-7161	53.891	1.6999	51.20	2	2	0	-0.235
54.455	1.6836	19.12	$Ca(OH)_2$: #01-084-1263	54.356	1.6865	14.30	1	1	1	-0.099
56.945	1.6158	0.15	$Ca(OH)_2$: #01-084-1263	56.199	1.6354	1.10	0	0	3	-0.746
59.635	1.5492	13.07	Yttrium Zirconium Oxide: #04-008-7255	59.296	1.5572	11.60	1	0	3	-0.339
59.351	1.5559	4.07	$Ca(OH)_2$: #01-084-1263	59.376	1.5553	2.10	2	0	0	0.025
60.279	1.5341	23.64	Yttrium Zirconium Oxide: #04-008-7255	60.043	1.5396	22.10	2	1	1	-0.236
62.632	1.4820	1.52	$Ca(OH)_2$: #01-084-1263	62.606	1.4826	9.80	2	0	1	-0.026
63.010	1.4741	6.21	Yttrium Zirconium Oxide: #04-008-7255	62.747	1.4796	5.50	2	0	2	-0.263
64.396	1.4456	13.39	CaO: #04-003-7161	64.194	1.4497	12.80	3	1	1	-0.202
64.921	1.4352	2.18	$Ca(OH)_2$: #01-084-1263	64.300	1.4476	9.20	1	0	3	-0.621
67.609	1.3845	13.51	CaO: #04-003-7161	67.417	1.3880	13.20	2	2	2	-0.192
68.733	1.3646	0.55	Yttrium Zirconium Oxide: #04-008-7255	68.493	1.3688	0.20	2	1	2	-0.240
71.964	1.3111	0.29	$Ca(OH)_2$: #01-084-1263	71.808	1.3136	7.10	2	0	2	-0.156
73.368	1.2894	1.90	Yttrium Zirconium Oxide: #04-008-7255	73.007	1.2949	1.70	0	0	4	-0.361
74.526	1.2722	4.19	Yttrium Zirconium Oxide: #04-008-7255	74.357	1.2747	4.00	2	2	0	-0.169
78.739	1.2144	0.35	$Ca(OH)_2$: #01-084-1263	77.807	1.2266	1.00	0	0	4	-0.932
78.742	1.2143	0.35	Yttrium Zirconium Oxide: #04-008-7255	78.406	1.2187	0.20	1	0	4	-0.336
79.567	1.2038	1.62	$Ca(OH)_2$: #01-084-1263	79.143	1.2092	1.80	1	1	3	-0.424
79.852	1.2002	5.44	CaO: #04-003-7161	79.710	1.2020	5.00	4	0	0	-0.142

Table A38: XRD peak list data for CaAc sample carbonated & decarbonated by TGA, then analysed for effect of hydration by TGA, and by overnight air exposure, with ICDD reference file number for CaO: 04-003-7161 [226], calcite: 00-005-0586 [221] and $Ca(OH)_2$: 01-084-1263 [289].

CaAc sample carbonated & decarbonated, then analysed for effect of hydration by TGA, and by overnight air exposure.			**Pattern Assignment**						
Pos. °2θ	**d-spacing (Å)**	**Relative intensity (%)**	**ICDD ref file**	**Pos. °2θ**	**d-spacing (Å)**	**Relative intensity (%)**	**h**	**k**	**l**	**Δ°2θ**
17.886	4.9592	74.21	$Ca(OH)_2$: #01-084-1263	18.066	4.9060	74.20	0	0	1	0.180
28.667	3.1141	29.72	$Ca(OH)_2$: #01-084-1263	28.676	3.1106	19.10	1	0	0	0.009
29.975	2.9770	7.54	Calcite: #00-005-0586	29.406	3.0350	100.00	1	0	4	-0.569
33.899	2.6445	100.00	$Ca(OH)_2$: #01-084-1263	34.101	2.6271	100.00	0	1	1	0.202
37.088	2.4241	9.18	CaO: #04-003-7161	37.377	2.4040	100.00	2	0	0	0.289
47.067	1.9308	32.17	$Ca(OH)_2$: #01-084-1263	47.144	1.9262	38.60	0	1	2	0.077
50.658	1.8020	49.21	$Ca(OH)_2$: #01-084-1263	50.798	1.7959	26.20	1	1	0	0.140
53.946	1.6997	24.96	$Ca(OH)_2$: #01-084-1263	54.356	1.6865	14.30	1	1	1	0.410
59.071	1.5639	9.76	$Ca(OH)_2$: #01-084-1263	59.376	1.5553	2.10	2	0	0	0.305
62.325	1.4898	15.79	$Ca(OH)_2$: #01-084-1263	62.606	1.4826	9.80	2	0	1	0.281
64.075	1.4515	15.21	$Ca(OH)_2$: #01-084-1263	64.300	1.4476	9.20	1	0	3	0.225
64.171	1.4514	12.52	CaO: #04-003-7161	64.194	1.4497	12.80	3	1	1	0.023
71.590	1.3170	10.17	$Ca(OH)_2$: #01-084-1263	71.808	1.3136	7.10	2	0	2	0.218

Chapter 6. Conclusions

The main aims of this research were to develop synthesis and characterisation protocols for two different nanoparticulate materials; hydroxyapatite (HA), which can be used as a biomaterial, and calcium oxide (CaO), which can be utilised as a powder sorbent for CO_2 capture. For the analysis of these nanoparticulate materials, various bulk and particle level characterisation techniques have been employed, and have been complemented by the use of current and newly developed analytical methods using the transmission electron microscope (TEM); including a low electron-fluence EDX technique for the reliable analysis of the Ca/P ratio of small nano-clusters of HA nanoparticles, and *in*- and *ex-situ* techniques for the analysis of nanoparticulate CaO with a reduced risk of sorbent hydration.

Characterisation of the physical and chemical properties of nanoparticulate HA powders produced by hydrothermal and sol-gel methods has been carried out using Fourier transform infrared spectroscopy (FTIR), laser ablation inductively coupled plasma mass spectrometry (LA-ICP-MS), X-ray diffraction (XRD), X-ray fluorescence (XRF), scanning electron microscopy (SEM) and transmission electron microscopy with energy dispersive X-ray analysis (TEM-EDX), with results compared to a commercially available HA powder (Sigma-Aldrich).

Sample analysis confirms that phase-pure HA with near-stoichiometric composition (Ca/P = 1.67) was achieved by the hydrothermal route, with particles displaying regular rod-shaped morphologies (typically 50 - 300 nm in length). The average Ca/P ratio from TEM-EDX, for the hydrothermal HA prepared at pH 11 was 1.61 (S.D = 0.17).

The sol-gel samples (calcined at 500 °C and 700 °C) produced impure HA; an additional phase of calcium carbonate ($CaCO_3$) was observed in the 500 °C sample, and β-tricalcium phosphate (β-TCP), dicalcium phosphate anhydrate (DCPA) and traces of calcium oxide (CaO) were observed in the 700 °C sample. The impurities observed in the sol-gel HA powders are attributed, in part, to the evaporative loss of triethyl phosphite during specimen preparation and the thermal decomposition of the primary HA phase during calcination (at 700 °C). The low fluence TEM-EDX technique highlighted particle to particle compositional variability, with greater variance in the Ca/P ratio observed in the samples prepared by the sol-gel method, in comparison to the HA samples prepared by the hydrothermal method and the commercial HA sample. The sol-gel powders displayed average Ca/P ratios of 1.72 for 500 °C (S.D = 0.38) and 1.65 for 700 °C (S.D = 0.35). Bulk analysis of the Ca/P ratio by XRF and LA-ICP-MS confirmed deviations away from the stoichiometric target of 1.67 for the phase-impure HA samples.

Both HA samples prepared by the sol-gel method exhibited equiaxed or rounded shaped particles, with extensive agglomeration of both observed by SEM. Increasing the calcination temperature from 500 °C to 700 °C increased the average particle length from 70 nm to 108 nm respectively, with some particles reaching lengths of 225 - 250 nm in the HA sample calcined at 700 °C.

Two additional samples of HA synthesised by the hydrothermal method, have been prepared with starting suspensions held at pH 9 and pH 11. The increase in pH of the starting suspension hindered particle growth with the pH 9 and pH 11 HA samples showing average particle lengths of ~200 nm and ~130 nm respectively. These samples were subsequently examined for cytotoxicity against a selection of cell lines (Caco-2, A549 and SH-SY5Y) by an undergraduate research group led by Dr Lars Jeuken at the Leeds Faculty of Biological Sciences. Results of HA

cytotoxicity indicated promising and expected biocompatibility, but were inconclusive as to the effect of particle size and shape, and would require further research. Assays carried out here showed little affect on cell viability across all cell lines tested, with decreases in cell viability only observed at very high particle doses, typically > 500 μg ml^{-1}.

The second component of this thesis has examined the thermal decomposition of calcium acetate hydrate (CaAc) for the formation of CaO-based nanoparticulate powder sorbents for CO_2 capture. Thermal analysis of the decomposition of CaAc was performed by thermogravimetric analysis (TGA) and *in-situ* hot-stage XRD, with results showing that full decomposition of CaAc to CaO was complete at 800 °C by TGA, and a longer dwell time using the hot-stage XRD showed the decomposition of CaAc to CaO was complete at 700 °C. Intermediate phases of dehydrated-CaAc and calcite ($CaCO_3$) were observed after decomposition at 300 °C and 500 °C respectively by hot-stage XRD, and vaterite ($CaCO_3$) was also observed (along with calcite) after decomposition at 500 °C by TGA. Analysis of the CaO product by SEM and TEM showed highly sintered agglomerates of fine plate-like particles (typically < 100 nm) with some nanoporosity observed. Complications with the analysis of CaO samples (collected from the TGA) by SEM, TEM and XRD arose due to the reactive nature of CaO with atmospheric moisture and CO_2 at ambient conditions, with $Ca(OH)_2$ and $CaCO_3$ phases regularly detected.

Calcium oxide produced by the decomposition of CaAc has shown to be an effective powder sorbent for the high temperature capture of CO_2, with 71.7% mass increase observed after carbonation at 650 °C (in 100% CO_2) for 15 minutes by TGA. This is equivalent to a molar conversion ratio (χ) of CaO to $CaCO_3$, of 0.92. The kinetics of carbonation were shown to be controlled firstly by fast linear growth which then developed into that controlled by solid-state diffusion of CO_2 through a

product layer of $CaCO_3$. From SEM and TEM analysis, the carbonated product layer was observed to be large, micron-sized agglomerates that are comprised of significantly sintered polygonal crystals (typically > 200 nm) with many particle boundaries meeting at equilibrium angles i.e. 120°. Overall growth of the individual carbonated particles appears limited by a large amount of particle densification.

The regenerability of CaO after carbonation ($CaO \xrightarrow{CO_2} CaCO_3$) was analysed by TGA with the development of a multicycle carbonation and decarbonation program. With increasing cycles of carbonation (in CO_2) at 650 °C for 5 mins followed by decarbonation (in N_2) at 800 °C with no dwell, the molar conversion ratio (χ) of CaO to $CaCO_3$ was shown to decrease from 0.89 after the first cycle, to 0.57 after 9 cycles. This decrease has been attributed to the sintering (reduction in surface area) of the sorbent upon decarbonation. Structural analysis by SEM and TEM of samples (extracted from the TGA at progressive stages of the multicycle process) showed an increasing average particle size of the sorbent with progressing decarbonation cycles, and an observed lower surface area. The initial sorbent showed an average particle size of 145 nm, this increased to 230 nm after the 9^{th} decarbonation cycle. With progressive carbonation cycles the particle size of $CaCO_3$ crystals was observed to gradually decrease. Analysis of decarbonated samples highlighted the issue of sorbent hydration upon storage, sample preparation and analysis; particle densification was observed by SEM however a decrease in crystallite size was observed by TEM with progressive decarbonations, which is attributed to the formation of ultra-fine polycrystalline $Ca(OH)_2$ particles (consistent with broad XRD peaks observed for $Ca(OH)_2$) upon storage. The amount hydration of each CaO sample is not considered to be related to the number of decarbonation cycles.

The above analysis of the sorbent by SEM and TEM, at progressive stages of the multicycle process, was significantly affected by hydration and small amounts of

carbonation when the sorbent was exposed to normal atmospheric conditions (during storage, sample preparation and analysis). To address this, a TEM based technique using an *ex-situ* environmental cell (E-cell) was developed for the analysis of a CaO sorbent during multicycle CO_2 capture. By performing carbonation and decarbonation steps in a sealed unit that can be directly transferred to the TEM under rotary vacuum, this method aimed to reduce the risk of sorbent hydration and carbonation at ambient conditions, allowing for more accurate structural analysis of the CaO sorbent. Results showed that slow, low-vacuum decarbonation (in the E-cell) creates a densified 'skeleton' of CaO, consistent with the drop in capture capacity observed by TGA. In comparison to the analysis of the decarbonated samples extracted from the TGA, and decarbonation by *in-situ* hot-stage TEM, the *ex-situ* E-cell technique is considered to provide the closest microstructural match to the conditions inside the TGA.

Modification of CaO sorbents were investigated using zirconia based- and mayenite dopant ('spacer') materials which aimed to reduce the sintering of the sorbent upon decarbonation. Results showed that cycle-by-cycle decay in CO_2 uptake capacity was achieved using spacer additive, with commercial YSZ powder shown to be most effective spacer material.

6.1. Future work

- Engineer bio-activity improvements (e.g. Sr substitution promotes bone growth [264, 265]) of nanoparticulate HA produced by the hydrothermal method with elemental substitutions (e.g. Na^+, Mg^{2+},

Sr^{2+}, F^{-}, Ag^{-}, Cu^{2+} and Zn^{2+}). Analyse potential cytotoxicity effects of these modified HA samples.

- Understand the relationship between sorbent microstructure and CO_2 capture capacity and durability through the development of novel *in-* and *ex-situ* TEM techniques to understand the structural changes of powder sorbents that are currently un-documented.
- Further develop the *ex-situ* E-cell TEM technique for the analysis of multicycle CO_2 capture. This includes: improving vacuum quality to remove risk of sorbent hydration, and investigating the origin of Si/Mo particles formed upon decarbonation at 800 °C.
- Understand the inter-dependence of microstructural alteration during low-temperature carbonation and high-temperature calcination and the effect of deliberate sorbent hydration between cycles.
- Synthesise new sorbent blends with additives which offset sintering during carbonation and are also beneficial to inhibiting densification during decarbonation, and therefore demonstrate improved durability over many (100+) thermal cycles.

References

1. Jillavenkatesa A and Condrate RA, *Sol-gel processing of hydroxyapatite.* Journal of Materials Science, 1998. **33**(16): p. 4111-9.
2. Legros, R., N. Balmain, and G. Bonel, *Age-related changes in mineral of rat and bovine cortical bone.* Calcified Tissue International, 1987. **41**(3): p. 137-144.
3. Suchanek, W. and M. Yoshimura, *Processing and properties of hydroxyapatite-based biomaterials for use as hard tissue replacement implants.* Journal of Materials Research, 1998. **13**(1): p. 94-117.
4. Koutsopoulos, S., *Synthesis and characterization of hydroxyapatite crystals: A review study on the analytical methods.* Journal of Biomedical Materials Research, 2002. **62**(4): p. 600-612.
5. Koch, C.F., *et al.*, *Pulsed laser deposition of hydroxyapatite thin films.* Materials Science and Engineering: C, 2007. **27**(3): p. 484-494.
6. Posner, A.S. and F. Betts, *Synthetic amorphous calcium phosphate and its relation to bone mineral structure.* Accounts of Chemical Research, 1975. **8**(8): p. 273-281.
7. Afferrante, L., M. Ciavarella, and E. Valenza, *Is Weibull's modulus really a material constant? Example case with interacting collinear cracks.* International Journal of Solids and Structures, 2006. **43**(17): p. 5147-5157.
8. Bohner, M., *Calcium phosphate emulsions: Possible applications.* Bioceramics, 2000. **192-195**: p. 765-768.
9. Ong, J.L. and D.C.N. Chan, *Hydroxyapatite and their use as coatings in dental implants: A review.* Critical Reviews in Biomedical Engineering, 2000. **28**(5-6): p. 667A-707A.
10. Torrisi, L. and R. Setola, *Thermally assisted hydroxyapatite obtained by pulsed-laser deposition on titanium substrates.* Thin Solid Films, 1993. **227**(1): p. 32-36.
11. Best, S.M., *et al.*, *Bioceramics: Past, present and for the future.* Journal of the European Ceramic Society, 2008. **28**(7): p. 1319-1327.
12. Bonfield, W., *et al.*, *Hydroxyapatite reinforced polyethylene: a mechanically compatible implant.* Biomaterials, 1981. **2**(3): p. 185-186.
13. Bonfield, W., M. Wang, and K.E. Tanner, *Interfaces in analogue biomaterials.* Acta Mater, 1998. **46**(7): p. 2509-2518.
14. de Groot, K., *et al.*, *Plasma sprayed coatings of hydroxylapatite.* Journal of Biomedical Research, 1987. **21**: p. 1375-1381.
15. de Groot, K., J.G.C. Wolke, and J.A. Jansen, *Calcium phosphate coatings for medical implants.* Proceedings of the Institution of Mechanical Engineers, Part H: Journal of Engineering in Medicine, 1998. **212**: p. 137-147.
16. Fernandez, E., *et al.*, *Calcium phosphate bone cements for clinical applications, part I, solution chemistry & part II, precipitate formation during setting reactions.* Journal of Materials Science, 1999. **10**: p. 169-184.
17. Zhang, R.Y. and P.X. Ma, *Poly(alpha-hydroxyl acids) hydroxyapatite porous composites for bone-tissue engineering. I. Preparation and morphology.* Journal of Biomedical Materials Research, 1999. **44**(4): p. 446-455.

18. Thomson, R.C., *et al*., *Hydroxyapatite fiber reinforced poly(alpha-hydroxy ester) foams for bone regeneration.* Biomaterials, 1998. **19**(21): p. 1935-1943.
19. Hartgerink, J.D., E. Beniash, and S.I. Stupp, *Self-assembly and mineralization of peptide-amphiphile nanofibers.* Science, 2001. **294**(5547): p. 1684-1688.
20. Earl, J.S., D.J. Wood, and S.J. Milne, *Nanoparticles for dentine tubule infiltration: an in-vitro study.* Journal of Nanoscience and Nanotechnology, 2009. **9**(11): p. 6668-6674.
21. Earl, J.S., D.J. Wood, and S.J. Milne, *Dentine infiltration - A cure for sensitive teeth.* American Ceramic Society Bulletin, 2006. **85**(7): p. 22-25.
22. Tschoppe, P., *et al*., *Enamel and dentine remineralization by nano-hydroxyapatite toothpastes.* Journal of Dentistry. **39**(6): p. 430-437.
23. LeGeros, R.Z. and R.G. Craig, *Strategies to affect bone remodeling: Osteointegration.* Journal of Bone and Mineral Research, 1993. **8**(S2): p. S583-S596.
24. Habraken, W., J.G.C. Wolke, and J.A. Jansen, *Ceramic composites as matrices and scaffolds for drug delivery in tissue engineering.* Advanced Drug Delivery Reviews, 2007. **59**(4-5): p. 234-248.
25. Shinto, Y., *et al*., *Calcium hydroxyapatite ceramic used as a delivery system for antibiotics.* Journal of Bone and Joint Surgery-British Volume, 1992. **74**(4): p. 600-604.
26. Liu, D.M., T. Troczynski, and W.J. Tseng, *Water-based sol-gel synthesis of hydroxyapatite: process development.* Biomaterials, 2001. **22**(13): p. 1721-1730.
27. Ergun, C., *Effect of Ti ion substitution on the structure of hydroxylapatite.* Journal of the European Ceramic Society, 2008. **28**(11): p. 2137-2149.
28. Mann, S., *Biomineralisation: Principles and concepts in bioinorganic materials chemistry* 2001, Oxford: Oxford University Press.
29. de Jong, W.F., *Le substance minerale dans le os.* Recueil des Travaux Chimiques des Pays-Bas, 1926. **45**: p. 445-450.
30. Náray Szabó, S., *The Structure of Apatite (CaF) Ca_4 $(PO_4)_3$.* Zeitschrift für Kristallographie, 1930. **75**: p. 387-398.
31. Mehmel, M., *Über die Struktur des Apatits.* Zeitschrift für Kristallographie, 1930. **75**: p. 323-331.
32. Parthe, E. and W. Rieger, *Nowotny Phases and Apatites: A Comparative Study.* Journal of Dental Research, 1968. **47**(5): p. 829-835.
33. Posner, A.S., *Crystal chemistry of bone mineral.* Physiological Reviews, 1969. **49**(4): p. 760-792.
34. Kay, M.I., R.A. Young, and A.S. Posner, *Crystal Structure of Hydroxyapatite.* Nature, 1964. **204**: p. 1050-1052.
35. Zapanta-Legeros, R., *Effect of Carbonate on the Lattice Parameters of Apatite.* Nature, 1965. **206**(4982): p. 403-404.
36. Posner, A.S., A. Perloff, and A.F. Diorio, *Refinement of the hydroxyapatite structure.* Acta Crystallographica, 1958. **11**(4): p. 308-309.
37. Sudarsanan K and R.A. Young, *Significant Precision in Crystal Structural Details: Holly Springs Hydroxyapatite.* Acta Crystallographica, 1969. **25**(8): p. 1534-1543.
38. Terra J, *et al*., *The structure of strontium-doped hydroxyapatite: an experimental and theoretical study.* Physical Chemistry Chemical Physics, 2008. **11**(3).

39. Hughes, J.M., *Structure and Chemistry of the Apatites and Other Calcium Orthophosphates.* Journal of the American Chemical Society, 1996. **118**(12): p. 3071-3072.
40. Elliott, J.C., *Structure, Crystal Chemistry and Density of Enamel Apatites*, in *Ciba Foundation Symposium 205 - Dental Enamel*, D.J. Chadwick and G. Cardew, Editors. 2007, John Wiley & Sons: London. p. 54-72.
41. LeGeros, R.Z., *et al*., *Formation and stability of apatites effects of some cationic substituents.* 2nd International Congress on Phosphorus Compounds: Proceedings, 1980: p. 88-103.
42. de Maeyer, E.A.P. and R.M.H. Verbeeck, *Possible substitution mechanisms for sodium and carbonate in calcium hydroxyapatite.* Bulletin des Sociétés Chimiques Belges, 1993. **102**(9): p. 601-609.
43. Teknimed. *Hydroxyapatite*. 2008. [Online] Available from: http://www.teknimed.com/en/pageLibre000104a1.htm [Accessed 12 Jan 2009].
44. Elliott, J.C. and R.A. Young, *Conversion of Single Crystals of Chlorapatite into Single Crystals of Hydroxyapatite.* Nature, 1967. **214**(5091): p. 904-906.
45. Rao, R.R., H.N. Roopa, and T.S. Kannan, *Solid state synthesis and thermal stability of HAP and HAP - beta-TCP composite ceramic powders.* Journal of Materials Science-Materials in Medicine, 1997. **8**(8): p. 511-518.
46. Han, Y., X. Wang, and S. Li, *A simple route to prepare stable hydroxyapatite nanoparticles suspension.* Journal of Nanoparticle Research, 2009. **11**(5): p. 1235-1240.
47. Cengiz, B., *et al*., *Synthesis and characterization of hydroxyapatite nanoparticles.* Colloids and Surfaces A: Physicochemical and Engineering Aspects, 2008. **322**(1-3): p. 29-33.
48. Zhang, Y. and J. Lu, *A simple method to tailor spherical nanocrystal hydroxyapatite at low temperature.* Journal of Nanoparticle Research, 2007. **9**(4): p. 589-594.
49. Earl J S, Wood D J, and Milne S J, *Hydrothermal synthesis of hydroxyapatite.* Journal of Physics Conference Series, 2006. **26**: p. 268.
50. Zhang, X. and K.S. Vecchio, *Hydrothermal synthesis of hydroxyapatite rods.* Journal of Crystal Growth, 2007. **308**(1): p. 133-140.
51. Zhou, Z.-H., *et al*., *Controllable synthesis of hydroxyapatite nanocrystals via a dendrimer-assisted hydrothermal process.* Materials Research Bulletin, 2007. **42**(9): p. 1611-1618.
52. Jinawath, S., D. Pongkao, and M. Yoshimura, *Hydrothermal synthesis of hydroxyapatite from natural source.* Journal of Materials Science: Materials in Medicine, 2002. **13**(5): p. 491-494.
53. Yoshimura, M., *et al*., *Hydrothermal Synthesis of Biocompatible Whiskers.* Journal of Materials Science, 1994. **29**(13): p. 3399-3402.
54. Liu, H.S., *et al*., *Hydroxyapatite synthesized by a simplified hydrothermal method.* Ceramics International, 1997. **23**(1): p. 19-25.
55. Ioku, K., *et al*., *Hydrothermal preparation of tailored hydroxyapatite.* Journal of Materials Science, 2006. **41**(5): p. 1341-1344.
56. Neira, I.S., *et al*., *Hydrothermal synthesis of hydroxyapatite whiskers with sharp faceted hexagonal morphology.* Journal of Materials Science, 2008. **43**(7): p. 2171-2178.
57. Liu, J.B., *et al*., *The influence of pH and temperature on the morphology of hydroxyapatite synthesized by hydrothermal method.* Ceramics International, 2003. **29**(6): p. 629-633.

58. Riman, R.E., *et al*., *Solution synthesis of hydroxyapatite designer particulates.* Solid State Ionics, 2002. **151**(1-4): p. 393-402.
59. Deptula, A., *et al*., *Preparation of spherical powders of hydroxyapatite by sol-gel process.* Journal of Non-Crystalline Solids, 1992. **147-148**: p. 537-541.
60. Masuda Y, Matubara K, and Sakka S, *Synthesis of hydroxyapatite from metal alkoxides through sol-gel technique.* Journal of the Ceramic Society of Japan, 1990. **98**(11): p. 1266-1277.
61. Brendel T, Engel A, and Russel C, *Hydroxyapatite coatings by a polymeric route.* Journal of Materials Science: Materials in Medicine, 1992. **3**: p. 175-179.
62. Qiu Q, *et al*., *Bone growth on sol-gel calcium phosphate thin films in vitro.* Cells and Materials, 1993. **3**(4): p. 351-360.
63. Takahashi, H., *et al*., *Synthesis of Stoichiometric Hydroxyapatite by a Gel Route from the Aqueous-Solution of Citric and Phosphonoacetic Acids.* European Journal of Solid State and Inorganic Chemistry, 1995. **32**(7-8): p. 829-835.
64. Lopatin, C.M., *et al*., *Hydroxyapatite powders and thin films prepared by a sol-gel technique.* Thin Solid Films, 1998. **326**(1-2): p. 227-232.
65. Chai CS, *et al*., *Sol-gel derived hydroxyapatite coatings for biomedical applications.* Materials and Manufacturing Processes, 1995. **10**(2): p. 205-216.
66. Haddow, D.B., P.F. James, and R. Noort, *Characterization of sol-gel surfaces for biomedical applications.* Journal of Materials Science: Materials in Medicine, 1996. **7**(5): p. 255-260.
67. Haddow, D.B., P.F. James, and R. Van Noort, *Sol-gel derived calcium phosphate coatings for biomedical applications.* Journal of Sol-Gel Science and Technology, 1998. **13**(1-3): p. 261-265.
68. Gross, K.A., *et al*., *Thin hydroxyapatite coatings via sol-gel synthesis.* Journal of Materials Science: Materials in Medicine, 1998. **9**(12): p. 839-843.
69. Kalita, S.J. and H.A. Bhatt, *Nanocrystalline hydroxyapatite doped with magnesium and zinc: Synthesis and characterization.* Materials Science & Engineering C-Biomimetic and Supramolecular Systems, 2007. **27**(4): p. 837-848.
70. Weng, W. and J.L. Baptista, *Sol–gel derived porous hydroxyapatite coatings.* Journal of Materials Science: Materials in Medicine, 1998. **9**(3): p. 159-163.
71. Stoica, T.F., *et al*., *Hydroxyapatite films obtained by sol-gel and sputtering.* Thin Solid Films, 2008. **516**(22): p. 8112-8116.
72. Sanosh, K., P., *et al*., *Preparation and characterization of nano-hydroxyapatite powder using sol-gel technique.* Bulletin of Materials Science, 2009. **32**(5): p. 465-470.
73. Kumar, G.S., *et al*., *Synthesis and characterization of bioactive hydroxyapatite-calcite nanocomposite for biomedical applications.* Journal of Colloid and Interface Science, 2010. **349**(1): p. 56-62.
74. Itatani, K., *et al*., *Preparation of various calcium-phosphate powders by ultrasonic spray freeze-drying technique.* Materials Research Bulletin, 2000. **35**(4): p. 575-585.
75. Liu, J., *et al*., *Rapid formation of hydroxyapatite nanostructures by microwave irradiation.* Chemical Physics Letters, 2004. **396**(4-6): p. 429-432.
76. Arami, H., *et al*., *Rapid formation of hydroxyapatite nanostrips via microwave irradiation.* Journal of Alloys and Compounds, 2009. **469**(1-2): p. 391-394.

77. Parr Instrument Company. *Selection Guide to Parr Non-Stirred Pressure Vessels*. 2012? [Online] Available from: http://www.parrinst.com/products/non-stirred-pressure-vessels [Accessed 05 Feb 2012].
78. Ito, A., *et al*., *Hydrothermal growth of carbonate-containing hydroxyapatite single crystals.* Journal of Crystal Growth, 1996. **163**(3): p. 311-317.
79. Vijayalakshmi, U. and S. Rajeswari, *Preparation and Characterization of Microcrystalline Hydroxyapatite Using Sol Gel Method.* Trends in Biomaterials & Artificial Organs, 2006. **19**(2): p. 57-62.
80. Ebelman, M., *Untersuchungen über die Verbindung der Borsaure und Kielselsaure mit Aether.* Annales de Chimie et de Physique, 1846. **57**: p. 319-355.
81. Chai, C.S., K.A. Gross, and B. Ben-Nissan, *Critical ageing of hydroxyapatite sol-gel solutions.* Biomaterials, 1998. **19**(24): p. 2291-2296.
82. Gross, K.A. and C.C. Berndt, *Thermal processing of hydroxyapatite for coating production.* Journal of Biomedical Materials Research, 1998. **39**(4): p. 580-587.
83. Fischman, G., A. Clare, and L. Hench, *Bioceramics: Materials and Applications* 1995: The Americam Ceramic Society.
84. Lucas, L.C., *et al*., *Calcium phosphate coatings for medical and dental implants.* Colloids and Surfaces A: Physicochemical and Engineering Aspects, 1993. **77**(2): p. 141-147.
85. Sun, L.M., *et al*., *Surface characteristics and dissolution behavior of plasma-sprayed hydroxyapatite coating.* Journal of Biomedical Research, 2002. **62**: p. 228-236.
86. Cullity, B.D. and S.R. Stock, *Elements of X-Ray Diffraction* Third ed 2001: Prentice Hall. 664.
87. Ślósarczyk, A., *et al*., *The FTIR spectroscopy and QXRD studies of calcium phosphate based materials produced from the powder precursors with different CaP ratios.* Ceramics International, 1997. **23**(4): p. 297-304.
88. Rey, C., *et al*., *A resolution-enhanced Fourier Transform Infrared spectroscopic study of the environment of the CO_3^{2-} ion in the mineral phase of enamel during its formation and maturation.* Calcified Tissue International, 1991. **49**(4): p. 259-268.
89. Gibson, I.R., S.M. Best, and W. Bonfield, *Chemical characterization of silicon-substituted hydroxyapatite.* Journal of Biomedical Materials Research, 1999. **44**(4): p. 422-428.
90. Pena, J. and M. Vallet-Regi, *Hydroxyapatite, tricalcium phosphate and biphasic materials prepared by a liquid mix technique.* Journal of the European Ceramic Society, 2003. **23**(10): p. 1687-1696.
91. Liu, D.M., *et al*., *Structural evolution of sol-gel-derived hydroxyapatite.* Biomaterials, 2002. **23**(7): p. 1679-1687.
92. Nicolopoulos, S., *et al*., *Characterization by TEM of Local Crystalline Changes during Irradiation Damage of Hydroxyapatite Compounds.* Journal of Solid State Chemistry, 1995. **116**(2): p. 265-274.
93. Williams, D.B. and C.B. Carter, *Transmission Electron Microscopy: A Textbook for Materials Science* 1996: Springer.
94. Eddisford, P., A. Brown, and R. Brydson. *Identifying and quantifying the mechanism of electron beam induced damage and recovery in hydroxyapatite*. in *EMAG: Electron Microscopy and Analysis Group Conference 2007*. 2008. Bristol: IOP Publishing Ltd.

95. Egerton, R.F., P. Li, and M. Malac, *Radiation damage in the TEM and SEM.* Micron, 2004. **35**: p. 399-409.
96. Hunt, G. and M.D. Mehta, *Nanotechnology: Risk, Ethics and Law* First ed 2006, London: Earthscan. 296.
97. Hester, R.H. and R.M. Harrison, *Nanotechnology: Consequences for Human Health and the Environment* 2007: RSC Publishing.
98. Kagan, V.E., *et al*., *Carbon nanotubes degraded by neutrophil myeloperoxidase induce less pulmonary inflammation.* Nature Nanotechnology, 2010. **5**(5): p. 354-359.
99. Singh, N., *et al*., *The role of iron redox state in the genotoxicity of ultrafine superparamagnetic iron oxide nanoparticles.* Biomaterials, 2012. **33**(1): p. 163-170.
100. Vakurov, A., R. Brydson, and A. Nelson, *Electrochemical Modeling of the Silica Nanoparticle-Biomembrane Interaction.* Langmuir, 2012. **28**(2): p. 1246-1255.
101. Lewinski, N., V. Colvin, and R. Drezek, *Cytotoxicity of nanoparticles.* Small, 2008. **4**(1): p. 26-49.
102. Nel, A., *et al*., *Toxic potential of materials at the nanolevel.* Science, 2006. **311**(5761): p. 622-627.
103. Motskin, M., *et al*., *Hydroxyapatite nano and microparticles: Correlation of particle properties with cytotoxicity and biostability.* Biomaterials, 2009. **30**(19): p. 3307-3317.
104. Oberdorster, G., E. Oberdorster, and J. Oberdorster, *Nanotoxicology: An emerging discipline evolving from studies of ultrafine particles.* Environmental Health Perspectives, 2005. **113**(7): p. 823-839.
105. Donaldson, K., V. Stone, and W. MacNee, *The toxicology of ultrafine particles*, in *Particulate matter: Properties and effects upon health* 1999. p. 115-129.
106. Zhu, S.H., *et al*., *Hydroxyapatite nanoparticles as a novel gene carrier.* Journal of Nanoparticle Research, 2004. **6**(2-3): p. 307-311.
107. Shi, Z.L., *et al*., *Size effect of hydroxyapatite nanoparticles on proliferation and apoptosis of osteoblast-like cells.* Acta Biomaterialia, 2009. **5**(1): p. 338-345.
108. Fan, L.S., *Chemical looping systems for energy conversions* 2010, New Jersey & Canada: American Institute of Chemical Engineers and John Wiley & Sons, Inc.
109. Gupta, H. and L.S. Fan, *Carbonation Calcination Cycle Using High Reactivity Calcium Oxide for Carbon Dioxide Separation from Flue Gas.* Industrial & Engineering Chemistry Research, 2002. **41**(16): p. 4035-4042.
110. de Boer, Y., *Kyoto Protocol Reference Manual: On Accounting of Emissions and Assigned Amount*, 2008, United Nations Framework Convention on Climate Change (UNFCCC) Bonn, Germany.
111. Cooper C D and Alley F C, *Air Pollution Control*. Second ed 1994, Prospect Heights, IL: Wavelend Press.
112. Hester R E and Harrison R M, *Carbon Capture - Sequestration and Storage* 2009: RSC Publishing.
113. Lackner, K.S., *Climate Change: A Guide to CO_2 Sequestration.* Science, 2003. **300**(5626): p. 1677-1678.
114. Marchetti, C., *Geo-Engineering and CO_2 Problem.* Climatic Change, 1977. **1**(1): p. 59-68.
115. Herzog, H., *What future for carbon capture and sequestration?* Environmental Science & Technology, 2001. **35**(7): p. 148A-153A.

116. Alvarez, D. and J.C. Abanades, *Determination of the Critical Product Layer Thickness in the Reaction of CaO with CO_2.* Industrial & Engineering Chemistry Research, 2005. **44**(15): p. 5608-5615.
117. Florin, N.H. and A.T. Harris, *Enhanced hydrogen production from biomass with in situ carbon dioxide capture using calcium oxide sorbents.* Chemical Engineering Science, 2008. **63**(2): p. 287-316.
118. Ramkumar, S., N. Phalak, and L.-S. Fan, *Calcium Looping Process (CLP) for Enhanced Steam Methane Reforming.* Industrial & Engineering Chemistry Research, 2012. **51**(3): p. 1186-1192.
119. Rochelle, G.T., *Amine Scrubbing for CO_2 Capture.* Science, 2009. **325**(5948): p. 1652-1654.
120. Knofel, C., *et al*., *Study of Carbon Dioxide Adsorption on Mesoporous Aminopropylsilane-Functionalized Silica and Titania Combining Microcalorimetry and in Situ Infrared Spectroscopy.* The Journal of Physical Chemistry C, 2009. **113**(52): p. 21726-21734.
121. Brennecke, J.F. and B.E. Gurkan, *Ionic Liquids for CO_2 Capture and Emission Reduction.* The Journal of Physical Chemistry Letters, 2010. **1**(24): p. 3459-3464.
122. Figueroa, J.D., *et al*., *Advances in CO_2 capture technology - The U.S. Department of Energy's Carbon Sequestration Program.* International Journal of Greenhouse Gas Control, 2008. **2**(1): p. 9-20.
123. Lu, H., *et al*., *Nanostructured Ca-based sorbents with high CO_2 uptake efficiency.* Chemical Engineering Science, 2009. **64**(9): p. 1936-1943.
124. Bates, E.D., *et al*., *CO_2 capture by a task-specific ionic liquid.* Journal of the American Chemical Society, 2002. **124**(6): p. 926-927.
125. Curran, G.P., C.E. Fink, and E. Gorin, *Carbon dioxide acceptor gasification process*, in *Fuel Gasification* 1967, American Chemical Society. p. 141-165.
126. Silaban, A. and D.P. Harrison, *High temperature capture of carbon dioxide characteristics of the reversible reaction between CaO(s) and CO_2 (g).* Chemical Engineering Communications, 1995. **137**(1): p. 177-190.
127. Abanades, J.C., *The maximum capture efficiency of CO_2 using a carbonation/calcination cycle of $CaO/CaCO_3$.* Chemical Engineering Journal, 2002. **90**(3): p. 303-306.
128. Lu, H., E.P. Reddy, and P.G. Smirniotis, *Calcium Oxide Based Sorbents for Capture of Carbon Dioxide at High Temperatures.* Industrial & Engineering Chemistry Research, 2006. **45**(11): p. 3944-3949.
129. Manovic, V. and E.J. Anthony, *Steam reactivation of spent CaO-based sorbent for multiple CO_2 capture cycles.* Environmental Science & Technology, 2007. **41**(4): p. 1420-1425.
130. Martavaltzi, C.S. and A.A. Lemonidou, *Development of new CaO based sorbent materials for CO_2 removal at high temperature.* Microporous and Mesoporous Materials, 2008. **110**(1): p. 119-127.
131. Booras, G.S. and S.C. Smelser, *An engineering and economic evaluation of CO_2 removal from fossil-fuel-fired power plants.* Energy, 1991. **16**(11-12): p. 1295-1305.
132. Manzano, H., *et al*., *Hydration of Calcium Oxide Surface Predicted by Reactive Force Field Molecular Dynamics.* Langmuir, 2012. **28**(9): p. 4187-4197.
133. Abanades, J.C., E.S. Rubin, and E.J. Anthony, *Sorbent Cost and Performance in CO_2 Capture Systems.* Industrial & Engineering Chemistry Research, 2004. **43**(13): p. 3462-3466.

134. Wang, Y., S.Y. Lin, and Y. Suzuki, *Experimental study on CO_2 capture conditions of a fluidized bed limestone decomposition reactor.* Fuel Processing Technology, 2010. **91**(8): p. 958-963.
135. Pacciani, R., *et al.*, *How does the concentration of CO_2 affect its uptake by a synthetic Ca-based solid sorbent?* American Institute of Chemical Engineers Journal, 2008. **54**(12): p. 3308-3311.
136. Florin, N.H. and A.T. Harris, *Reactivity of CaO derived from nano-sized $CaCO_3$ particles through multiple CO_2 capture-and-release cycles.* Chemical Engineering Science, 2009. **64**(2): p. 187-191.
137. Liu, W., *et al.*, *Calcium Precursors for the Production of CaO Sorbents for Multicycle CO_2 Capture.* Environmental Science & Technology, 2009. **44**(2): p. 841-847.
138. Abanades, J.C., *et al.*, *Capture of CO_2 from combustion gases in a fluidized bed of CaO.* American Institute of Chemical Engineers Journal, 2004. **50**(7): p. 1614-1622.
139. Manovic, V., E.J. Anthony, and D. Loncarevic, *CO_2 looping cycles with CaO-based sorbent pretreated in CO_2 at high temperature.* Chemical Engineering Science, 2009. **64**(14): p. 3236-3245.
140. Lee, D.K., *An apparent kinetic model for the carbonation of calcium oxide by carbon dioxide.* Chemical Engineering Journal, 2004. **100**(1-3): p. 71-77.
141. Niu, S., *et al.*, *Thermogravimetric analysis of the relationship among calcium magnesium acetate, calcium acetate and magnesium acetate.* Applied Energy, 2010. **87**(7): p. 2237-2242.
142. Shimizu, T., *et al.*, *A Twin Fluid-Bed Reactor for Removal of CO_2 from Combustion Processes.* Chemical Engineering Research and Design, 1999. **77**(1): p. 62-68.
143. Abanades, J.C., *et al.*, *Cost Structure of a Postcombustion CO_2 Capture System Using CaO.* Environmental Science & Technology, 2007. **41**(15): p. 5523-5527.
144. Hughes, R.W., *et al.*, *Improved Long-Term Conversion of Limestone-Derived Sorbents for In Situ Capture of CO_2 in a Fluidized Bed Combustor.* Industrial & Engineering Chemistry Research, 2004. **43**(18): p. 5529-5539.
145. Silaban A, Narcida M, and Harrison D P, *Characteristics of the reversible reaction between $CO_2(g)$ and calcined dolomite.* Chemical Engineering Communications, 1996(146): p. 149–162.
146. Aihara, M., *et al.*, *Development of porous solid reactant for thermal-energy storage and temperature upgrade using carbonation/decarbonation reaction.* Applied Energy, 2001. **69**(3): p. 225-238.
147. Abanades, J.C. and D. Alvarez, *Conversion limits in the reaction of CO_2 with lime.* Energy & Fuels, 2003. **17**(2): p. 308-315.
148. Gonzalez, B., *et al.*, *Modeling of the Deactivation of CaO in a Carbonate Loop at High Temperatures of Calcination.* Industrial & Engineering Chemistry Research, 2008. **47**(23): p. 9256-9262.
149. Blamey, J., *et al.*, *The calcium looping cycle for large-scale CO_2 capture.* Progress in Energy and Combustion Science, 2011. **36**(2): p. 260-279.
150. Barker, R., *The reversibility of the reaction $CaCO_3 = CaO + CO_2$.* Journal of Applied Chemistry and Biotechnology, 1973. **23**(10): p. 733-742.
151. Lysikov, A.I., A.N. Salanov, and A.G. Okunev, *Change of CO_2 Carrying Capacity of CaO in Isothermal Recarbonation-Decomposition Cycles.* Industrial & Engineering Chemistry Research, 2007. **46**(13): p. 4633-4638.
152. Salvador, C., *et al.*, *Enhancement of CaO for CO_2 capture in an FBC environment.* Chemical Engineering Journal, 2003. **96**(1-3): p. 187-195.

153. Sun, P., *et al*., *The effect of CaO sintering on cyclic CO_2 capture in energy systems.* American Institute of Chemical Engineers Journal, 2007. **53**(9): p. 2432-2442.
154. Blamey, J., *et al*., *The calcium looping cycle for large-scale CO_2 capture.* Progress in Energy and Combustion Science, 2010. **36**(2): p. 260-279.
155. Grasa, G.S. and J.C. Abanades, *CO_2 Capture Capacity of CaO in Long Series of Carbonation/Calcination Cycles.* Industrial & Engineering Chemistry Research, 2006. **45**(26): p. 8846-8851.
156. Manovic, V. and E.J. Anthony, *Reactivation and remaking of calcium aluminate pellets for CO_2 capture.* Fuel, 2011. **90**(1): p. 233-239.
157. Blamey, J., *et al*., *Reactivation of a CaO-based sorbent for CO_2 capture from stationary sources.* Proceedings of the Combustion Institute, 2011. **33**(2): p. 2673-2681.
158. Li, Z.S., *et al*., *Synthesis, experimental studies, and analysis of a new calcium-based carbon dioxide absorbent.* Energy & Fuels, 2005. **19**(4): p. 1447-1452.
159. Wu, S.F., *et al*., *Properties of a Nano CaO/Al_2O_3 CO_2 Sorbent.* Industrial & Engineering Chemistry Research, 2007. **47**(1): p. 180-184.
160. Liu, W., *et al*., *Synthesis of Sintering-Resistant Sorbents for CO_2 Capture.* Environmental Science & Technology, 2010. **44**(8): p. 3093-3097.
161. Hannink, R.H.J., P.M. Kelly, and B.C. Muddle, *Transformation Toughening in Zirconia-Containing Ceramics.* Journal of the American Ceramic Society, 2000. **83**(3): p. 461-487.
162. West, A.R., *Basic Solid State Chemistry* 1999: John Wiley & Sons, Ltd.
163. Scott, H.G., *Phase relationships in the zirconia-yttria system.* Journal of Materials Science, 1975. **10**(9): p. 1527-1535.
164. Callister Jr., W.D., *Materials Science and Engineering: An Introduction. 6th Edition*. Sixth ed 2003: John Wiley & Sons, Inc.
165. Dell'Agli, G. and G. Mascolo, *Hydrothermal synthesis of ZrO_2-$Y2O_3$ solid solutions at low temperature.* Journal of the European Ceramic Society, 2000. **20**(2): p. 139-145.
166. Piticescu, R.R., *et al*., *Hydrothermal synthesis of zirconia nanomaterials.* Journal of the European Ceramic Society, 2001. **21**(10-11): p. 2057-2060.
167. Vasylkiv, O. and Y. Sakka, *Synthesis and Colloidal Processing of Zirconia Nanopowder.* Journal of the American Ceramic Society, 2001. **84**(11): p. 2489-2494.
168. Kolen'ko, Y.V., *et al*., *Synthesis of ZrO_2 and TiO_2 nanocrystalline powders by hydrothermal process.* Materials Science and Engineering: C-Biomimetic and Supramolecular Systems, 2003. **23**(6-8): p. 1033-1038.
169. Guiot, C., *et al*., *Nano Single Crystals of Yttria-Stabilized Zirconia.* Crystal Growth & Design, 2009. **9**(8): p. 3548-3550.
170. Hayashi, H., *et al*., *Hydrothermal synthesis of yttria stabilized ZrO_2 nanoparticles in subcritical and supercritical water using a flow reaction system.* Journal of Solid State Chemistry, 2009. **182**(11): p. 2985-2990.
171. Kumari, L., *et al*., *Controlled Hydrothermal Synthesis of Zirconium Oxide Nanostructures and Their Optical Properties.* Crystal Growth & Design, 2009. **9**(9): p. 3874-3880.
172. Piticescu, R.M., *et al*., *Hydrothermal synthesis of ceramic nanomaterials for functional applications.* Nanotechnology, 2003. **14**(2): p. 312-317.
173. Tyagi, B., *et al*., *Synthesis of Nanocrystalline Zirconia Using Sol-Gel and Precipitation Techniques.* Industrial & Engineering Chemistry Research, 2006. **45**(25): p. 8643-8650.

174. Heshmatpour, F. and R.B. Aghakhanpour, *Synthesis and characterization of nanocrystalline zirconia powder by simple sol–gel method with glucose and fructose as organic additives.* Powder Technology, 2011. **205**(1–3): p. 193-200.
175. Gaudon, M., E. Djurado, and N.H. Menzler, *Morphology and sintering behaviour of yttria stabilised zirconia (8-YSZ) powders synthesised by spray pyrolysis.* Ceramics International, 2004. **30**(8): p. 2295-2303.
176. Khollam, Y.B., *et al.*, *Synthesis of yttria stabilized cubic zirconia (YSZ) powders by microwave-hydrothermal route.* Materials Chemistry and Physics, 2001. **71**(3): p. 235-241.
177. Combemale, L., *et al.*, *Microwave synthesis of yttria stabilized zirconia.* Materials Research Bulletin, 2005. **40**(3): p. 529-536.
178. Earl, J.S., *Hydroxyapatite nanoparticles and dentine tubule infiltration* in *Institute for Materials Research*2007, University of Leeds: Leeds. p. 199.
179. Correia, R.N., *et al.*, *Wet synthesis and characterization of modified hydroxyapatite powders.* Journal of Materials Science: Materials in Medicine, 1996. **7**(8): p. 501-505.
180. Christoffersen, J., *et al.*, *A contribution to the understanding of the formation of calcium phosphates.* Journal of Crystal Growth, 1989. **94**(3): p. 767-777.
181. Rakovan, J., *Growth and Surface Properties of Apatite.* Reviews in Mineralogy and Geochemistry, 2002. **48**(1): p. 51-86.
182. Meyer, J.L. and G.H. Nancollas, *The effect of pH and temperature on the crystal growth of hydroxyapatite.* Archives of Oral Biology, 1972. **17**(11): p. 1623-1627.
183. West, A.R., *Solid State Chemistry and it's Applications* 1984: John Wiley & Sons, Ltd.
184. Orton. *Thermal Gravimetric Analysis*. Servicios e Instrumentos de México, S.A de C.V. 2003. [Online] Available from: http://www.docstoc.com/docs/55946964/Thermal-Gravimetric-Analysis [Accessed 07 July 2009].
185. Meenan, B.J., C. McClorey, and M. Akay, *Thermal analysis studies of poly(etheretherketone)/hydroxyapatite biocomposite mixtures.* Journal of Materials Science: Materials in Medicine, 2000. **11**(8): p. 481-489.
186. Mosmann, T., *Rapid colorimetric assay for cellular growth and survival: Application to proliferation and cytotoxicity assays.* Journal of Immunological Methods, 1983. **65**(1-2): p. 55-63.
187. Vandeloosdrecht, A.A., *et al.*, *A tetrazolium-based colorimetric MTT assay to quantitate human monocyte mediated cytotoxicity against leukemic cells from cell lines and patients with acute myeloid leukemia.* Journal of Immunological Methods, 1994. **174**(1-2): p. 311-320.
188. Alley, M.C., *et al.*, *Feasibility of Drug Screening with Panels of Human Tumor Cell Lines Using a Microculture Tetrazolium Assay.* Cancer Research, 1988. **48**(3): p. 589-601.
189. Shimadzu. *Thermogravimetric anaylzers: TGA-50 series. Online Product Brochure*. 2000? [Online] Available from: http://www.ssi.shimadzu.com/products/literature/Thermal/C160-E012.pdf [Accessed 06 Oct 2011].
190. Li, Z.-s., *et al.*, *Synthesis, Experimental Studies, and Analysis of a New Calcium-Based Carbon Dioxide Absorbent.* Energy & Fuels, 2005. **19**(4): p. 1447-1452.

191. Rodríguez, N., M. Alonso, and J.C. Abanades, *Average activity of CaO particles in a calcium looping system.* Chemical Engineering Journal, 2010. **156**(2): p. 388-394.
192. Jenkins, R., *X-ray Fluorescence Spectrometry* 1988, Canada: John Wiley & Sons, Inc.
193. Scherrer, P., *Bestimmung der Grösse und der inneren Struktur von Kolloidteilchen mittels Röntgenstrahlen.* Nachrichten von der Gesellschaft der Wissenschaften zu Göttingen, 1918. **26**: p. 98-100.
194. Glocker, R. and H. Schreiber, *Quantitative Röntgenspektralanalyse mit Kalterregung des Spektrums.* Annalen der Physik, 1928. **390**(8): p. 1089-1102.
195. Hoffmann, P. and H.R. Verma, *Atomic and nuclear analytical methods. XRF, Massbauer, XPS, NAA and ion-beam spectroscopic techniques.* Analytical and Bioanalytical Chemistry, 2008. **391**(6): p. 2103-2104.
196. Govindaraju, K., *1994 Compilation of working values and sample description for 383 geostandards.* Geostandards Newsletter, 1994. **18**(1): p. 1-158.
197. Imai, N., *et al*., *Compilation of analytical data for minor and trace elements in seventeen GSJ geochemical reference samples, "igneous rock series".* Geostandards Newsletter, 1995. **19**(2): p. 135-213.
198. Imai, N., *et al*., *Compilation of analytical data on nine GSJ geochemical reference samples, "Sedimentary rock series".* Geostandards Newsletter, 1996. **20**(2): p. 165-216.
199. Imai, N., *et al*., *1998 compilation of analytical data for five GSJ geochemical reference samples: The "instrumental analysis series".* Geostandards Newsletter, 1999. **23**: p. 223-250.
200. Mayer, J. *X-Ray Fluorescence*. 2000? [Online] Available from: http://ion.asu.edu/descript_xrf.htm [Accessed 15 Apr 2011].
201. Ferraro, J.R. and K. Krishnan, *Practical Fourier transform infrared spectroscopy : industrial and laboratory chemical analysis* 1990, San Diego; London: Academic Press. 534.
202. Gunther, D., *et al*., *Capabilities of an Argon Fluoride 193 nm Excimer Laser for Laser Ablation Inductively Coupled Plasma Mass Spectometry Microanalysis of Geological Materials.* Journal of Analytical Atomic Spectrometry, 1997. **12**(9): p. 939-944.
203. Wolf, R. *What is ICP-MS?… and more importantly, what can it do?* 2005. U.S Geological Survey. [Online] Available from: http://minerals.cr.usgs.gov/icpms/intro.html [Accessed 07 Jul 2011].
204. Reimschuessel, A.C., *Scanning electron microscopy - Part I.* Journal of Chemical Education, 1972. **49**(8): p. A413.
205. Fultz B and Howe J M, *Transmission Electron Micrscopy and Diffractometry of Materials*. 2nd ed2002, Verlag Berlin Heidelberg New York: Springer.
206. Garrat-Reed, A. and D. Bell, *Energy Dispersive X-ray Analysis in the Electron Microscope*2003: BIOS Scientific Publishers Ltd.
207. Head, M. *Energy Dispersive X-Ray (EDX) Analysis*. 2006. [Online] Available from: http://www.concrete.cv.ic.ac.uk/durability/research%20techniques%20sem%20edx.htm#Point%20Analysis [Accesses 19 Dec 2008].
208. Belkoura, L., L. Liz-Marzán, and J. Crawsha, *Energy Dispersive X-ray Microanalysis (EDX)*, 2006, Soft Matter Composites.
209. Allen, T., *Particle size measurement*. Third ed 1981: Chapman and Hall. 678.

210. Powers, K.W., *et al*., *Research strategies for safety evaluation of nanomaterials. Part VI. Characterization of nanoscale particles for toxicological evaluation.* Toxicological Sciences, 2006. **90**(2): p. 296-303.
211. Hondow, N., *et al*., *Quantitative Characterization of Nanoparticle Agglomeration within Biological Media.* Journal of Nanoparticle Research, 2012. **14**(7): p. 977.
212. Filipe, V., A. Hawe, and W. Jiskoot, *Critical Evaluation of Nanoparticle Tracking Analysis (NTA) by NanoSight for the Measurement of Nanoparticles and Protein Aggregates.* Pharmaceutical Research, 2010. **27**(5): p. 796-810.
213. Holzmann, D., *et al*., *Hydroxyapatite nanoparticles as novel low-refractive index additives for the long-term UV-photoprotection of transparent composite materials.* Journal of Materials Chemistry, 2009. **19**(43): p. 8102-8106.
214. Malvern Instruments Ltd. *Dynamic Light Scattering Instrumentation for classical 90 degree scattering measurements*. 2010? [Online] Available from: http://www.malvern.com/LabEng/technology/dynamic_light_scattering/classical_90_degree_scattering.htm [Accessed 01 Jun 2012].
215. Jevtic, M., *et al*., *Crystal structure of hydroxyapatite nanorods synthesized by sonochemical homogeneous precipitation.* Crystal Growth & Design, 2008. **8**(7): p. 2217-2222.
216. Westheimer FH, Huang S, and C. F., *Rates and mechanisms of hydrolysis of esters of phosphorus acids.* J Am Chem Soc, 1988. **110**: p. 181-185.
217. NCBI. *Triethyl phosphite - compound summary*. U.S. National Library of Medicine. 2006. [Online] Available from: http://pubchem.ncbi.nlm.nih.gov/summary/summary.cgi?cid=31215 [Accessed 03 Mar 2011].
218. NCBI. *Triethyl phosphate - compound summary*. U.S. National Library of Medicine. 2006. [Online] Available from: http://pubchem.ncbi.nlm.nih.gov/summary/summary.cgi?cid=6535&loc=ec_rcs [Accessed 03 Mar 2011].
219. Cason, J. and W.N. Baxter, *Reaction of Trialkyl Phosphites with Methanol1*. The Journal of Organic Chemistry, 1958. **23**(9): p. 1302-1305.
220. Mukaiyama, T., O. Mitsunobu, and T. Obata, *Oxidation of Phosphites and Phosphines via Quaternary Phosphonium Salts.* The Journal of Organic Chemistry, 1965. **30**(1): p. 101-105.
221. Swanson H E and R.K. Fuyat, *Calcite.* Standard X-ray Diffraction Patterns, 1953. **539**: p. 52-53.
222. Arends, J., *et al*., *Preparation of pure hydroxyapatite single crystals by hydrothermal recrystallization.* Journal of Crystal Growth, 1979. **46**(2): p. 213-220.
223. Ermrich, M. and F. Peters, *PDF# 55-0898.* Reinheim, Germany, Private Communication 2004.
224. Ermrich, M. and F. Peters, *X-ray powder diffraction data of synthetic beta-Tricalcium Phosphate.* Materialwissenschaft Und Werkstofftechnik, 2006. **37**(6): p. 526-529.
225. Catti, M., G. Ferraris, and A. Filhol, *Hydrogen-Bonding in Crystalline State - $CaHPO_4$ (Monetite), P1bar or P1? - Novel Neutron-Diffraction Study.* Acta Crystallographica Section B: Structural Science, 1977. **33**(4): p. 1223-1229.

226. Jay, A.H. and K.W. Andrews, *Note on Oxide Systems Pertaining to Steel-Making Furnace Slags. FeO-MnO, FeO-MgO, CaO-MnO, MgO-MnO.* The Journal of the Iron and Steel Institute, 1945. **152**(15): p. 18.
227. Raynaud, S., *et al*., *Calcium phosphate apatites with variable Ca/P atomic ratio I. Synthesis, characterisation and thermal stability of powders.* Biomaterials, 2002. **23**(4): p. 1065-1072.
228. Fathi, M.H. and A. Hanifi, *Evaluation and characterization of nanostructure hydroxyapatite powder prepared by simple sol-gel method.* Materials Letters, 2007. **61**(18): p. 3978-3983.
229. Ruys, A.J., *et al*., *Hydroxyapatite sintering phenomena: densification and dehydration behaviour.* Ceramics: Adding the Value., 1992. **2**: p. 605-610.
230. Barinov, S.M., *et al*., *Carbonate release from carbonated hydroxyapatite in the wide temperature range.* Journal of Materials Science-Materials in Medicine, 2006. **17**(7): p. 597-604.
231. Ettarh, C. and A.K. Galwey, *A kinetic and mechanistic study of the thermal decomposition of calcium nitrate.* Thermochimica Acta, 1996. **288**(1-2): p. 203-219.
232. Dickens, B., S. L., and W.E. Brown, *Crystallographic Studies of Role of Mg as a Stabilizing Impurity in Beta-$Ca_3(PO_4)_2$ .1. Crystal-Structure of Pure Beta-$Ca_3(PO_4)_2$.* Journal of Solid State Chemistry, 1974. **10**(3): p. 232-248.
233. Chowdhury, A., *et al*., *Fundamental Issues in the Synthesis of Ferroelectric $Na_{0.5}K_{0.5}NbO_3$ Thin Films by Sol Gel Processing.* Chemistry of Materials, 2010. **22**(13): p. 3862-3874.
234. Chowdhury, A., P.R. Thompson, and S.J. Milne, *TGA-FTIR study of a lead zirconate titanate gel made from a triol-based sol-gel system.* Thermochimica Acta, 2008. **475**(1-2): p. 59-64.
235. van der Houwen, J.A.M., *et al*., *The effect of organic ligands on the crystallinity of calcium phosphate.* Journal of Crystal Growth, 2003. **249**(3-4): p. 572-583.
236. Slosarczyk, A., Z. Paszkiewicz, and C. Paluszkiewicz, *FTIR and XRD evaluation of carbonated hydroxyapatite powders synthesized by wet methods.* Journal of Molecular Structure, 2005. **744-747**(0): p. 657-661.
237. Arends, J., *et al*., *A Calcium Hydroxyapatite Precipitated from an Aqueous-Solution - an International Multimethod Analysis.* Journal of Crystal Growth, 1987. **84**(3): p. 515-532.
238. Apfelbaum, F., *et al*., *An FTIR study of carbonate in synthetic apatites.* Journal of Inorganic Biochemistry, 1992. **45**(4): p. 277-282.
239. Panda, R.N., *et al*., *FTIR, XRD, SEM and solid state NMR investigations of carbonate-containing hydroxyapatite nano-particles synthesized by hydroxide-gel technique.* Journal of Physics and Chemistry of Solids, 2003. **64**(2): p. 193-199.
240. Krajewski, A., *et al*., *Synthesis of carbonated hydroxyapatites: efficiency of the substitution and critical evaluation of analytical methods.* Journal of Molecular Structure, 2005. **744**: p. 221-228.
241. Berry, E.E., *The structure and composition of some calcium-deficient apatites.* Journal of Inorganic and Nuclear Chemistry, 1967. **29**(2): p. 317-327.
242. Reed, W.P., *Bonemeal - Certificate of Analysis. Standard Reference Material 1486*, 1992, National Institute of Standards & Technology: Gaithersburg, MD 20899.
243. Jahl, M.J. and R.M. Barnes, *Sealed inductively coupled plasma-atomic emission spectroscopy II: determination of phosphorus.* Spectrochimica Acta Part B: Atomic Spectroscopy, 1992. **47**(7): p. 923-934.

244. Bruchert, W. and J. Bettmer, *DNA quantification approach by GE-ICP-SFMS and complementary total phosphorus determination by ICP-SFMS.* Journal of Analytical Atomic Spectrometry, 2006. **21**(11): p. 1271-1276.
245. Shah, M. and J.A. Caruso, *Inductively coupled plasma mass spectrometry in separation techniques: Recent trends in phosphorus speciation.* Journal of Separation Science, 2005. **28**(15): p. 1969-1984.
246. Christoffersen, J., J. Dohrup, and M.R. Christoffersen, *The importance of formation of hydroxyl ions by dissociation of trapped water molecules for growth of calcium hydroxyapatite crystals.* Journal of Crystal Growth, 1998. **186**(1-2): p. 275-282.
247. Prado Da Silva, M.H., *et al*., *Transformation of monetite to hydroxyapatite in bioactive coatings on titanium.* Surface and Coatings Technology, 2001. **137**(2-3): p. 270-276.
248. Nobbmann, U., *et al*., *Dynamic light scattering as a relative tool for assessing the molecular integrity and stability of monoclonal antibodies.* Biotechnology & genetic engineering reviews, 2007. **24**: p. 117-28.
249. Kaszuba, M., *et al*., *Resolving concentrated particle size mixtures using dynamic light scattering.* Particle & Particle Systems Characterization, 2007. **24**(3): p. 159-162.
250. Bilton, M., A.P. Brown, and S.J. Milne, *Comparison of Hydrothermal and Sol-Gel Synthesis of Nano-Particulate Hydroxyapatite by Characterisation at the Bulk and Particle Level.* Open Journal of Inorganic Non-metallic Materials, 2012. **2**(1): p. 1-10.
251. Bilton, M., A.P. Brown, and S.J. Milne, *Sol-gel synthesis and characterisation of nano-scale hydroxyapatite.* Journal of Physics: Conference Series, 2010. **241**(1).
252. Daculsi, G., *Biphasic calcium phosphate concept applied to artificial bone, implant coating and injectable bone substitute.* Biomaterials, 1998. **19**(16): p. 1473-1478.
253. Shimazaki, K. and V. Mooney, *Comparative-Study of Porous Hydroxyapatite and Tricalcium Phosphate as Bone Substitute.* Journal of Orthopaedic Research, 1985. **3**(3): p. 301-310.
254. Shimizu, T., *et al*., *Bone Ingrowth into Porous Calcium-Phosphate Ceramics - Influence of Pulsing Electromagnetic-Field.* Journal of Orthopaedic Research, 1988. **6**(2): p. 248-258.
255. Ohgushi, H., *et al*., *Marrow Cell Induced Osteogenesis in Porous Hydroxyapatite and Tricalcium Phosphate - a Comparative Histomorphometric Study of Ectopic Bone-Formation.* Journal of Biomedical Materials Research, 1990. **24**(12): p. 1563-1570.
256. Hench, L.L., *Bioceramics - From Concept to Clinic* American Ceramic Society Bulletin, 1993. **72**(4): p. 93-98.
257. Tamimi, F., *et al*., *Bone regeneration in rabbit calvaria with novel monetite granules.* Journal of Biomedical Materials Research Part A, 2008. **87A**(4): p. 980-985.
258. Klammert, U., *et al*., *Cytocompatibility of brushite and monetite cell culture scaffolds made by three-dimensional powder printing.* Acta Biomaterialia, 2009. **5**(2): p. 727-734.
259. Hsieh, M.-F., *et al*., *Phase purity of sol-gel-derived hydroxyapatite ceramic.* Biomaterials, 2001. **22**(19): p. 2601-2607.
260. Orlovskii, V.P., V.S. Komlev, and S.M. Barinov, *Hydroxyapatite and Hydroxyapatite-Based Ceramics.* Inorganic Materials, 2002. **38**(10): p. 973-984.

261. Thurman, R.B., C.P. Gerba, and G. Bitton, *The molecular mechanisms of copper and silver ion disinfection of bacteria and viruses.* Critical Reviews in Environmental Control, 1989. **18**(4): p. 295-315.
262. Kim, T.N., *et al*., *Antimicrobial effects of metal ions (Ag^{+}, Cu^{2+}, Zn^{2+}) in hydroxyapatite.* Journal of Materials Science: Materials in Medicine, 1998. **9**(3): p. 129-134.
263. Rameshbabu, N., *et al*., *Antibacterial nanosized silver substituted hydroxyapatite: Synthesis and characterization.* Journal of Biomedical Materials Research Part A, 2007. **80A**(3): p. 581-591.
264. Bigi, A., *et al*., *Strontium-substituted hydroxyapatite nanocrystals.* Inorganica Chimica Acta, 2007. **360**(3): p. 1009-1016.
265. Grynpas, M.D., *et al*., *Strontium increases vertebral bone volume in rats at a low dose that does not induce detectable mineralization defect.* Bone, 1996. **18**(3): p. 253-259.
266. Thian, E.S., *et al*., *Silicon-substituted hydroxyapatite thin films: Effect of annealing temperature on coating stability and bioactivity.* Journal of Biomedical Materials Research Part A, 2006. **78A**(1): p. 121-128.
267. Thian, E.S., *et al*., *Novel silicon-doped hydroxyapatite (Si-HA) for biomedical coatings: An in vitro study using acellular simulated body fluid.* Journal of Biomedical Materials Research Part B: Applied Biomaterials, 2006. **76B**(2): p. 326-333.
268. Chappell, H. and P. Bristowe, *Density functional calculations of the properties of silicon-substituted hydroxyapatite.* Journal of Materials Science: Materials in Medicine, 2007. **18**(5): p. 829-837.
269. Qaisar, S.A., *et al*., *Sol-gel synthesis and TEM-EDX characterisation of hydroxyapatite nanoscale powders modified by Mg, Sr or Ti.* Journal of Physics Conference Series, 2010. **241**(1).
270. Uchida, A., *et al*., *Slow Release of Anticancer Drugs from Porous Calcium Hydroxyapatite Ceramic.* Journal of Orthopaedic Research, 1992. **10**(3): p. 440-445.
271. Alwan, W.H., *et al*., *Hydroxyapatite and Urate Crystal Induced Cytokine Release by Macrophages.* Annals of the Rheumatic Diseases, 1989. **48**(6): p. 476-482.
272. Ginebra, M.P., T. Traykova, and J.A. Planell, *Calcium phosphate cements as bone drug delivery systems: A review.* Journal of Controlled Release, 2006. **113**(2): p. 102-110.
273. Tschoppe, P., *et al*., *Enamel and dentine remineralization by nano-hydroxyapatite toothpastes.* Journal of Dentistry, 2011. **39**(6): p. 430-437.
274. Potoczek, M., *Hydroxyapatite foams produced by gelcasting using agarose.* Materials Letters, 2008. **62**(6-7): p. 1055-1057.
275. Silaban, A., M. Narcida, and D.P. Harrison, *Calcium acetate as a sorbent precursor for the removal of carbon dioxide from gas streams at high temperature.* Resources, Conservation and Recycling, 1992. **7**(1-3): p. 139-153.
276. Lu, H., *et al*., *Flame-Made Durable Doped-CaO Nanosorbents for CO_2 Capture.* Energy & Fuels, 2008. **23**(2): p. 1093-1100.
277. Koirala, R., *et al*., *Effect of Zirconia Doping on the Structure and Stability of CaO-Based Sorbents for CO_2 Capture during Extended Operating Cycles.* The Journal of Physical Chemistry C, 2011. **115**(50): p. 24804-24812.
278. Musumeci, A.W., R.L. Frost, and E.R. Waclawik, *A spectroscopic study of the mineral paceite (calcium acetate).* Spectrochimica Acta Part A: Molecular and Biomolecular Spectroscopy, 2007. **67**(3-4): p. 649-661.

279. Panzer, J., *Nature of Calcium Acetate.* Journal of Chemical & Engineering Data, 1962. **7**(1): p. 140-142.
280. Judd, M.D., B.A. Plunkett, and M.I. Pope, *Thermal-Decomposition of Calcium, Sodium, Silver and Copper(Ii) Acetates.* Journal of Thermal Analysis, 1974. **6**(5): p. 555-563.
281. Xu, W.Z., D. Raftery, and J.S. Francisco, *Effect of irradiation sources and oxygen concentration on the photocatalytic oxidation of 2-propanol and acetone studied by in situ FTIR.* Journal of Physical Chemistry B, 2003. **107**(19): p. 4537-4544.
282. Kazarian, S.G., *et al*., *Specific Intermolecular Interaction of Carbon Dioxide with Polymers.* Journal of the American Chemical Society, 1996. **118**(7): p. 1729-1736.
283. de Leeuw, N.H. and S.C. Parker, *Surface Structure and Morphology of Calcium Carbonate Polymorphs Calcite, Aragonite, and Vaterite:â€‰ An Atomistic Approach.* The Journal of Physical Chemistry B, 1998. **102**(16): p. 2914-2922.
284. Domingo, C., *et al*., *Calcite precipitation by a high-pressure CO_2 carbonation route.* The Journal of Supercritical Fluids, 2006. **36**(3): p. 202-215.
285. Prah, J., J. Macek, and G. Drazic, *Precipitation of calcium carbonate from a calcium acetate and ammonium carbamate batch system.* Journal of Crystal Growth, 2010. **324**(1): p. 229-234.
286. Rodriguez-Blanco, J.D., S. Shaw, and L.G. Benning, *The kinetics and mechanisms of amorphous calcium carbonate (ACC) crystallization to calcite, via vaterite.* Nanoscale, 2011. **3**(1): p. 265-271.
287. Ramachandran, V.S., P.J. Sereda, and R.F. Feldman, *Mechanism of Hydration of Calcium Oxide.* Nature, 1964. **201**(4916): p. 288-289.
288. Rouse, R., *Private Communication*, 1980: Dept. of Geological Sciences, Univ. of Michigan, Ann Arbor, MI, USA.
289. Chaix-Pluchery, O., *et al*., *Structural prereactional transformations in $Ca(OH)_2$.* Journal of Solid State Chemistry, 1987. **67**(2): p. 225-234.
290. Mess, D., A.F. Sarofim, and J.P. Longwell, *Product Layer Diffusion during the Reaction of Calcium Oxide with Carbon Dioxide.* Energy & Fuels, 1999. **13**(5): p. 999-1005.
291. Swanson H E and Fuyat R K, Natl. Bur. Stand (US) Circ., 1953. **539**: p. 23.
292. Li, Z.S., N.S. Cai, and Y.Y. Huang, *Effect of preparation temperature on cyclic CO_2 capture and multiple carbonation-calcination cycles for a new Ca-based CO_2 sorbent.* Industrial & Engineering Chemistry Research, 2006. **45**(6): p. 1911-1917.
293. Howard, C.J., R.J. Hill, and B.E. Reichert, *Structures of ZrO_2 polymorphs at room temperature by high-resolution neutron powder diffraction*, in *Acta Crystallographica Section B* 1988. p. 116-120.
294. Varez, A., E. Garcia-Gonzalez, and J. Sanz, *Cation miscibility in CeO_2-ZrO_2 oxides with fluorite structure. A combined TEM, SAED and XRD Rietveld analysis.* Journal of Materials Chemistry, 2006. **16**(43): p. 4249-4256.
295. Horiuchi, H., *et al*., *Time-of-flight neutron-diffraction study of a single-crystal of yttria-stabilized zirconia, $Zr(Y)O_{1.862}$, at high-temperature and in an applied electrical field.* Acta Crystallographica Section B-Structural Science, 1984. **40**(Aug): p. 367-372.
296. Lamas, D.G., *et al*., *Crystal structure of pure ZrO_2 nanopowders.* Scripta Materialia, 2006. **55**(6): p. 553-556.

297. Levin, I., *et al*., *Phase equilibria, crystal structures, and dielectric anomaly in the $BaZrO_3$-$CaZrO_3$ system.* Journal of Solid State Chemistry, 2003. **175(**2): p. 170-181.
298. Boysen, H., *et al*., *Structure and oxygen mobility in mayenite ($Ca_{12}Al_{14}O_{33}$): a high-temperature neutron powder diffraction study.* Acta Crystallographica Section B-Structural Science, 2007. **63**: p. 675-682.
299. Bilton, M., A.P. Brown, and S.J. Milne, *Investigating the optimum conditions for the formation of calcium oxide, used for CO_2 sequestration, by thermal decomposition of calcium acetate.* Journal of Physics: Conference Series, 2012. **371**(1).
300. Molinder, R., *et al*., *In situ X-ray diffraction of CaO based CO_2 sorbents.* Energy & Environmental Science, 2012.